CRANFIELD UNIVERSITY

SAFIAH BINTI ZULKIFLI

DEVELOPMENT OF A K-BAND FMCW FLEXIBLE RADAR PROTOTYPE FOR DETECTION AND CLASSIFICATION OF NANO-DRONES

CRANFIELD DEFENCE AND SECURITY
Centre for Electronic Warfare Information & Cyber

PhD
Academic Year: 2016-2020

Supervisor: DR ALESSIO BALLERI
December 2020

CRANFIELD UNIVERSITY

CRANFIELD DEFENCE AND SECURITY
Centre for Electronic Warfare Information & Cyber

PhD

Academic Year 2016 - 2020

SAFIAH BINTI ZULKIFLI

DEVELOPMENT OF A K-BAND FMCW FLEXIBLE RADAR PROTOTYPE FOR DETECTION AND CLASSIFICATION OF NANO-DRONES

Supervisor: DR ALESSIO BALLERI
December 2020

This thesis is submitted in partial fulfilment of the requirements for the degree of PhD

ABSTRACT

Nano-drones of the size of an insect can be used to perform stealthy surveillance or to gather intelligence crucial to attack roles at a relatively short range and within enclosed spaces and buildings. Conventional radar systems have been optimised to detect and classify bigger targets and are not specifically designed to detect nano-targets of less than 5 cm in size. Hence, this project aims to develop a radar system to detect and classify an insect-like size drone that corresponds to a low RCS. This will exhibit challenges due to the nature of the weak echoed signal that will be masked by an uninterested target with a stronger echoed signal. To tackle this sort of problem, micro-Doppler extraction is applied for better target detection. This type of target that consists of a bladed propeller will give rise to a significant micro-Doppler signature that will contribute to the discernment of the interested target.

An ad-hoc S-band FMCW radar prototype using off-the-shelf components has been successfully delivered. This prototype act as a groundwork for the next research phase of design and development for a higher frequency. Then, with the strong foundation of the S-band demonstrator, a flexible K-band FMCW radar prototype has successfully delivered aiming to meet the research purpose. The radar prototype offers a wide range of flexibility for the user to select the radar parameters (like operating frequency, ramp duration, bandwidth and integration time) and configure its performance. It will collect the signatures of real targets (nano-drone model) so that their performance can be assessed on experimental data. The results demonstrated that a nano-drone, a small size of less than 5 cm can be detected with the radar prototype developed.

Keywords:

Micro-Doppler Signature, FMCW Radar Prototype, Time-Frequency Analysis, Nano-size Target, Nano-drones.

ACKNOWLEDGEMENTS

I would like to extend my deepest gratitude to the following below:

For his teaching, guidance, assistance throughout the research progress. I am grateful in abundance for all the supervision given that polishes me to become a radar engineer. Without any fundamentals and background in the beginning it would be impossible for me to complete my study. Despite my supervisor's direction, my pace in this journey become enlightened and possible. Special thanks go to him, Dr Alessio Balleri.

For the investment in funding my study, heartfelt thanks go to the school of Aerospace Engineering, Universiti Sains Malaysia (USM) and Ministry of Education Malaysia for the meaningful budget throughout the year. Special thanks go to Cranfield University Shrivenham campus for the comfy working area, equipped lab and generous skills courses were available.

For the supportive and welcoming friendship, many thanks go to Nasyitah Ghazali, Krasin Georgiev, Luc Fourtinon, Leon Kocjancic, Gareth Frazer, Benjamin Griffin, and Michelle Charles. Not to forget Andre for his marvellous circuit connection. This research would not be a success without his help. And Mandy Smith, for the writing guidelines and radar resources that alleviate my understanding and comprehension of this research.

For the love, patience, endurance and valuable support for me and my family members. Deepest gratitude for your helping hand, Safwan Abd Nasir. My four babies; Aeshah, Fawwaz, Irfan and Anas for motivating me in their unique ways. They are my prime factors behind success. I am truly indebted to my beloved parents; they are both my driving force to pursue my path. Last but not least, my in-laws, siblings, great family members and friends.

TABLE OF CONTENTS

LIST OF FIGURES

LIST OF TABLES

LIST OF ABBREVIATIONS

ADAS	Advanced Driver Assistance System
ADC	Analogue-to-Digital Converter
AM	Amplitude Modulation
AWG	Arbitrary Waveform Generator
CA-CFAR	Cell Averaging – Constant False Alarm Rate
CAMD	Circular Average Magnitude Difference
CC	Circular Correlation
CVD	Cadence Velocity Diagram
CW	Continuous Wave
CWT	Continuous Wavelet Transform
DAR	Digital Array Radar
DC	Direct Current
DSP	Digital Signal Processing
EHT	Extended Hough Transform
EM	Electromagnetic Waveform
EMD	Empirical-Mode Decomposition
FCC	Federal Communication Commission
FFT	Fast Fourier Transform
FM	Frequency Modulation
FMCW	Frequency Modulated Continuous Wave
FSR	Forward Scatter Radar
GNSS	Global Navigation Satellite System
HERM	Helicopter Rotor Modulation
HLR	Horizontal Looking Radar
HT	Hough Transform
IF	Intermediate Frequency
IR	Infrared
LFM	Linear Frequency Modulation
LHS	Left-Hand Side
LIDAR	Light Detection & Ranging
LNA	Low Noise Amplifier
LO	Local Oscillator

LPF	Low Pass Filter
MAV	Micro Air Vehicle
MIMO	Multiple Input Multiple Output
MuRPSB	Multi-Channel Radar for Perimeter Surveillance
NAV	Nano Air Vehicle
PAV	Pico Air Vehicle
PBR	Passive Bistatic Radar
PD	Power Divider
PM	Phase Modulation
PRF	Pulse Repetition Frequency
RADAR	Radar Detection & Ranging
RAM	Radar Absorbing Material
RAWIS	Radar Warning and Information System
RC	Remote Control
RCS	Radar Cross Section
RDM	Range-Doppler Map
RF	Radio Frequency
RHS	Right-Hand Side
RTI	Range Time Intensity
RTT	Round-Trip Time
SDR	Software-Defined Radar
SSRS	Scanning Surveillance Radar System
SNR	Signal-to-Noise Ratio
STFT	Short-Time Fourier Transform
SVC	Support Vector Classifier
SVD	Singular Value Decomposition
TVD	Time Velocity Diagram
UAV	Unmanned Aerial Vehicle
UWB	Ultra-Wideband
VCO	Voltage Control Oscillator
VLR	Vertical Looking Radar
μUAV	Micro-Unmanned Aerial Vehicle

1 INTRODUCTION

This chapter gives an overview of the whole project on which this thesis is based. Section 1.1 presents the motivation and background of the research. Then, Section 1.2 briefly explains the outline of this research which includes the aims, objectives and significance of the study. Section 1.3 describes the layout of the thesis with some of the accomplishments and achievements from this study.

1.1 Motivation & Research Background

Military operations have reaped the benefits of drones back in the 1900s [1]. Initiated during World War 1, and this innovation continuously revolutionized into an advanced and sophisticated air force technology. More emerging drones had been deployed over the past years and the most well-known military drones were Predator (Length 8.23 m, Wingspan 14.8 m, Height 2.1 m), Reaper (Length 11 m, Wingspan 20 m, Height 3.81 m) and Global Hawk (Length 14.5 m, Wingspan 39.9 m, Height 4.7 m) that were integrated with modern avionics and navigation system. These types of drones were among the pioneers that are being updated from time to time, even though the size is still reasonably large. The pilotless, remote control and pre-programmed route have put the drones in the catbird seat. A lot of attention has been focused on the improved model of drones with a variety of features embedded with them. And surprisingly, these drones have become mostly acceptable by the civilian after the drone is made with reduced in weight, size and inherently cost.

Authors in [2] have outlined and grouped some of the drones according to their size and weight as shown in Figure 1.1. The spectrum illustrates that the drone can be as large as a commercial aircraft with a wingspan of 61 m long and as small as a speck of dust with a 1 mm long wingspan. The size of the drones will depend on the operational task it is made. Referring to Figure 1.1, Unmanned

Aerial Vehicle (UAV) for example, are made for a heavy-duty task. So, using a combustion engine will result in a longer flight endurance and larger radial distance that it can fly. Whereas others used electrical motors is enough for a shorter radial distance and a shorter flight endurance. Hence, this reduces the cost and is affordable to everyone. The micro-UAV (μUAV) which is in between UAV and MAV are sometimes consider as mini-UAVs with a wingspan between 1 m to 2 m in size. Micro Air Vehicle (MAV), Nano Air Vehicle (NAV) and Pico Air Vehicle (PAV) are sometimes inconsistent with the dimension. However, this research will be mainly interested in between the NAV and PAV which is less than 5 cm in size and will refer to it as nano-drone. These insect-like size drones are already proven to be existing today.

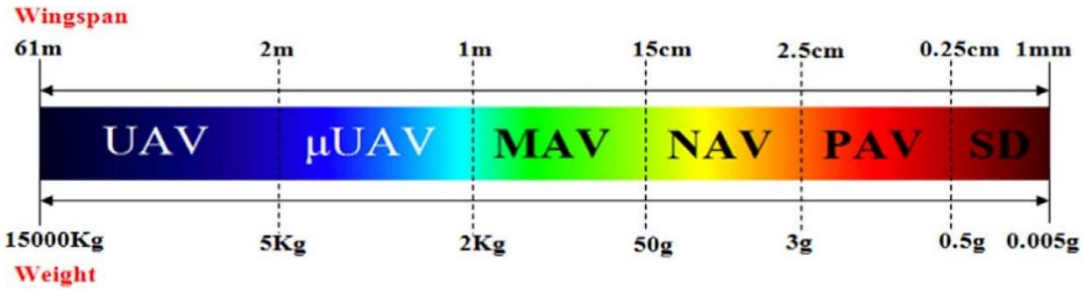

Figure 1.1: Spectrum of Drones Classification According to Size and Weight [2]

This great breakthrough in the drone field has great implications for national security and privacy [2-4]. Black Hornet, one of the recent military nano-drone that is actively used these days have become a significant transformation to the military operation [5]. The size of the Black Hornet that fits in the palm of one hand is just 16.8 cm long [6]. A closed-up of this nano-drone is illustrated in Figure 1.2 that presents the properties of the drone. This gives an advantage to the drone to intrude and invade a certain building without the awareness of the opponent. On top of that, it is equipped with a thermal camera that enables the user to navigate and control within 2 km away from the drone. This pocket-sized technology is lightweight, portable and easily operated after a few minutes of training will allow the military squad to plan the best mission execution and avoid any harmful situation. In 2011, the British army was one of the earlier squads who have first deployed this nano-drone back in Afghanistan. And by 2018, these Black Hornets again had already been used by several countries

(like Australia, France, Germany, Netherlands, Norway, and India) for their military operations. Australian army, as in Figure 1.3, is one of the biggest users that utilized this nano-drone in their military operation. It is believed that a more sophisticated nano-drone will emerge to meet this purpose.

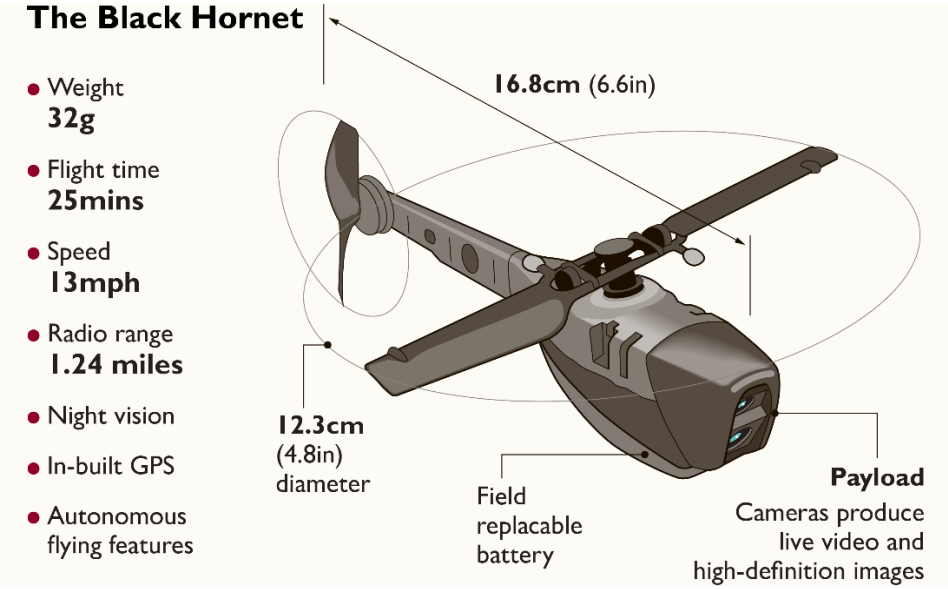

Figure 1.2: Closed-Up of Black Hornet Nano-Drone [6]

Figure 1.3: An Australian Army with the Black Hornet [7]

Historically, the application of drones was originated for warfare missions. But then more applications have been extended to meet the civilian needs such as agriculture surveillance, police trafficking, structure building inspection and immediate medical deliveries. Astonishingly, the growing number of civilian drones have now far exceeded the military drones and are widely available in

the market. Owing to the micro-electronic revolutions that have opened up the door of possibility to a small-scale, compact, miniature and low-cost without trading the high performance of nanotechnology, Figure 1.4 shows some of the examples of nano-drone that are already existed in the market at an inexpensive price. There are categorized as the smallest drones that are available nowadays, with the dimension of (a) 5 cm Arcade Pico Drone (b) 6.5 cm long for a Nano Falcon Drone, and (c) 5.5 cm long for a Pico Falcon Drone. These drones are about half the size of the smallest military drone, the Black Hornet. Even though the flight endurance of these nano-drones is much shorter than the Black Hornet. In this regard, the size of drones has largely reduced. A variety of advanced features could also be integrated in the future like high-resolution camera, thermal camera, collision avoidance, artificial intelligence, flight controller board with fully autonomous controller for a pre-programmed route.

Figure 1.4: Commercial Nano-Drones; (a) Arcade Pico-Drone, (b) Nano Falcon Drone, (c) Pico Falcon Drone

Birds and insects are one of the bio-inspiration for the design and development of these nano-drones [8]. The capability to fly within a complex environment and confined spaces will make these nano-drones the perfect tool for stealthy surveillance and intelligence attack. This spy-like technology package may become an advantage to a certain party but may become a threat to the other opponent. Hence, to protect national and institutional security, there is a need to

detect and classify these nano-drones as protective and defence measures. Other nano-targets that are relatively small in size are insects themselves. Insect detection has been of great interest too until now, especially those that can cause damage to agriculture and widespread diseases. The early stage of detection helps from further massive destruction to happen. The past has shown that entomologists have indeed successfully detected a swarm of insect migration. The most actively used for insect observation was Vertical Looking Radar (VLR), which is historically a modification of naval radar. This VLR is a pulsed radar type design used to detect an individual big target or a collective of small targets in a large group. Because it is pulsed, it has a blind range constraint that is unable to detect a close-range target, especially below 150 m height. Hence, this research proposed Frequency Modulated Continuous Wave (FMCW) radar which is suitable for a short-range detection application.

Micro-Doppler signature is one of the possible ways to distinguish between nano-drones and insects. This is because the technique allows the radar to extract the targets' features and characteristics. Traditionally, radar is used to detect the Doppler shift of a certain target that tells the speed and the direction in which the target is moving. This Doppler shift is caused by the bulk motion of a target. As the main body of the target moves, there can be a possibility that involves another small movement relative to the body moves like the rotational blade of the drone's propeller and the flapping wing of the insect could also contribute to the modulation of the Doppler. This modulation is known as micro-Doppler [9-10]. This kind of micro-motion will induce their unique signature describing their movement relative to the body of the target. It offers complementary information of the target like kinematic properties which designate the motion of the object interested. And these properties can be used for target identification and classification. So far, the extraction of micro-Doppler signatures towards birds and micro-drones have gain popularity in this research area. No prominent literature and experimental study show on the extraction of micro-Doppler signature of a nano-size target which is smaller than 5 cm yet.

Hence, this research aims to develop a flexible prototype of K-band FMCW radar that could detect and extract micro-Doppler signatures from an insect-like size target (nano-targets). Radar is fast becoming a key instrument in target detection as it is not easily disrupted by weather and the surroundings compared to other sensors that are limited to the scenario. Research on the subject has been mostly used a higher frequency band and this causes more dissipation loss. To date, there is no in the literature that can detect a small such target at a K-band frequency. In this case, a K-Band was chosen as a compromise between a high-frequency band to a low-frequency band. The Doppler frequency f_d which is defined by an echo of a moving target v can be expressed as $f_d = \frac{2vf_0}{c}$, where the carrier frequency f_0 is relative to the speed of light c. For a given fixed speed, the higher the carrier frequency the higher the Doppler frequency. Hence, a higher carrier frequency is preferable but not too high as a wider range coverage is equally important. The prototype is flexible so that the user can select the best parameters (i.e., carrier frequency, ramp duration, frequency bandwidth and time integration) for its diverse application.

1.2 Outline of the Research

1.2.1 Aims and Objectives

The main purpose of this study is to develop a radar prototype system that could detect an individual nano-drone target that is less than 5 cm in size. This can be achieved by these four core objectives:

i. To build a standard signal processing that could extract the micro-Doppler signature of nano-size target by using MATLAB programming.
ii. To design an S-band radar prototype and develop the radar with the minimum cost available. This can be achieved by excluding the IQ demodulator.

iii. To design and develop a wide-ranging, flexible prototype of a K-band FMCW radar according to the user's interest. The parameters are user-selectable mode.

iv. To detect a nano-drone of 5 cm in size or less using the prototype built. Then, to observe and analyse the Doppler signature of the target.

1.2.2 Significance of Study

There is a civilian and defence interest in this project. The end goal of this study is to fill in the gap in both these areas:

- to serve defence purposes in dealing with drones

The growing number of nano-drones are alarming. There is a significant amount of literature on the detection of micro-drones with a larger size. But very little if any in the detection of nano-drone specifically less than 5 cm in size. Because nano-drone poses a much smaller Radar Cross Section (RCS), hence the detection of nano-drone will become impossible to conventional radar.

- to serve civilian purposes in dealing with insects

Entomologists have made a remarkable study on insects' migration. Insects usually migrated for food, breed and shelter but will be left with significant destruction to crops. Vertical Looking Radar (VLR), for example, monitor flying insect movement are within the range of 150 m to 1,200 m above the ground level. Because it is pulsed radar, it suffers the blind range below 150 m.

Hence, with these two gaps in mind, a K-band FMCW flexible radar prototype is a proposed solution and a suitable application to cater for these problems.

1.3 Thesis Layout

The overall structure of the study takes the form of seven chapters, including this introductory chapter.

Chapter 1: The thesis begins with the problem statement of the research. Why it is important to go through these daunting processes are clearly described in the background and motivation section. The significance of this study and the contribution of this study are outlined.

Chapter 2: This chapter briefly introduces the radar background and specifically more detail in FMCW radar. Then, the chapter listed some of the literature reviews on drone detection from the past to the latest and current technology in this field. Lastly, the possible target of interest in this research was presented.

Chapter 3: The chapter mainly is devoted to the theoretical dimensions of the research. Signal processing of the radar is introduced. The parameters and the performance of the FMCW radar are discussed. Doppler & micro-Doppler principles and radar range equations are described in this chapter that will be applied in the following chapter.

Chapter 4: The fourth chapter is concerned with the methodology used for this research. This part covers the algorithm of FMCW radar with the micro-Doppler extraction apart from the Doppler movement.

Chapter 5: This chapter presented one of the key achievements of the research, that is, the design and development of the S-band FMCW radar prototype. The chapter described the architecture of the prototype and then demonstrated four case studies that verify the operation of the system. The micro-Doppler of the targets are analysed.

Chapter 6: The following chapter presented another key finding of the research; the design and development of a K-band FMCW flexible radar prototype. The architecture of the prototype is first presented. Followed by several tests on the detection of small bearing steel spheres. Finally, a nano-drone with 5 cm less in size is successfully detected with the prototype developed.

Chapter 7: This chapter draws upon the entire thesis, tying up the various theoretical and empirical stands, the contributions of each experiment that will enlighten a positive outcome for a future study. Lastly, areas for further research are identified.

1.3.1 Key Achievements

(i) Successful delivery of S-band demonstrator

(ii) Successful delivery of a K-band flexible prototype

(iii) Successful in nano-drone detection using the built prototype

1.3.2 List of Publications

Journal & Conference Papers

- S. Zulkifli, A. Balleri “FMCW Radar Prototype Development for Detection and Classification of Nano-Targets”, *2020 IEEE International Radar Conference*, April 2020, Washington DC, US.
- S. Zulkifli, A. Balleri “Design and Development of K-Band FMCW Radar for Nano-Drone Detection”, *2020 IEEE Radar Conference*, September 2020, Florence, Italy.
- S. Zulkifli, A. Balleri, “Detection of Nano-Drone with a Flexible K-Band FMCW Radar Prototype”, In a submission to IEEE Sensor Journal.

Presentation without Papers

- S. Zulkifli, A. Balleri “Absence of Presence”, Digital presentation in *2019 Defence and Security Doctoral Symposium*, Swindon, November 2019
- S. Zulkifli, A. Balleri “Losing Contact with Nano-Object”, 3MT presentation in *2019 Defence and Security Doctoral Symposium*, Swindon, November 2019

- S. Zulkifli, A. Balleri “Algorithm for Micro-Size Target Detection with Frequency Modulated Continuous Wave (FMCW) Radar”, Poster presentation in *2018 Defence and Security Doctoral Symposium*, Swindon, November 2018
- S. Zulkifli, A. Balleri “Detection of Micro-Size Target with FMCW Radar (MATLAB Simulation and Analysis)”, Poster presentation in *Radar Away Day*, Birmingham, June 2017

2 LITERATURE REVIEW

Chapter 2 is a literature review of the past and current relevant work with recent technology and methodology presented recently. There are four sections in this chapter. Section 2.1 is an overview of FMCW radar and its applications, then Section 2.2 presents literature on drone detection using FMCW radar. Section 2.3 introduces reviews on the micro-Doppler signature, its method of extraction and features for classification. Last Section 2.4 concludes and describes more on the target of interests. The radar designs overviewed are very diverse. It offers different functionalists and features.

2.1 Radar Background & FMCW Radar

RADAR which is a short term of radio detection and ranging is a sensor that can detect a target using a radio wave. However, the term radar does not holistically describe itself. Apart from being able to detect the target and measure the target range, it could also determine the target velocity and angle. This is due to radar advancement that keeps on revolutionising to update with current needs. The operating principles of radar involve in these 5 steps; (i) Electromagnetic (EM) waveform is emitted (ii) the waveform hits the target (iii) that waveform then reflects from the target (iv) the waveform returns to the receiver and (v) the echo waveform is processed and analysed. This sub-section is a brief introduction to the radar and FMCW radar specifically.

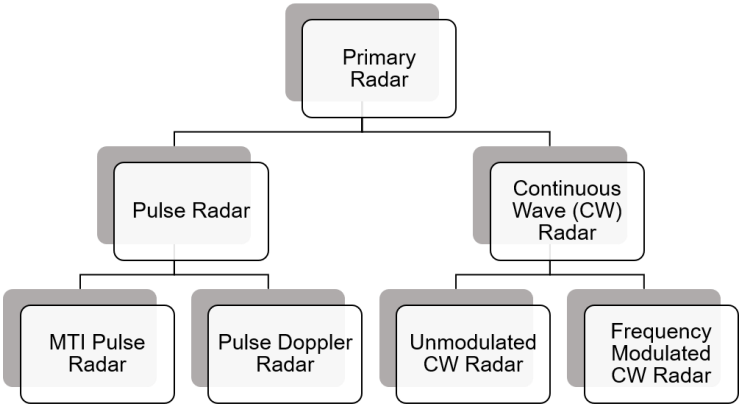

Figure 2.1: Types of Radar

Figure 2.1 depicts the most common types of radar according to the waveform. It can either be Continuous Wave (CW) radar or Pulse radar. CW radar constantly transmits and receives EM wave signals. The receiver is always switched on. Hence, the radar will respond and update immediately to the measurement. It is capable of velocity measurements but unfortunately, it is not capable of range measurements. However, when some modifications are made then the range calculation is possible. FMCW uses Linear Frequency Modulated (LFM) waveform so that both range and velocity can be determined. The FMCW radar will measure the frequency difference of transmitted and received signal, which is the beat frequency signal that will represent the range of the target.

The traditional pulse radar uses a single antenna, so it is either transmit or receive at one time. When the transmitter is switched on, the receiver is switched off until the pulse has completely left the transmitter and alternately the receiver is switched on. It transmits a pulse and then measures the time delay of the target returns. Hence, there is a minimum range where the radar is unable to receive which is called the blind range. Equation (2-1) shows the relationship of the blind range where τ is the pulse width. Having a very short pulse will help minimise the blind range. Let say, two different radar with a pulse width of 1 μs and 10 μs respectively. A longer pulse width of 10 μs will have a blind range of 1500 m while a shorter pulse width of 1 μs will have a shorter blind range of 150 m.

$$R_{min} = \frac{c\,\tau}{2} \quad \textbf{(2-1)}$$

FMCW radar typically uses two antennas so it can do both transmitting and receiving at the same time. Since the transmitter and receiver are always switched on, it eliminates the blind range which is one of the important advantages of choosing this option. FMCW radar transmits continuously and varies in frequency. This means that the further away the target is the bigger the beat frequency. The waveform can be triangular, sinusoidal, saw-tooth or any other waveforms.

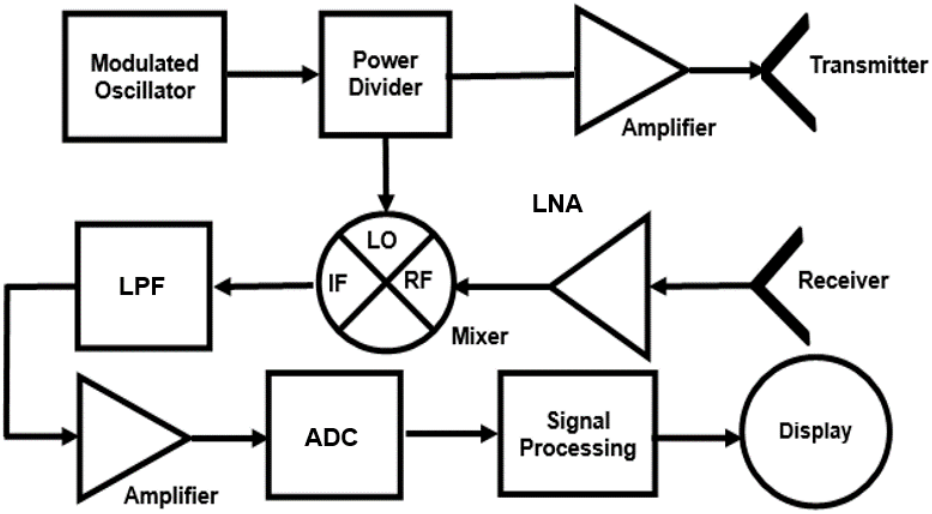

Figure 2.2 A Generic FMCW Block Diagram

Figure 2.2 above shows a generic FMCW block diagram with its important components. The modulated frequency is first generated from the oscillator. The shape of the modulation is typically a sawtooth type where the value of frequency is linearly increasing over time or triangular type where the operating frequency changes linearly increasing then linearly decreasing over time. This signal is then split into two parts by the power divider. One is carried forward to the power amplifier for the amplification then to the antenna of a transmitter and radiated out to space. Another one is being fed to the Local Oscillator (LO) of the mixer as a reference to the transmitted signal. Once the waveform signal propagates through space and hits the target, an echo is produced that will be collected by the received antenna. The signal is then amplified by the Low Noise Amplifier (LNA) and this Radio Frequency (RF) is fed to the mixer. This is where an important process of FMCW radar takes place. The received signal with a time delay is multiplied with the transmitted signal to obtain the Intermediate Frequency (IF) of the beat signal. The beat signal is proportional to the range of the target. A Low Pass Filter (LPF) is usually placed after the mixer to reject undesirable frequency products. The IF is amplified, digitized and processed for signal analysis.

2.1.1 Advantages & Disadvantages of FMCW Radar

FMCW has certain dominant properties over pulse radar; (i) FMCW radar only requires a low transmit power. Hence, it will have a lesser component involves, making it low cost, compact radar and one of the great portable package (ii) the signal processing of the beat signal is at Direct Current (DC) or low intermediate frequency making it simple in circuit design (iii) FMCW also provides high quality of resolution which results in a better display due to less clutter effect (iv) CW radar offers low emission, low transmitted power which will be difficult to detect for receiver interception [11]. Usually, 5 W is sufficient for a CW radar. Thus, this is advantageous for stealth where the radar's ability to see without being seen [12]. This is in the sense that it is secured from jammers. Pulsed radar, on the other hand, has an advantage of a larger detection range but suffers the minimum range and is exposed to intercept receivers because of the high peak power transmitted.

The disadvantage of FMCW is that; (i) it will hugely suffer for long-range detection due to the low emission power. Especially the one with a high operating frequencies radar with a shorter wavelength. The power transmitted will be absorbed into the atmosphere. Hence, high-frequency radar is much more efficient for shorter-range detection. (ii) because of the low peak power output as well, the signal transmission will be easily interfered with by a nearby RF.

2.1.2 Applications

FMCW radar is widely used for short-range distance measurement as it provides a robust and accurate measurement. Below are some of the examples that are relatively used nowadays in the industry:

(a) It is widely popular used in radio altimeter aircraft. A signal is transmitted downwards to the ground from the aircraft and bounced back to the receiver.

That echoed signal is delayed with a frequency offset after mixing the transmitted and echoed signal, it carries the height information which acts as an altitude sensor in aviation applications. It is critically used for terrain avoidance systems and low altitude flight.

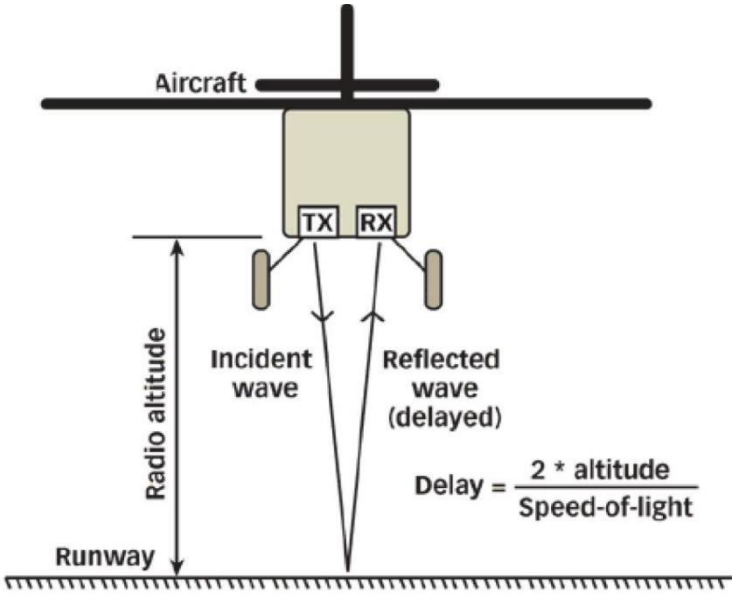

Figure 2.3: Aircraft Radio Altimeter in [13]

(b) Radar level sensor is another application that acts as the radio altimeter. It is placed vertically pointed downwards and capable to measure the height of the liquid in the tank. In this case, the radar sensor is chosen over the ultrasonic sensor because it is quick-updating, contact-less and functions well in all types of temperature, pressure and weather. The radar wave's propagation is excellent since it used a short wavelength of EM wave and is not easily blocked by other disrupting particles.

(c) Apart from that, another crucial application of FMCW is in an automotive application. Although this application is still ongoing research, there are a numbered of studies in Advanced Driver Assistance System (ADAS) radar which is one of the preferences over other sensors like video, infrared (IR), ultrasonic and Light Detection & Ranging (LIDAR) sensors being used. This is basically due to the low sensitivity to the surrounding or background noise and the ability to extract the Doppler characteristic of the object.

2.2 Drone Detection with FMCW Radar

As was pointed out in the introduction of Chapter 1 to this thesis, this work project will be using FMCW waveforms in order to meet the objectives of the research. A wide variety of sensor can be opted for drone detection like LIDAR [14], camera [15-17], acoustical [18-20] and electro-optical IR [21] sensors. Some of these sensors are far much cheaper. However, most of them are affected by the weather condition, while radar provides the best solution and offers a few advantages compared to others. FMCW waveform is continually transmitted and received signals. The frequency bandwidth ranges from the start frequency to the stop frequency and will determine the range resolution of the radar. The frequency is linearly modulated within the ramp duration. And this ramp duration will affect the Doppler spectrum bandwidth of the radar performance. More theoretical concepts and technical design of FMCW radar are thoroughly explained in Chapter 3.

The dramatic and wide-reaching change in drone operation started from a remote control and unpiloted full-size aircraft. Later, the size of the drone has slowly reduced and offered the drone an unmanned solution. According to the Library of Congress [22], the size of a mini drone is in the range of 2 m to 30 cm long wingspan. Contrarily to the size of a micro drone, the range is less than 30 cm wingspan. This micro drone for example has become dominant these days. The mass production of civilian drones has contributed to the safety of society in general, as it could outreach unapproachable and inaccessible areas. It is widely used for a variety of reasons such as search and rescue operation, physical infrastructure inspection (i.e. utility, oil and gas infrastructure inspection), agriculture monitoring and police patrolling. The emerging of the micro-drone phenomenon has highly impacted society with a greater cost-effective and progressive safety measure. The micro drone can potentially replace the task of human beings in dangerous places like collapse buildings, flooding, landslides etc. However, the rise of these well-known technology has

gained a lot of primary concern throughout the world due to their invasive nature and misuse of property. Detecting and evaluating these micro-drones is a key to protect national security and defend against threat attacks.

The micro-drone detection using FMCW waveforms has been carried out and tested at Fraunhofer Institute IAF, Wachtberg, Germany [23-25]. In [23] for example, the authors investigated the DJI Phantom quadcopter movement with two types of system namely; (i) Scanning Surveillance Radar System (SSRS) (ii) and Multi-Channel Radar for Perimeter Surveillance (MuRPS) utilizing mono-pulse principle where only one FMCW chirp is analyzed. These two combination systems operated at a centre frequency of 94 GHz but slightly differ in bandwidth which is 750 MHz (range resolution 20 cm) and 1 GHz (range resolution 15 cm) respectively. The results have shown that the quadcopter can be detected, localized, and tracked within the range of 10 m to hundreds of meters away from the radar with 360° of coverage. Then, the experiment was repeated in [25] under conditions in which the poor signal ratio was improved.

J. Drozdowicz et al. [26] presented another drone detection system where the authors have developed a 35 GHz FMCW radar and the radar was later tested at Air Force Institute of Technology Poland with two types of micro-drones; Quad-Rotor DJI Phantom 2 (35 cm) and Octocopter DJI S1000 Premium (45.5 cm). The distance between the radar and the target is about 30 – 90 m. A wide Doppler spread is noticeable in the Doppler range map which indicates the Doppler velocity induced by the propeller blade of these two micro drones. While a homodyne configuration of FMCW may offer several advantages (i. e., simple design, compact size, and low cost), however, it has one major problem that is the isolation between RF and LO ports. There is a Doppler shift observed however the micro-Doppler was not considered. The disadvantage of not taking the micro-Doppler into account is that when the drone is hovering. The main Doppler shift is not present since there is no radial velocity. But when a micro-

Doppler is considered, the signature is significant due to the fast rotation of the blades.

Shin *et al* on the other hand [27] have proposed an alternative way that could reduce the leakage signal. To conserve the power transmitted that could propagate to the atmosphere more than from being absorbed by the nearby antenna, the author suggested that the antennas should be at different platforms. This will eliminate the mixing of the LO port to the leakage. Apart from that, the authors have also come up with a better solution to reduce the propagation losses particularly to increase the sensitivity of the radar in dealing with the low RCS target. In their study, the fibre-optic links are being replaced by the RF cables. This provides a higher radar sensitivity. BumbleBee F820 Hexacopter was measured within the range of 15 to 500 m at 24.95 GHz centred frequency.

In another major study, the authors in [28] demonstrated that the micro drone with the RCS of -20 dBsm (0.01 m^2) can be detected with the manufactured X-band FMCW radar system. Two identical drones of DJI Phantom II was flying at different altitudes 20 m apart can be resolved. A frequency synthesizer was used to generate a sawtooth waveform 150 MHz bandwidth and a ramp duration of 0.25 ms and 0.5 ms.

Stasiak et al highlight the variety of designs of continuous wave radar at different frequency bands; started with a lower frequency C-band [29] and then at a higher frequency K-band (24 GHz) & mm-Wave (120 GHz) [30]. Both publications presented the detection of micro-drone with CW radar. Universal Software Radio Peripheral (USRP) was practically used for digital FMCW [31] and CW radar implementation. This USRP device offers rapid prototyping of radar development. An analogue FMCW design was also discussed in [32]. The IF signal generation makes it different between both FMCW designs.

A model of the blade and arm propeller is presented in [33]. The simulation using FEKO is used to observe the strongest response reflected by the propeller at a certain angle. As the small changes of the angle will highly impact the RCS of the target. Then, measurements were taken with a commercial 24 GHz FMCW radar to detect the OktoXL drone hovering at 5 – 10 m away from the radar. Two different bandwidths was used, that are 250 MHz and 2 GHz. The drone was detected with aliasing because of the low sweep repetition frequency. In [34], on the other hand, a multi-mode Software-Defined Radar (SDR) simulated S-band, X-band and K-band LFM chirp waveforms to detect a drone RCS of 0.01 m^2 to 0.1 m^2. A quadcopter drone with the size of 90 x 20 x 90 cm was detected within the range of about 100 m away from the radar. Authors in [35], on the other hand, demonstrate a 5G phased-arrays that could also act as an FMCW radar. It can detect DJI Phantom III SE drone up to 250 m away from the radar system. Drawing on an extensive range of sources, the authors in [36] set out the different ways in which a digital array of FMCW radar was employed to detect a DJI Phantom 4 within a range of up to 2 km. The X-band radar system was initially tested on larger targets and presented in [37 - 38]. This system of digital array radar has intensively described its architecture in the published papers [39 - 40] where the microstrip receiving antennas with 8 channel receivers was implemented. de Quevedo *et al* proved that even with a low RCS target of this drone, it can still be detected when flying just over the tree clutter with RAD-DAR designed. This RAD-DAR system has a similar advantage to mechanical or electrical scanning radar.

To date, it is apparent that there is no in the literature of a nano-drone detection and majority of the targets detected were micro-drone with an average size of about 35 cm. Table 2.1 summarize the past to the current activity of drone detection with an FMCW radar.

Table 2.1: The Update of Drones Detection using FMCW Radar

Reff.	Details of the Sensor	Target and Its Size (cm)

[23][24][25]	94 GHz (W-Band) FMCW Radar [DDS Chip + LO + Optical Camera]	DJI Phantom	Diagonal length: 35 cm
[26]	35 GHz FMCW radar. Analogue front-end + pre-processing FPGA board + based processing PC	DJI Phantom 2	Diagonal length: 35 cm
		DJI S1000 Premium	51.1 x 45.5 x 29.5 cm
[27]	24.59 GHz (K-Band) FMCW Radar based on Fibre-Optic Links	HexacopterBumbleBee F820	82 x 82 x 44 cm Diameter Propeller: 38 cm
[29]	Digital C-Band FMCW vs Analog FMCW vs CW Noise Radar	Xiro Xplorer Drone	31 x 31 x 5.5 cm
[30]	XY-DemoRad FMCW: 24 GHz (K-Band) vs 120 GHz (mm-Wave)	Xiro Xplorer Drone	31 x 31 x 5.5 cm
[33]	24 GHz FMCW Radar (from IMST GmbH)	OktoXL Mikrokopter	Propeller: 30.5cm
[34]	Multi-Band Multi-Mode SDR Radar	Quadcopter Drone	90 x 20 x 90 cm
[35]	28GHz Phased-Array FMCW Radar	DJI Phantom 3 SE	Diagonal length: 35 cm
[36] – [40]	8.75 GHz (X-Band) FMCW Radar, RAD-DAR Digital Array Radar	DJI Phantom 4	Diagonal length: 35 cm

2.3 Micro-Doppler Analysis & Target Classification

The basic understanding of the micro-Doppler signature can be found in Chen [41]. As introduced in Chapter 1, apart from conventional Doppler shift, there is another component that can contribute to the aggregate amount of Doppler shift which is micro-Doppler. The micro-Doppler signature is the resultant of micro-motion or oscillatory motion which is induced by Doppler frequency modulation. And this micro-movement has its signature that is useful for classification, recognition and identification [9]. Micro-Doppler technology has helped civilians and the military to recognise the target and classify them based on the distinctive characteristic of the signature. A wide range of applications was inspired to apply this technique, particularly in the classification of vehicles, human and animal motion. A complete review of the micro-Doppler signature is explained in [42][43][44]. In [45][46][47] are some of the examples where human motion was classified. Smart classifiers were described and explained. The scope of this review section will then be focused on micro-Doppler signature induced by airborne objects like jet engines, helicopters, drones, birds, insects

and the possible sources of false alarm contribution. A large and growing body of literature has been investigated on micro-Doppler extraction of air vehicles.

2.3.1 Micro-Doppler Modelling

Early detection of drones has emphasized the bulk motion of the target that results in a Doppler shift relative to the translational motion of the target. And a few ongoing kinds of research in the past decades have been dedicated to the study of micro-motion of the drone that leads to a distinct micro-Doppler signature. Several micro-Doppler based techniques have been reported in order to identify and classify a helicopter [48 - 52]. The ability to extract distinctive features from the signature has become an important characteristic in classification. In [9], detailed information of the micro-Doppler signature has been explained in particular as illustrated in Figure 2.4. The blade will make one complete cycle 2π which is between two successive peaks T_c. And within this one cycle of 2π, the number of blades N rotates at a rotation rate of Ω

$$T_c = \frac{2\pi}{N\Omega} \tag{2-2}$$

The blade flashes reflected from the even number of blades has a significantly different signature from the odd number of blades. If the positive Doppler and negative Doppler have a symmetrical spectrum, then it is likely that the target has an even number of blades. Several parameters can be extracted from this signature analysis including (i) maximum Doppler of the blade flash that leads to the estimation of the blade tip velocity, (ii) the rotational rate of the rotor Ω, (iii) the length of the blade L and (iv) the number of blades N.

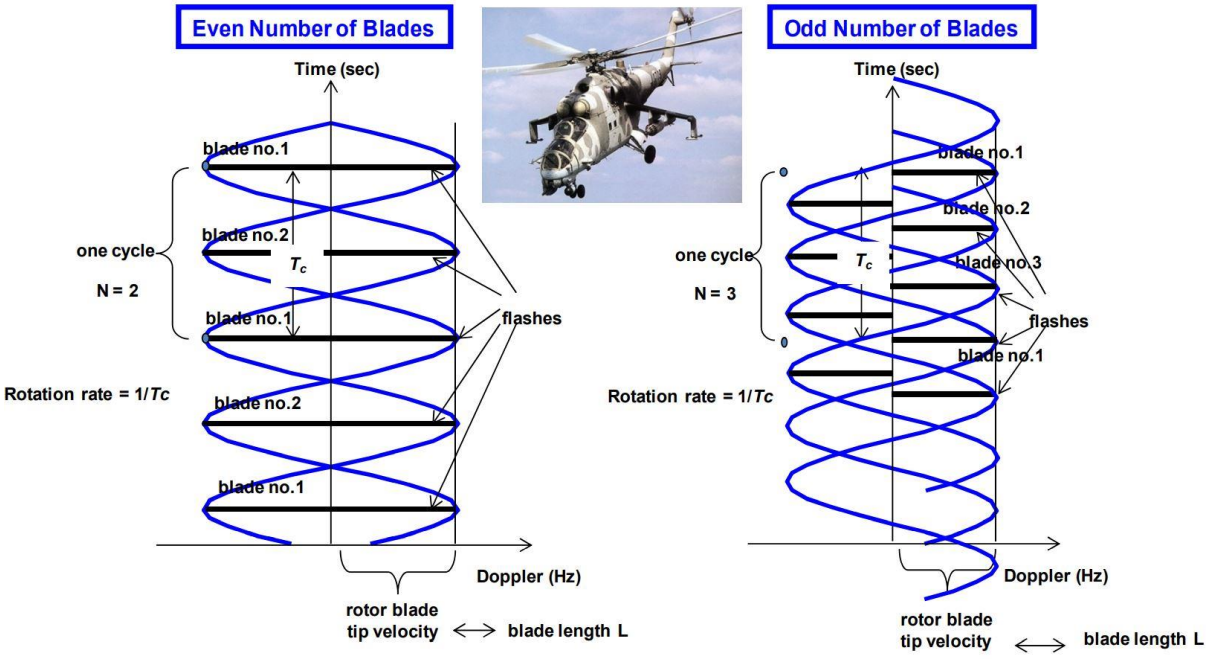

Figure 2.4: Micro-Doppler Signature of A Helicopter; between Even and Odd Number of Blades [9]

Then, Govoni [53] for example have modelled a micro drone and looked into different responses of the micro-Doppler spectra when using a different operating frequency of 1, 10 and 100 GHz. The number of the propeller blade hub k and the number of blades in one hub M are the major concern as it will affect the micro-Doppler spectra. Each of the propeller blade hubs will have a different rotation rate f_r revolutions/second (r/s) for balancing and stability of the drone. Hence, the angular rotational rate $\Omega_k = 2\pi f_r$ will also differ from one another and will reveal k number of sinusoidal signals in the micro-Doppler spectra.

Conversely, Pan *et al* [54] describe the attempt to utilize the Circular Correlation (CC) coefficients and the Circular Average Magnitude Difference (CAMD) coefficients to estimate the micro-Doppler frequency of a rotating target. These two methods offer an advantage to examine a target with a rotational motion with or without a translational motion as well. The author proves that it is less

computational load compared to Hough Transform (HT) or Extended Hough Transform (EHT). Whereas Ren in [55], have come up with a better spectral analysis that could assist an automatic classification. The conventional way of micro-Doppler extraction was by either spectrogram, cepstrogram or Cadence Velocity Diagram (CVD). But these methods only concern with the magnitude spectrums and discarding the phase spectrums. Hence, the authors proposed a 2D complex-log spectral analysis that will take into account both the magnitude and the phase spectrums. It is proven that this approach has reduced the error rate for classification between almost identical signatures from the drone and bird.

The mathematical model of a rotating blade can be found in [56, 57]. These reviews presented the micro-Doppler signature that arises from the rotating target. Wang *et al* [56] have included the modelling of a turbojet and prop aircraft where the rotating planes are in a vertical position relative to the flying object. Contrarily to the helicopter, where the rotating planes are parallel to the object flying path. So, a mathematical model for the vertical plane is developed and compared with the CADFEKO model. Then this model can be used as a reference to differentiate micro-Doppler spectra between helicopter, prop aircraft and turbojet. While most of the researchers had focused on a single-rotor target, Yong-bin [57] have attempted to model multi-rotors in one target. Ka-50 helicopter (length 16 m, wingspan 14.5 m), AH-64 Apache attack helicopter (length 17.7 m, wingspan 14.6 m) and MV-22 Osprey transport aircraft (length 17.48 m, wingspan 25.78 m) are the targets that have been modelled and simulated.

2.3.2 Helicopters and Jet Engines

A large number of studies have focused on the classification of helicopters and jet engines using micro-Doppler techniques. Molchanov *et al* [58] have proposed cepstrum and bio-coherence for the classification of AH-64

helicopters, An-26 aircraft and B-52 aircraft. Clemente in [59 - 61] uses the Global Navigation Satellite System (GNSS) as an illuminator for Passive Bistatic Radar (PBR). It is suggested that when the target is approaching the forward scattering position where the bistatic angle β between 165° - 180°, the RCS of the target increases and make it susceptible to detection. The authors have simulated AW-109 Agusta (Blade Length: 5.5 x Width: 0.6 m), AH-64 Apache (Blade 7.3 x 0.6 m), UH-60 Black Hawk (Blade 8.18 x 0.6 m) and MD 500E Defender (Blade 4 x 0.6 m) to extract its micro-Doppler signature and used it for target classification.

Later, Zhang [62] suggested for a better classification rate result, a multi-aspect signature of the helicopter should be considered. As the helicopter will hover and cruise at a different level to the line of sight of the radar, hence the micro-Doppler signature of the target will differ. The length of the blade L and the number of the blade of the main rotor N quotient (L/N) represents the characteristic of the target that can be extracted from the signature. And this estimation of the L/N quotient will be affected by the aspect angle of the helicopter to the radar. A novel approach of the classification algorithm is presented in [63 - 64] which does not rely on the aspect angle and initial position of the helicopter. The number of blades N and the rotation speed R can be determined through an iterative process. Nine different types of helicopters have been simulated [63] and then verified by GAUI X3 remote control helicopter [64]. The blade length of the helicopter was 36 cm and the body length were 70.9 cm. The study shows about more than 80% are correctly categorized.

2.3.3 Drones and Birds

De Wit *et al.* [65] provides an in-depth analysis of mini-drones & micro drones using X-band CW radar and X-band FMCW radar. The authors verified that the experimental data taken during the field test meets the expected modelled

targets. And the targets are chosen was; (i) a helicopter where the rotor diameter was 71 cm, (ii) a quadcopter with a rotor diameter of 20 cm, (iii) a hexacopter with an overall diameter of 60 cm and (iv) an octocopter with the rotor diameter of 30 cm. In their analysis, the authors show that from the spectrogram of micro-Doppler analysis, the rotation rate and the velocity tip of the blade can be extracted. Then the following year later, Molchanov *et al.* [66] extended the research with a wide variety of drones and birds for target classification based on the micro-Doppler signature extract from the spectrogram. In [67] and [68] presented micro-Doppler feature extraction using spectrogram & cepstrogram and using the Singular Value Decomposition (SVD) respectively. Their work then has inspired others to look further at details in this area.

In [69], Tahmoush draws on extensive parameters that can be extracted from the blade of a small helicopter, this includes the rotation rate of the propeller blade, the length of the blade and the number of the blades. With these parameters extract from micro-Doppler analysis, the author could differentiate the echoes from moving clutter to the rotating propeller blade of the target. Similarly, in [70], Brewster *et al* attempted to extract the micro-Doppler signature of a rotating blade and a miniature helicopter by using the Empirical-Mode Decomposition (EMD) method. The data collected from the experimental trials were gathered by a 10 GHz CW radar.

The later research on this topic was demonstrated by Fioranelli *et al* [71] where the authors proposed a multi-static radar configuration rather than a conventional monostatic radar configuration. A coherent pulsed radar that operates at S-band (2.4 GHz) investigated quadcopter DJI Phantom Vision 2+ carrying payload and without carrying a payload. And the results obtained from the spectrogram analysis concludes that a micro-drone with a payload will show almost consistent straight Helicopter Rotor Modulation (HERM) lines uniformly and the velocity tip or the blade Doppler value is much higher compare to an

unloaded micro drone. This is probably because the heavier the micro-drone, the stable it is which is not easily blown by the wind. And a higher rotational blade is probably due to a higher requirement to lift the payload. Hoffmann in [72] on the other hand, managed to discriminate between the micro drone return with the clutter. This study can be empirically appreciated as the Doppler return from the micro drone is far lower compared to the clutter outside the building. However, by observing the micro-Doppler pattern collected from the experiment, the HERM lines are shown in the spectrogram of time-frequency analysis which represent the rate of the rotational blades of that micro drone. This study proves that the micro drone can be discriminated from the background clutter. In contrast to Ritchie [73] who investigated the multiple types of birds and differentiated them from a micro drone return signal. There were three samples of birds and a quadcopter of a size 35cm. The radar signatures in both the range and Doppler domain is being observed and proved the significant difference among those targets. Ritchie in [74] concluded the possibility of classification of loaded and unloaded micro drones with the feature extract from a different angle and applying micro-Doppler signature analysis.

A more diverse target of micro-drone detection had been employed with similar techniques as mentioned above. In [75] for example, Radar Warning and Information System (RAWIS) Ka-band Multiple Input Multiple Output (MIMO) radar was constructed to test a wide-ranging micro drone including fixed-wing plane, helicopter, quadcopter and octocopter. The micro-drone data was analysed and the parameters for each target was extracted (i.e., the rotation rate, the number of rotors and the length of the propeller blade). While in [76], the author has extended his project in micro-Doppler signature observation to identify the micro-drones out of birds. The measurements were collected with an X-band CW radar and classify the target signature from Time Velocity Diagram (TVD).

The majority of the micro-Doppler extraction from the past used a Fourier-Time frequency analysis method especially Short-Time Fourier Transform (STFT). However, this method requires a longer time integration to obtain the required spectral and there is a trade-off between time and frequency resolution at the STFT plot. Therefore, an alternative way has been applied by Oh *et al.* [77] with a non-Fourier Time-Frequency analysis to extract the signature which is the EMD method. The data were collected by Thales Nederland with an X-band CW radar towards 11 different objects including birds and six different types of mini-drones. Distinct features are present in the figure between the helicopter, fixed-wing plane and quadcopter.

Rahman also presented a similar work in [78 - 81]. In [78], a milli-meter wave radar operated at 94 GHz with CW and FMCW radar is simulated and compared with the experimental result. A DJI Phantom 3 Standard was observed and blade flashes induce by the propeller are visible. Later on in [79], with a similar radar as previous, the authors collected data on a bionic bird and the data was decomposed between the bulk Doppler with the micro-Doppler. The wavelet transform method was used to extract the micro-Doppler so that the time-frequency resolution can be adjusted by shifting the time localization or scaling the frequency localization. After looking at the millimetre wave radar, Rahman moved to a K-Band FMCW radar operated at 24 GHz [80]. The radar system which was developed at the University of St Andrews is based on Analog Devices EV-RADAR-MMIC2 chipset. The radar built is then verified with three different types of targets which are human walking, Tawny Eagle bird and DJI Phantom 3 Standard. And each of them presented their unique signature. A comparison of radar performance is then made between the K-band and W-band radar with a wide variety of targets [81]. The targets were added to three drones (DJI Phantom 3 Standard, DJI Inspire 1 and DJI S900 Hexacopter) and four birds (Nothern Hawk Owl, Harris Hawk, Indian Eagle Owl and Tawny Eagle) with each one of them have different sizes and different weight.

On the other hand, Aldowesh *et al* [82] have developed an S-band Digital Array Radar (DAR) to detect a DJI Mavic Pro micro-UAV. Then in [83], three frequency bands were used (C-band, S-band and X-band) to detect and classify more targets i.e., DJI Phantom, Mavic Pro and Mavic Air with FMCW radar. The measurements were taken with an instantaneous bandwidth of 200 MHz and a ramp duration of 50 μs. From the authors observation, it is noticeable that as the operating frequency is increased, the Doppler resolution is finer resulting in a better micro-Doppler display of the oscillation of the propeller blade. Yet, the Signal-to-Noise Ratio (SNR) strength is weaker as the operating frequency increases as the shorter the wavelength of the waveform, the more losses to the atmosphere. Since the blade size of the Mavic Air drone is the smallest, i.e., 13.5 cm long it shows slightly unclear blade flashes compared to the other two drones; Phantom with 24 cm long and Mavic Pro with a 21 cm long blade. This proves that the smaller the target, the difficult it is to extract the signature. With the same drone as the previous review, DJI Phantom 3 was also used in [84] to observe its Doppler signature. The authors have proposed Forward Scatter Radar (FSR) for drone detection purposes as this geometry allows an enhancement in the RCS of the target. It is believed that the rotation rate of each rotor will be different for a quadcopter.

Diversely, Ezuma *et al* [85] have included the clutter model in their micro drone detection where has been neglected by other literature in the past. Cell Averaging – Constant False Alarm Rate (CA-CFAR) was developed to encounter the target detection in a low altitude flight automatically. The micro-Doppler signature of the target was also extracted to identify and classify the target. DJI Phantom 4 Pro Quadcopter with RCS approximately 0.01 dBsm was detected with a 24 GHz FMCW radar. Huang *et al* in [86] highlighted the importance of having a high Pulse Repetition Frequency (PRF) for a complete period of the micro-Doppler spectrum. The radar PRF will have to be double the tip velocity of the blade. However, having a larger PRF will raise an issue in range ambiguity. Hence, an alternative method proposed is that to have a

longer window duration in STFT processing. This will result in the visibility of several lines which represent the HERM lines or the rotation rate of the blade. The peak Doppler frequency is characterised by the product of the rotation rate with the number of blades. In this case, a log harmonic summation algorithm was implemented in order to extract the HERM lines to determine the rotation rate of the blade target. Xethru X4 Ultra-Wideband (UWB) pulsed radar was deployed to detect and determine the rotational rate of a mini helicopter, which is about the same size as the Black Hornet drone.

From the literature review presented above, it is proven that the micro-Doppler research area is a highly active and ongoing phase. It has been demonstrated that the micro-Doppler techniques offer a significant benefit for target classification. From the overall research, there is no nano-target size of 5 cm below in size that has been considered yet. The smallest size so far was a plane with its one side blade which is 10cm. And many institutions have paid much attention to the detection of DJI Phantom and Mavic Pro drones.

2.3.4 Birds, Bats and Insects

Looking at a more diverse airborne target like birds and insects, Zaugg [87] with the data gained from radar meteorology have observed and demonstrated a distinct pattern of micro-Doppler signature. The targets were classified according to different types of birds, insects, clutter and unknown target. Figure 2.5(a) for example is a kind of bird that continuously flaps its wing, hence an almost consistent Doppler fluctuation is observed. On the other hand, Figure 2.5(b) is a kind of bird that flaps within an interval of time, so at one point it is noticed that the micro-Doppler fluctuation is higher, and at another point, the micro-Doppler is flattened. It is believed that at this time, the bird is gliding without flapping its wing. Figure 2.5(c) is the Doppler signature of an insect which shows a small spread of the Doppler due to the size of the insect which is far smaller compared to the bird. And the nature of the insect itself which fly at a

lower airspeed than the bird. The micro-Doppler signature is extracted with Continuous Wavelet Transform (CWT) and the presence of Doppler fluctuation is useful for classification. All the datasets were classified by Support Vector Classifier (SVC).

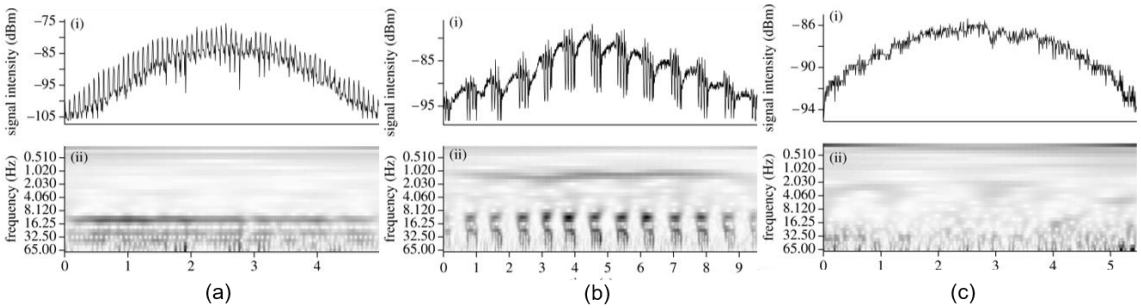

Figure 2.5: Doppler Signature of Airborne Targets; (a) A Bird Flapping Continuously, (b) A Bird Flapping Intermittently and (c) A Flying Insect [87]

In [88], Qun Zhang *et al* have modelled a big and small bird with a wing length of 40 cm and 10 cm respectively. The flapping wing of a bird was assumed to be similar to the pendulum Doppler signature, with a sinusoidal representation. Most of the big birds used to glide and do not persistently flap their wing. So, there is in a certain region that the micro-Doppler signature will not be trace except only the Doppler from the bulk motion. On the other hand, small birds used to repetitively flap their wings continuously and the wing beat frequency are much faster than the big birds. The authors utilized a frequency-stepped chirp radar with an operating frequency of 94 GHz.

Identification and classification between avian targets were also observed in [89]. Alabaster *et al* utilized a 24 GHz CW radar to detect and discover the distinct Doppler signature of the targets that can be used for classification. Stealthy aircraft for example that was used for military purposes may have almost similar RCS to the birds and leading to arise a false alarm. The data was collected with trials of a Peregrine Falcon bird, a Serotine bat and a Pipistrelle bat. STFT was applied in order to extract the wing-beat stroke pattern of the

targets. A mallard duck has been detected with a 24 GHz CW radar in [90]. The micro-Doppler signature was extracted with STFT spectrogram and the Doppler shift was removed so that the flying mechanism become more significant. While in [91], flying gannets were detected with an X-band pulsed radar and the operating frequency was at 9.2 GHz. From the range-Doppler map analysis, the micro-Doppler signature is extracted. Gannets, a large seabirds type have a wingspan of 1.8 m and a weight of 3.5 kg.

In [92], the authors proposed a machine learning algorithm with six automated classifiers in order to distinguish between a non-biological target and a biological target. Then, within the biological target interest, the species of birds are also categorized. A marine radar was utilized with an X-band Vertical Looking Radar (VLR) and S-band Horizontal Looking Radar (HLR) to gather the data. The insect detection was excluded during the data collection by setting the airspeed interested higher than 8 m/s. Even though the micro-Doppler extraction was not applied for this classification, but the authors realized the importance of target classification mainly because of these three factors; (i) reduce the bird-strike collision, (ii) minimize crop damage caused by birds and (iii) reduce bird collision towards operating wind turbines.

Other micro-targets that are relatively small in size are the insect itself. Insect detection has been of great interest too until now, especially those that can cause damage to agriculture and widespread diseases. The early stage of detection helps from further massive destruction to happen. Most entomology radars that are being used now are pulsed-wave radars whereas FMCW radar offers a better detection in a closer range target which is less than 150 m to the target. Radar is a useful tool for faraway detection and has been employed for many years to detect airborne insects. Radar meteorology, ornithology, biology and entomology carries their purposes to detect a certain kind of target in a different scenario. However, these different alternatives of radar may overlap each other and provide an additional complement to the radar being used.

Meteorological radar detects masses of swarm insects rather than individual insects. So, the echo from these insects is usually larger than a bird. An array of techniques has been deployed for insect detection and investigation. Wide-ranging studies have been carried out on pest migration.

2.4 Review of RCS of a Target

In principle, RCS reflects the strength of the echoed signal bounced from the target and it is usually expressed in square meters. But practically, RCS is not similar to the definition of the area of a target because it is the power level that is being reflected by the target and it also indicates the efficiency of a target conductivity. So, it is always stated in decibels with reference to a square meter (dBm^2 or dBsm) by taken the logarithmic calculation $10 * \log(RCS(m^2))$ into account. This logarithmic value enables us to make a fair judgement in the level of comparison between different types of targets that have dissimilar properties. When an EM wave interacts with the target, that amount of energy bounces back to the radar or the effective electrical area which is scattered back to the radar will reflect this RCS. RCS of radar targets can widely vary, and it depends on the operating radar factors, which includes the aspect, frequency (or wavelength λ) and polarization of radar. The RCS also depend on the characteristic of the target like material, size, shape and orientation of the target. Table 2.2 is a rough estimation of the RCS of the target and not considered as a single-value RCS that have been listed in [93, 95]. The carrier frequency is at 10 GHz. It is perceptible that the RCS of the target can range from the maximum of +41.46 dBsm to the minimum of -50 dBsm.

Table 2.2: Typical Radar Cross Section at 10 GHz Frequency Band

EXAMPLE OF TARGETS	RCS (m^2)	RCS (dBsm)	REFERENCES
Air Vehicle			
Jumbo Jet	100	20.00	[93]
Large Bomber or Large Jet Airliner	40	16.02	[93]

Medium Bomber or Medium Jet Airliner	20	13.01	[93]
Large Fighter	6	7.78	[93]
Helicopter	3	4.77	[93]
Small Fighter or four-passenger jet	2	3.01	[93]
Small, Single Engine Aircraft	1	0.00	[93]
Conventional Winged Missile	0.1	-10.00	[93]
Sea Vehicle			
Navy Cruiser (200 m long)	14000	41.46	[95]
Cabin Cruiser (40-50 ft)	10	10.00	[93]
Small Pleasure Boat (20-30 ft)	2	3.01	[93]
Small Open Boat	0.02	-16.99	[93]
Land Vehicle			
Pickup Truck	200	23.00	[93]
Automobille	100	20.00	[93]
Bicycle	2	3.01	[93]
Man	1	0.00	[93]
Biological Targets			
Large Bird	10^{-2}	-20	[93], [95]
Medium Bird	10^{-3}	-30	[93]
Large Insect (Locust)	10^{-4}	-40	[93]
Small Insect (Fly)	10^{-5}	-50	[93], [95]

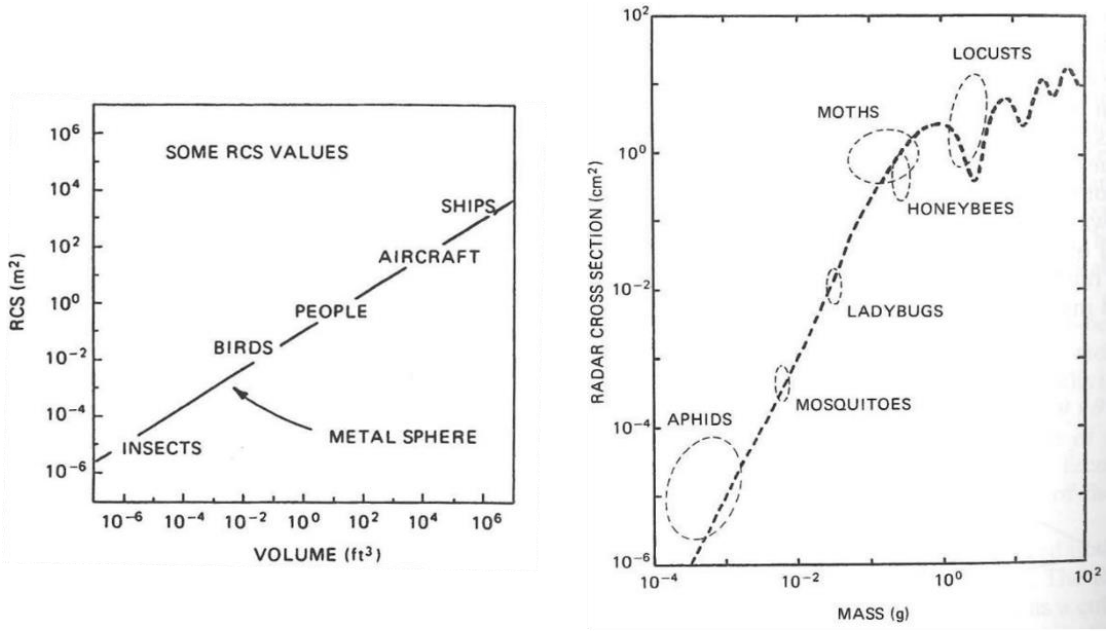

(a) (b)

Figure 2.6: A Comparison of RCS Values; (a) RCS of Different Kinds of Target, (b) RCS Values of Different Class of Insects [93]

Figure 2.6(a) shows each target with their RCS values and the metal sphere with a radius of a few cm have the closest value to the insects. The carrier frequency of the radar to obtain the RCS results as in the figure above is at 10 GHz X-band frequency. Hence, a metal sphere that can be used as the control measurement is a perfect resemblance to the insects RCS. The higher the RCS values, the better energy return from that target and vice versa. Insects with the smallest RCS values makes it nearly impossible to track until a radar is designed specifically to meet the need for insect detection. Figure 2.6(b) shows the distribution span of an insect species. Large insects like honeybees, moths and locusts are within the span of -40 to -30 dBsm RCS. While smaller insects have lower RCS than that, within a span of -60 to -90 dBsm like ladybugs, mosquitoes and aphids.

The ratio of the circumference of a sphere to the wavelength of the signal is defined by

$$k = 2\pi a/\lambda \qquad \textbf{(2-3)}$$

where a is the radius of the sphere. The RCS may differ by the diverse exhibition of structure and size of the target.

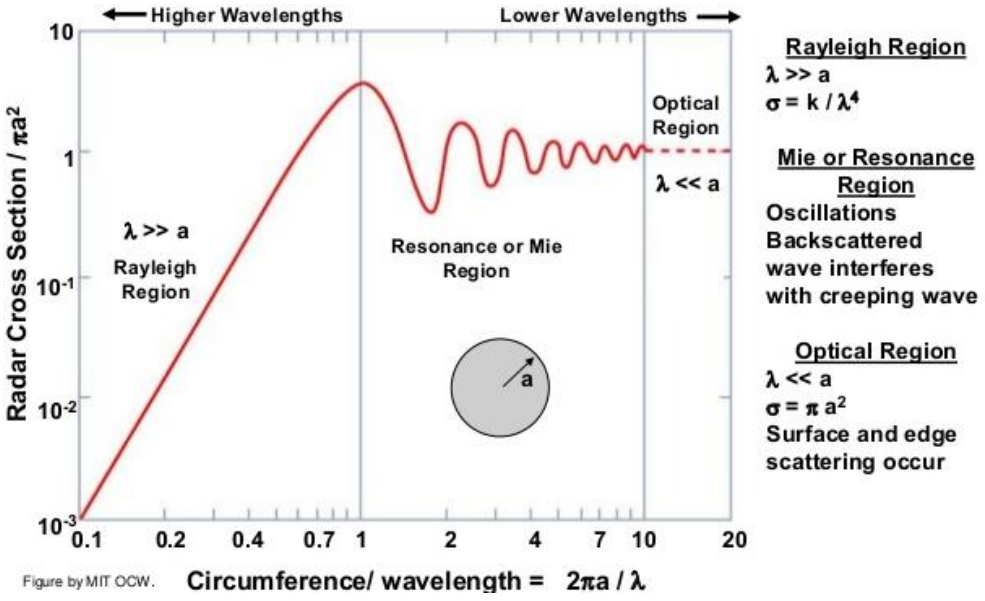

Figure 2.7: RCS of a Sphere [94]

Three different regions can be categorized to represent the RCS of the target as in Figure 2.7 and described in detail below:

Rayleigh region ($2\pi a << \lambda$): A region where the radar operates at low frequency and the wavelength is far much bigger in relation to the size of the sphere. This region is where RCS is linearly dependent on the signal wavelength to the power of four.

Mie or Resonance region ($2\pi a \sim \lambda$): At this region, the ratio k falls within the range of 1 until 10 and the value of RCS varies since it is dependent on the circumference $2\pi a$ of the sphere. As the $2\pi a$ approaches to λ, it reaches the maximum point of the RCS.

Optical or Far-Field region ($2\pi a >> \lambda$): This is where the maximum RCS will reach. In a region where operating frequency is high enough, then the wavelength of the signal is far much smaller than the size of the target. In this region, the RCS is no longer dependent on the operating frequency of the radar. And the RCS of a sphere is a constant value of the projected area, $\sigma = \pi a^2$.

It can be seen that the target of interest can be broadened from commercial nano-drone (or any insect like-size drones) to insect pests and harmful insects. All of these targets share nearly the same RCS value. And these targets will be the aim of this research specifically to a target with 5 cm less in size.

2.5 Summary

This chapter briefly presents the fundamental of radars and then introduce more details of FMCW radar specifically. Initially, the publications related to drone detection with FMCW radar are outlined. The literature survey presented the past publications until the current work in drone detection coupled with micro-Doppler signature are becoming popular as such this technique provide an effective solution for target classification. Primarily the review started with the modelling of the radar scatterers that will contribute to the Doppler spectrum.

The diverse contemporary paper utilizing micro-Doppler techniques were then reported. From the literature review of the past work, it can be concluded that nano drones of 5 cm less in size has not been fully investigated yet. Hence, this lack of study has become the key motivator for this research study.

3 FMCW RADAR SIGNAL PROCESSING

The working process of FMCW radar and signal processing concepts are outlined in this chapter, which is the central part of the radar discipline. The importance of certain parameters and their dependable performance are briefly explained as well. This chapter is the basics that one should have in mind to have an idea of the whole research that will be shared in a later chapter. The FMCW radar model without the IQ demodulator in the system is being discussed. Then, briefly explained the micro-Doppler extraction model and the radar range equation is presented.

3.1 Signal Processing

This sub-section has been mainly inspired by the following textbook; *Principles of Electronic Communication Systems* [96] and *Communication System* [97]. Digital Signal Processing (DSP) is a vital part of radar, this is where the signal is modified and analysed in order to optimise the performance of the system. The majority of the conversion process and various operations occur in this session. Transmit signal is defined as a function of time and Fourier Transform allows the signal to be represented in the time domain or frequency domain. The relation of time and frequency domain is describing by these two equations below:

$$G(f) = \int_{-\infty}^{\infty} g(t) e^{-j2\pi f t} dt \quad \textbf{(3-1)}$$

$$g(t) = \int_{-\infty}^{\infty} G(f) e^{j2\pi f t} df \quad \textbf{(3-2)}$$

From the time domain to the frequency domain, a Fourier Transform is performed. And from the frequency domain to the time domain, an Inverse Fourier Transform is performed. Time, t is measure in seconds (s) and frequency, f is measured in Hertz (Hz). The relation between angular

frequency, ω which is measured in radians per second (rad/s) and frequency is as follow:

$$\omega = 2\pi f \quad \textbf{(3-3)}$$

The baseband signal is the original state of the signal. Theoretically speaking, it is possible to transmit these original signals without any modification but realistically it is impractical. It is exposed to noise and distortion during transmission. Hence, in order to transmit a signal from one place to another, the signal goes through a modulation process so that the signal is being transmitted efficiently [96]. The original signal usually is modulated into a higher frequency signal (or a carrier signal) which is then radiated into space which enables the signal to travel within long distances. This is where most of the RF waves of the radar is basically in the range of a few GHz. The modification of the signal from the baseband into a high-frequency signal is called modulation as in Figure 3.1.

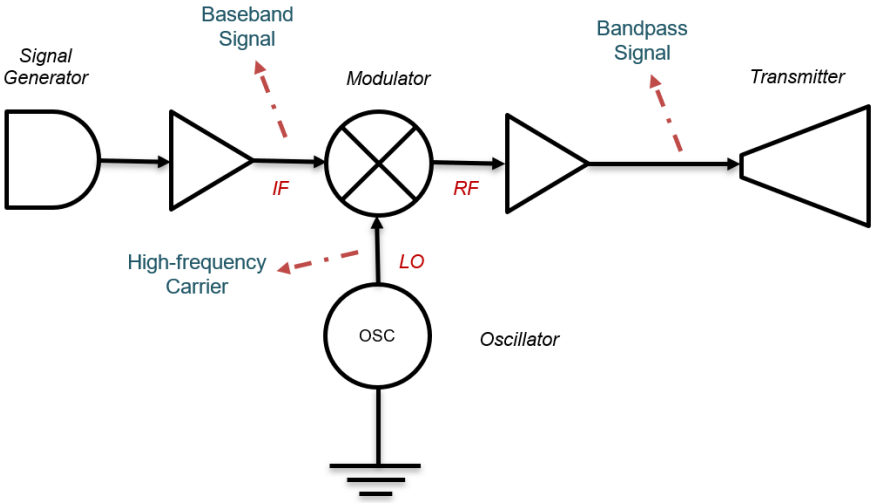

Figure 3.1: A Baseband Signal Modulated to Bandpass Signal in Transmitter

This process is achieved by an oscillator that generates a sine wave as a frequency carrier of the signal just before it is being amplified and transmitted. Once the signal is carried forward to the antenna for transmission, that transmission is usually known as bandpass transmission. On the other hand, once the signal bounced back to the receiver, the echo signal is amplified and demodulated to draw out the original baseband as in Figure 3.2. The down-conversion process will shift the RF higher frequency back to the IF lower

frequency. These two essential processes in radar systems can be illustrated in the figures below.

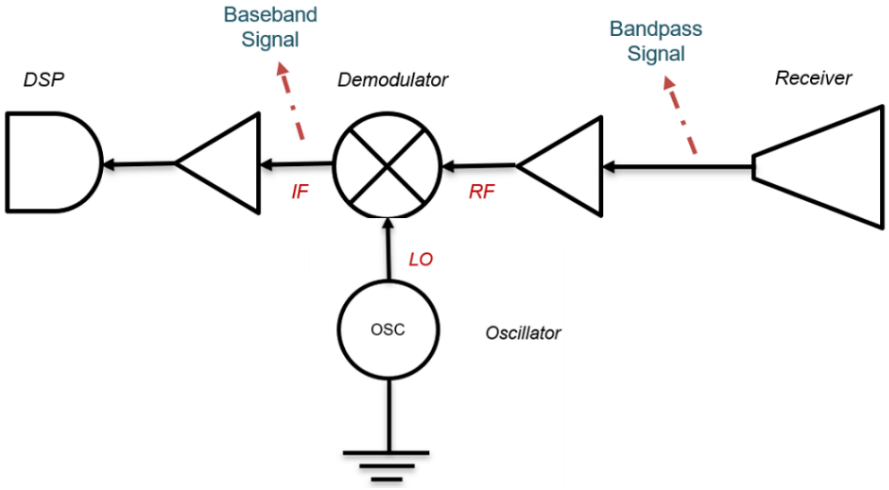

Figure 3.2: Demodulation of Bandpass Signal to Baseband Signal in Receiver

The modulation of up-conversion and down-conversion signals can be realised by using an analogue mixer or digital mixer. For the up-conversion case, the IF signal will be multiplied with the LO port signal $\cos(2\pi f_{LO}t)$. Whereas, for the down-conversion case, the RF signal will be multiplied by the LO signal $\cos(2\pi f_{LO}t)$. The output of the RF mixer is the summation $f_{RF} + f_{LO}$ or difference $f_{RF} - f_{LO}$ between the two input channels. One will be injected to the left of f_{LO} (i.e., lower sideband) and another one is injected to the right f_{LO} (i.e., upper sideband).

3.1.1 Down Sampling Signal

The general expression for a bandpass radar signal can be written as:

$$S_R(t) = A(t)\cos(2\pi f_0 t + \phi(t)) \quad \textbf{(3-4)}$$

Where $A(t)$ is the amplitude modulation, $\phi(t)$ is the phase modulation and f_0 is the carrier frequency. Using the trigonometry identity of

$$\cos(\alpha + \beta) = \cos(\alpha)\cos(\beta) - \sin(\alpha)\sin(\beta)$$

The radar signal can also be written by,

$$S_R(t) = A(t)\cos(\phi(t))\cos(2\pi f_0 t) - A(t)\sin(\phi(t))\sin(2\pi f_0 t) \quad \textbf{(3-5)}$$

Where,

$$S_I(t) = A(t)\cos(\phi(t)) \quad \textbf{(3-6)}$$

$$S_Q(t) = A(t)\sin(\phi(t)) \quad \textbf{(3-7)}$$

The signal, $S_I(t)$ and $S_Q(t)$ are called in-phase and quadrature components respectively. In order to digitize a high-frequency signal, a sampling frequency of tens of GHz would be required. This is because according to the Nyquist rule, the bandwidth needs to be doubled the carrier frequency. But this is not possible in a real case, there is no current technology that could cope with high-frequency sampling and it also requires a lot of time to digitize it. Hence, a mixer is being used to solve this issue. It will shift the spectrum to a much lower frequency. This process is known as down-conversion. Figure 3.3 shows the scheme of deriving the in-phase and quadrature components of a bandpass signal. The conversion of the signals is explained mathematically as written below. From equation (3-4), it can also be written as,

$$S_{BP}(t) = A(t)\cos\big(2\pi f_0 t + \phi(t)\big)$$

$$S_{BP}(t) = S_I(t)\cos(2\pi f_0 t) - S_Q(t)\sin(2\pi f_0 t) \quad \textbf{(3-8)}$$

$$S_{BP}(t) = Re[S_{LP}(t)e^{j2\pi f_0 t}]$$

$$S_{BP}(t) = \frac{S_{LP}(t)e^{j2\pi f_0 t} + S_{LP}^*(t)e^{-j2\pi f_0 t}}{2} \quad \textbf{(3-9)}$$

Where,

$$S_{LP}(t) = S_I(t) + jS_Q(t) \quad \textbf{(3-10)}$$

$$S_{LP}(t) = A(t)e^{j\phi(t)} \quad \textbf{(3-11)}$$

$S_{BP}(t)$ is a bandpass signal and $S_{LP}(t)$ is a baseband equivalent signal or also known as a complex envelope of the bandpass signal. A bandpass signal is usually represented in a complex baseband equivalent form. This is because the baseband equivalent form simplifies the analysis and simulation of bandpass communication systems. From Figure 3.3, the processor combines the I and Q components into one single complex signal. The signal can now be digitised with a much lower sampling frequency.

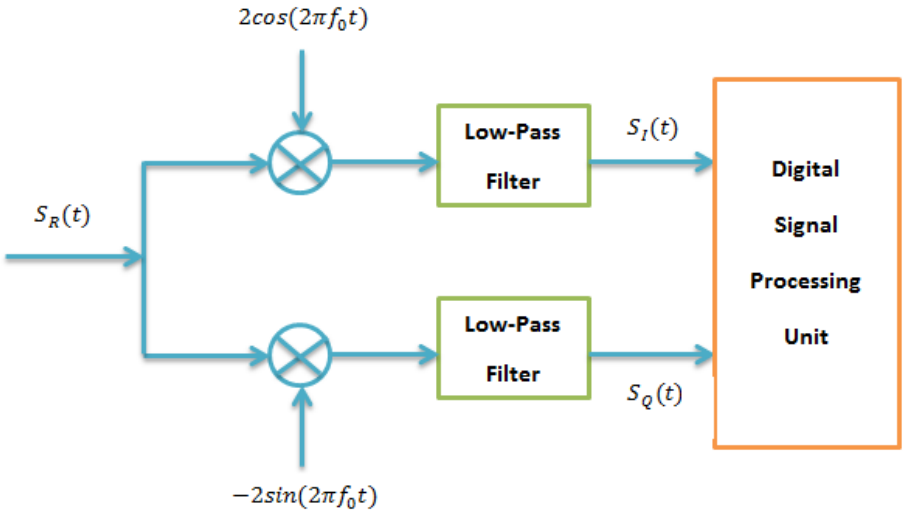

Figure 3.3 Received Signal Block Diagram of IQ Demodulation

Figure 3.4 shows a spectral representation of IF input where the spectral is centred at the frequency, f_{IF}. The right side is the positive part of the signal and the left-hand side is the negative part of the signal. The positive part corresponds to the complex envelope.

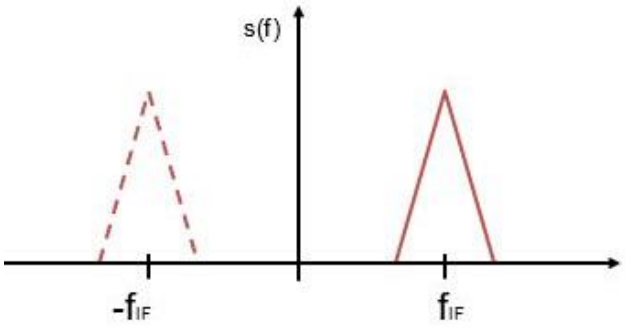

Figure 3.4: Spectral Representation of IF

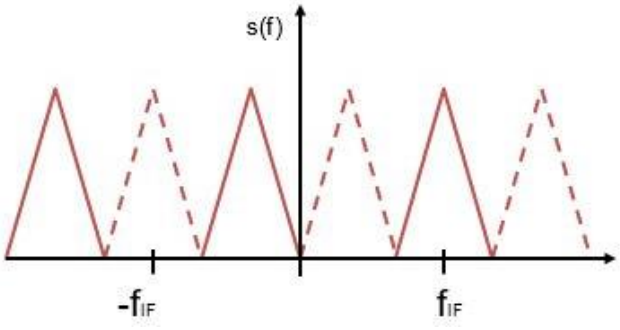

Figure 3.5: Periodic Spectrum of the Digitized Signal

The spectrum of a digitized signal is periodic as in Figure 3.5. The periodic is inversely proportional to the sampling rate $1/T_s$ which is equal to the sampling frequency F_s.

3.2 Signal Waveform & the Characteristic

A sinusoidal waveform can be represented as follow $s = A\cos\phi$. This illustrates that there are two important parameters which are the amplitude A and the phase angle ϕ. In order to get the best performance according to the application, it is possible to modulate these two parameters resulting in an amplitude modulation (AM) signal and angle modulation. According to [97], the angle modulation here can be either frequency modulation (FM) or phase modulation (PM). So, an angle-modulation waveform can be express as follows,

$$s(t) = A\cos[\phi(t)] \quad \textbf{(3-12)}$$

This sinusoidal wave makes a complete circle after every 2π radians. $\phi(t)$ increases with increasing time. The instantaneous frequency of the signal $f_i(t)$ can be defined as follows,

$$f_i(t) = \lim_{\Delta t \to 0} f_{\Delta t}(t) \quad \textbf{(3-13)}$$

$$f_i(t) = \lim_{\Delta t \to 0}\left[\frac{\phi_i(t+\Delta t) - \phi_i(t)}{2\pi\Delta t}\right]$$

$$f_i(t) = \frac{1}{2\pi}\frac{d}{dt}\phi_i(t)$$

From equation (3-13), the FM equation can be derived. Let say the instantaneous phase angle is expressed as

$$\phi_i(t) = 2\pi \int_0^t f_i(\tau)d\tau + \phi_0 \quad \textbf{(3-14)}$$

Where ϕ_0 is the initial phase offset and assuming that $\phi_0 = 0$

$$\phi_i(t) = 2\pi \int_0^t f_i(\tau)d\tau \quad \textbf{(3-15)}$$

Let say $f_i(\tau) = \gamma t + f_0$, which represents a linear chirp and f_0 is the carrier frequency. By taking the integration of equation (3-15) resulting

$$\phi_i(t) = 2\pi \int_0^t (\gamma t + f_0)\, d\tau = 2\pi \left[\gamma \frac{t^2}{2} + f_0 t\right]_0^t \quad \textbf{(3-16)}$$

By simplifying the equation above

$$\phi_i(t) = 2\pi f_0 t + \pi\gamma t^2 \quad \textbf{(3-17)}$$

where gamma γ here denotes the frequency modulator where will be discussed in the next section. Again, from equation (3-12), it is obvious that the amplitude of the waveform is constant for all time t

3.2.1 Time Delay & Beat Frequency

The extraction of time delay and beat frequency information can be obtained by the analysis of the IF output signal of the mixer. These will be explained in the following sub-sections; (i) the first sub-section is when the IQ demodulator is present in the circuit, (ii) the second sub-section is when the IQ demodulator is excluded from the circuit. The second option is where the concept will be practically used throughout the experimental work in Chapter 5 and Chapter 6.

3.2.1.1 With IQ Demodulator

The transmitted and received signal is in the form of a chirp signal where the waveform looks like an accordion waveform. It has a lower frequency in the beginning then slowly starts to increase as time increases. As explained in the previous subsection, the angle modulation of FM is described in equation (3-17). So, a transmitted linear chirp can be defined as,

$$S_T(t) = A\cos\left(2\pi f_0 t + \gamma\pi t^2\right)$$

$$S_T(t) = Ae^{j\phi(t)} = Ae^{j\left(2\pi f_0 t + \gamma\pi t^2\right)} \quad \textbf{(3-18)}$$

whereas the received signal is a delayed version of equation (3-18) with a time delay t_0. It can be expressed as following equation

$$S_R(t) = A\cos\left(2\pi f_0(t - t_0) + \gamma\pi(t - t_0)^2\right)$$

$$S_R(t) = Ae^{j\phi(t)} = Ae^{j\left(2\pi f_0(t-t_0) + \gamma\pi(t-t_0)^2\right)} \quad \textbf{(3-19)}$$

To fully comprehend the relationship of S_T and S_R, one must refer back to the FMCW block diagram in Figure 2.2. These two signals are two important inputs in the mixer block with different phases. The transmit signal S_T is multiplied with the received signal S_R within the mixer component resulting in one output which is considered as extra information that could be extract compared to CW radar. Figure 3.6 is a diagram of a single target in front of the radar and produces the IF signal. The blue line colour in that figure is the instantaneous frequency of the transmitted signal whereas the green colour is the instantaneous frequency of the received signal.

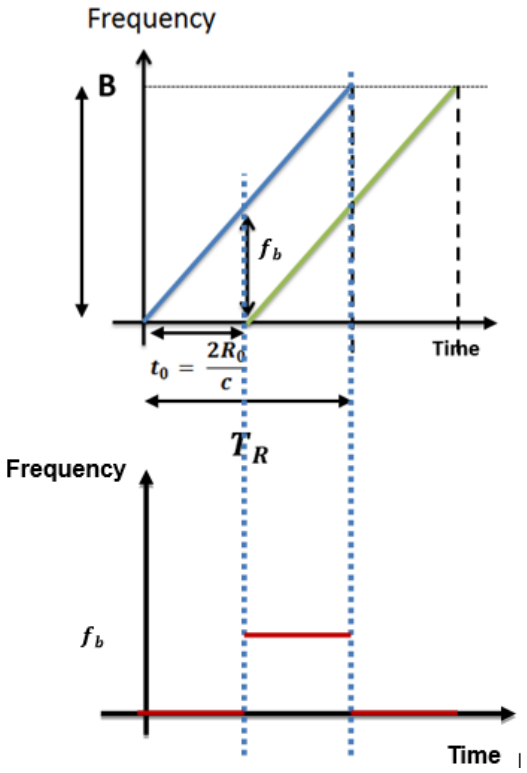

Figure 3.6: FMCW Chirp in Time-Frequency Relation. (Above) Linear Up-Ramp Chirp with Transmitted & Received Signal. (Below) Frequency offset

$$S_T . S_R = |S_T||S_R| \cos\theta \qquad \textbf{(3-20)}$$

The multiplication product of two RF vectors of the transmitted signal, S_T and the received signal, S_R are shown as in the above equation. If the two vectors are parallel, then $\theta = 0℃, 180℃$. Resulting $\cos\theta = 1$, the optimum constant. When two parallel ramps are multiplied together, there is a constant offset as shown in Figure 3.6 above. When the mixed signal is plotted in a frequency vs time graph, there is a constant frequency offset. This offset refers to the range of the target to the radar. The bigger the value of the offset, the further the target is from the radar. The range properties make the FMCW radar more valuable compared to unmodulated frequency CW radar.

To do the multiplication of these two vectors, it is written in a complex form to ease the calculation. Hence,

$$S_T(t) = Ae^{j2\pi f_0 t}.e^{j\gamma\pi t^2} \quad \textbf{(3-21)}$$

$$S_R(t) = Ae^{j2\pi f_0 (t-t_0)}.e^{j\gamma\pi (t-t_0)^2} \quad \textbf{(3-22)}$$

The mixed-signal of these two vectors are,

$$S_T(t)^*.S_R{}'(t) = A^2 e^{j2\pi f_0 t}.e^{j\pi\gamma t^2}.e^{-j2\pi f_0 (t-t_0)}.e^{-j\pi\gamma (t-t_0)^2} \quad \textbf{(3-23)}$$

$$S_T(t)^*.S_R{}'(t) = A^2 e^{j[2\pi f_0 t + \pi\gamma t^2 - 2\pi f_0 t + 2\pi f_0 t_0 - \pi\gamma t^2 + 2\pi\gamma t t_0 - \pi\gamma {t_0}^2]}$$

$$S_{f_b}(t) = S_T(t)^*.S_R{}'(t) = A^2 e^{j2\pi f_0 t_0}.e^{j2\pi\gamma t_0 t}.e^{-j\pi\gamma {t_0}^2} \quad \textbf{(3-24)}$$

Equation (3-24) is a simplified version of the multiplication product. From that equation, there is one term which is changing with time $e^{j2\pi\gamma t_0 t}$ and the other two is constant $A^2 e^{j2\pi f_0 t_0}.e^{-j\pi\gamma {t_0}^2}$. Hence, the instantaneous frequency of the beat frequency f_b is simply the phase derivation with respect to time

$$f_b = \frac{1}{2\pi}\frac{d}{dt}\phi(t) = \gamma t_0 \quad \textbf{(3-25)}$$

Where γ is defined as the slope of frequency sweep, which is the rate of change in transmitted frequency and time delay t_0 is the round-trip time (RTT) of the target. These parameters are shown clearly in Figure 3.6,

$$\gamma = \frac{B}{T_r} \quad \textbf{(3-26)}$$

$$t_0 = \frac{2R_0}{c} \quad \textbf{(3-27)}$$

Where B is the bandwidth or maximum frequency and T_r is the ramp duration. By inserting equation (3-26) and equation (3-27) in equation (3-25), the mixed-signal can be written as,

$$f_b = \frac{B}{T_r}.\frac{2R_0}{c} \quad \textbf{(3-28)}$$

where R_0 is the initial range of the target to the radar and c is the speed of light.

Equation (3-18) until equation (3-28) are the measurements and calculations within the mixer whereby the transmitted signal is mixed with the conjugate of the received signal. Equation (3-28) demonstrate important parameters in affecting the beat frequency which is the initial range of the target R_0, bandwidth B and ramp duration T_r. These parameters are important in FMCW radar.

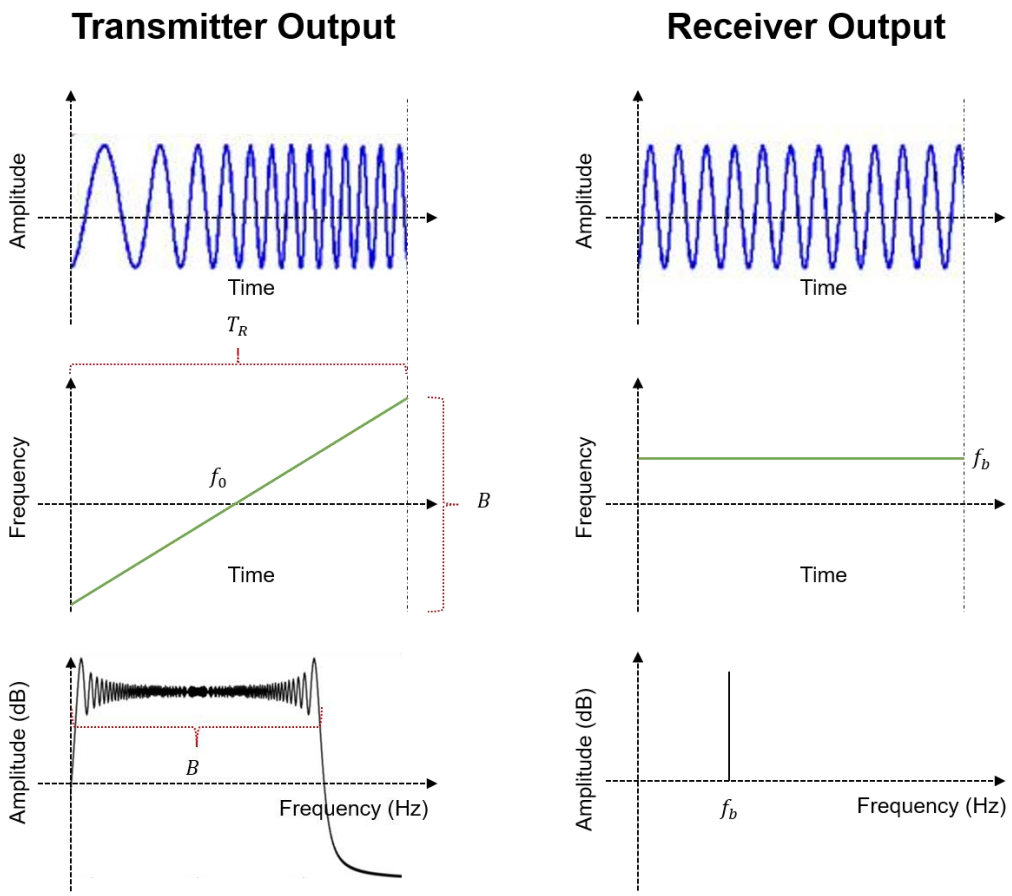

Figure 3.7: Signal before and after Mixing Operation: (a) Time Domain Representation, (b) Frequency-Time Relation, (c) Frequency Spectrum

3.2.1.2 Without IQ Demodulator

An alternative way to write the last subsection is as follows. The generated and the transmitted signal is,

$$S_T(t) = cos(2\pi f_o t + \gamma\pi t^2) \quad \textbf{(3-29)}$$

As the echo signal reflected and bounced back from the target to the receive antenna and the LNA amplifies the signal. The received signal is,

$$S_R(t) = cos(2\pi f_o(t - t_o) + \gamma\pi(t - t_o)^2) \quad \textbf{(3-30)}$$

$$x(t)y(t) = \frac{AB}{2}\cos(\omega_1 - \omega_2)t \cdot \frac{AB}{2}\cos(\omega_1 + \omega_2)t \quad \textbf{(3-31)}$$

By using the trigonometric formula as in equation (3-31), the received signal S_R is mixed with a copy of the transmitted signal S_T so that the signal output can be determined. The two products of cosine are a summation of two cosines. The first term is the subtraction of two products and the second term is the addition of the two products. By substituting $S_T(t)$ and $S_R(t)$ in the trigonometry formula as in equation (3-31), it is possible to determine the frequency spectrum after the mixer.

$$\begin{aligned} S_T(t) \cdot S_R(t) = {} & [Acos(2\pi f_o t + \gamma\pi t^2)] \\ & \cdot [Bcos(2\pi f_o(t - t_o) + \gamma\pi(t - t_o)^2)] \end{aligned} \quad \textbf{(3-32)}$$

$$\begin{aligned} S_T(t) \cdot S_R(t) = \frac{AB}{2}\{ & cos(2\pi f_o t + \gamma\pi t^2 - (2\pi f_o(t - t_o) + \gamma\pi(t - t_o)^2)) \\ & + cos(2\pi f_o t + \gamma\pi t^2 + 2\pi f_o(t - t_o) + \gamma\pi(t - t_o)^2)\} \end{aligned}$$

Equation (3-32) is simplified to

$$\begin{aligned} S_T(t) \cdot S_R(t) = \frac{AB}{2}\{ & cos(2\pi f_o t_o + 2\pi\boldsymbol{\gamma t_o} t - \pi\gamma {t_o}^2)) \\ & + cos(4\pi f_o t + 2\pi\gamma t^2 - 2\pi f_o t_o - 2\pi\boldsymbol{\gamma t_o} t + \pi\gamma {t_o}^2)\} \end{aligned} \quad \textbf{(3-33)}$$

The frequency of the signal can be determined by simply taking the time derivative of the phase function above. The first phase of cosine is written as

$$f_1(t) = \frac{1}{2\pi}\frac{d}{dt}\phi_1(t) = \frac{1}{2\pi}\frac{d}{dt}[2\pi f_o t_o + 2\pi\boldsymbol{\gamma t_o} t - \pi\gamma {t_o}^2] \quad \textbf{(3-34)}$$

While the second phase of cosine is placed as

$$f_2(t) = \frac{1}{2\pi}\frac{d}{dt}\phi_2(t) = \frac{1}{2\pi}\frac{d}{dt}[4\pi f_o t + 2\pi\gamma t^2 - 2\pi f_o t_o - 2\pi\boldsymbol{\gamma t_o} t + \pi\gamma {t_o}^2] \quad \textbf{(3-35)}$$

Hence by taking the derivative with respect to time and discarding the constant term in both of the phase function $\phi(t)$, where the time delay t_o is a constant value, the instantaneous frequency of the mixed-signal are as follows,

$$f_1(t) = \frac{1}{2\pi}[2\pi\boldsymbol{\gamma t_o}] = \boldsymbol{\gamma t_o} \quad \textbf{(3-36)}$$

$$f_2(t) = \frac{1}{2\pi}[4\pi f_o + 4\pi\gamma t - 2\pi\boldsymbol{\gamma t_o}] = 2f_o + 2\gamma t - \boldsymbol{\gamma t_o} \quad \textbf{(3-37)}$$

Regarding the result above, two terms can be found. The frequency of the first term is the beat frequency f_b which is equal to the product between the ramp slope γ and the time delay, $(f_b = \gamma t_o)$. The time delay measures the range of the target. As discussed in the previous section, γ is directly proportional to the bandwidth and inversely proportional to the ramp duration. The second term is a cosine wave at double the frequency carrier and is filtered out with a low-pass filter before the Analogue-to-Digital Converter (ADC). The second term also shows the negative of the beat frequency. Which will have the opposite value of the first term. So, let say the ramp duration is 1 ms, bandwidth is 50 MHz and the initial range of the target is 3 m.

$$f_b = \left(\frac{B}{T_r}\right)\frac{2R}{c} = \left(\frac{50x10^6}{1x10^{-3}}\right)\frac{2(3)}{3x10^8} = 1{,}000\ Hz \quad \textbf{(3-38)}$$

The bandwidth of the spectrum is 1,000 Hz that is inversely proportional to the ramp duration. By increasing the ramp duration, the spectrum bandwidth will be narrower and the beat frequency f_b becomes smaller. These spectrum frequencies are roughly located as in Figure 3.8.

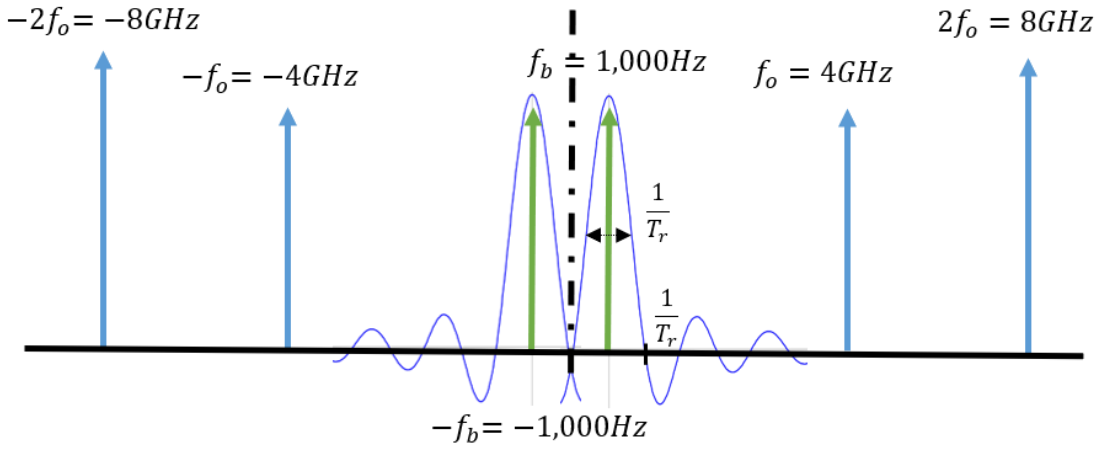

Figure 3.8: Spectrum Frequencies after Mixer

If the target is close to the radar, and the range is approximately equal to zero, f_b shifts to the centre resulting in an overlap between the positive spectrum and the negative spectrum components.

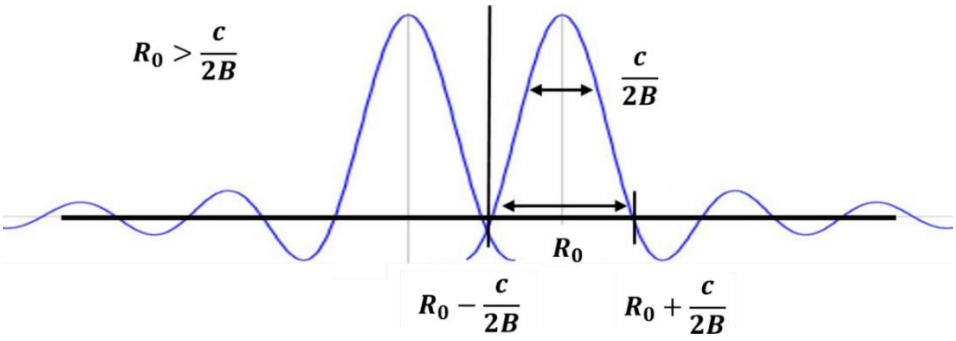

Figure 3.9: The Maximum State Before Overlapping of the Two Spectrums Occur

Considering that this radar design does not include the usage of an IQ demodulator mixer, hence, these two-sided spectrums are unavoidable. Because of the state of cutting costs and reducing expenses due to the limitation in the budget, an alternative way to IQ mixer replacement is the chosen radar parameters. Figure 3.9 exemplified the maximum state before the two spectrums can overlap. It is shown that if the two spectrums shift towards the zero range, then overlapping occurs. Hence, to avoid this overlapping zone is to select the parameters so that the range of the target is always larger than the radar range resolution. In this case, a bandwidth with 50 MHz, will have a range resolution of 3 m. A target that is further away from 3 m, will not get affected. However, having an even greater frequency bandwidth will minimize

further the limitation of the target range. Let say, a radar with a 500 MHz bandwidth will have a range resolution of 0.3 m (or 30 cm). The larger the frequency bandwidth, the narrower the range resolution. And the f_b in Figure 3.8 will also shift towards the non-zero Doppler region (i.e. shifts away from the overlapping region), without affecting the Doppler resolution.

3.2.2 Range Definition

The relationship between f_b and the target range can simply be found by rearranging equation (3-28) to obtain

$$R = \frac{c\, f_b\, T_r}{2B} \tag{3-39}$$

After the demodulator, the beat signal will go through other vital processes, which is filtered, amplified, digitized and Fourier Transform. The amplification signal is the input of the ADC. ADC is the heart of digital signal processing where it plays a great model in assigning binary values to analogue samples. This is a quantization process. Then, it is transferred to DSP to perform Fast Fourier Transform (FFT) as well as STFT for time-frequency analysis. STFT which is the segmented sequence of FFT provides both frequency and time information. DSP is similar to the microprocessor where pre-advanced math takes part. Then the plotted result is being displayed for analysis. Since the IF will be digitized for further DSP, hence the beat signal will be limited to the sampling frequency of the digitizer that satisfies the Nyquist criteria.

$$Fs \geq 2\, f_{b_{max}} \tag{3-40}$$

By using the beat frequency definition and by considering the ADC limitation, the unambiguous range detection can be defined as

$$R_u = \frac{c\, Fs\, T_r}{2B} \tag{3-41}$$

Where R_u is directly proportional to the sampling rate of ADC, Fs. The Doppler resolution is inversely proportional to the dwell time. Then, in order to resolve

between multiple targets, it is mainly depending on the bandwidth of the chirp as follows

$$f_{b_{resolution}} = \frac{1}{T_r} = \frac{B}{T_r}.\frac{2R_{resolution}}{c} \quad \textbf{(3-42)}$$

The dwell time, in this case, is the ramp duration since the analysis processing is according to the length of chirp time. By simplifying the equation above will result as follows

$$R_{resolution} = \frac{c}{2B} \quad \textbf{(3-43)}$$

It is obvious that the bigger the chirp bandwidth, the better the range resolution, the better the radar to resolve between two targets that are closed to each other. However, this range resolution is also dependent on the chirp linearity. If the non-linearity increases, the range resolution will suffer and degrades. In conventional pulse radar, the integration time, T will affect the main lobe length by $B = \frac{1}{T}$. The smaller the T, the bigger the B, resulting in a better range resolution. The relationship is defined as follows, $R_{Resolution} = \frac{cT}{2} = \frac{c}{2B}$. In some radar applications, FMCW radar is preferable over conventional pulse radar because of this matter. Instead of range resolution dependent on the pulse width, it is dependent on bandwidth.

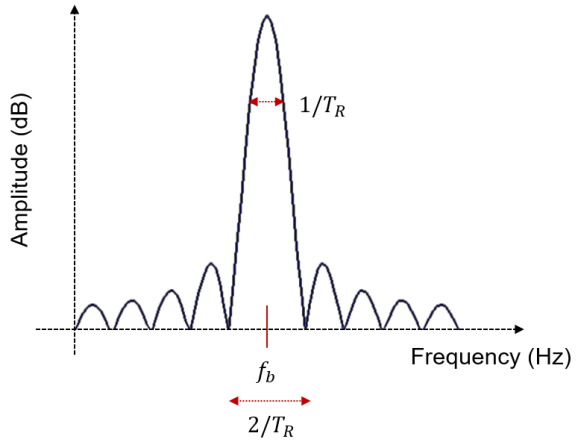

Figure 3.10: Mixed Signal, an IF signal which represents the beat frequency

This main lobe bandwidth is $\frac{1}{T_r}$ as illustrated in Figure 3.10 which is determined at a point of -3dB below the maximum of the peak spectrum. It can also be defined as the distance between the two nulls of the main lobe as double of the $\frac{1}{T_r}$.

3.2.3 Doppler Definition

The process of target detection involves two major steps. The first step is to apply FFT to the output signal from the mixer. The signal received in Figure 3.6, which is the result of after multiplication of received and transmitted signal, will be segmented into small windows of the length of chirp duration. This is generally illustrated as in Figure 3.11. Then the first FFT is applied resulting in a frequency spectrum for each chirp. Each of these chirps will extract the time delay that represents the range information of the target to the radar. The beat frequency f_b is direct proportional to the range of the target. This process will execute a spectral frame of Range Time Intensity (RTI) plot, as discussed in the previous sub-section. The frequency spectrum of each FFT is arranged in a 2D matrix where each column represents a single chirp.

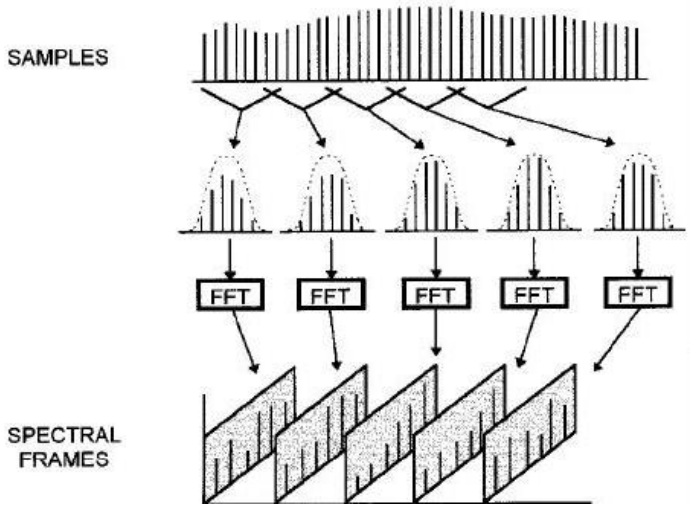

Figure 3.11: The STFT Process, which is a Sequence of FFT Corresponding to Every Segmented Window [98]

Then, second FFT is performed in each row horizontally from the last matrix, in order to extract the Doppler of the target. This can be identified by looking at the peak of the Range-Doppler Map (RDM). By taking a zero-Doppler removal, that is by removing the mean value in each row, the moving target will be detected and the Doppler shift from the signal can be found.

In radar, EM waveform is used in transmitting and receiving signals. It behaves much similar to visible light but with different frequencies, where both, the propagation of EM wave uses the speed of light c as its constant reference. It is obvious that the speed of the target is significantly slower than the speed of light, that is, $v<<c$ where $v/c \approx 0$. EM source at a frequency f will be moving in straight lines with the velocity v of a target. Since the EM wave will travel at a double path (from radar to the target and reflected by the target to the radar), the Doppler shift is expressed as $f_d = \frac{2v}{\lambda}$ where the wavelength λ of a signal is defined as $\lambda = \frac{c}{f_0}$. Thus, the Doppler frequency shift can simply be written as

$$f_d = -\frac{2f_0 v}{c} \tag{3-44}$$

Where v is the radial velocity of a target relative to the radar. In the last sub-section, the target is assumed to be stationary during data collection. Once the target is moving, then the time delay changes due to the changes from the range of the target.

$$t_0 = \frac{R(t)}{c} = \frac{R_0 \pm vt}{c} \tag{3-45}$$

Velocity is expressed as positive velocity when the target is moving away from the source of the EM wave. Resulting in the Doppler shift becomes negative. The Doppler shift is negative when the target is moving away from the radar and the Doppler shift is positive when the target is moving towards the radar. Recalling equation (3-24), the t_0 is no longer constant resulting in the last equation is expressed as follow

$$S_T(t)^*.S_R{}'(t) = A^2 e^{\left(j2\pi f_0\left(\frac{R_0 \pm vt}{c}\right)+j2\pi\gamma\left(\frac{R_0 \pm vt}{c}\right)t - j\pi\gamma\left(\frac{R_0 \pm vt}{c}\right)^2\right)} \tag{3-46}$$

$$S_T(t)^*.S_R{}'(t) = A^2 e^{(j2\pi f_0\left(\frac{R_0}{c}\right)+j2\pi f_0\left(\frac{\pm vt}{c}\right)+j2\pi\gamma\left(\frac{R_0 t}{c}\right)+j2\pi\gamma\left(\frac{\pm vt^2}{c}\right))}$$

The last term $e^{\left(-j\pi\gamma\left(\frac{R_0\pm vt}{c}\right)^2\right)}$ is considered negligible as the radial velocity of the target v are relatively much slower than the double speed of light c^2.

$$f_b = \frac{1}{2\pi}\frac{d}{dt}\left[2\pi f_0\left(\frac{R_0}{c}\right) + 2\pi f_0\left(\frac{\pm vt}{c}\right) + 2\pi\gamma\left(\frac{R_0 t}{c}\right) + 2\pi\gamma\left(\frac{\pm vt^2}{c}\right)\right] \quad \textbf{(3-47)}$$

$$f_b = f_0\left(\frac{\pm v}{c}\right) + \gamma\left(\frac{R_0}{c}\right) + \gamma\left(\frac{\pm 2vt}{c}\right) \quad \textbf{(3-48)}$$

$$f_b = f_0\left(\frac{\pm v}{c}\right) + \gamma\left(\frac{R_0 \pm 2vt}{c}\right) \quad \textbf{(3-49)}$$

From equation (3-49), assuming that $t = 0$ where it is at the initial phase, the first term is due to Doppler shift and the second term is due to the time delay of the target. The total instantaneous frequency of an echoed signal included two basic elements which are Doppler shift, f_d and the beat frequency, f_b.

$$f_{IF} = f_d + f_b \quad \textbf{(3-50)}$$

$$f_{IF} = \frac{2v}{\lambda} + \frac{B}{T_r}.\frac{2R_0}{c}$$

When a target approaches the radar, the received waveform in Figure 3.6 will shift downwards in the y-axis. The beat frequency will add to the Doppler frequency resulting in the instantaneous frequency will increase. This is called the up-Doppler phenomenon. On the other hand, when the target moves away from the radar, the received waveform in Figure 3.6 will shift upward at the y-axis. Hence, the beat frequency will subtract to the Doppler frequency resulting in the instantaneous frequency will decrease.

The difference between the transmitted signal and the received signal is a phase shift of a sinusoidal wave. From equation (3-14), this phase shift occurs due to time delay

$$\phi_{shift} = 2\pi f_0 t_0 \ = 2\pi \left(\frac{c}{\lambda}\right)\left(\frac{2R_0}{c}\right) = \frac{4\pi R_0}{\lambda} \quad \textbf{(3-51)}$$

The reflected phase shift is changing with respect to the changing of range with time. By replacing distance $R_0 = vT_r$,

$$\phi_{shift} = \frac{4\pi(vT_r)}{\lambda} \quad \textbf{(3-52)}$$

To tell apart from two different frequencies, the phase shift will need to be bigger than 2π and to avoid ambiguous velocity, the phase shift needs to be less than π.

$$\phi_{shift} = \frac{4\pi(vT_r)}{\lambda} > \frac{2\pi}{N} \quad \textbf{(3-53)}$$

N represents the number of ramps. The frequency resolution of FFT is written as

$$f_{resolution} = \frac{1}{T_{dwell}} = \frac{1}{NT_r} \quad \textbf{(3-54)}$$

Where the dwell time, T_{dwell} is equivalent to the ramp duration, T_r times with the number of ramps, N. And rearranging the equation above resulting a velocity resolution as below

$$v_{resolution} = \frac{\lambda}{2\,(NT_r)} \quad \textbf{(3-55)}$$

However, the $v_{resolution}$ calculation is only necessary when the targets are in the same range but have different velocities.

$$\phi_{shift} = \frac{4\pi(vT_r)}{\lambda} < \ \pi \quad \textbf{(3-56)}$$

By rearranging the equation above, resulting in unambiguous velocity as

$$v_{max} = \frac{\lambda}{4\,T_r} \quad \textbf{(3-57)}$$

It can be concluded that for a fast-moving target, it is expected to have a larger Doppler shift, referring to equation (3-44) where the unambiguous velocity corresponds to the unambiguous (maximum) Doppler shift, $v_{max} = \frac{\lambda(f_{d_{max}})}{2}$. And this will require a shorter ramp duration in the radar design as expressed below

$$T_r = \frac{1}{2(f_{d_{max}})} \tag{3-58}$$

this maximum T_r is required to avoid ambiguity. That is, it is advisable to be lesser than that value, $T_r < \frac{1}{2(f_{d_{max}})}$ to avoid aliasing.

3.3 Micro-Doppler Theory

From the last chapter discussed, it is known that any sort of moving object either from bulk or micro-motion movement will generate Doppler shift and micro-Doppler respectively. A considerable amount of literature has been published on the micro-Doppler effect in radar especially written by Chen [9 - 10]. In that published work, a mathematical model of the micro-Doppler equation can arise from the conventional Doppler equation as discussed in [9 - 10]. The radar is fixed in a stationary position, with no translational and rotational movement. While the target, on the other hand, will have a translational and rotational movement. Assume a target that is located at a distance R_0 from the radar, is moving translationally at velocity v and the micro-component of a target moving rotationally with an angular velocity ω. This micro-component of a target has a length of r from the main body of the target. Hence the total range R_{total} of the entire motion is express as follows

$$R_{total}(t) = R_0 + vt + \Re r \tag{3-59}$$

Where $\Re$ is the rotation matrix of the target. Hence, the return signal is

$$s(t) = \rho(x,y)e^{j2\pi f\left(\frac{2R_{total}(t)}{c}\right)} = \rho(x,y)e^{j\phi(t)} \tag{3-60}$$

Where $\rho(x,y)$ is the reflection scattered off the target in the xy-plane. The term in exponential term is the phase of the signal

$$\phi(t) = 2\pi f_0 \frac{2R_{total}(t)}{c} \tag{3-61}$$

In order to determine the instantaneous frequency of the signal, the range-varying phase signal is differentiating to time

$$f_d = \frac{1}{2\pi}\frac{d\phi}{dt} = \frac{2f_0}{c}\frac{d}{dt}R_{total}(t) \tag{3-62}$$

It is assumed that a target as in Figure 3.12 is moving linearly while the propeller blade is rotating about its body axis

$$f_d = \frac{2f_0}{c}[v + (\omega \text{ x } r)] \tag{3-63}$$

Hence, two movements will contribute to the Doppler. The first term represents the Doppler shift of the target due to translational. Whereas, the second term represents the micro-Doppler of a target due to rotation.

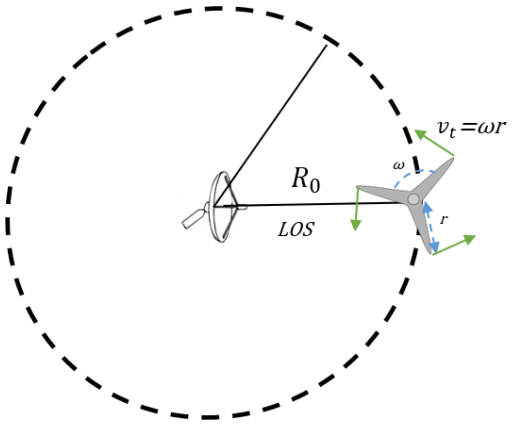

Figure 3.12: An Example of a Rotating Blade Propeller

The frequency oscillation of a target is concluded as in the equation below.

$$f_{md} = \frac{2f_0}{c}(\omega \text{ x } r) \tag{3-64}$$

This background will be utilised throughout the investigation in Chapter 5 and Chapter 6.

3.4 Radar Range Equation

The following discussion is mainly based on a book titled *Introduction to Airborne Radar* [99]. One important performance parameter in radar detection is the maximum range R_{max} at which a radar can detect targets over the background noise. It concludes the overall radar performances. And this R_{max} related to the SNR which is the signal power P_S from the target to the noise power P_N,

$$SNR = \frac{P_S}{P_N} \quad \textbf{(3-65)}$$

The detection of a target is largely depending on the strength of its echoes relative to the strength of its background noise within the radar line of sight. P_S represents the concentration power that hit the target and is received by the system while P_N represents the concentration power of unwanted background noise. The derivation of this radar range equation will be discussed in detail in the following subsection where the parameters that contributed to the signal power and the noise power will be outlined.

3.4.1 Signal Power

The signal energy is computed via four essential steps started once the signal is leaving the transmitter from radar then reflected by the target and captured by the receiver [99].

(i) Transmitted power density ρ_T or intensity of a signal is the amount of energy flowing through a unit area that is perpendicular to the wave propagation. This defines the transmitted power, P_T multiplied by the antenna gain, G_T.

(ii) Then the power density will attenuate due to dispersion and absorption in the atmosphere. The coefficient of absorption is relatively low and neglected for a shorter wavelength. However, the dispersion of the energy will affect the energy

of the signal and is reduced by $4\pi R^2$ in the sense of the propagating losses are in a spherical manner. Since the wave propagates two times the path back and forth, so the attenuation is $(4\pi R^2)^2$.

(iii) The ability of the target's reflectivity, directivity and geometry also affect the signal power concentration. This is defined by one single factor, which is the radar cross-section, σ. RCS does not dependent on the size, geometry and material of the target only, but it also depends on the polarization of the antenna and the aspect angles of the target with respect to the antenna.

(iv) Once the backscattered wave reaches the receiver, it will intercept with the effective area, $A_{e,R}$ of the antenna times the length of integration time on target, t. The general A_e is expressed in terms of the gain of an antenna is

$$A_e = \frac{G\lambda^2}{4\pi} \quad \textbf{(3-66)}$$

This effective area aperture A_e is directly proportional to the gain of the antenna. The larger the G, the larger the A_e.

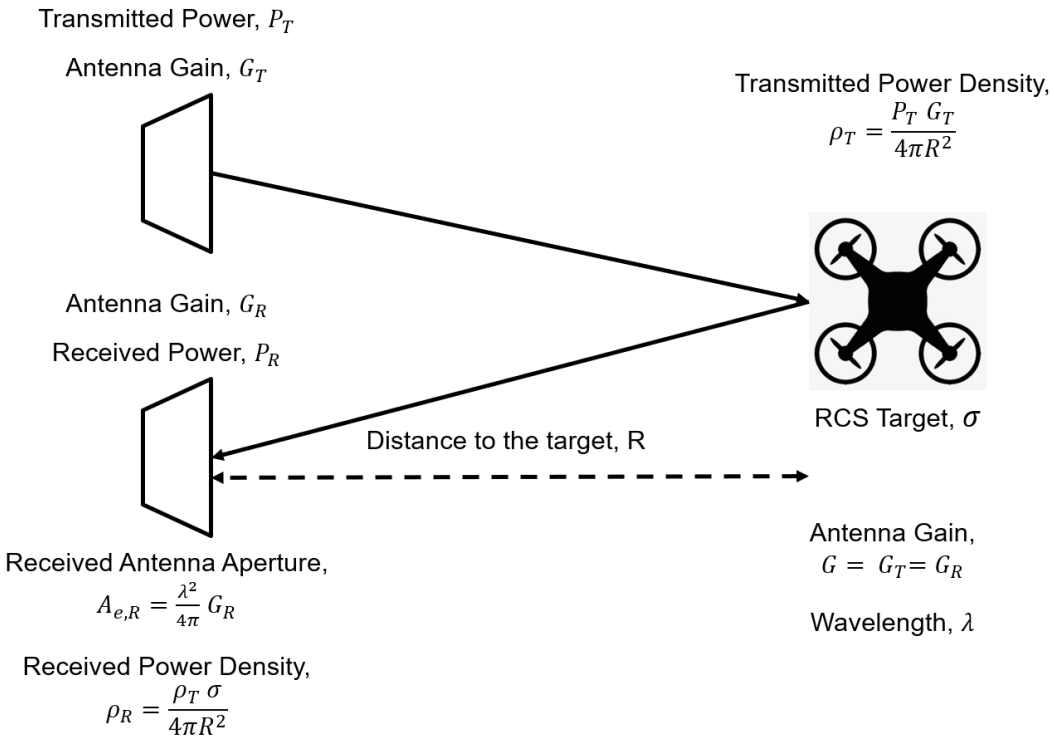

Figure 3.13: Factors that determined the amount of received signal power

Hence, from Figure 3.13, the power received signal, or the target signal energy in one integration time can be expressed by the following equation

$$Signal\ Energy = P_S \mathrm{t} \tag{3-67}$$

Where the signal power P_S is considered as the received power P_R of the system

$$Signal\ Energy = P_R \mathrm{t} = (\rho_R) A_{e,R} \mathrm{t}$$

$$Signal\ Energy = \frac{(\rho_T)\sigma}{4\pi R^2} A_{e,R} t \tag{3-68}$$

$$Signal\ Energy = \frac{P_T\ G_T}{4\pi R^2} . \frac{\sigma}{4\pi R^2} A_{e,R} \mathrm{t} = \frac{P_T\ G_T \sigma (A_{e,R})}{(4\pi)^2 R^4} \mathrm{t}$$

There is another way to express the receive signal energy in terms of wavelength, λ and by assuming the radar have the same type of antenna used in transmission and reception, $G = G_T = G_R$.

$$Signal\ Energy = \frac{P_T\ G_T \sigma}{(4\pi)^2 R^4} \frac{G_R \lambda^2}{4\pi} \mathrm{t} = \frac{P_T G^2 \lambda^2 \sigma}{(4\pi)^3 R^4} \mathrm{t} \tag{3-69}$$

Then removing t, the signal power reflected from the target and received by the antenna can be expressed as

$$P_R = \frac{P_T G^2 \lambda^2 \sigma}{(4\pi)^3 R^4} \tag{3-70}$$

The signal power here shows a very strong relationship with the range R parameter. Equation (3-70) summarized that if the radar transmits the power of P_T, then the received power by the radar is P_R which represents the backscattered signal.

3.4.2 Noise Power

The undesired background noise mainly contributed from these two sources which are the internal radar thermal noise (also named as Johnson or Nyquist

noise) and from the external radar clutter. The radar clutter is the unwanted echoes that disturbed the desired signal energy. It can be within the main lobe clutter where the noise returns are within the radar beamwidth or it can also be the sidelobe clutter. The ground returns are the common clutter in radar systems and some of them can be masked the target returns especially the ones that have a weak signal.

The radar thermal noise power on the other hand is measured as

$$P_N = k\, T_O\, F_N\, B_N \qquad \textbf{(3-71)}$$

Where the amount of noise appears in the receiver is due to

(i) Boltzmann's constant, k: it is valued as $1.38x10^{-23} watt - second/^oK$

(ii) Absolute temperature, T_o: the value of T_o is given by 290^oK which represents the approximation of the room temperature. The temperature has a slight effect on the movement of the free electrons in each conductor and creates a voltage imbalance.

(iii) Noise figure, F_N: is the measurement of SNR degradation caused by each component in the circuit system. It is the ratio of the actual noise to the ideal noise. The ideal noise basically comes from external sources and does not generate any internal noises. Each component has its gain G_N and F_N specification that is stated in the datasheet provided by the supplier especially LNA and amplifier. However, other components like mixers, filters, attenuators, and others are stated as insertion loss which is also considered as noise figure.

(iv) Noise Bandwidth, B_N: In general, the noise bandwidth of the receiver is inverse proportional to the integration time, $B_N = 1/t$. In the case of the FMCW system, the noise bandwidth of the receiver is inversely proportional to the chirp duration, T_r since the data is collected within T_r for FFT.

3.4.3 Detection Process

The power of the backscattered must be larger than the power of noise in order for the target to be detected. Back to the SNR estimation in equation (3-65), by integrating equation (3-70) and equation (3-71), this ratio can be written as

$$SNR = \frac{P_T G^2 \lambda^2 \sigma}{(4\pi)^3 R^4} \cdot \frac{1}{k\, T_O\, F_N B} = \frac{P_T G^2 \lambda^2 \sigma}{(4\pi)^3 R^4 k\, T_O\, F_N B} \quad \textbf{(3-72)}$$

Here the radar range equation concludes that (i) by increasing power, P_T and antenna gain, G^2 of the radar, the detection is more efficient, (ii) by decreasing the radar cross-section, σ of a target, the detection is more incapable, (iii) by increasing the range, the strength of the signal decreases while the mean strength of the noise remains the same, hence resulting weaker detection.

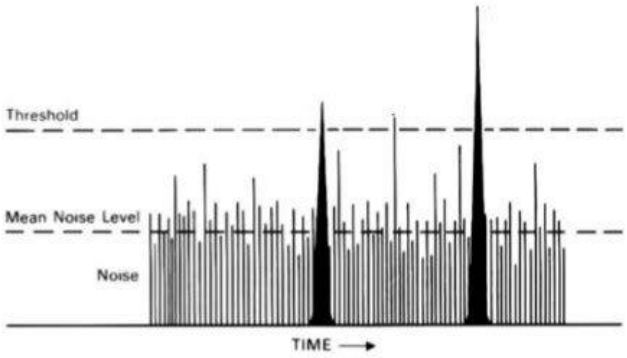

Figure 3.14: Signal Power Relative to the Mean Noise Level [99]

The detection process relies on the setting of the threshold. If the setting is too high, then the presence of the target might not be detected and if the threshold setting is too low, then the spark from the noise will falsely be detected as a target. This situation regards as a false alarm. From Figure 3.14, in order for the target to be detected, the signal power requires to be above the threshold. The minimum detectable signal power $P_{S_{min}}$ is assume equal to the minimum detectable signal of the receiver $P_{R_{min}}$.

$$P_{S_{min}} = P_{R_{min}} = \frac{P_T G^2 \lambda^2 \sigma}{(4\pi)^3 (R_{max})^4} \quad \textbf{(3-73)}$$

The minimum detectable signal power will give rise to the maximum detectable range. Hence, it can also be written as follows

$$R_{max} = \left[\frac{P_T G^2 \lambda^2 \sigma}{(4\pi)^3 P_{R_{min}}}\right]^{1/4} \quad \textbf{(3-74)}$$

From equation (3-72), radar range equation can be also be expressed as [11],

$$R_{max} = \left[\frac{P_T G^2 \lambda^2 \sigma}{(4\pi)^3 k T_0 F_N B (SNR)_{min}}\right]^{1/4} \quad \textbf{(3-75)}$$

Where,

Maximum Radar Range, R_{max} [Meter]

Peak Transmitted Power, P_T [Energy / Time]

Transmit & Receive Gain, G [Dimensionless]

Frequency Wavelength, λ [Meter]

Radar Cross Section, σ [Meter^2]

Mean Noise Energy, kT_0 [Energy]

Noise Figure, F_N [Dimensionless]

Bandwidth, B [Time^{-1}]

Signal-to-Noise Ratio, SNR [Dimensionless]

The power of the backscattered signal equation (3-70) hence, will influence the SNR radar and eventually the maximum range. Both equations (3-72) and (3-75) represent the radar equation as the basis in radar analysis.

3.5 Summary

The main principles of FMCW radar are to determine the frequency differences of the transmitted signal with the echoed signal. From there, the range of the target can be extract as well as the Doppler of a target. Extensively low transmit power is adequate for the detection process resulting in a compact size and less expensive compared to the pulse wave.

Apart from identifying the target location, Doppler observation is one of the important analyses in this research. As the target may have a Doppler shift, it may also have the micro-Doppler in addition to it. The extraction of this Doppler signature is presented in this chapter. The next chapter will explain in detail the analysis of radar signal processing simulation with some of the examples provided.

This chapter discussed the basics of FMCW theory as an introductory step towards prototyping. The related equations of the design and development of FMCW radar are summarized in Table 3.1. These are the key parameters to be considered for an efficient radar design.

Table 3.1: The Summary of FMCW Parameters and Its Relations to Radar Design

Equation	Description	The Relation
(3-28)	The beat frequency signal is highly dependent on two parameters: the ramp bandwidth B and the ramp duration T_r	$f_b = \frac{B}{T_r}.\frac{2R_0}{c}$
(3-40)	The maximum frequency that can be converted rely on the chosen ADC sampling frequency	$Fs \geq 2\, f_{b_{max}}$
(3-41)	The unambiguous range that depends on the sampling rate of the ADC	$R_u = \frac{c\, Fs\, T_r}{2B}$
(3-42)	$f_{b_{resolution}}$ or Δf_b is the beat frequency resolution that is dependent on the ramp duration	$\Delta f_b = \frac{1}{T_r}$

(3-43)	$R_{resolution}$ or ΔR is the minimum value where the two targets apart can be resolved. It depends on the ramp bandwidth	$\Delta R = \frac{c}{2B}$
(3-54)	$f_{resolution}$ or Δf is the Doppler resolution that depends on the number of consecutive ramps	$\Delta f = \frac{1}{T_{dwell}} = \frac{1}{NT_r}$
(3-55)	$v_{resolution}$ or Δv is where the minimum of two velocities that can be resolved	$\Delta v = \frac{\lambda}{2NT_r}$
(3-57)	The maximum velocity observed without aliasing with a given ramp duration at a certain frequency band	$v_{max} = \frac{\lambda}{4\,T_r}$
(3-58)	The maximum required for the ramp duration to avoid aliasing	$T_r < \frac{1}{2(f_{d_{max}})}$

4 RADAR SIMULATION & ANALYSIS

The previous chapter introduced the basic theoretical background of FMCW radar as well as the concept of micro-Doppler. This chapter seeks to explain the design performance of the radar; it assesses the simulation matter and signals processing issues. It covers the post-processing methodology used in this thesis, starting from the raw data collected from the radar module to the results displayed by a MATLAB-based algorithm.

4.1 CW Radar Analysis

CW radar measures the instantaneous speed by continuously illuminating the target without switching the transmitter and receiver on and off. Radar transmitting a constant frequency signal offers constant information in Doppler. However, they do not provide range information and hence do not offer the range resolution as well.

4.1.1 General Signal Study

This section is an example that describes a Doppler detection of stationary radar towards stationary and moving targets. The radar system can detect and record a movement by a target. The transmitted signal $S_T(t)$ and the received signal $S_R(t)$ is expressed as follows

$$S_T(t) = Ae^{j2\pi f_0 t} \quad \textbf{(4-1)}$$

$$S_R(t) = Ae^{j2\pi f_0 (t-t_0)} \quad \textbf{(4-2)}$$

where t_0 corresponds to the time delay and the carrier frequency f_0 is assumed to be 10 GHz. For the easiness of calculation, the amplitude signal A is assumed to be one. The signal is sampled with 20 kHz of sampling frequency Fs within an integration time T of 5 ms. The sampling period Ts is inversely proportional to the sampling frequency Fs (i.e., $Ts = 1/Fs$). To shift the

spectrum of the signal from f_0 to 0, the received signal is multiplied by an exponential of $e^{-j2\pi f_0 t}$. Figure 4.1 shows the spectrum of the complex envelope of the transmitted signal from the radar with the parameters stated before. Since Fs is 20 kHz, so the frequency span axis is from -10 kHz to 10 kHz in the frequency spectrum. The spectral lines are present under the complex envelope at the multiple of 200 Hz (that is $\frac{1}{T}$) of the frequency spectra. X-Band CW signal is radiated towards the target and scattered.

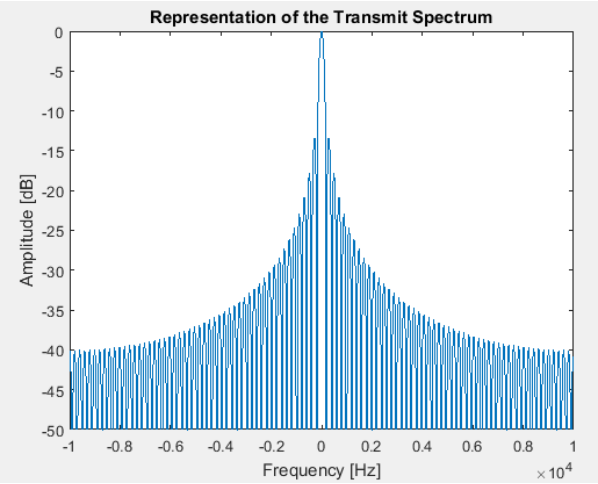

Figure 4.1 Complex Envelope of the Transmitted Signal

When the target is stationary, then the received signal spectrum will look like a frequency-shifted version of the transmitted signal where the main lobe is at 0 Hz as shown in Figure 4.1. This is due to only a fixed time delay present, hence no frequency shift of the spectrum. But once the target moves, then there will be a time-varying delay on the received signal resulting in the main lobe moving to the left or right axis depending on the direction of the target with respect to the radar. When a target is moving towards the radar, the spectrum shifts to the positive frequencies which are to the right. When a target is moving away from the radar, the Doppler will shift towards the negative frequencies which are to the left. The Doppler effect is clearly illustrated in Figure 4.2 where it represents the distance measurement of a target relative to the radar. The relationship between the radar wavelength, λ and the radar frequency, f_0 is defined by

inversely proportional to each other as $\lambda = \frac{c}{f_0}$, where c is the speed of light which is a constant.

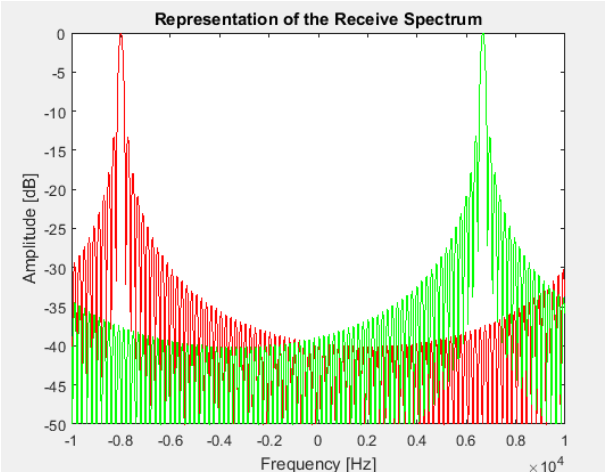

Figure 4.2 The Receiving Signal without Aliasing

When the target is moving with a velocity v, then the distance R to the radar is no longer constant as the distance will varying respect to time, $R = R_0 + vt$, where R_0 is the initial distance of the target. The varying of R resulting in the varying of phase with respect to time.

$$\emptyset_{shift}(t) = -2\pi f_0 t_0 = -2\pi f_0 \left(\frac{2(R_0 + vt)}{c}\right) \quad \textbf{(4-3)}$$

the first term that contributes to the static phase will be ignored. The frequency shift is defined by the rate change of phase

$$f_d = \frac{1}{2\pi}\frac{d\emptyset}{dt} = -\frac{2v}{\lambda} \quad \textbf{(4-4)}$$

Figure 4.2 shows the receiving signals from two different targets. There are two delays here, one with a target velocity of 120 m/s (shown in red colour in the figure) moving away from the radar and another one for a target velocity of -100 m/s (shown in green colour in the figure) moving towards the radar. The Doppler shift from these two targets is collected in Table 4.1 below and by employing equation (4-3).

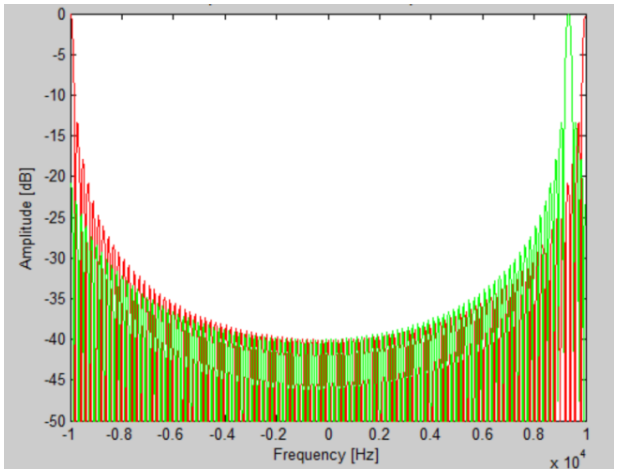

Figure 4.3 The Receiving Signal with Aliasing

Figure 4.3 shows the receiving signals as well but they are in the wrong position, namely called aliasing. For a target velocity of 150 m/s (shown in red colour in the figure), the Doppler frequency shift is the maximum allowable in the correct position. But it can be seen that there is a mirror image on the right-hand side. This is according to the sampling theorem or well known as the Nyquist theorem equation (4-5), the maximum unambiguous Doppler occurs when the Doppler frequency is equal to half of the frequency sampling. This relates to the equation (3-40) in the last chapter.

$$f_{d_{max}} \leq \frac{Fs}{2} \tag{4-5}$$

$$v_{max} = \frac{\lambda f_{d_{max}}}{2} \tag{4-6}$$

In this case, by referring to the definition of equation (4-5), a sampling frequency of 20 kHz will correspond to the $f_{d_{max}}$ of 10 kHz. This is correspondent to a maximum unambiguous velocity v_{max} of 150 m/s as expressed in equation (4-6). Back to Figure 4.3, another target is moving away from the radar with a velocity of 160 m/s (shown in green colour in the figure), the Doppler shift is supposed to be on the left-hand side, but when simulated it is on the right-hand side which is not in the correct position as the expected value.

Table 4.1 Information of Targets

Target	Velocity, v (m/s)	Doppler Frequency, f_d (Hz)	
		Simulated	Calculated
Target 1	-100	6,683	6,667
Target 2	120	-8,000	-8,000
Target 3	150	±10,000	-10,000
Target 4	160	9,332	-10,667

A well-known application of CW radar is the traffic control radar which acts as a speed gauge. This radar is usually mounted on a tripod or a police car and it helps the officer to detect any speedy car. When an object moves towards the radar, the wavelength shortens, hence the frequency is higher. The net result is an upward shift to the transmitted frequency, and this is called a Doppler shift. As when the object moves away, the wavelength lengthens, hence the frequency is lower. For speeders, the measured speed is always lower than the actual. Where the distance of the peak (or crest) wave to the next peak (or crest) wave is symbolized as the wavelength of a signal. It can summarize that the Doppler shift is a frequency change of the EM wave caused by the relative motion between the radar and target.

4.1.2 Preliminary Study

As a rule of thumb, the smaller the object, the less energy reflection from it, and therefore the smaller the RCS. This is exemplified in Chapter 2, a comparison of three different sizes with three different RCS (the typical RCS of human 1 m^2, bird 0.01 m^2 and insect 0.00001 m^2). Smaller RCS makes it a challenging task for radar detection unless a higher operating frequency is implemented in the radar system. The higher the frequency, the shorter the wavelength, hence it could contribute to increase the RCS of a small size target and increase the probability of detection. High frequency, however, demands a higher sampling rate of ADC so that the discrete digital signal can best replicate the analogue signal. An insufficient sample rate will cause loss of information and it can misinterpret that the signal is oscillating at a much lower frequency [100].

Because the carrier frequency of RF radar is usually operated at a higher frequency, hence, the IQ mixer will convert the RF signal to baseband signal to be adapted for further processing.

Figure 4.4 is considered as an extension study from the previous chapter, where the position of the radar and target is placed in a 2D XY plane. In this case, the radar is stationary while the target moves. The target has both movements; translation and rotation velocity meaning that it consists of two sources of scatterer which are from the bulk motion of the main body target and the micromotion of the connected structural components of the body target. The translational velocity is represented by v symbol and the rotational velocity is represented by angular rotational velocity ω. The R_0 is the initial distance of the target towards radar and t is the time. Several types of insects with different size and different wingbeat frequency is modelled. An ideal insect movement uses two pairs of wings that flap up and down as the body moves forward to be oriented and get balanced in flight. In this modelling scenario, an assumption has been made for the purpose of modelling simplicity. Instead of the wing of the target that flaps up and down, it is assumed that the wing moves rotationally centred to the body. This results in a breakdown of x-component and y-component movements. The x-component of the target will consist of the initial range, the translational movement of the target and the x-component of rotational as in equation (4-7). While for y-component of the target only involve in the y-component of rotational movement as seen in equation (4-8). The total distance of the target to the radar is simply the theorem Pythagoras of both equations. From equation (4-9) then it is possible to find out the delay of the target which is then substituted in equation (4-3). Equation (4-10) shows the relationship of wingbeat frequency and angular velocity of an insect.

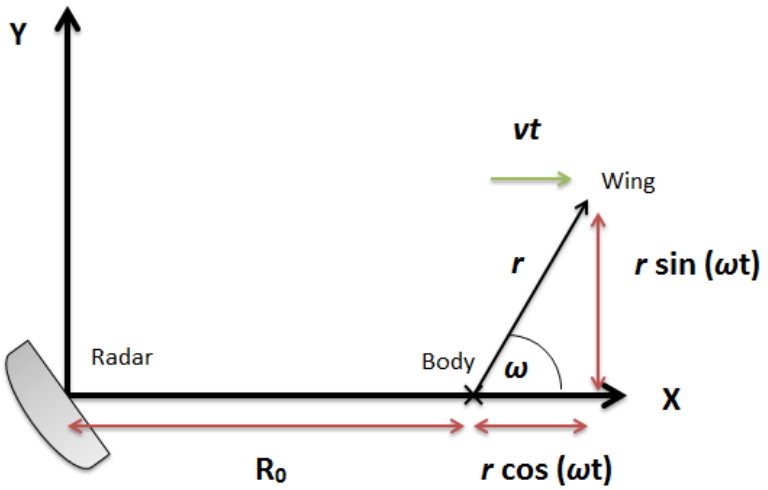

Figure 4.4 The Layout of the Radar & a Target in a 2D Plane

$$Wing_X = R_0 + vt + r\cos(\omega t) \quad \textbf{(4-7)}$$

$$Wing_Y = r\sin(\omega t) \quad \textbf{(4-8)}$$

$$R_{total} = \sqrt{(Wing_X)^2 + (Wing_Y)^2} \quad \textbf{(4-9)}$$

Where,

$$\omega = 2\pi f_{target} \quad \textbf{(4-10)}$$

There are three different types of insects which are considered; bee, fly and mosquito. Figure 4.5 below is the run simulation of the backscattered signal of these three insects in the time domain within the integration time T of 5 ms, whereas Figure 4.6 is the frequency spectrum of the signals. There are three different plots in that figure with three different sampling frequencies. In order to have a clear frequency spectrum, it is best to increase the sampling frequency Fs. Because, increasing sampling frequency will extend the frequency bandwidth that can be recorded. But the signal is still illegible, and the values of frequency Doppler are not clear since it is a non-stationary signal. When dealing with non-stationary signals, doing FFT does show that frequencies do exist in the frequency domain, but it does not show where these frequencies are located in time. Hence, it is required to do a time-frequency analysis where the

whole signal is cut into small segments and FFT is applied in each segment. This process is known as STFT which is Short Time Fourier Transform.

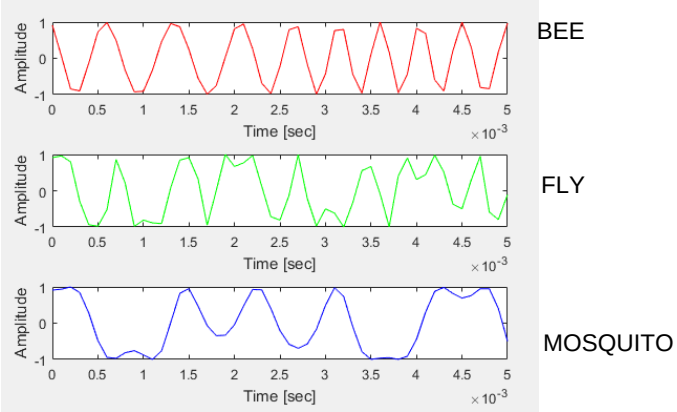

Figure 4.5 Backscattered Signal from the Insects in Time Domain

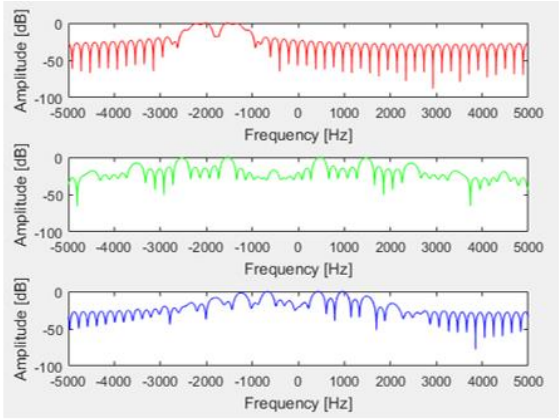

(a)

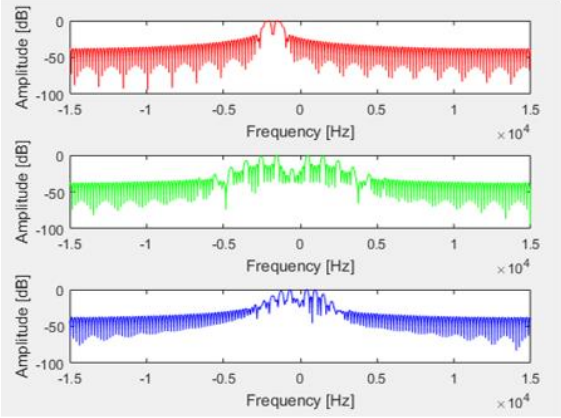

(b)

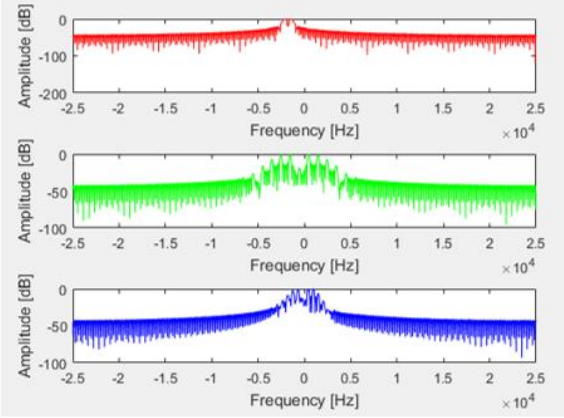

(c)

Figure 4.6: Backscattered Signal from the Insects in Frequency Domain. Where (a) Fs = 10e3, (b) Fs = 30e3, (c) Fs = 50e3

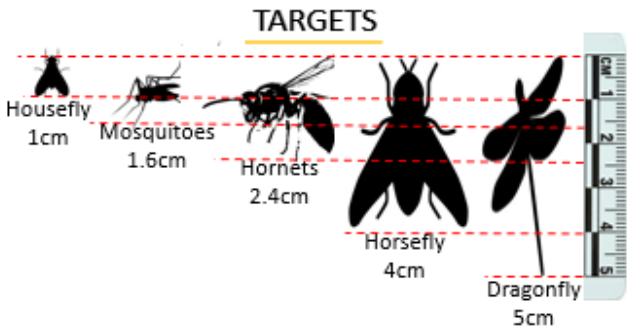

Figure 4.7: Targets of Interest - Different Types of Insect

Table 4.2: A Few Types of Insect Properties

Types	Length (cm)	Translational Speed (m/s)	Frequency of Flap (Hz)
Dragonfly	5.0	8	100
Horsefly	4.0	40	1000
Hornet	2.4	11	200
Mosquito	1.6	0.50	500
Housefly	1.0	2.00	300

More details of the insect properties especially pest insects can be found in [101]. The Doppler and micro-Doppler behaviour of each target is discussed in the analysis below. Each Doppler behaviour is dependent on the beat frequency of the flap. Five different targets as in Table 4.2 have been evaluated and examined its characteristics. The biggest size that was simulated is 5 cm and it goes smaller to 1 cm as in Figure 4.7. The analysis of this individual insect is assumed to be 50 m away from the radar. The sampling frequency is 200 kHz, the integration time T were 10 ms and then increases to 100 ms while the window time for STFT is 0.1 ms. To observe the difference between these insects, the translational velocity is assumed constant at $v = 0\, m/s$ and the observation is only made on the rotational velocity that contributed by the

flapping wing of each insect. A perfect point reflector vibrating at different beat frequencies is modelled and simulated.

Figure 4.8 illustrates the micro-Doppler signature due to the beat frequency of the flapping wings. The left-hand side of the figure represents the frequency spectrum of the echoed signal. From Figure 4.8 1(a), it is shown that the horsefly has the widest frequency bandwidth spectrum that corresponds to the oscillation from the beat frequency of 1 kHz, followed by Figure 4.8 4(a) the mosquito with 500 Hz beat frequency. Then, housefly 300 Hz, hornet 200 Hz and dragonfly 100 Hz. The middle plot of Figure 4.8 is the time-frequency analysis within the time duration of 10 ms. Higher beat frequencies will have a disperse signature along with the frequency bandwidth and lots of complete cycles repetition present. Figure 4.8 1(b) only displayed one complete cycle within 10 ms. Hence, the beat frequency is $\frac{1}{10\ ms} = 100\ Hz$. 3(b) and 5(b) shows two and three complete cycle respectively which, hence, represent a beat frequency of $\frac{2}{10\ ms} = 200\ Hz$ and $\frac{3}{10\ ms} = 300\ Hz$. While 2(b) illustrate the most complete cycle with $\frac{10}{10\ ms} = 1000\ Hz$. Horsefly shows the largest frequency Doppler which is between $\pm$60 kHz and then mosquito with the maximum Doppler of 13 kHz. Housefly, hornet and dragonfly have the maximum Doppler which is not more than 5 kHz. However, this maximum Doppler does not merely depend on the beat frequency of the flaps. But it is also depending on the size of the insect. For example, a mosquito originally has a size of 1.6 cm long. Then the size is increased to 5 cm with a constant beat frequency of 500 Hz for comparative analysis. A bigger size of mosquito in Figure 4.10 shows a more disperse and wide micro-Doppler bandwidth compared to Figure 4.9, the smaller size of the same insect. This is because the radial velocity is bigger if the insect is bigger given the same beat frequency. Even with the same beat frequency of the flap but different size, will contribute to different maximum Doppler as the given plot.

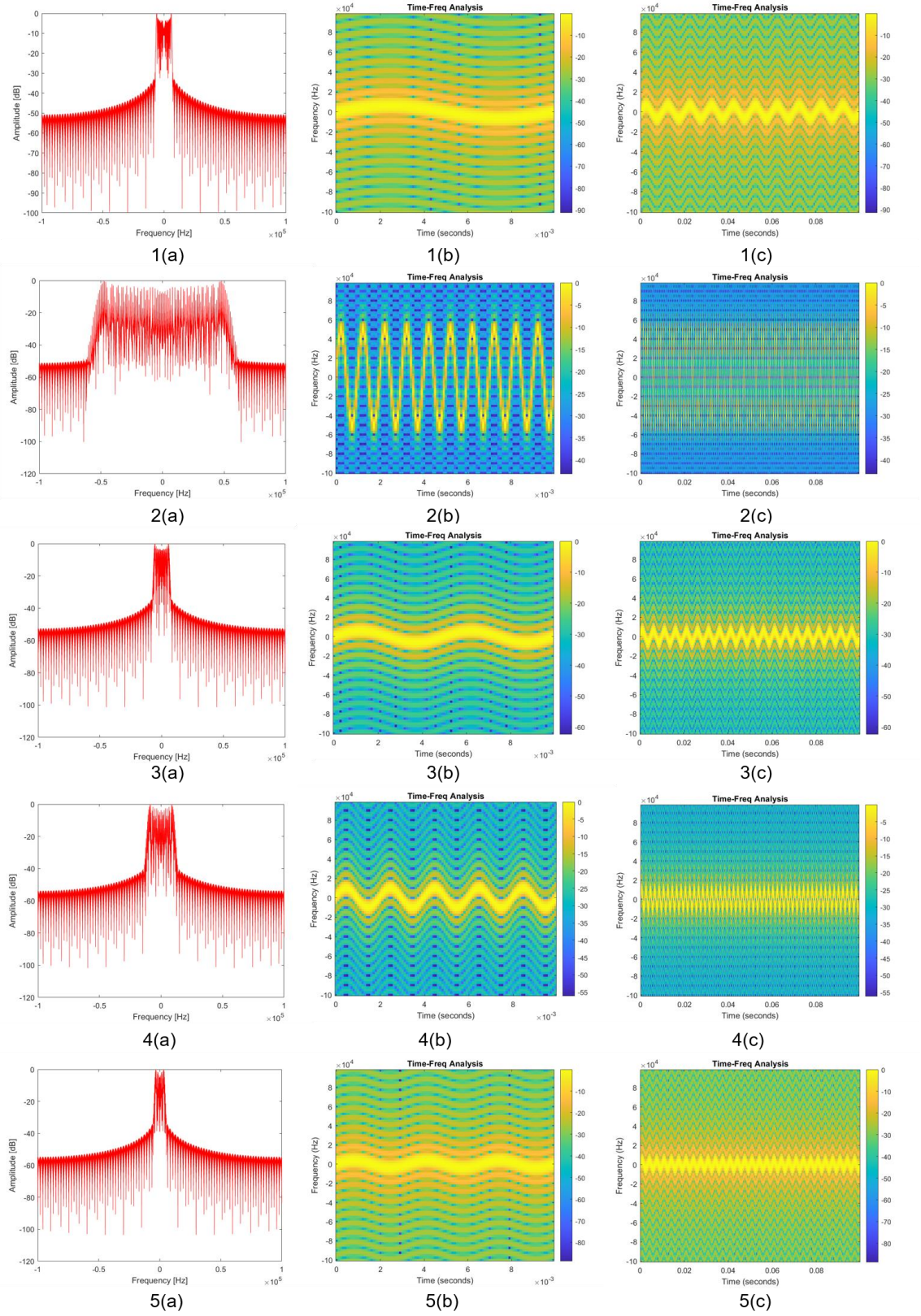

Figure 4.8: Signature of the Flapping Scatterers; 1(a) - 1(c) Dragonfly, 2(a) - 2(c) Horsefly, 3(a) - 3(c) Hornet, 4(a) - 4(c) Mosquito, and 5(a) - 5(c) Housefly

The right-hand side of Figure 4.8 (i.e., referring to Figure 4.8 1(c) – 5(c)) is the micro-Doppler signatures of the vibrating scatterer plotted at a longer observation time, which is ten times longer than the middle plot (referring to Figure 4.8 1(b) – 5(b)). This is when the complete cycle calculation from the horsefly 2(c) and mosquito 4(c) is no longer possible and challenging with a higher observation time except if it is zoomed in or cut to a shorter period. But the housefly 5(c), hornet 3(c) and dragonfly 1(c) even though increases as the observation time increases, the complete cycle is still obvious and visible.

The resolution of the time-frequency analysis depends on the window duration T_{window}. There is a trade-off between frequency resolution and time resolution. The STFT frequency resolution $f_{STFT\,resolution} = 1/T_{window}$ is proportional to the window duration where the larger the T_{window} the better the frequency resolution. However, larger T_{window} results in poorer time resolution. The study of the Doppler signature induced by the micro-motion of the target could potentially help the entomologists to classify the insects according to the beat frequency of insects.

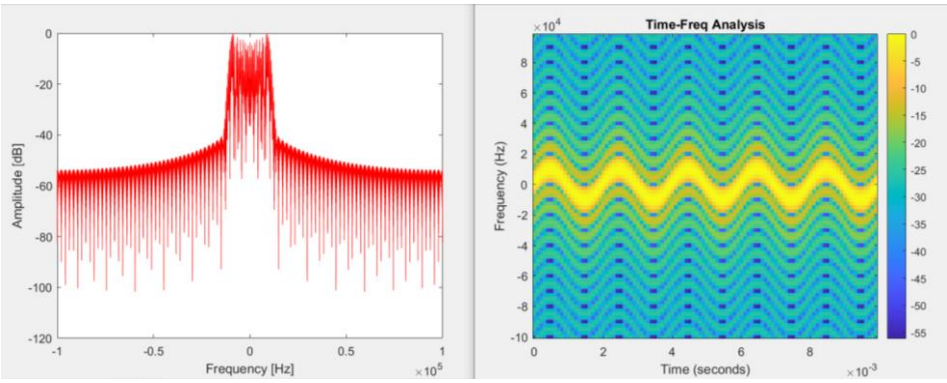

Figure 4.9: 500 Hz Flapping Scatterer of Mosquito with a 1.6 cm long

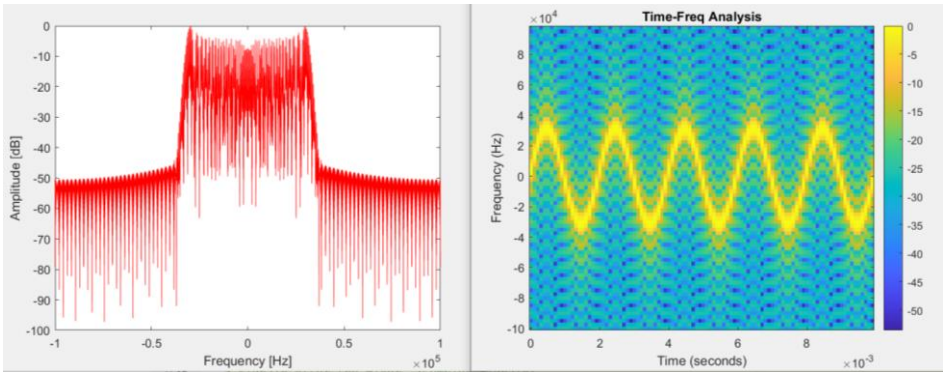

Figure 4.10: 500 Hz Flapping Scatterer of Mosquito with a 5 cm long

4.2 FMCW Radar Analysis

FMCW analysis provides extra information of the range than CW analysis. While CW analysis offers information on Doppler and micro-Doppler of the target. The product of mixing between two signals of transmit signal and the echo signal produced a low-frequency beat signal which is proportional to the range being measured.

4.2.1 Signal Formation

A general band-pass LFM waveform with amplitude A and frequency f_0 can be expressed as

$$S(t) = A\cos\left(2\pi f_0 t + \pi\gamma t^2\right).Rect\left[\frac{t}{T}\right] \quad \textbf{(4-11)}$$

Assuming that the transmit signal of FMCW radar is a continuous repetition of the same chirps. The complex envelope of equation (4-11) is given by $e^{j\pi\gamma t^2}Rect(\frac{t}{T})$. Hence, it can be expressed as

$$S_T(t) = \sum_{a=0}^{m} e^{j\pi\gamma(t-aT_R)^2}.Rect\left[\frac{t-aT_R}{T_R}\right] \quad \textbf{(4-12)}$$

Where a is any positive integer. Meanwhile, the echoed complex signal is the transmit signal with a delay relative to the target

$$S_R(t) = S_T(t - t_0).e^{-j2\pi f_0 t} \tag{4-13}$$

$$S_R(t) = \sum_{i=0}^{m} e^{j\pi\gamma(t-aT_R-t_0)^2}.Rect\left[\frac{t - aT_R - t_0}{T_R}\right] \tag{4-14}$$

Because the nature of $Rect\left[\frac{t}{T}\right]$ is within the interval from $-0.5T$ until $0.5T$ and starting the waveform at zero will ease the calculation as in Figure 4.11. Hence, the transmitted signal is

$$S_T(t) = e^{j\pi\gamma(t-a*T_R)^2}.Rect\left[\frac{t - (a+0.5)T_R}{T_R}\right] \tag{4-15}$$

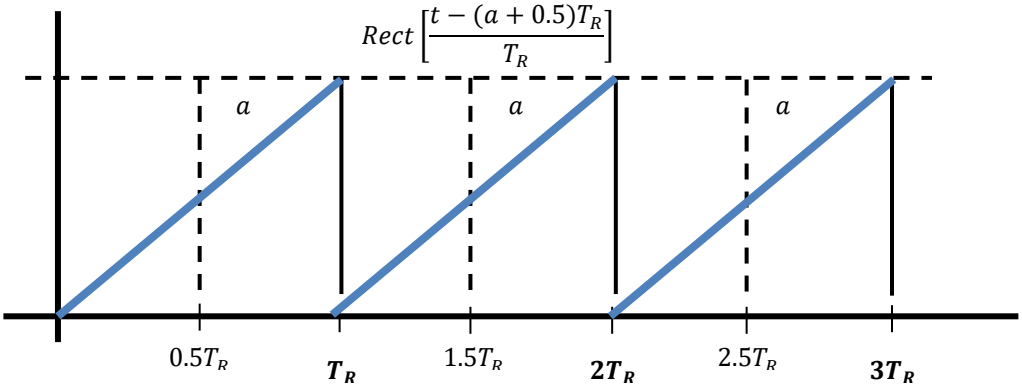

Figure 4.11: A Waveform Design of LFM Radar Chirp

The received signal referring to equation (4-15) is given

$$S_R(t) = e^{j\gamma\pi(t-a*T_R-t_0)^2}.Rect\left[\frac{t - (a+0.5)T_R - t_0}{T_R}\right] \tag{4-16}$$

4.2.2 Extraction of Doppler & Micro-Doppler

Consider a proposed prototype that excludes the IQ demodulator, the echoed signal will only have the I channel and the Q channel is discarded. Recalling equations (4-16), an initial FMCW signal $S(t)$ are expressed in the time domain

$$S(t) = e^{j2\pi f_0 t}.e^{j\gamma\pi(t-a*T_R-t_0)^2}.Rect\left[\frac{t-(a+0.5)T_R-t_0}{T_R}\right]$$

$$S_R(t) = e^{j\gamma\pi(t-a*T_R-t_0)^2}.Rect\left[\frac{t-(a+0.5)T_R-t_0}{T_R}\right]$$

where $S_R(t)$ is the complex envelope of $S(t)$, the equation above is simplified to

$$S(t) = e^{j2\pi f_0 t}S_R(t)$$

where the first term in the equation above is a frequency shift of the carrier waveform. And the second term is the complex envelope which usually consists of in-phase and quadrature components. Recalling equation (3-8),

$$S_{BP}(t) = S_I(t)\cos(2\pi f_0 t) - S_Q(t)\sin(2\pi f_0 t)$$

In this case, the band pass signal will only consist of the in-phase component

$$S_R(t) = S_{BP}(t) = S_I(t)\cos(2\pi f_0 t)$$

The process of Doppler and micro-Doppler extraction is depicted in Figure 4.12. The IF signal which is the output of a double-balanced mixer $S_{f_b}(t)$ is first digitized by ADC with a sampling rate of Fs_1 into a number of samples N. The $1\ x\ N$ length vector represents the beat signal which contains the range information of the target in the time-domain signal. This vector is first segmented into small windows where the window duration is chosen so that it is equal to the ramp duration. The FFT is then applied to each small segment to obtain a frequency spectrum which is later placed in every column of a matrix. Matrix size is defined by the number of rows that represents each frequency bins of N_{FFT1} and the number of columns that represent the number of ramps involved. The integration time of the radar system is $t_{integration} = N/Fs$. This RTI matrix will exhibit the target range in every frequency spectrum.

The second FFT is then applied to the RTI matrix across the row. Because the window duration was selected in the last STFT which is equal to the ramp duration T_R, hence, the new sampling Fs_2 is simply the reciprocal of T_R. This is because the interval between each of the sampled points are now T_R. A new matrix arrangement of RDM is laid out where it signifies the Doppler shift of the target whether it is approaching or receding the radar. The micro-Doppler signature can also be detected by observing the spread out of the signatures that are present in some of the frequency bins, both positive and negative sides of the frequency main Doppler shift of the target. Usually, there is a periodical line or spot in the plot that represents the rotational rate or wingbeat frequency of the target.

To extract more detailed information from the Doppler signatures, the location of the target is identified from the RDM matrix. At that point, the row (the range bin) of the target location is selected for another STFT processing. This time, the window duration must be chosen so that it is less than the peak-to-peak period of the rotation or vibration frequency of the target. A shorter window duration will include more local details from the signal but a lower frequency resolution. However, it comes with a computational cost. The Doppler bandwidth of the micro-Doppler matrix is the reciprocal of ramp duration, $1/T_R$. Hence, in this case, the maximum unambiguous Doppler is determined by $\pm 1/2T_R$.

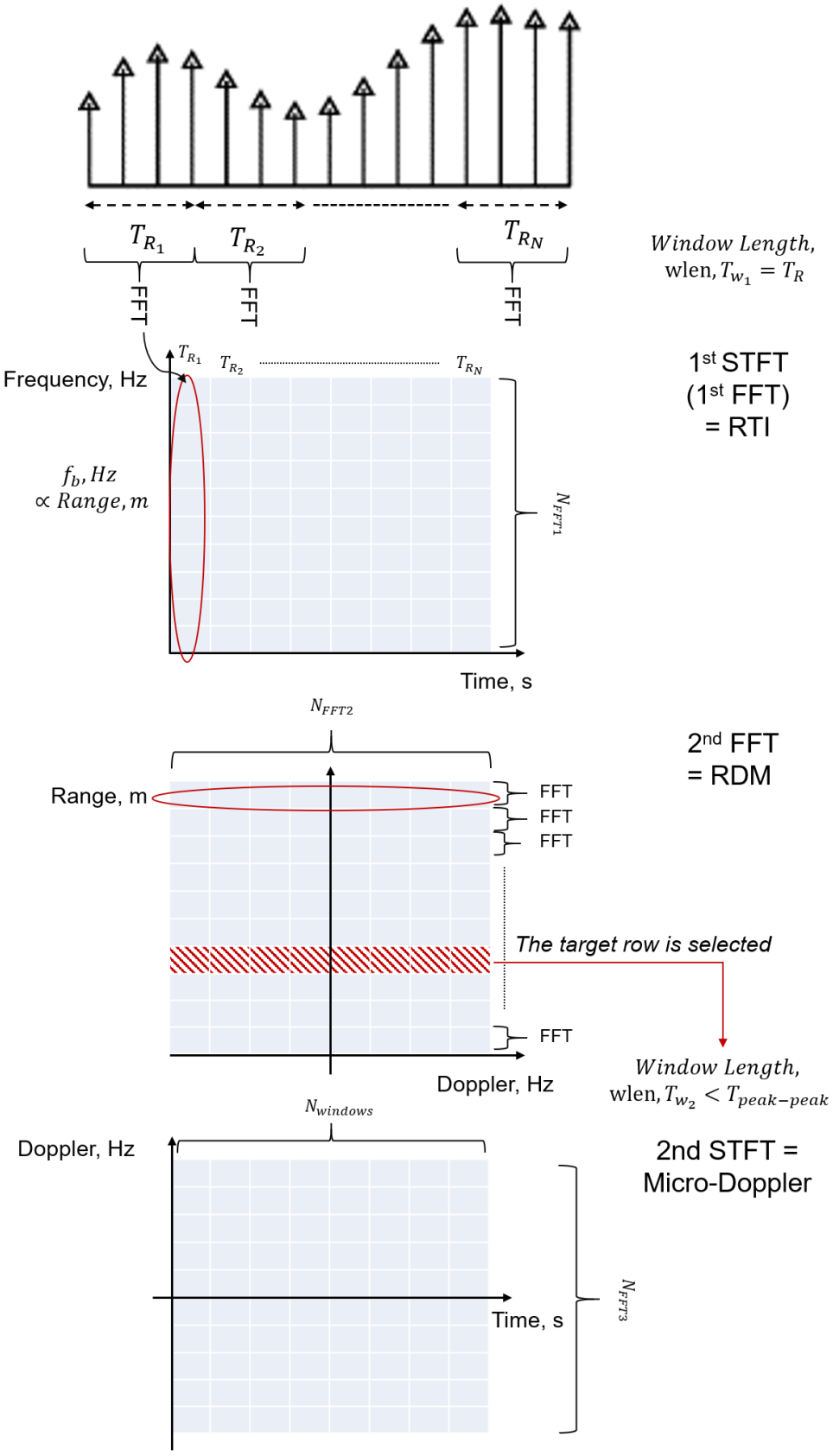

Figure 4.12: The Processing of the Doppler Signature

4.2.3 Diverse Model Properties & Variables

Since CW radar is unable to determine the range measurement, the modification into an FMCW radar enables the range extraction by looking at the frequency shift. From the beat frequency signal, there is a constant offset when plotting the frequency versus time. This offset is the shift frequency that enables the radar to extract the range of the target. RTI, RDM and Micro-Doppler signature are three important things in order to characterized and classify the targets. Because the signals are non-stationary, to understand the behaviour of the targets, time-frequency techniques are used for the analysis. The FMCW radar processing has been successfully simulated and studied in this section which then will be utilized for the real radar hereafter. The waveform that is being used for the analysis is a sawtooth pattern with multiple chirps. The study is divided into 3 sections which are:

I. The characteristic of the target is held constant. But the radar parameters like the **bandwidth** and **ramp duration** is manipulated. This is in order to observe the capability of the radar performance.

II. Both the characteristics of the target and the radar parameters are held constant. But the **velocity** and the **initial range** of the target relative to the radar is manipulated. This will only affect the Doppler shift of the target.

III. Radar parameters are held constant. But the characteristics of the target like the **size** and the **beat frequency of the target** is manipulated. This is in order to observe the signatures obtained from different characteristics.

These three sections will help to understand the relationship of each parameter that affects the radar performance and the ability of its target detection.

4.2.3.1 Bandwidth & Ramp Duration

The first analysis is where the target is assumed to be 5 cm in size and the relative distance of the target and radar is kept constant with 500m apart.

Results are analysed for different bandwidths B as well as ramp durations T_r. The study is performed by assuming the wingbeat frequency is 50 Hz. The dwell time is constant as $50\,ms$. The longer the dwell time, the bigger the number of ramps. The larger the number of chirps the better the micro-Doppler signature of the target observed since the frequency resolution becomes better with increasing dwell time. But by increasing the dwell time will result in high computational time even though it offers a high-frequency resolution. The number of chirps is determined by the ratio between radar dwell time T to the ramp duration T_r, where $n_{Pulses} = T/T_r$. The tangential velocity or the tip velocity v_{tip} can be determined once the rotational rate of a target ω_{target} is known

$$v_{tip} = 2\pi\omega_{target}r \tag{4-17}$$

where r is the size of the target. The v_{tip} here is dependent on two factors of the target which are ω_{target} and r.

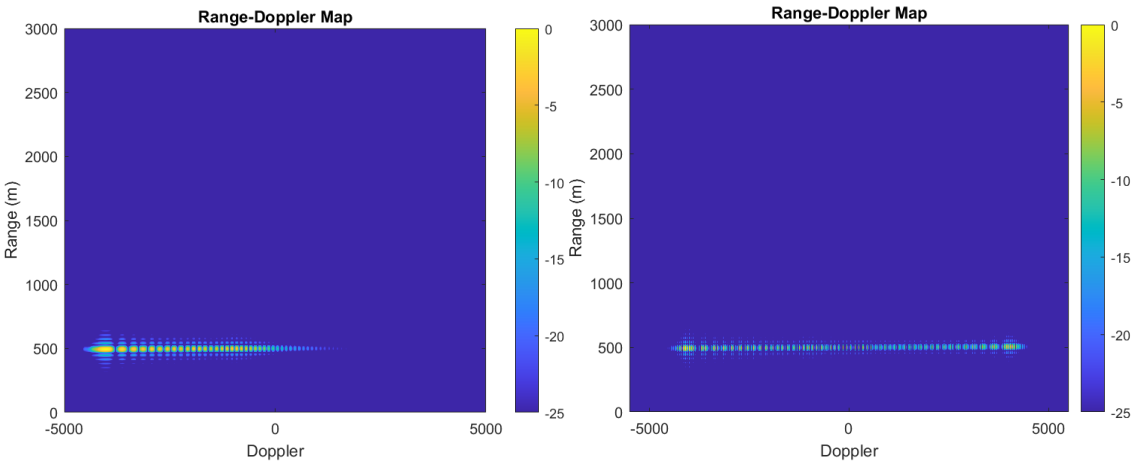

Figure 4.13: RDM of Ramp Duration 50μs; Dwell time of 0.01s (Left), Dwell time of 0.05s (Right)

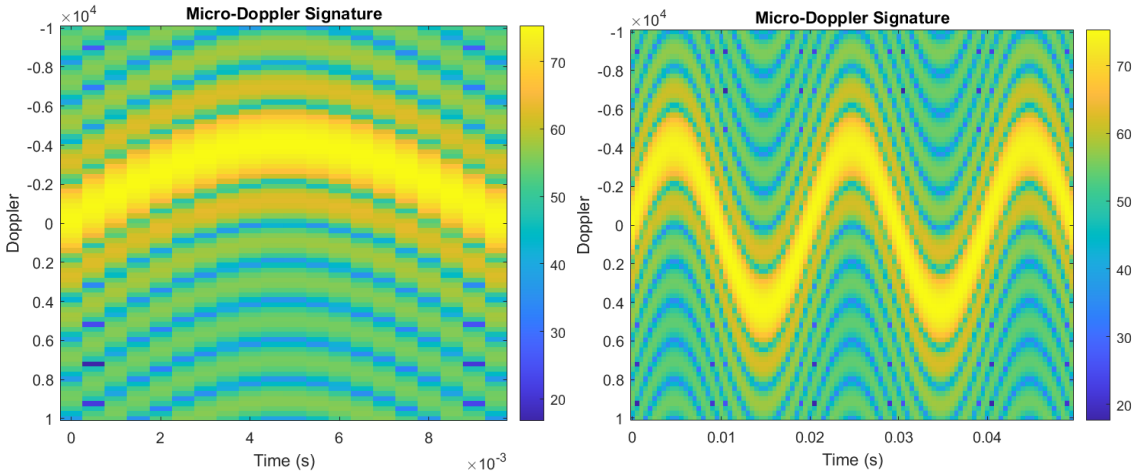

Figure 4.14: Micro-Doppler of Ramp Duration 50 µs; Dwell time of 0.01s (Left), Dwell time of 0.05s (Right)

Figure 4.13 and Figure 4.14 show the plot of ramp duration is $50\mu s$. Hence, the maximum unambiguous Doppler is $\pm\frac{1}{2T_R} = \pm\frac{1}{2(50\mu s)} = \pm 10\ kHz$. From the RDM plot, the target is at 500 m away from the radar and the maximum Doppler shift is less than 5 kHz. It is found that the energy is spread across multiple Doppler bins with several dots shown. The intervals between each dot show a separation of 50 Hz which represent the wingbeat frequency as expected. The micro-Doppler plot, on the other hand, shows the number of sinusoidal cycles present in a certain period and the maximum frequency Doppler achievable of the target. Two and a half cycle is present within 0.05 s that indicates a 50 Hz rotational rate. Hence, leading to a tangential velocity of 15.7 m/s. The maximum frequency Doppler in Figure 4.14 is found to slightly differ from Figure 4.13. This can be improved by tuning the window duration T_w to attain a better frequency resolution of the STFT plot. The T_w was 0.5 ms to obtain the micro-Doppler signature. Both figure on the left-hand side show the partial rotational period. In RDM, the spectrum is spread out on one side only and shows an asymmetrical spectrum. Where from the micro-Doppler plot shows that it undergoes uncompleted one full rotational period. This proves that within 0.01 s is insufficient and only managed to go a half cycle, whereby, to complete one full cycle will require approximately 0.02 s. From equation (4-17), the v_{tip} exhibit

the same value as the last case since the size and the wingbeat frequency is the same.

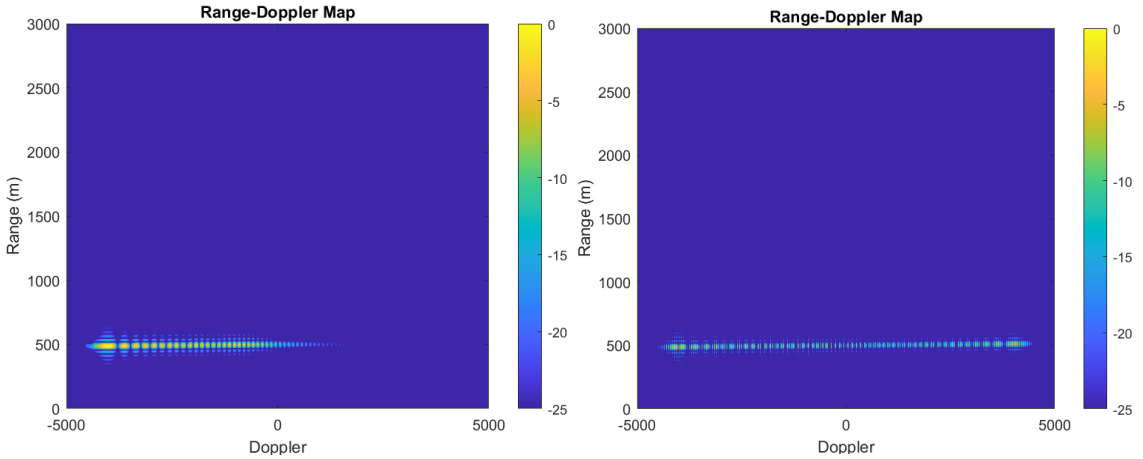

Figure 4.15: RDM of Ramp Duration 100μs; Dwell time of 0.01s (Left), Dwell time of 0.05s (Right)

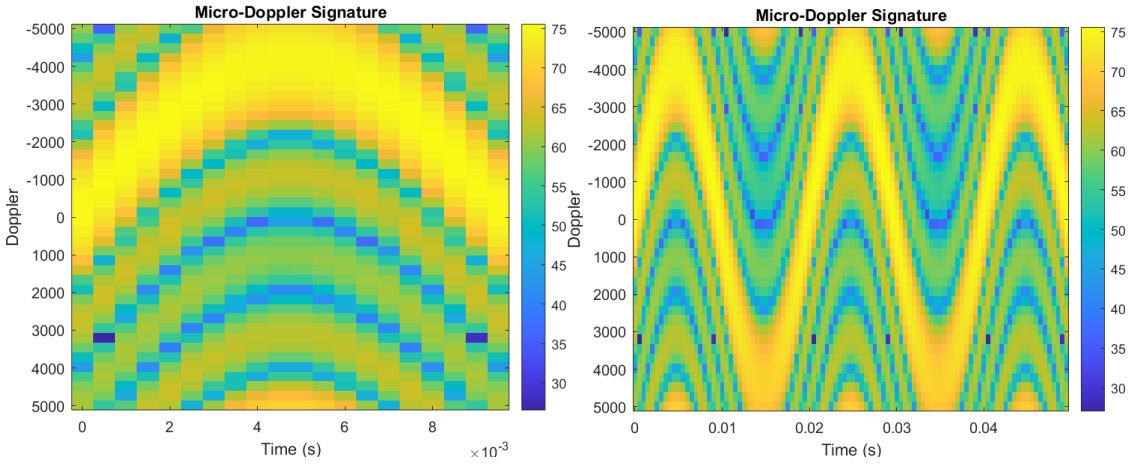

Figure 4.16: Micro-Doppler of Ramp Duration 100 μs; Dwell time of 0.01s (Left), Dwell time of 0.05s (Right)

Figure 4.15 and Figure 4.16 illustrate the plot with a longer ramp duration, that is $100\mu s$. It is noticed that the Doppler signature started to reach the maximum Doppler bandwidth, $\pm\frac{1}{2(100\mu s)} = \pm 5\ kHz$. While Figure 4.17 and Figure 4.18 represent the ambiguous Doppler where the maximum Doppler achievable is higher than the maximum unambiguous Doppler, $\pm\frac{1}{2(150\mu s)} = \pm 3.33\ kHz$. Hence,

some parts of the Doppler signature shown on the other way wrong. All of the left-hand side plots in this sub-section is where the dwell time has chosen was $10\ ms$ and the right-hand side plot is $50\ ms$. The dwell time increases in order to see a longer Doppler signature.

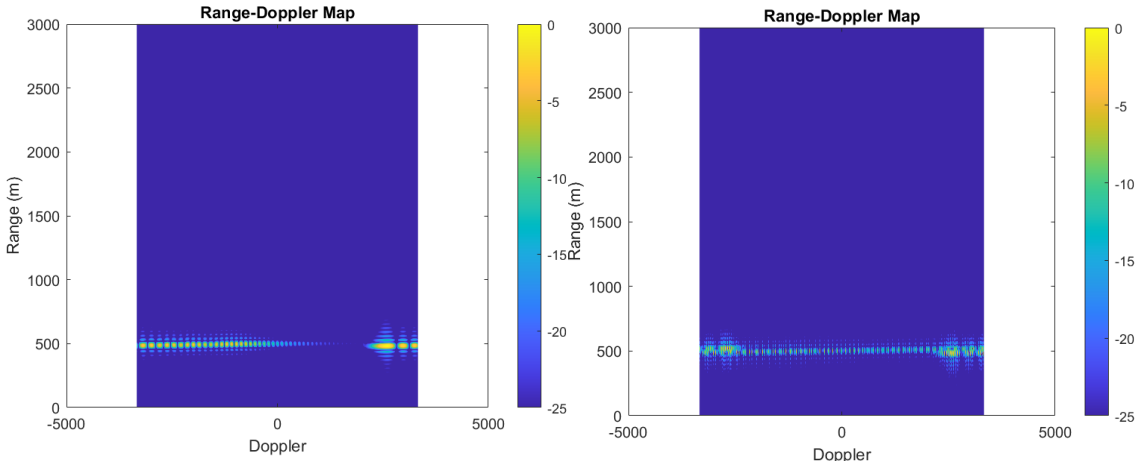

Figure 4.17: RDM of Ramp Duration 150μs; Dwell time of 0.01s (Left), Dwell time of 0.05s (Right)

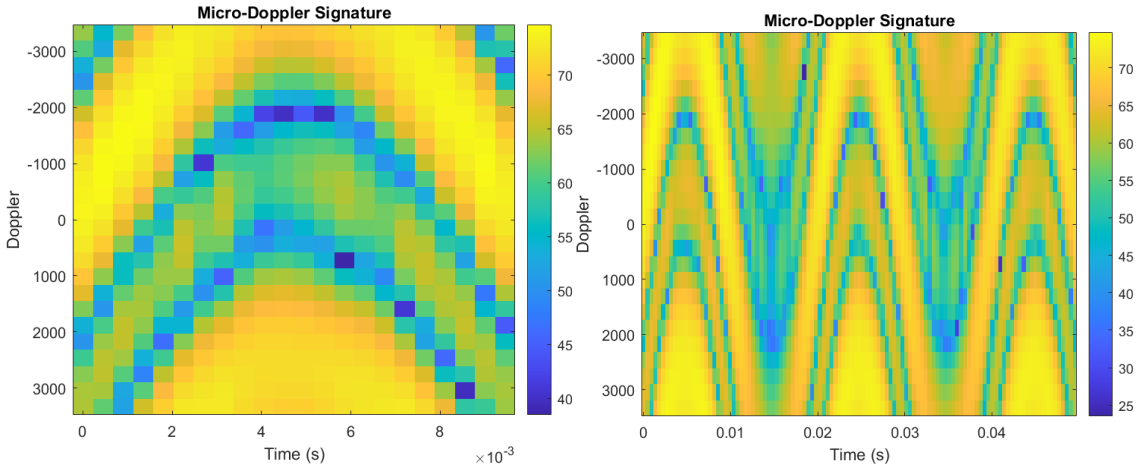

Figure 4.18: Micro-Doppler of Ramp Duration 150 μs; Dwell time of 0.01s (Left), Dwell time of 0.05s (Right)

The study suggests that the ramp duration will affect the span Doppler or the unambiguous Doppler. A larger rotational rate of a target will require a smaller ramp duration so that it has a larger span Doppler and will avoid the Doppler ambiguity. The sampling rate relates to bandwidth. By increasing bandwidth, means increasing the sampling rate. This sampling rate will affect the range

ambiguity. If the sampling rate is too high, then the ambiguous range detection reduces.

4.2.3.2 Velocity & Range Target

Equation (3-51) relates to the phase shift of the transmitted signal with a carrier frequency f_0 and a time delay t_0. This time delay relates to the range of the target. When the target is moving, the range is varying with time

$$\emptyset_{shift} = \frac{4\pi R_{total}(t)}{\lambda} \quad \textbf{(4-18)}$$

From equation (4-9), the phase shift due to range varying time can be expressed as

$$\emptyset_{shift} = \frac{4\pi}{\lambda}\sqrt{(R_0 + vt + \ r\,cos(\omega t))^2 + (r\,sin(\omega t))^2} \quad \textbf{(4-19)}$$

Where λ is the wavelength of the operating signal. From equation (4-19), the arises of Doppler shift & Doppler signature are contributed from the radial velocity and the frequency oscillation of the target respectively. Three different scenarios are considered in this analysis; (i) the target is at 500 m away, with no translational and no rotational velocity (ii) the target is at 500 m away, with no rotational velocity but the target is moving at $v = 50\ m/s$ (iii) the target is at 500 m away, with $\omega = 400\ Hz$ frequency oscillation and the target is moving at $v = 50\ m/s$. The operating frequency of the radar was 40 GHz.

Figure 4.19 illustrate a target in a stationary position at 500 m away from the radar. The RTI plot shows a straight line at 500 m within the integration period. Whereas the RDM plot shows that the target with a point at 500 m and a zero-Doppler line. Then the target is assumed to be moving with a radial velocity of 50 m/s. Figure 4.22 shows that the RTI plot is almost similar to the last case, except that the straight line has moved upwards a little more than 500 m. From the RDM plot, there is a Doppler shift present towards the positive Doppler which indicates the target is moving closer to the radar. The Doppler shift is approximately equal to 13 kHz which agrees to the expected value.

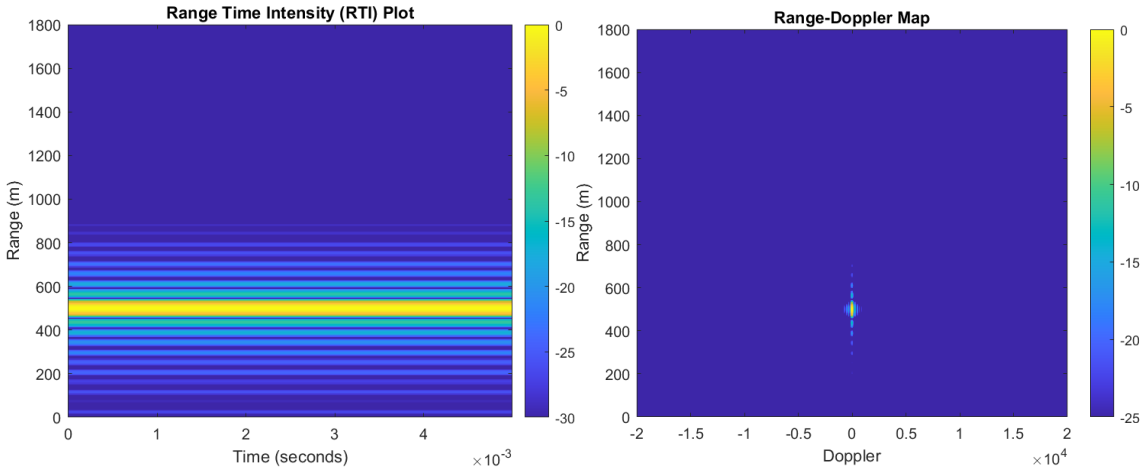

Figure 4.19: The Target is Stationary at 500 m Away

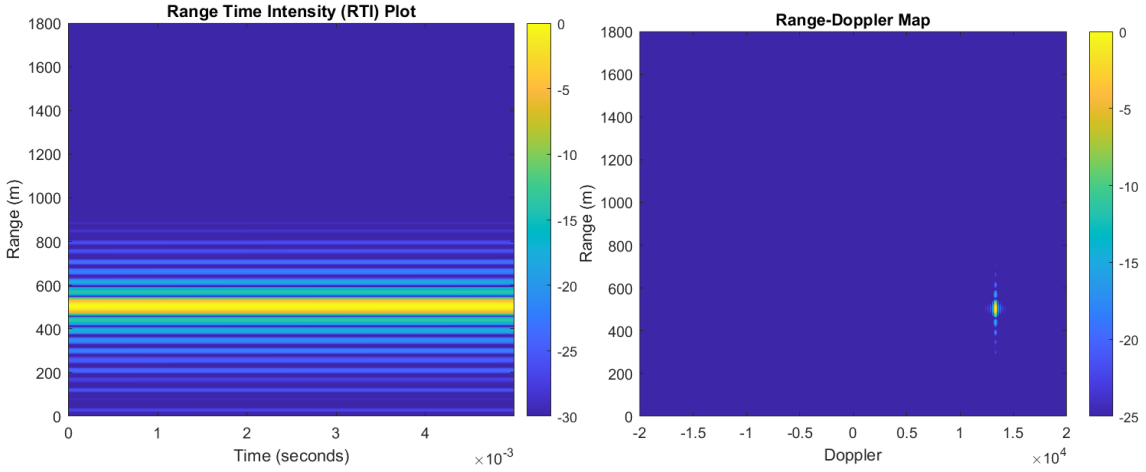

Figure 4.20: Target is Moving with a Radial Velocity of 50 m/s

As the target moves with the radial velocity, there is a frequency oscillation of 400 Hz on top of that which is shown in Figure 4.21. The RTI plot shows an oscillation is present, instead of having a straight line and the RDM plot shows that the oscillation centred approximately 13 kHz. Figure 4.22 illustrates the micro-Doppler signature of the target. On the Left-Hand Side (LHS) is where the target moves only with the radial speed and on the Right-Hand Side (RHS) where apart from the speed, there is an oscillation from the target.

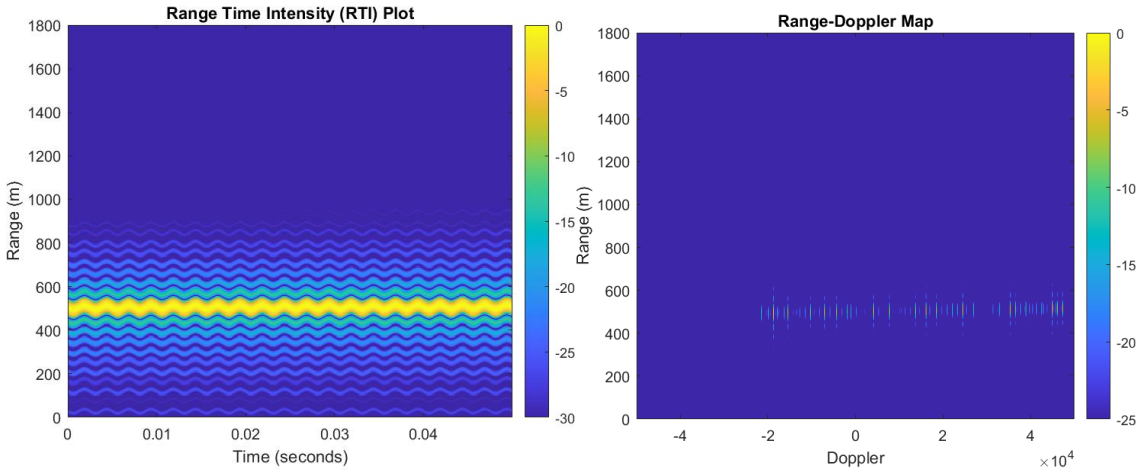

Figure 4.21: Target with a Radial Velocity of 50 m/s & a Frequency Oscillation of 400 Hz; RTI Plot (Left) and RDM Plot (Right)

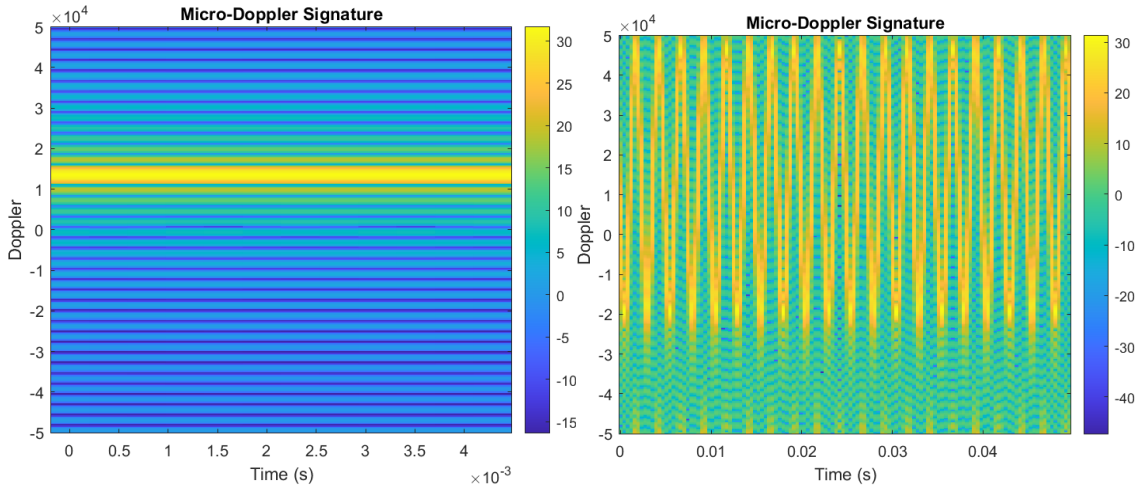

Figure 4.22: (i) Target with Radial Velocity and No Oscillation (Left), (ii) Target with Radial Velocity & Frequency Oscillation (Right)

4.2.3.3 Size & Wingbeat Frequency

A different Doppler signature can be obtained from different characteristics of the target. This will help the observer to classify and identify each of the individual targets. The goal of this sub-section is to present various models of targets that will contribute to the different patterns of signatures. The analysis is performed with various wingbeat frequencies that represent a normal insects'

wingbeat frequency which is between 100 Hz to 500 Hz. The bandwidth and ramp duration is kept constant throughout the analysis which is $5\,MHz$ and $10\,\mu s$ respectively. The dwell time is 10 ms. The time-varying of the range is also held constant to ease the comparisons. The R_0 is 500 m away and the v is 0 m/s.

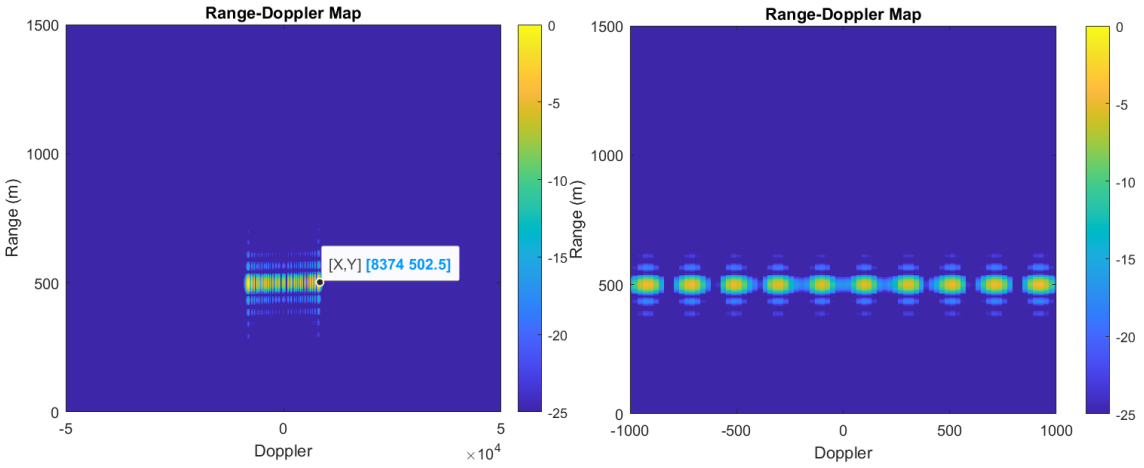

Figure 4.23: Wingbeat Frequency of 100 Hz

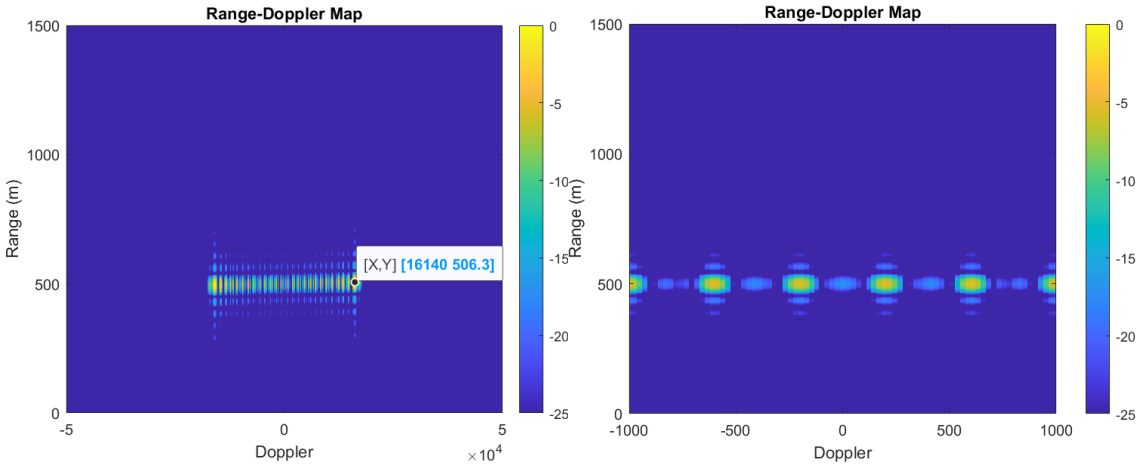

Figure 4.24: Wingbeat Frequency of 200 Hz

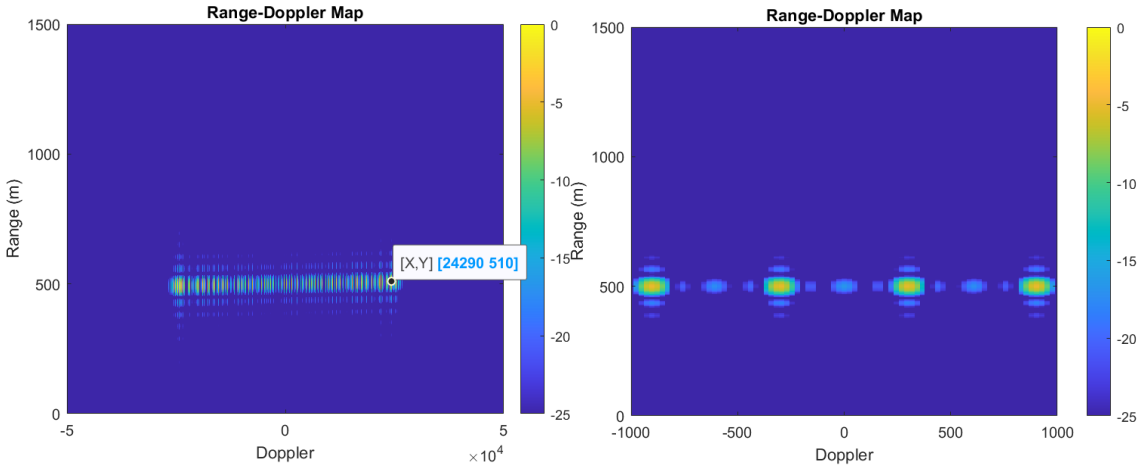

Figure 4.25: Wingbeat Frequency of 300 Hz

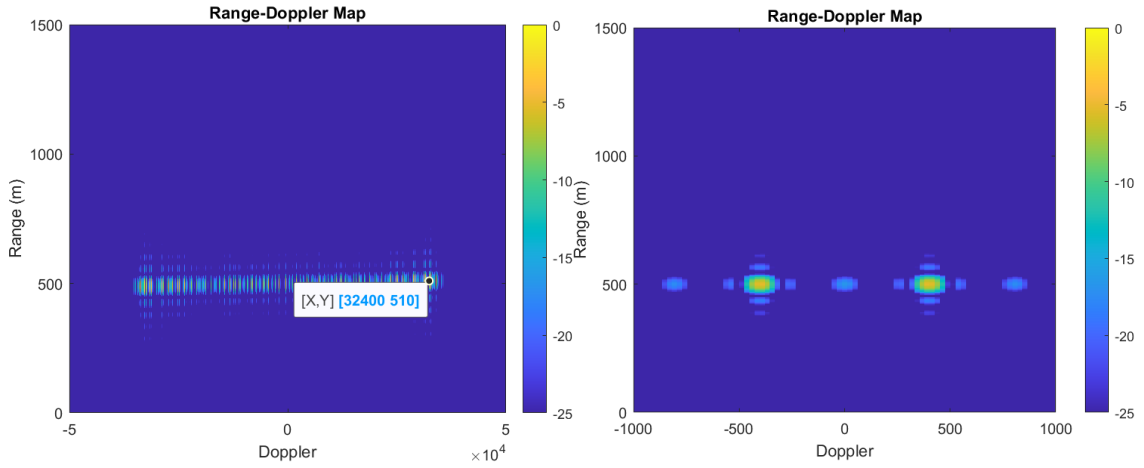

Figure 4.26: Wingbeat Frequency of 400 Hz

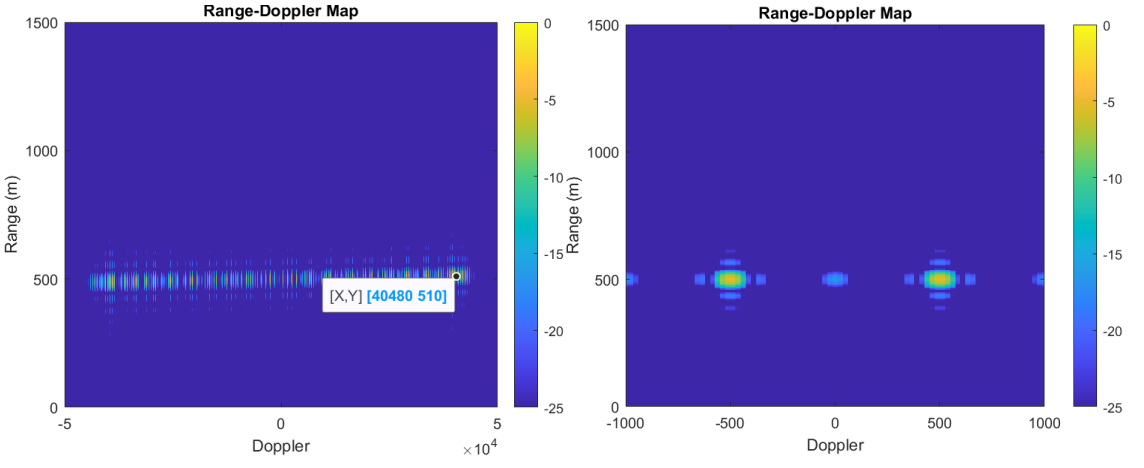

Figure 4.27: Wingbeat Frequency of 500 Hz

Figure 4.23 represents the smallest wingbeat frequency of the target. The separation between the two dots in the RHS figure is 100 Hz which indicates the rotational rate of the target. And the maximum achievable Doppler in the LHS figure is approximately ±8.37 kHz. Figure 4.24 until Figure 4.27 shown the increase of wingbeat frequency, hence, the interval between each dots increases and the maximum Doppler is also more disperse and spread out across the Doppler.

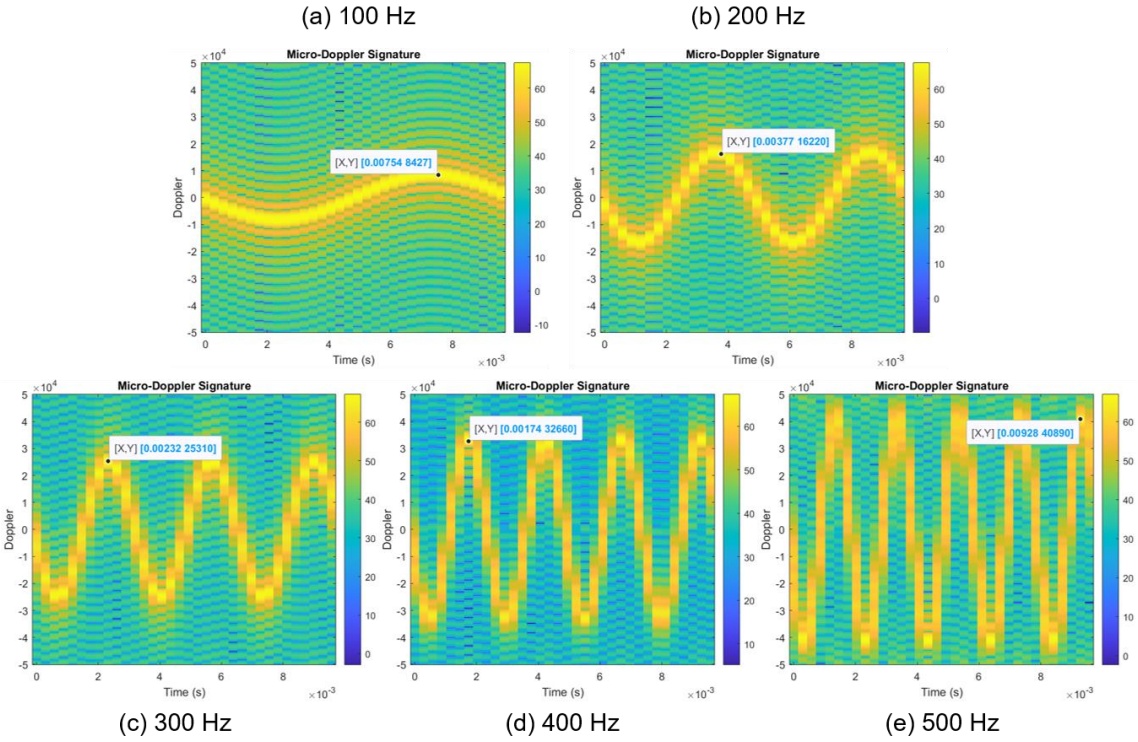

Figure 4.28: Micro-Doppler Signature of Different Rotational Rate

Figure 4.28 which correspond to the Doppler from the RDM plot signifies some properties that could be extracted from the signature. First, in terms of the rotational rate, which indicates the number of complete sinusoidal cycles available in a certain time. Second, is the maximum Doppler attained (or the peak of the sinusoidal) which represents the very end of the dots in the RDM plot. Lastly, the micro-Doppler plot also indicates the size of the target, which will be discussed later. For the micro-Doppler extraction, the window duration T_w of STFT is chosen so that it is shorter than the peak-to-peak spectrum duration $T_{peak-to-peak}$ in RDM plot.

For instance, a target with a wingbeat frequency of 100 Hz, will have

$$T_{peak-to-peak} = \frac{1}{f_{target}} \tag{4-20}$$

a period of $T_{peak-to-peak}$ is 0.01 s. Therefore, in the relation of $T_w < T_{peak-to-peak}$, the T_w is selected so that it is shorter than 0.01 s.

The next analysis is based on different sizes, 5 cm and 10 cm long of the target. The radar parameters and other characteristics of the target are kept constant. With the same wingbeat frequency, a smaller size target in Figure 4.29 has a smaller maximum Doppler attain compared to Figure 4.30. That bigger size of the target also has extended its maximum Doppler towards the maximum unambiguous Doppler. From this observation, it is possible to predict the size of the target r with the assist of equation (3-64), knowing that the rotational rate of the target ω.

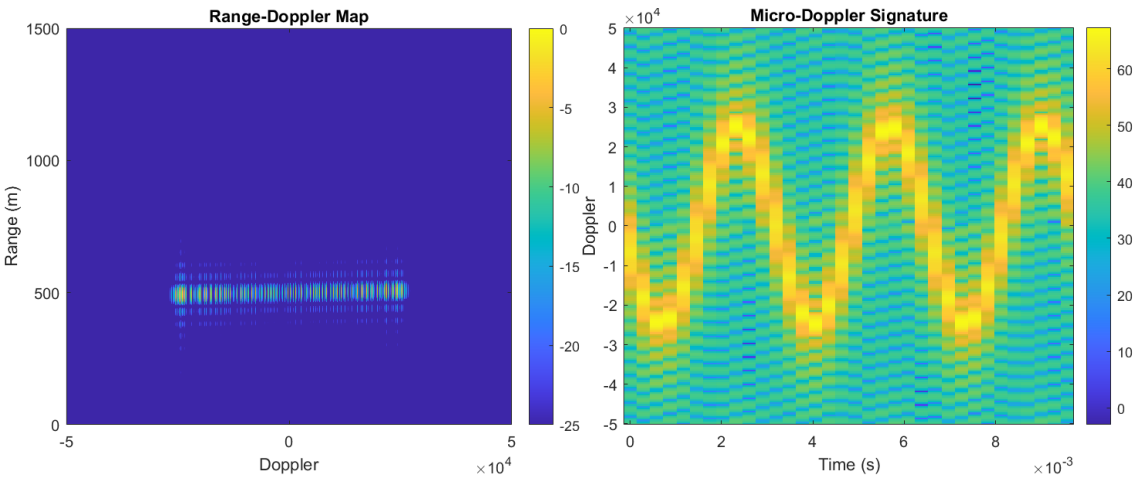

Figure 4.29: The size of the Target is 5 cm

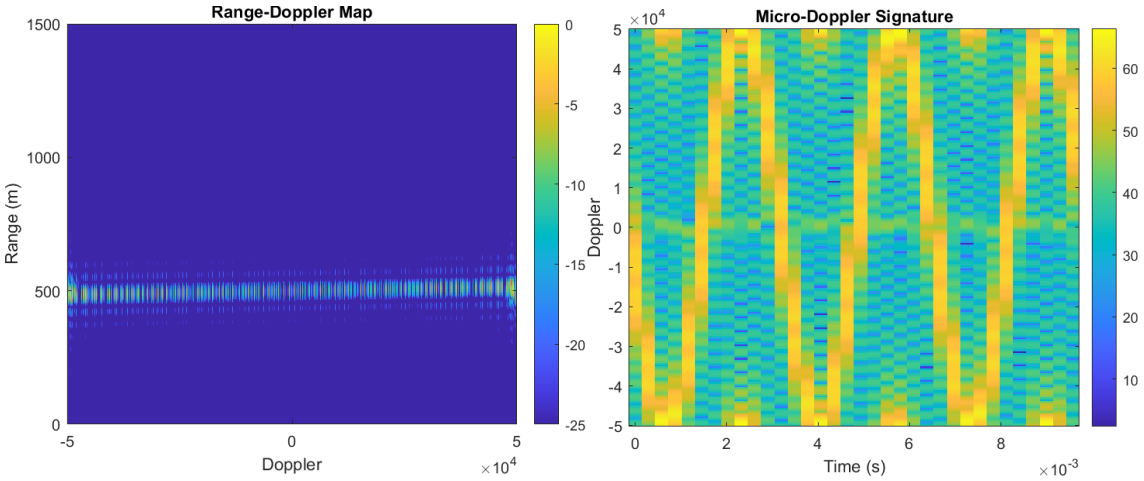

Figure 4.30: The size of the Target is 10 cm

4.2.4 A Recapitulation for FMCW Radar Designer

The findings of this study suggest that two important parameters will affect the ambiguity of the radar system. The ramp duration T_R will affect the Doppler ambiguity and the bandwidth of the radar B will affect the range ambiguity. The expected ω_{target} will determine the required value of T_R to avoid ambiguity.

$$2f_{Doppler} = 2\left(\frac{2v_{radial}}{\lambda}\right) = \frac{4(2\pi\omega_{target}r)}{\lambda} \quad \textbf{(4-21)}$$

The minimum of the ramp duration is inversely proportional to the equation (4-21), that is

$$T_R = \frac{\lambda}{8\pi\omega_{target}r} \quad \textbf{(4-22)}$$

It is stated here that the higher the ω_{target} of a target, the shorter T_R that is needed to capture the dynamic of the Doppler. A micromotion of the rotating blade propeller or the flapping of the wing insect will induce a symmetrical Doppler of positive and negative sides. However, insufficient dwell time will present an incomplete cycle of the motion, that is the $T_{dwell} \geq \frac{1}{f_{target}}$ .The expected value of f_{target} drones and insects are believed to be around the

average of 500 Hz and 1000 Hz respectively. Thus the T_R suggested would be around at least 2 ms for the drone and 1 ms for the insect.

4.3 Summary

The small size of the target relates to small RCS. This will be a challenging task for the target detection as it could be masked by other uninterested targets or clutter. The micro-Doppler signature offers the ability to detect this small size target as these interesting targets have the frequency oscillation that induced the frequency modulation on the echoed signal. Hence, it will assist the target detection even though the radial velocity is far much slower and not obvious. Thus, the variation of this Doppler signature from different kinds of the target can be observed over time with the study of time-frequency analysis.

The purpose of this chapter is to allow the reader to comprehend the expected results obtained from the run simulations. It is to develop the understanding of signal processing and analysis for the future experimental work that will be demonstrated in the next chapters. An example of a possible target, like an insect of less than 5 cm in size has been simulated and analysed. This finding would seem to suggest that a chirp duration of 1 ms should be implemented for these targets detection purposes. The analyses show that the rotational rate, the maximum frequency Doppler and the size can be determined from the study. Because the extraction of the Doppler signature provides more information about the target characteristics, therefore, this enables us to classify them accordingly.

5 S-BAND FMCW RADAR DESIGN

A prior prototype was delivered first at a lower frequency to demonstrate that the proposed design solution worked. A lower frequency model was configured because it offers a lower cost before expending on a higher price at 24 GHz. This prototype acts as a demonstrator before involving in a higher frequency radar. Therefore, this chapter seeks to explain an S-band FMCW radar prototype design and development of a real baseband signal and its implementation. The chapter has been organized in the following way; the proposed design and several data collection with four different targets are performed as a validation to the radar design that has been developed.

5.1 S-Band FMCW Architecture

The components and hardware used in this section are operated at S-band frequency which is within a range of 1.5 GHz to 3.9 GHz. It acts as an early exposure and a little step further before building a higher-frequency radar. The procurement with a lower frequency band is presented and discussed. A setup of FMCW is assembled to analyse the characteristic signal after each component. The signal is generated, and the power level is measured by using an Anritsu MS2691A spectrum analyser to ensure that the power is suitable to activate the components. The signal generated is a sawtooth chirp waveform with a bandwidth of 50 MHz and a chirp duration of 1 ms. The bandwidth of the signal is pushed to the limit of the hardware components which is 50 MHz, whereby the author must acknowledge the limitation of the hardware.

The chirp signal generated with a carrier frequency of 3.5 GHz is first amplified with a mini-circuits ZX60-362GLN-S+ amplifier and the signal is split into two by a mini-circuits ZX10-2-622+ splitter; one signal is carried forward to the antenna for transmission and another one serves as a reference signal in the LO port of a double-balanced mixer. This mini-circuits ZX05-C42-S+ mixer can operate over the frequency range between 1 GHz to 4.2 GHz. The power level generated from Anritsu MS2691A is 0 dBm, which is the maximum possible,

and the power level needed to drive the LO mixer is +7 dBm. This clarifies the role of having an amplifier after the signal generator and before the signal is split into the mixer.

The transmitting antenna and the receiving antenna are working simultaneously as this is an FMCW radar. They are both identical antennas (Broadband Horn Antenna LB-7180) which operate from 0.7 to 18 GHz, with a gain of 12 dBi. The length of the antenna is 288 mm, and the size of the aperture is 244 x 160 mm. Since most of the noise develops in the receiver, a low-noise amplifier ZX60-362GLN-S+ is used in order to achieve a suitable strength of the signal over the noise mean power (that is the SNR). The received signal is then mixed with a copy of the transmitted signal to obtain the beat signal. This beat signal will then be digitised by a TiePie HS5 oscilloscope, which is directly connected to the host computer. The signal will be filtered by the digitiser. So, an LPF is not required in this prototype as illustrated in Figure 2.2. Plus, the result obtained can still be compromised without the added component. Figure 5.1 illustrates the FMCW radar block diagram and the detailed components are summarised in Table 5.1. This setup is favourable mainly because of the less complexity of the calculation on top of a low-cost structure as only minimum components are required.

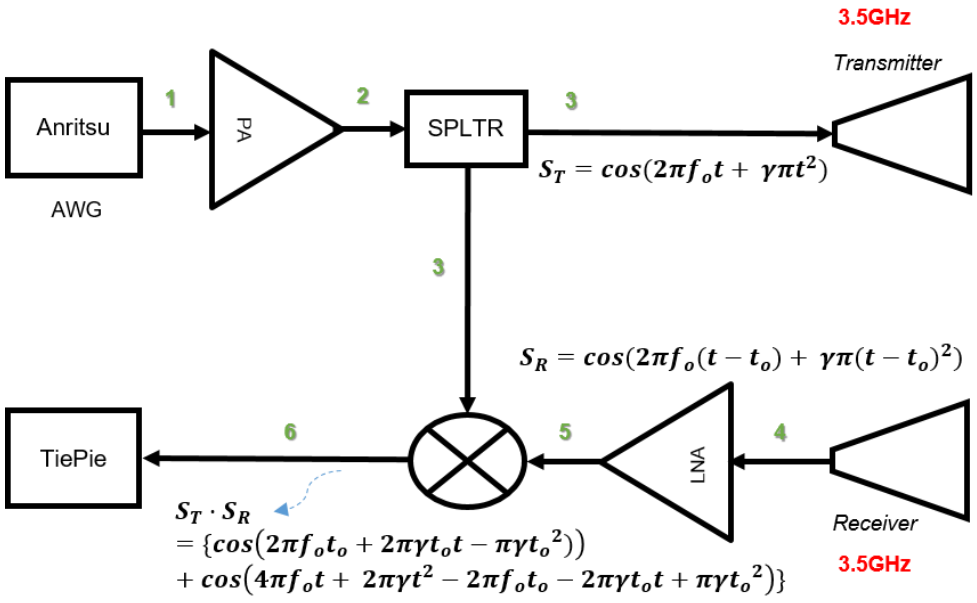

Figure 5.1: Block Diagram of S-Band Prototype

Table 5.1: Lists of RF Components

COMPONENTS	Frequency Range	MODEL NO	Company	Cost ($)
POWER AMPLIFIER	3.3GHz – 3.6GHz	ZX60-362GLN-S+	Mini-Circuits	79.95
MIXER (LO Power +13dBm)	3.2GHz - 15GHz	ZX05-153MH-S+	Mini-Circuits	48.95
LOW NOISE AMPLIFIER	1.5GHz - 6GHz	ZX60-5916MA+	Mini-Circuits	79.95
POWER SPLITTER	2.9GHz - 6.2GHz	ZX10-2-622-S+	Mini-Circuits	34.95
SMA CONNECTORS (2units)	DC – 18GHz	SM-SM50+	Mini-Circuits	11.90
			TOTAL	255.70

5.1.1 Signal Analyser Anritsu MS2691A

Anritsu MS2691A plays an important role in signal generation for this design. It can generate any waveform design within the instrument bandwidth. This hardware is also used for testing the signal characteristics especially the power level of the signal for the verification process. Both tasks can be realised by using the signal generator and spectrum analyser mode respectively. Figure 5.2 is the model hardware that was used for this S-band prototype.

Figure 5.2: Anritsu MS2691A

The frequency range for the signal generator is between 125 MHz to 6 GHz with a modulation bandwidth of up to 120MHz, whereas the frequency range for the signal analyser is 50 Hz to 13.5 GHz with a maximum bandwidth of 31.25 MHz. Spectrum analyser and signal analyser are both interchangeable frequency-domain analyses.

The waveform generation procedure involves in built-in IQ component from Anritsu, where the carrier frequency is in a baseband form. The chirp signal is generated from MATLAB programming as in Figure 5.3, the IQ components for the up-chirp signal is written in a CSV file. Then the file is transferred to Anritsu. By using the IQ Producer interface, the CSV file is converted into the signal generator, the signal is uploaded and selected before being used for FMCW signal transmission.

```
clear all
close all
clc


B = 50e6; % bandwidth of the LFM
Tr = 1e-3; % ramp duration
Gamma = B/Tr;
CSVfile = 'ChirpB50MHzTr1ms.csv';

DataPoints = 200e3;
Fs = 4*B; % Sampling rate [Hz]

t = 0 : 1/Fs : (DataPoints/Fs-1/Fs);

I = cos((Gamma*pi*(t).^2));
Q = sin((Gamma*pi*(t).^2));

x = I + Q*1j;

% Writing File
data = [I' Q'];
csvwrite (CSVfile,data);
```

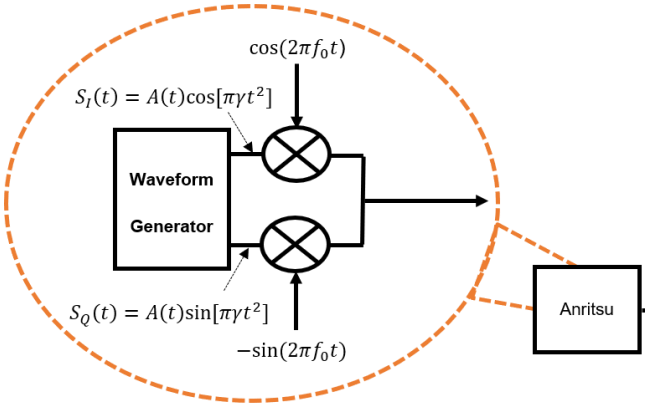

Figure 5.3: LFM Signal Formation

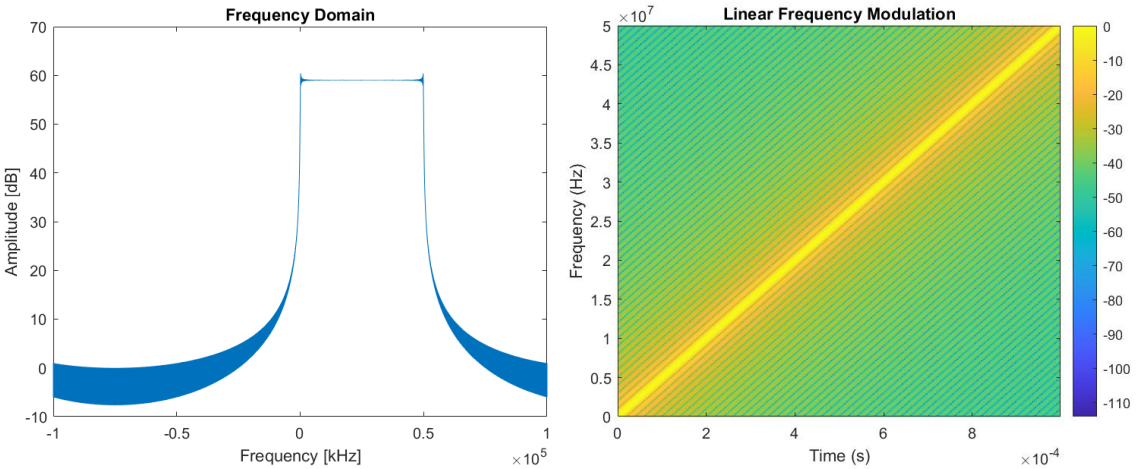

Figure 5.4: Frequency Spectrum of Generated Signal

The bandwidth B of the signal generated is 50 MHz within the ramp duration T_R of 1 ms. Figure 5.4 on the RHS represents the STFT of the signal generated in MATLAB where the frequency modulates within a period. The time dwell is equal to the ramp duration since the aim is to generate one chirp. The frequency rises linearly from 0 to 50 MHz. The spectrum of that signal is shown in the LHS of Figure 5.4, where it could be seen that the deviation starts from 0 until 50 MHz.

5.1.2 TiePie Handyscope HS5

Figure 5.5: TiePie Handyscope HS5 Oscilloscope

TiePie HS5 is a type of oscilloscope that connects directly to the computer for power supply. There are two channels input available for this handy scope and one for Arbitrary Waveform Generator (AWG) signal. The TiePie is used as a digitiser and gathered the data throughout the experiment. The data collected is saved in *MAT* file and then processed in MATLAB for post-processing.

5.1.3 Mini-Circuits ZX05-C42-S+ Mixer

A mixer is a device that shifts a signal from one frequency to another frequency. It is either from RF frequency to baseband frequency or vice versa. The mixer provides two inputs and one output. This output can either be the summation of the two inputs or the difference between the two inputs.

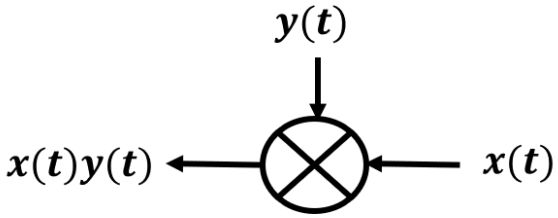

Figure 5.6: An Ideal Mixer

Let say the two inputs at the RF and LO port of the mixer are

$$x(t) = A\cos\omega_1 t \quad \textbf{(5-1)}$$

$$y(t) = B\cos\omega_2 t \quad \textbf{(5-2)}$$

Therefore, the IF output of the mixer is defined as

$$x(t)y(t) = A\cos\omega_1 t \cdot B\cos\omega_2 t \quad \textbf{(5-3)}$$

5.1.4 Low-Noise Amplifier ZX60-362GLN-S+

Amplifiers are mainly known for boosting the signal power to a higher value without modifying the original input signal. The output of the signal will have the same waveform and frequency, but different amplitude against the input signal. The attribute of an amplifier can be described as

$$x_{Amp}(t) = G \cdot x(t) \quad \textbf{(5-4)}$$

Where G is the amplifier gain and $x(t)$ is the input signal. And the equation is linear time-varying. However, any device especially this amplifier has its physical limitation. The system will saturate once the output exceeded the limit range. To verify the workability of the component, the following setup is performed as in Figure 5.7. The source of the signal from the Anritsu MG3700A signal generator is connected to the input of the amplifier and the output of the amplifier is connected to the Anritsu MS2691A signal analyser. DC power supply is also connected to the amplifier to provide voltage from 2.8 to 5 volts.

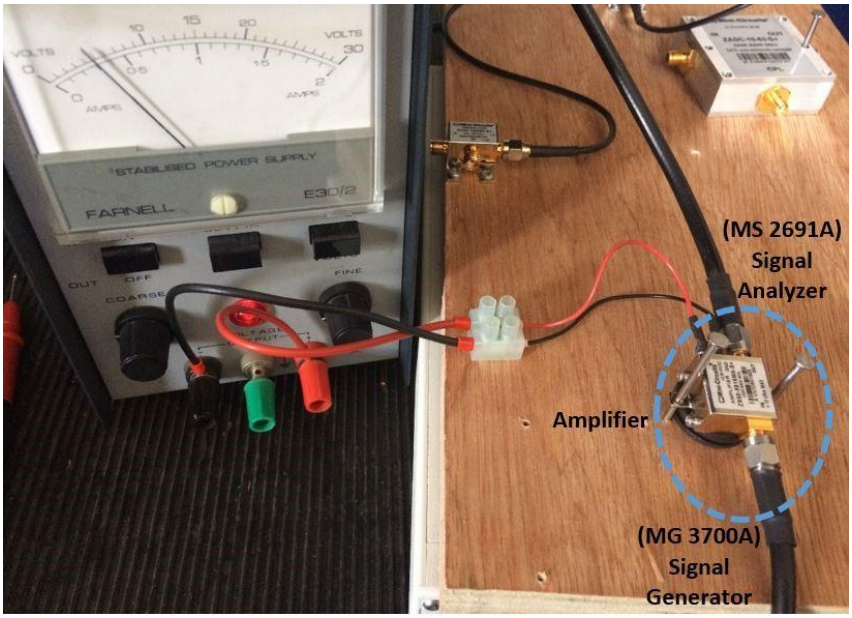

Figure 5.7: A Setup for Amplifier Verification

The principal connection of the DC power supply is always the positive terminal (red pin) to the negative terminal (black pin) and neglecting the ground terminal (green pin). The floated instrument ground will be grounded within the power cord of the power supply and to the third pin of the wall socket as pictured in Figure 5.8. There are two types of ground; the common ground is the negative terminal (black pin) of power supply whereas earth ground is represented by the green pin. By joining the red pin to the green pin, it will not allow the current to flow within the circuit, hence, does not activate the amplifier properly and can lead to malfunction.

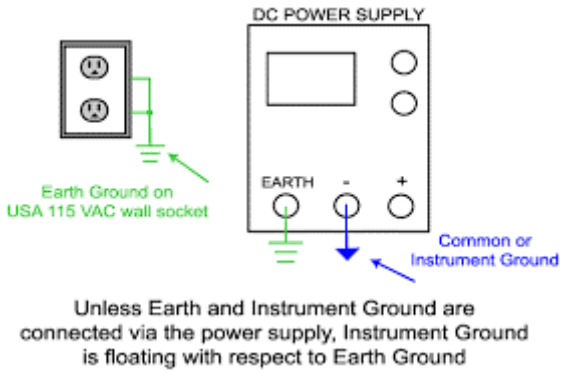

Figure 5.8: Description of DC Power Supply

An LNA is placed at the receiver part after the received antenna as in Figure 5.1 for amplification. The ZX60-362GLN-S+ LNA gain is between 19 - 24 dB and the noise figure is in the range of 3.3 – 3.7 dB. This means that the LNA also contribute to a small amount of noise to whatever is amplified. Ideally, it is suggested to have a filter just after the LNA and before the mixer input to reject the noise contribution that might fall within the unwanted mixer image.

5.2 Power Budget

This section mainly covers the power output measurement of the signal. The identification of power output is hugely important in radar prototypes mainly because of two reasons which are (i) the power that is allowable by Federal Communication Commission (FCC) which is stated here [102]. The transmitted power stated by FCC regulations must not exceed 1W (30 dBm). (ii) the power output will depend on the SNR ratio whereby the minimum power should use to at least detect the return signal. So, in order to assess the power level at different stages of the signal, the setup in Figure 5.9 is employed. This feedback loop arrangement is performed to evaluate the system response and the verification of each component in Figure 5.1.

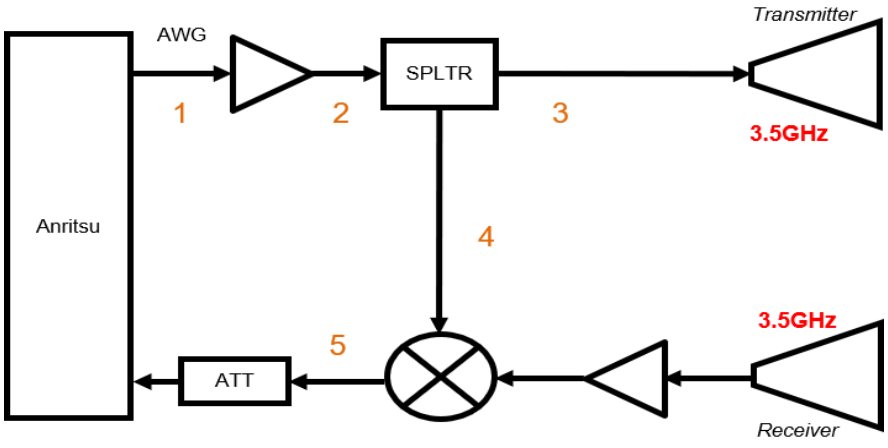

Figure 5.9: The Set-Up for Power Level Measurement in the Feedback Loop

The signal is generated by Anritsu MS2691A and received by the same hardware. Anritsu features a magnitude measurement where it enables the measurement of the strength of the signal. The *Channel Power* menu in the

Spectrum Analyser tab will display the power level of a signal at the right bottom of the screen. Once the *Channel Power* is switched on, the measurement is activated. It is important to adjust the *Channel Width* and *Channel Centre* of the marker so that it covers up the whole spectrum bandwidth of the signal. Below are the results of the power measured taken at each point. At point 1 in Figure 5.9, the generated signal will be amplified. So, within the closed-loop measurement taken, an attenuator VAT-30+ is used, which is a 30 dB attenuator with a frequency operation range between DC to 6 GHz. The main purpose of this attenuator is to ensure that the power level measurement is readable in the spectrum analyser display once the signal is amplified. The built-in attenuator in the spectrum analyser is set to 0 dB. Figure 5.10 displays the signal generated properties where the frequency spectrum is centred at 3.525 GHz and the channel width is set to 55 MHz which correspond to the bandwidth of the signal 50 MHz. So, the origin of the power level measured was 1.76 dBm. Then, it is attenuated by 30dB, so the amplitude dropped to -29.91 dBm as in Figure 5.11.

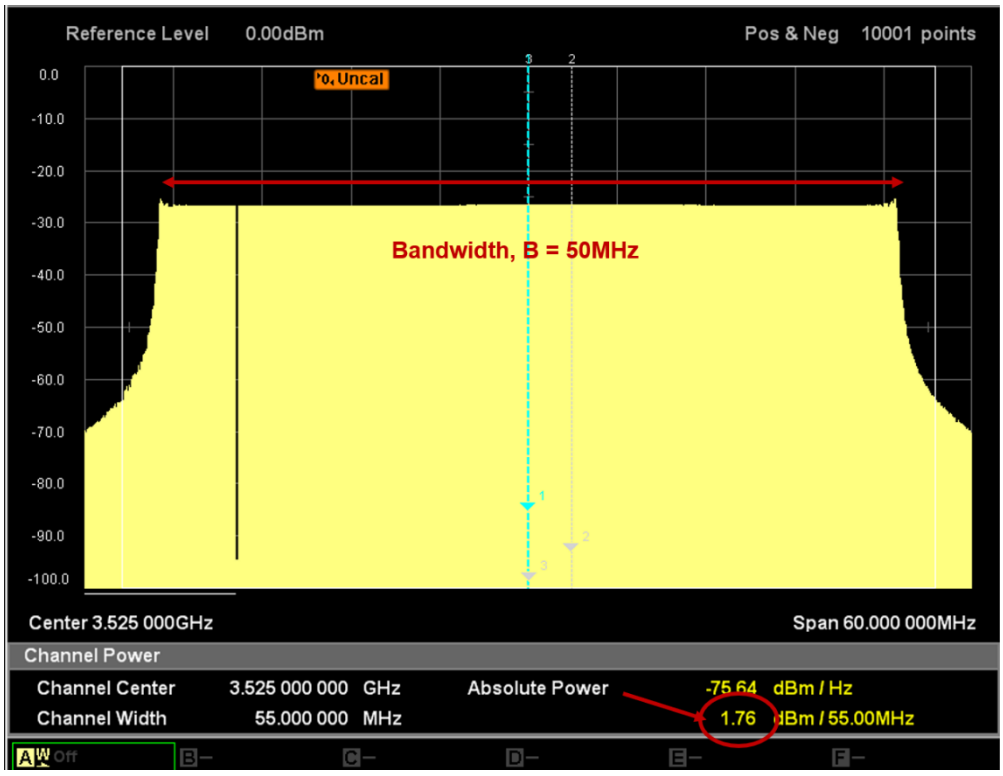

Figure 5.10: Power Level of Signal Generated at Point 1 Before Attenuation

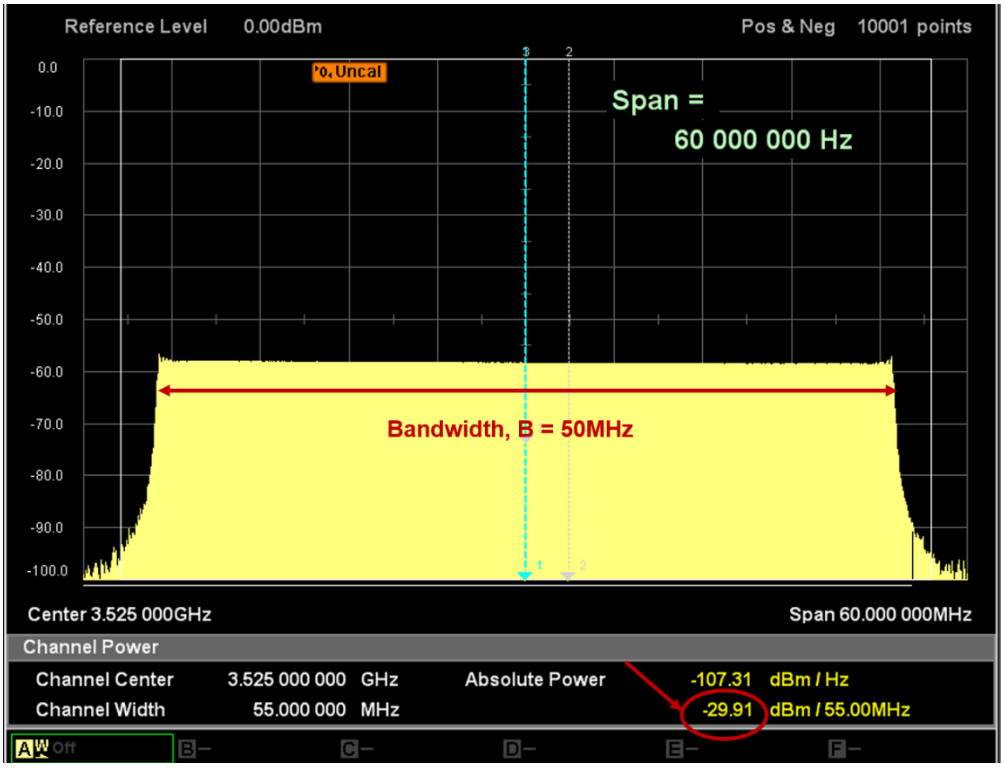

Figure 5.11: Power Level at Point 1 after 30dB Attenuation

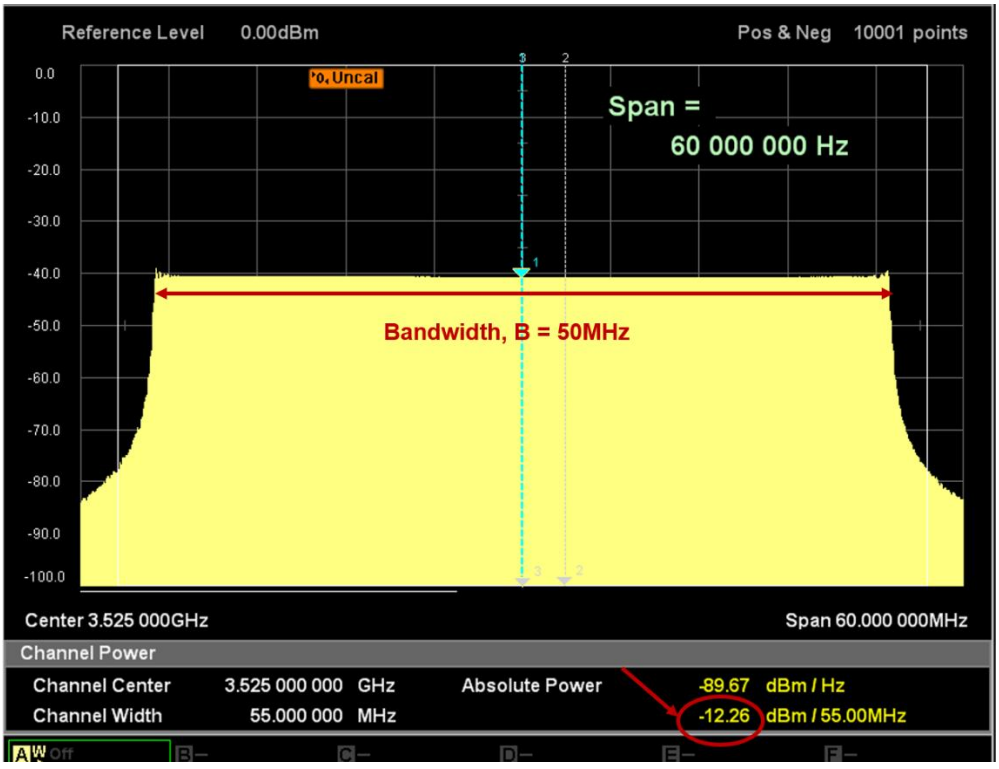

Figure 5.12: Power Level of Amplified Signal at Point 2

Then, Figure 5.12 displays a power level after LNA amplification at point 2. This is in line with the datasheet where there is a gain of around 20.15 dB gain. So, the power level increases to -12.26 dBm (i.e. 17.74 dBm when discarding the 30dB attenuator). But just after that, the power level decreases after the splitter to -16.27 dBm (13.73 dBm by discarding the 30dB attenuator) and -16.37 dBm (13.63 dBm by discarding the 30dB attenuator) at points 3 and 4 respectively as in Figure 5.13.

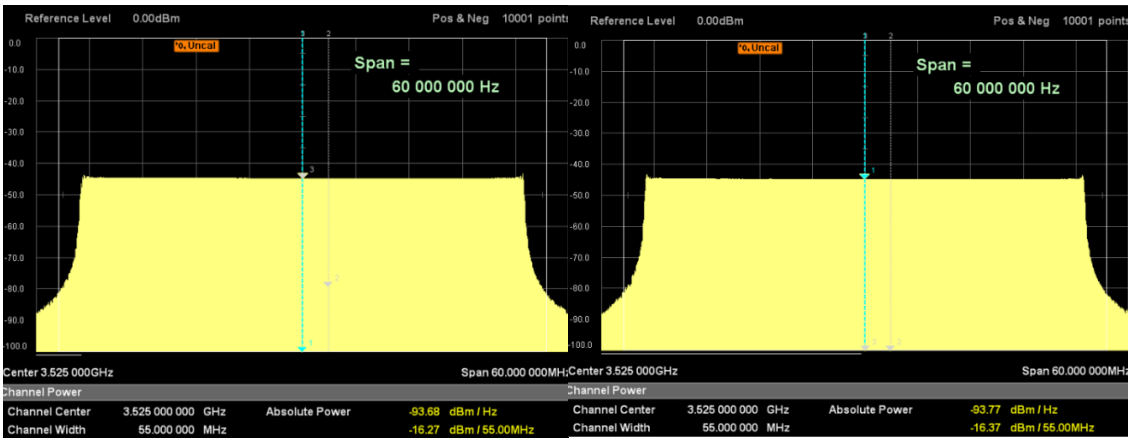

Figure 5.13: Power Level after Splitter at Point 3 and Point 4

The analysis above is the matter of power level identification after each RF component in the circuit at the transmitter part. It is summarized in Table 5.2. This is equally important particularly to ensure enough power to drive the LO port of a double-balanced mixer and to determine the power output P_{out} of the radar system before transmission. In this case, the P_{out} of the prototype was approximately +13 dBm. The maximum transmits power for a short-range FMCW application is usually about +17 dBm (which is a signal power of up to the maximum of 50 mW).

Table 5.2: Power Level Estimation in the Transmitter

Component	Model	Gain	RF Power	Measured Power Level
Anritsu	MS2691A	-	0 dBm	1.76 dBm
Cable 1	FLC-6FT-SMSM+	-2.26 dB	-2.26 dBm	
PA	ZX60-362GLN-S+	+20.26 dB	+18.00 dBm	+17.74 dBm
Splitter	ZX10-2-622+	-3.95 dB	+14.05 dBm	+ 13.73 dBm
Cable 2	FLC-2M-SMNM+	-2.54 dB	+11.51 dBm	
Antenna	LB-7180	+12 dBi	+23.51 dBm	

The power $P_{(dBm)}$ in dBm is equal to 10 times the base 10 logarithms of 1000 times the power $P_{(W)}$ in watts (W) divided by 1 watt (W),

$$P_{(dBm)} = 10\log_{10}(1000.P_{(W)}/1W) = 10\log_{10}(P_{(W)}/1W) + 30 \quad \textbf{(5-5)}$$

While the power conversion of dBm to W, on the other hand, is given by 10 raised to the power $P_{(dBm)}$ in dBm divided by 10, then divided by 1000,

$$P_{(W)} = 1W.\frac{10^{\left(\frac{P_{(dBm)}}{10}\right)}}{1000} = 10^{\left[\frac{\left(P_{(dBm)}-30\right)}{10}\right]} \quad \textbf{(5-6)}$$

$$P_{(W)} = 10^{\left[\frac{\left(23.51_{(dBm)}-30\right)}{10}\right]} = 0.22\,W$$

This concludes that the transmit power in W is more or less

$$P_T = P_{(W)} = 0.22\,W \quad \textbf{(5-7)}$$

Before any experimental data is carried out, the noise and background measurement is important. It is to assess the state of the radar system as well as the ambient condition. In order to measure the noise, the transmitting signal is switched off while the radar is on (i.e., the amplifier in the circuit is switched

on). Figure 5.14 shows the noise response. The left picture shows before the mean value removal where the peak shown indicates the DC signal contribution. The right picture, on the other hand, shows after the mean value removal for the noise removal and to ensure that the noise is still at a tolerable level.

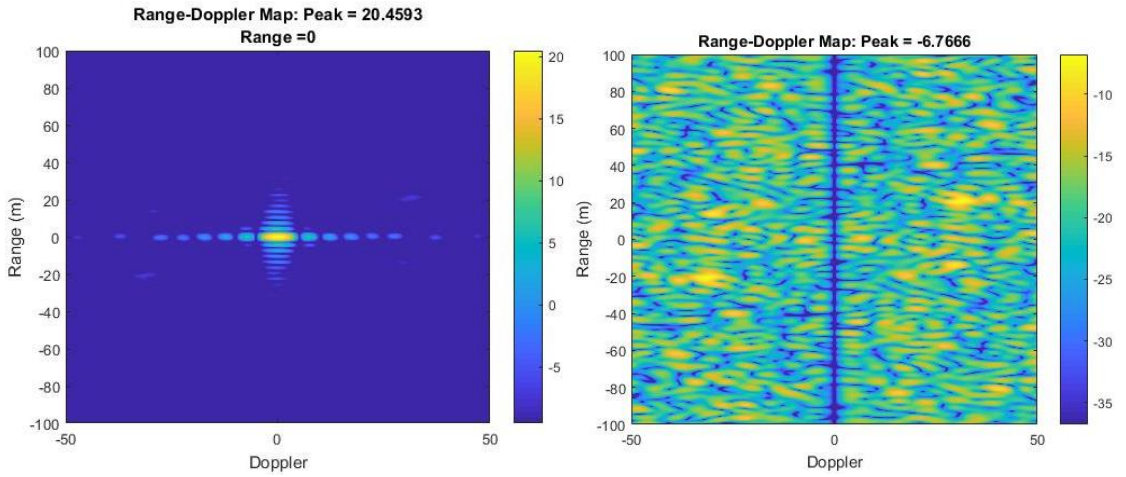

Figure 5.14: The Response Signal when Transmitted Signal is Switched Off (Noise Measurement)

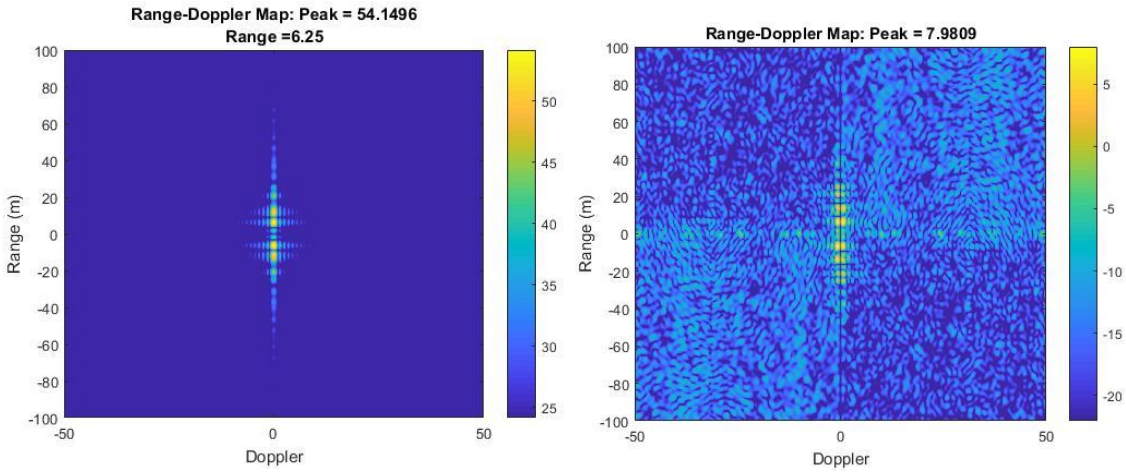

Figure 5.15: The Response Signal when Transmitted Signal is Switched on with A Stationary Rotor Blade (Background Measurement)

Then a measurement is taken when the transmitter is switched on, and the target is in a stationary state as in Figure 5.15. In order to measure the Signal Noise Ratio from the measurement taken, and by referring to equation (3-43), the instantaneous power of the received signal before the digitizer is

$$P_{Signal} = |S_R(t)|^2 = {A_R}^2 \quad \textbf{(5-8)}$$

Where A_R is the peak or the maximum power of the received signal. Whereas the noise power is determined by taking the average of the random noise in the plot,

$$P_{Noise} = random(N^2)_{Average} \quad \textbf{(5-9)}$$

Therefore, the signal-to-noise ratio from the RDM can be determined by

$$SNR = \frac{P_{Signal}}{P_{Noise}} = \frac{{A_R}^2}{(N^2)_{Average}} \quad \textbf{(5-10)}$$

5.3 Case Study I: Single-Moving Target

The radar was tested with real field experiments in order to demonstrate the prototype worked. An initial experiment is carried out on Cranfield University Shrivenham campus. The measurements collected was on a non-busy day. Literally, no other moving target is accidentally involved other than the intended target throughout the measurements. The purpose of this case study is to investigate the Doppler shift created by a single target movement. A large RCS is chosen for this initial test, which is a car brand Chevrolet Lacetti. The shape at the front is not identical to the rear of the car. So, the RCS of the target between the front and rear are different, meaning that, this probably will affect the SNR in this comparison. The arrangement of the experiment and the equipment used is illustrated in Figure 5.16 until Figure 5.19.

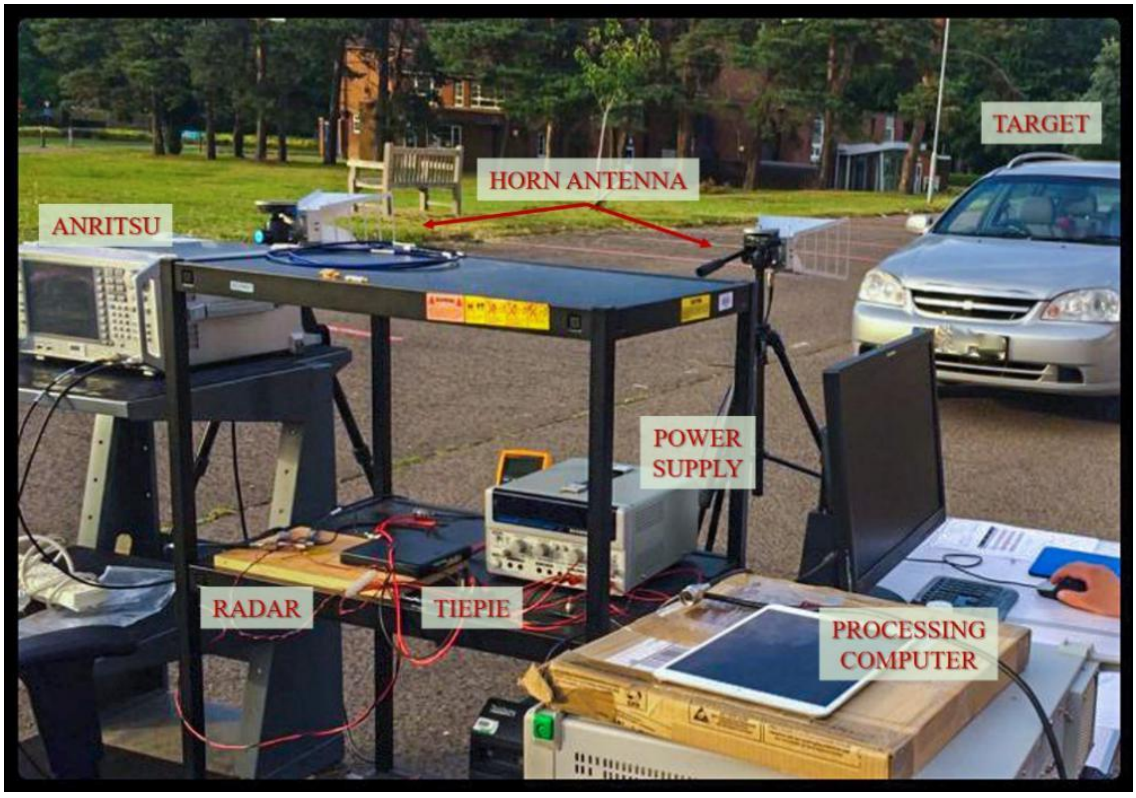

Figure 5.16: A 3.5 GHz FMCW Radar Experiment Arrangements

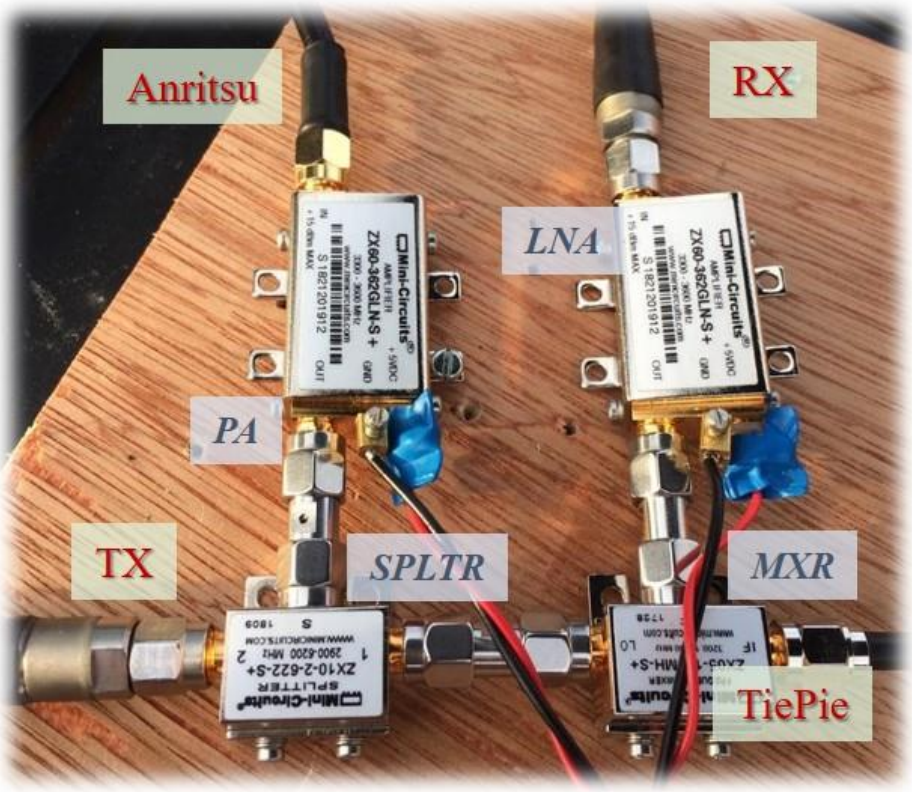

Figure 5.17: Closed-Up of Radar Prototype

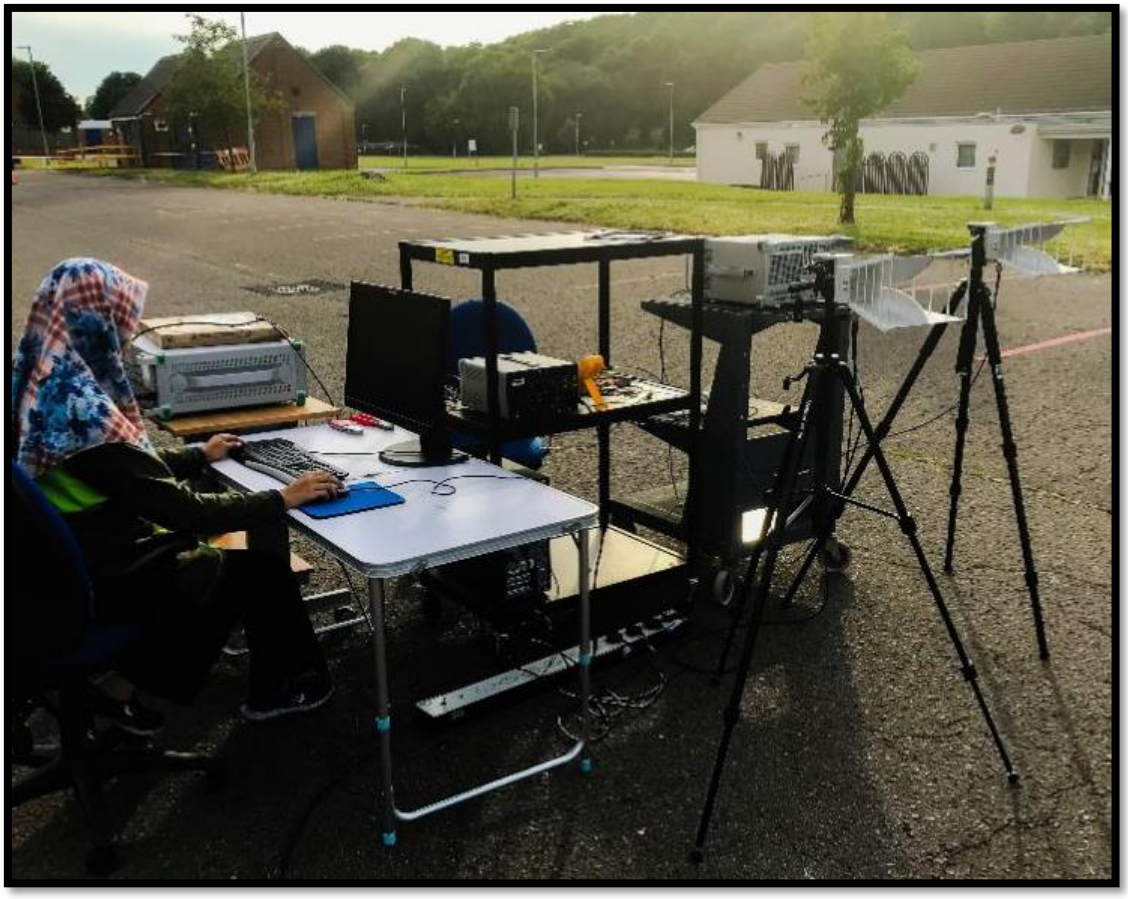

Figure 5.18: The Experimental Arrangement from Other View Angle

Figure 5.19: The Rear of the Car Facing towards the Radar

A ramp duration of 1 ms is tested in this session and a ramp bandwidth of 50 MHz. A sample rate of 50 kSamples/s with 10 kilo Samples resulting in a dwell time of 0.2 s, a short dwell time is enough in this case as the author is not interested to observe the micro-Doppler behaviour yet. Before the test on a target is performed, noise measurement is taken to identify the surrounding environment response. The total system noise power is measured with the transmitted signal is switched off. Figure 5.20 shows the radar feedback by receiving the signal from the surrounding without switching on the transmitter. The figures give a null response which indicates no other noise or intervention is present at that location. Only the system noise contributed to the range profile.

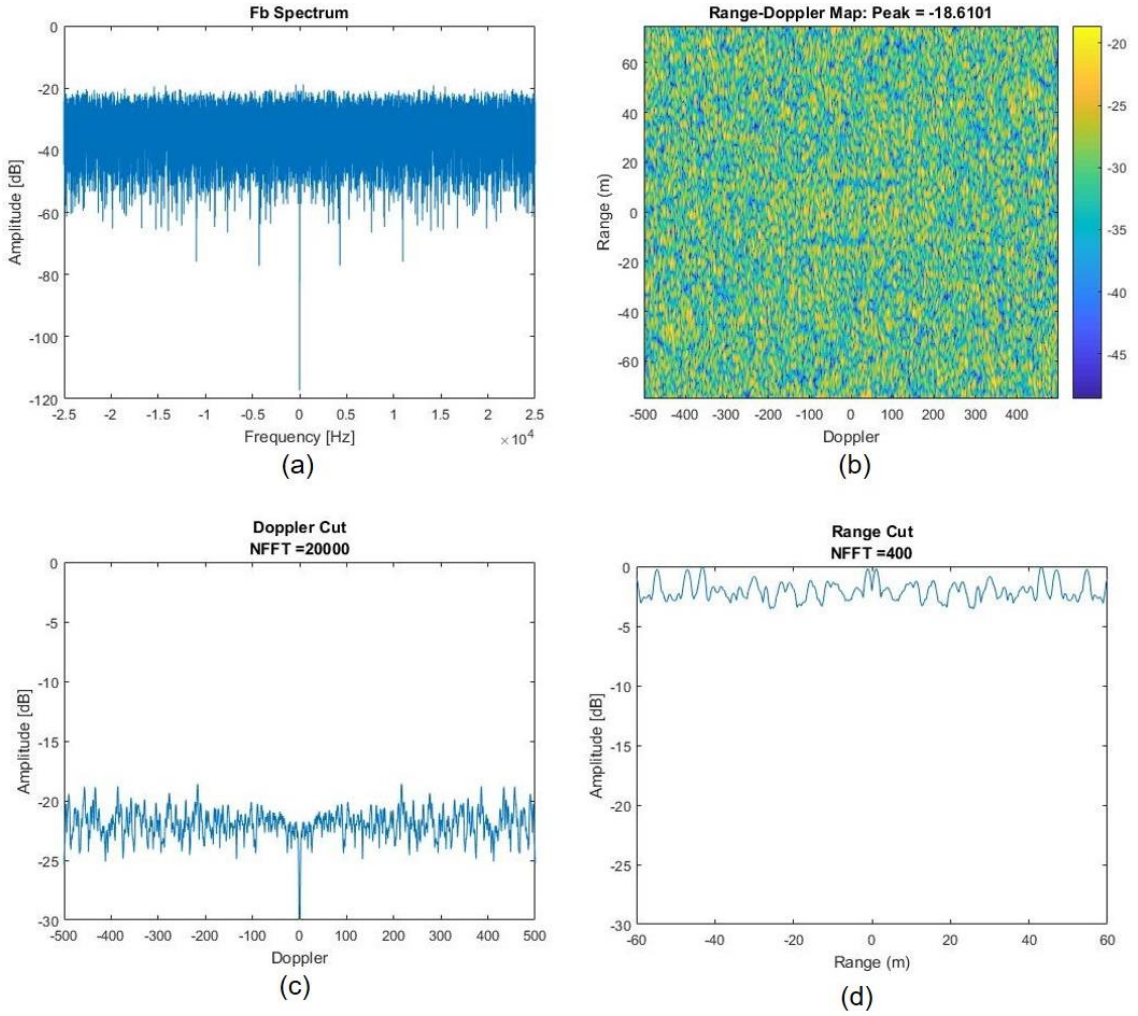

Figure 5.20: Noise Measurement (a) Beat Frequency Spectrum (b) RDM (c) Doppler Cut and (d) Range Cut

From Figure 5.21, the car located approximately 5 m away from the radar starts to accelerate and getting further away from the radar. The figure presented in the first row shows the initial stage of the car moving, where at that point 6 m away from the radar, the radial velocity has just started with 0.945 mph. The middle row shows that the car has accelerated to 12.27 mph at 18.75 m away and the SNR has dropped to 33 dB. The car accelerated further to 15.4 mph at point 33.38 m away from radar which is represented in the last row of the figure. The energy response from the target is reduced as the target is moving away. The unambiguous range can be determined by applying equation (3-41) where $R_u = \frac{(3e8)[(50e3)/2](1e-3)}{2(50e6)} = 75\ m.$

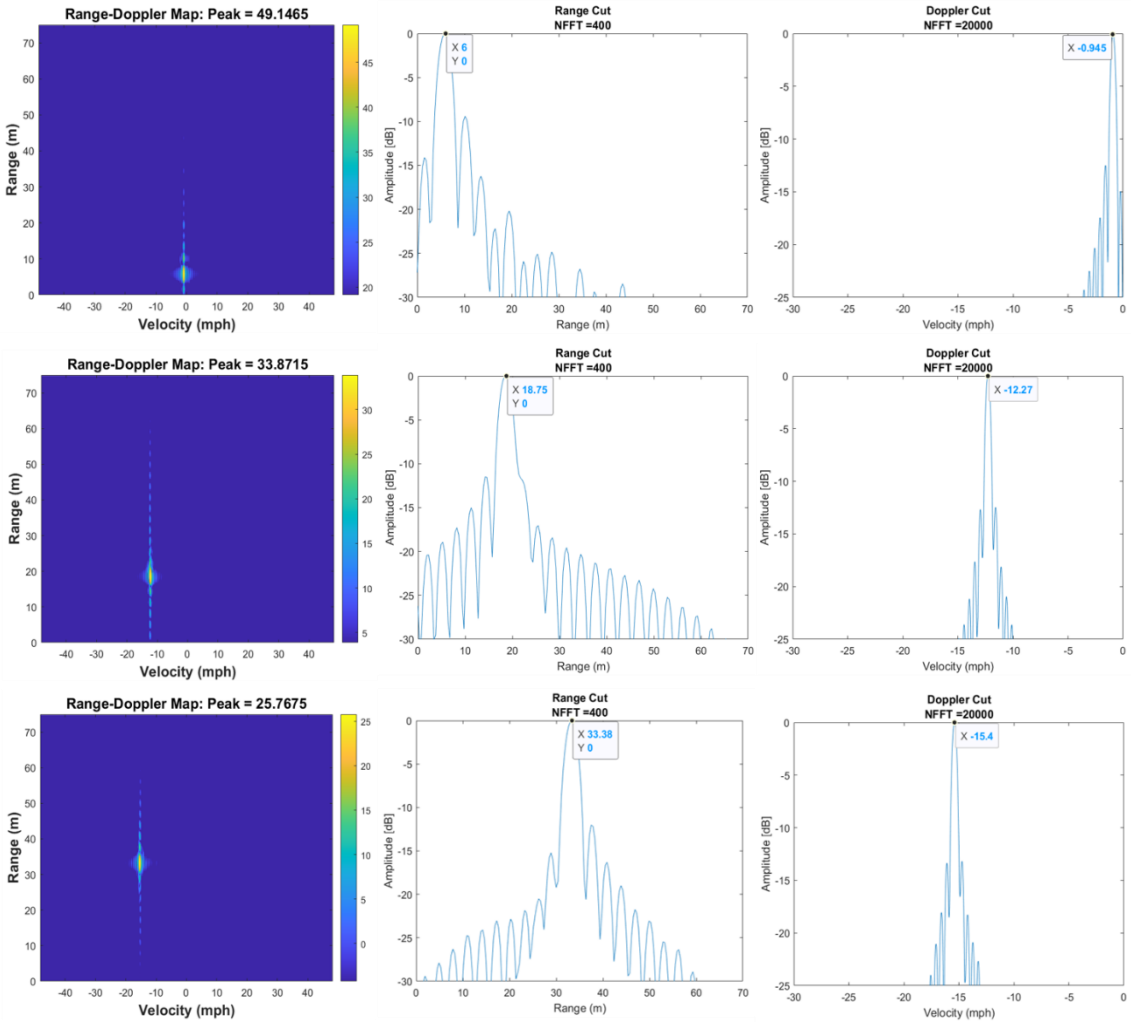

Figure 5.21: Target Moving Away from Radar (From the picture above towards the bottom picture)

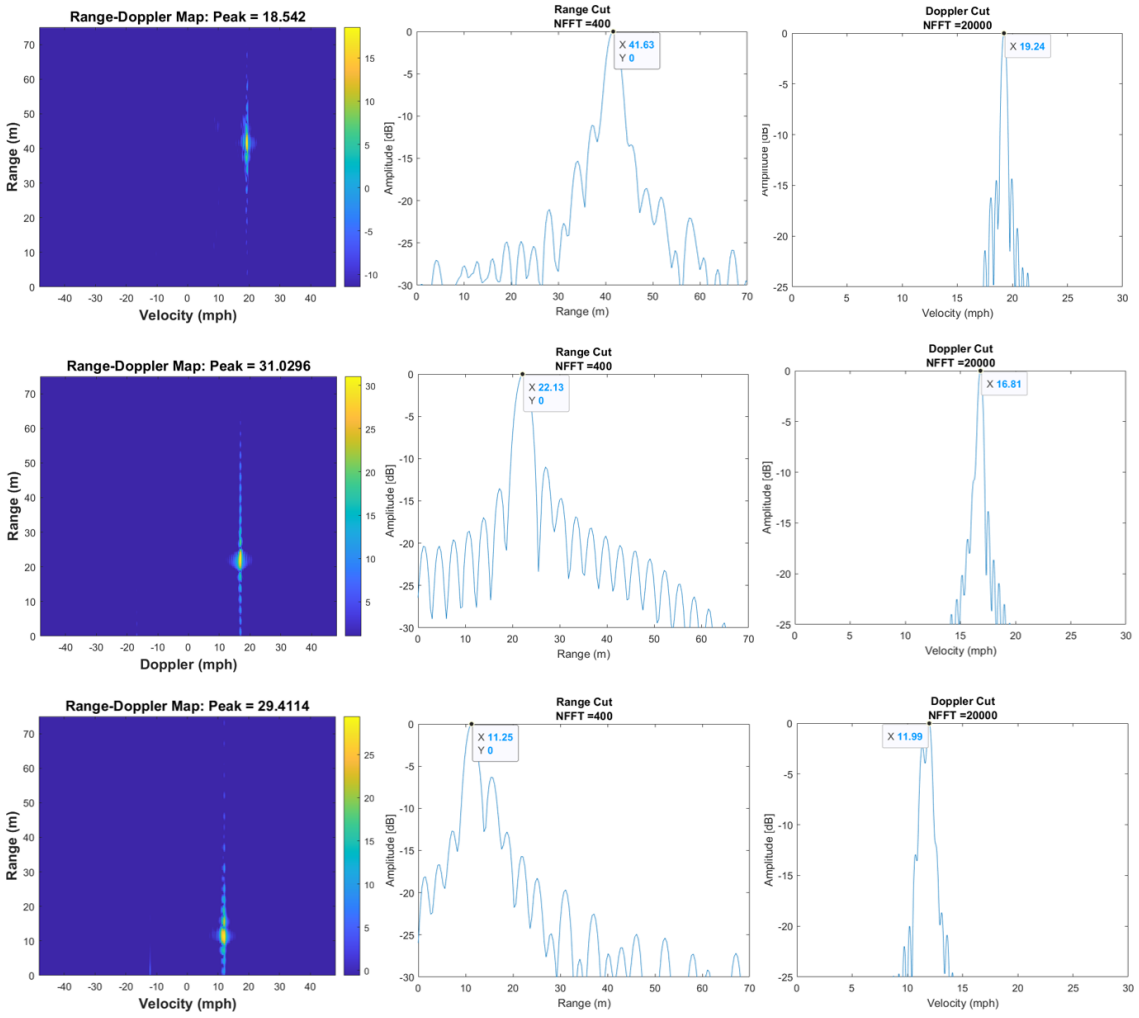

Figure 5.22: Target Moving Towards Radar (from Top to Bottom Pictures)

Once the car has reached the end of the corner and stopped, it started to turn back facing towards the radar. From further away, the car starts to accelerate from 0 speed until it reached the approximate speed of 19 mph, slowly getting near the radar. Then, it starts to decelerate as it's getting closer, illustrated in Figure 5.22. As in the first row of the figure, the instantaneous speed at 41.63 m away from radar was 19.24 mph. The middle row shows that as the car getting near to the radar where at point 22.13 m, the SNR getting larger to 31 dB and the car decelerated to 16.81 mph. And lastly, before the car come to a halt, at point 11.25 m from the radar which is represented in the last row of the figure, the speed was 11.99 mph. the car completely stopped at 5m away from the

radar. Moving away from the radar will give a lower intensity of frequency resulting in a negative Doppler and moving towards the radar will give a higher intensity of frequency making a positive Doppler. By measuring the Doppler frequency enables us to measure the velocity of the target. The strength of the echoes that are reflected by the target is inversely proportional to the distance of the target with respect to radar. It is related to the fourth power of the target's range $(1/R^4)$. So, it is rapidly become weaker or grow stronger if the target moves away or approaches respectively. The reflecting characteristics of the car are similar except for the shape of the target which gives a higher reflectivity from the rear of the car compared to the front of the car. This is because the rear of the car gives a partly rounded shape of a sphere that is believed to arise in a stronger signal return. Other factors that could affect the strength of the signal is kept constant including the transmitted power, antenna gain, signal wavelength and the noise background.

5.4 Case Study II: One-Blade Propeller

A rather different experiment is presented in this section. This time, an indoor experiment is conducted in Heaviside Lab, Cranfield University, Shrivenham campus. The purpose of this study is to extract a micro-Doppler signature from the rotating target and determine the rotational speed of the target. A target with a 46 cm long one-blade propeller was placed in the boresight of the radar prototype. The target for this study is pictured in Figure 5.23 and was placed 5 m away from the radar. The propeller is facing side-ways to the radar in order to obtain the optimum Doppler detection. Placing the propeller in a front-view position will result in a static reflection with ideally no Doppler from the target since no radial movement is involved in the line of sight of the radar. The radar antenna is in a co-polar position.

Since the ramp duration is 1ms, the bandwidth of the main lobe is inversely proportional to ramp duration which in this case is 1,000Hz. So, the required sampling rate of the digitizer is only 20 kHz (±10 kHz Doppler span in each

side). The chosen ADC sampling rate will determine the span of the Doppler bandwidth in the frequency domain, where it is half of the sampling rate on negative and positive sides. And the chosen ramp duration and bandwidth will determine the span of the Doppler in the STFT spectrum. The larger the bandwidth the better the resolution. However, due to the bottleneck of the signal generator, the author left the bandwidth to the maximum possible. If the target has a high rotational frequency induced by the micro-motion of the target, then a lower ramp duration is required in order to capture the micro-Doppler signature and avoid ambiguity.

Figure 5.23: One-Blade Propeller (a) Side-View (b) Front-View

The sample rate is 100 kHz and 100-kilo samples. Hence, leading towards the dwell time measurement taken is within one second. The smaller the sampling rate but with the same number of samples, the more time integration will be extended. This enables a longer time observation of micro-Doppler signature. The radar parameters are concluded in Table 5.3.

$$Dwell\ Time = \frac{Number\ of\ Samples\ (kS)}{Sampling\ Rate\ (\frac{kS}{s})} \quad \textbf{(5-11)}$$

$$Number\ of\ Ramps = \frac{Dwell\ Time\ (s)}{Ramp\ Duration\ (s)} \quad \textbf{(5-12)}$$

Table 5.3: The Radar Parameters

PARAMETERS	VALUES
Chirp Bandwidth	50 MHz
Ramp Duration	1 ms
Frequency	3.5 GHz
Sampling Rate	50 kS/s or 100 kS/s
Number of Samples	100 kilo Samples
Dwell Time	2 s or 1 s
Number of Ramps	2,000 or 1,000

The measurement was collected when the target is at a stationary position, where no rotational blade is involved yet. And the analysis result is discussed. Since the use of IQ mixer is discarded from the conventional system, hence, there are positive and negative sides of f_b spectrum. Due to this matter, the radar parameters are chosen so that both spectrums do not overlap each other. Figure 5.24 shows the spectral lines with an interval of $\frac{1}{T_R} = \frac{1}{1\ ms} = 1\ kHz$ and f_b shown is 2 kHz.

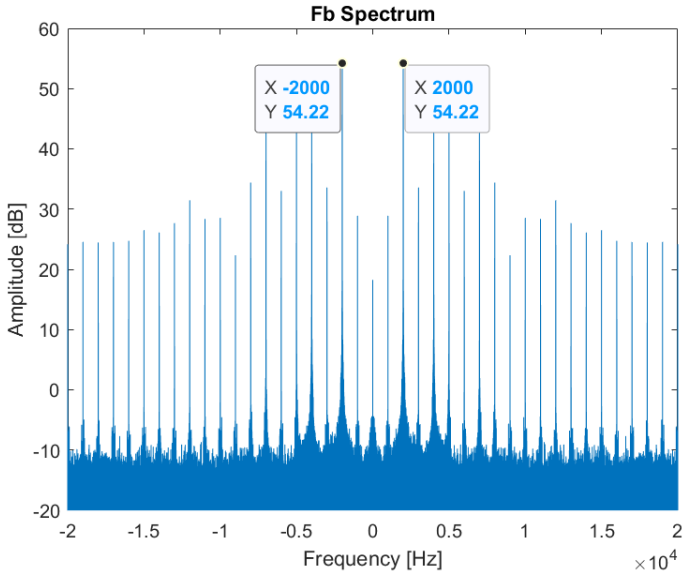

Figure 5.24: Frequency Spectrum of IF Signal

Figure 5.25 shows that the target is 6 m away from the radar. Since the target is in a stationary state, hence, the frequency spectrum is centred at the zero-Doppler as in Figure 5.26, with no Doppler shift and no micro-Doppler presence. The range cut in Figure 5.26 shows that there is a multi-path propagation occurred and this is due to the reflection of the room with limited space in the lab.

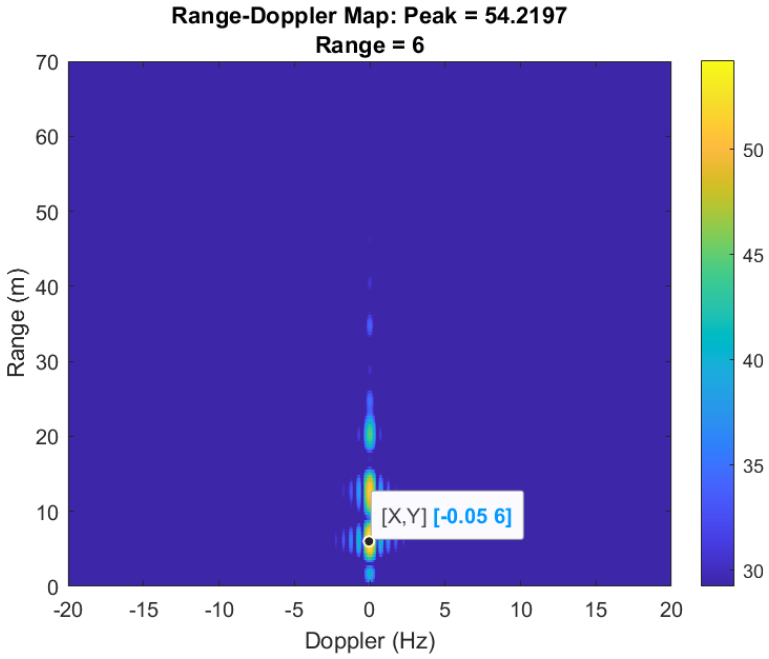

Figure 5.25: RDM of Stationary Target

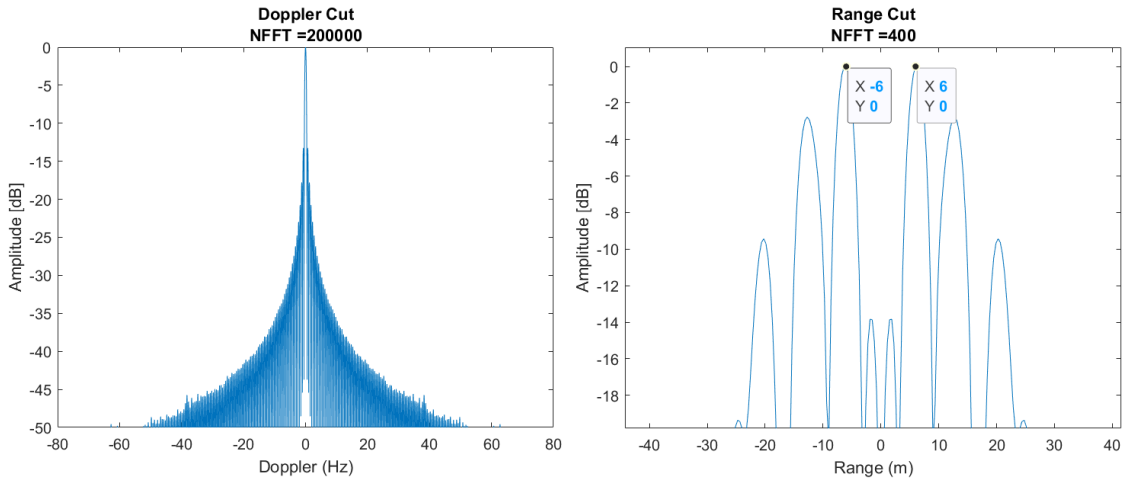

Figure 5.26: Doppler Cut (LHS) & Range Cut (RHS) of Stationary Target

The following study, which is represented from Figure 5.27 until Figure 5.31 are the results of a one-blade propeller in a state of rotating but still stationary at a fixed place. A comparison between the two groups where RHS are the results from a sampling frequency of 100 kHz and LHS are the results of a sampling frequency of 50 kHz. Since the number of samples is similar between the two groups, so the dwell time is 1 s and 2 s respectively.

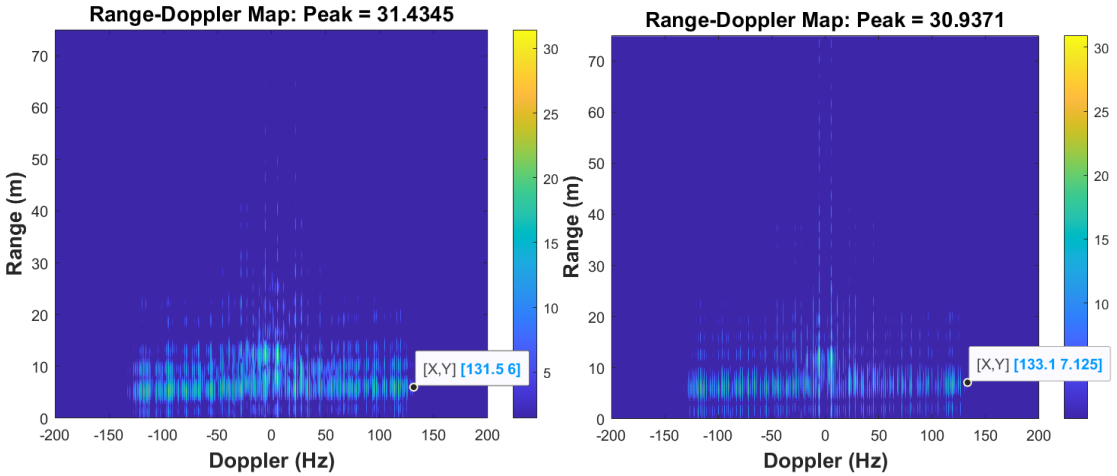

Figure 5.27: RDM of a Rotating Target; Fs 100 kHz (RHS) & 50 kHz (LHS)

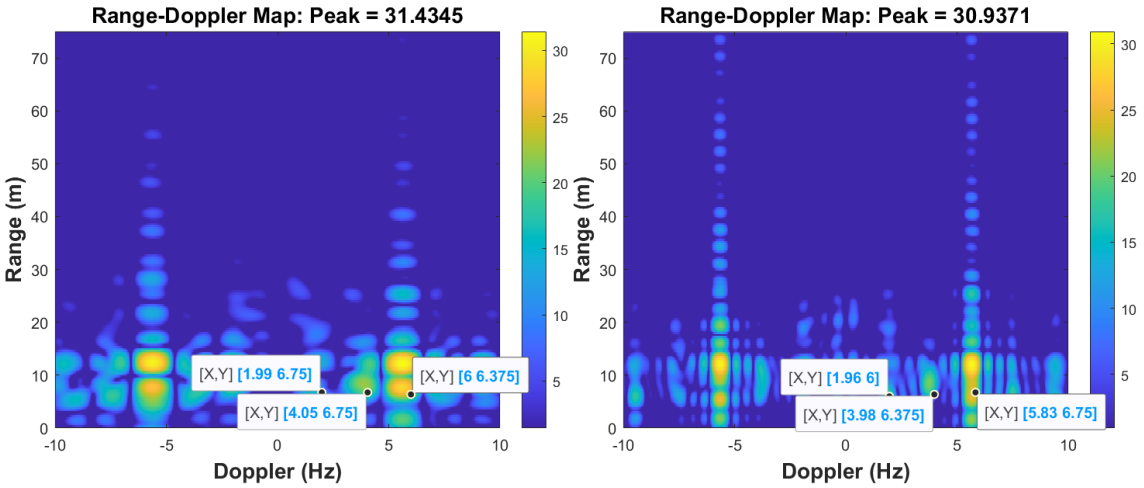

Figure 5.28: Zoomed in RDM; Fs 100 kHz (RHS) & 50 kHz (LHS)

Figure 5.27 is the RDM of a rotating target that demonstrates the Doppler tip of the blade and confirmed that the Doppler tip is about 132 Hz. Whereas Figure 5.28 is the closed up RDM that determines the rotational rate of the blade and revealed that the rotational rate Ω of the blade is 2 Hz. This Ω is determined by observing the interval between the two successive dots or lines in Figure 5.28. Figure 5.29 represents the Doppler cut of the rotating target and found out that the sideband is induced at a 0 Hz Doppler and the rotating scatterer spread over ±132 Hz. This ±132 Hz is considered the Doppler tip achievable. The amplitude from the micro-motion is higher than -15 dB, meaning that it will have a significant signature in STFT analysis.

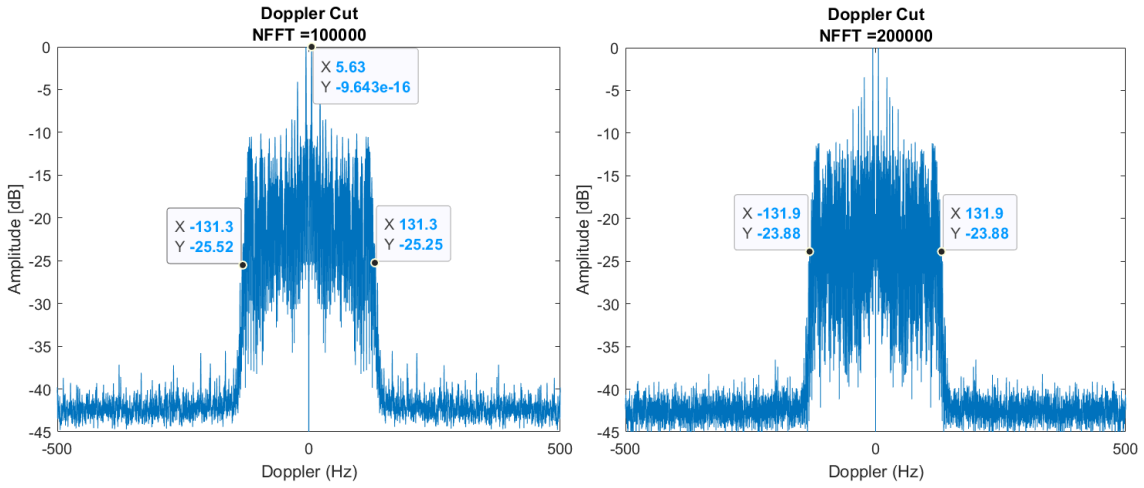

Figure 5.29: Doppler Cut of a Rotating Target; Fs 100 kHz (RHS) & 50 kHz (LHS)

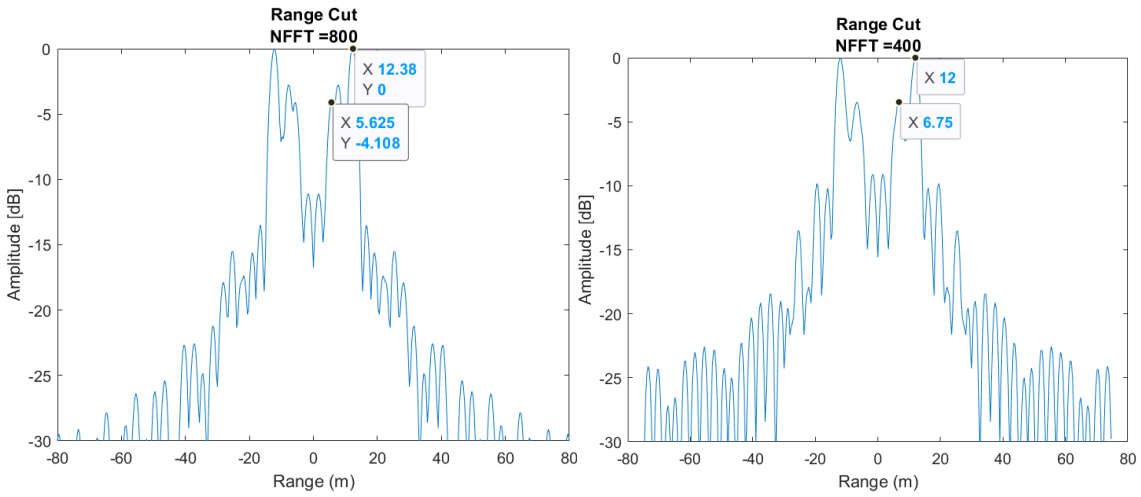

Figure 5.30: Range Cut of a Rotating Target; Fs 100 kHz (RHS) & 50 kHz (LHS)

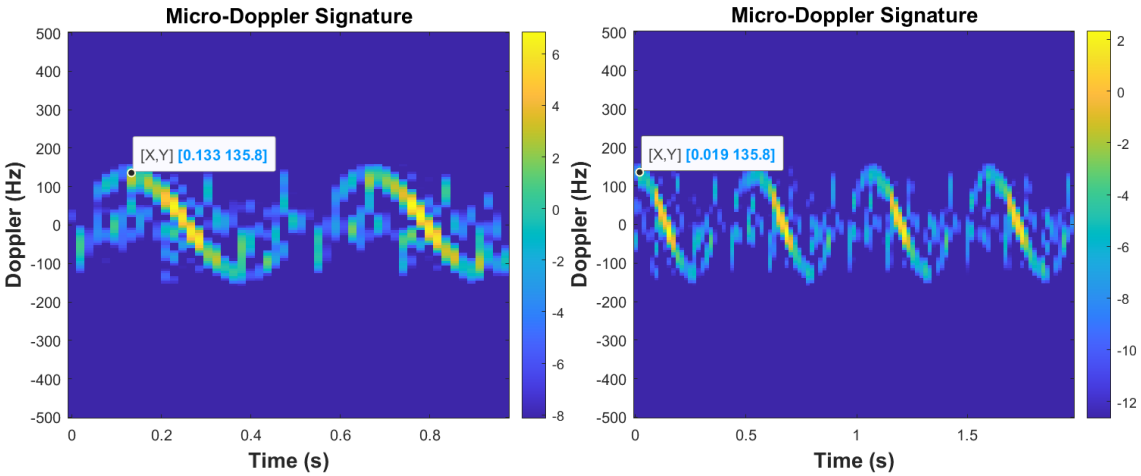

Figure 5.31: Micro-Doppler Signature of a Rotating Target; Fs 100 kHz (RHS) & 50 kHz (LHS)

The range cut in Figure 5.30, on the other hand, showing that the peak was not at 6 m away from the radar, but instead was 12 m away. Believing that the peak in the range cut was represented by the multipath signal instead of the echo from the target. The ground truth of the target was 6 m away from the radar. Lastly, Figure 5.31 is the time-frequency analysis of the micro-Doppler signature of the target. The window duration was 19 ms for both groups. It is noticeable that two complete cycles of periodical sinusoidal are present within 1 s and four complete cycles are present within 2 s which means that the rotational rate Ω of the blade of the target is 2 Hz.

Based on the discussion in the last chapter, it can be concluded that the minimum value of the ramp duration

$$T_{R_{min}} = \frac{1}{2f_{Doppler}} = \frac{\lambda}{4v_{radial}} \quad \textbf{(5-13)}$$

Where the v_{radial} in this case, is due to the rotational rate of the target.

$$v_{radial} = v_{tip} = 2\pi L\Omega \quad \textbf{(5-14)}$$

Where Ω is the rate of the rotor which is rotation in 1 second. By inserting equation (5-14) into equation (5-13), the rotational $f_{Doppler}$ of the blade target can be determined

$$2f_{Doppler} = \frac{8\pi L\Omega}{\lambda} = \frac{8\pi(0.65)(2)}{0.085} = 384.4 = 2(\pm 192.2Hz) \quad \textbf{(5-15)}$$

Hence, the minimum required for the ramp duration to avoid ambiguity is smaller than 2.6 ms, that is $T_{R_{min}} = \frac{1}{2f_{Doppler}} = \frac{1}{2(\pm 192.2Hz)} = 2.6\,ms$. So, it is advisable that T_R should be less than 2.6 ms to capture the signature at the right position and in this case, the T_R chosen was 1 ms that is good enough to see the micro-Doppler.

5.5 Case Study III: RC Helicopter

An almost identical scenario like the previous, an indoor experiment but with a rather smaller blade size is presented in this section. The target chosen in this case study is a remote-control (RC) helicopter, with two blades at the top and a smaller blade size at the tail of the helicopter. The target is positioned on top of the stand as in Figure 5.32. The length of the main rotor blade is approximately 18 cm (0.18m). Again, the wavelength of the radar is 8.5 cm. There are three possibilities of Doppler spectrum reflectivity from observation of this target which are from:

(i) the main body, with stronger energy return but low Doppler frequency

(ii) the main rotor blade, with lower energy return but higher Doppler

(iii) the tail rotor blade, much weaker return and usually higher Doppler frequency compared to the main rotor

Figure 5.32: Remote Control Helicopter

By using the TiePie HS5 oscilloscope, the sampling rate of 100 kHz with 100,000 samples was collected, resulting in a 1 s sequence recording. The data is stored in a block for every one second and this allows the author to observe the changes after a few seconds. The purpose of this experiment is to examine the effect of changing the rotational speed against the micro-Doppler signature. A measurement was collected when the target rotor blade is started to be slowing down. Figure 5.33 until Figure 5.36 presented the changes recorded during this motion state. It is noticeable that the tip Doppler of the target reduces slowly from the maximum speed in Figure 5.33 where the rotational scatterer spread across ±438.4 Hz in the RDM. The micro-Doppler signature in Figure 5.33 is visible even though it is unclear, but the maximum tip Doppler can be determined, which in this case is approximately ±421.5 Hz. And this verifies the RDM plot. Figure 5.34 shows that the rotational speed reduces to ±347.8 Hz in RDM and approximately ±346.5 Hz from the micro-Doppler signature. Then, a further declination of rotational speed was demonstrated in Figure 5.35, where the maximum Doppler achieved was ±296.3 Hz in RDM and ±298.9 Hz in the micro-Doppler plot. Less dispersion of rotational scatterer can be found in Figure 5.36, where the maximum of rotational Doppler was ±260.3 Hz in RDM and ±261.3 Hz found in the micro-Doppler signature.

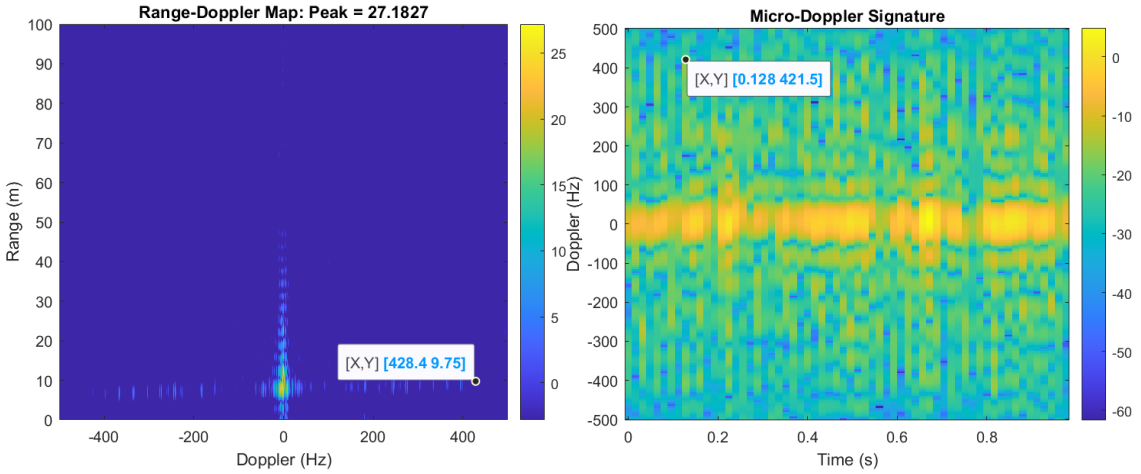

Figure 5.33: 6th Block Sequence of the Recorded Data

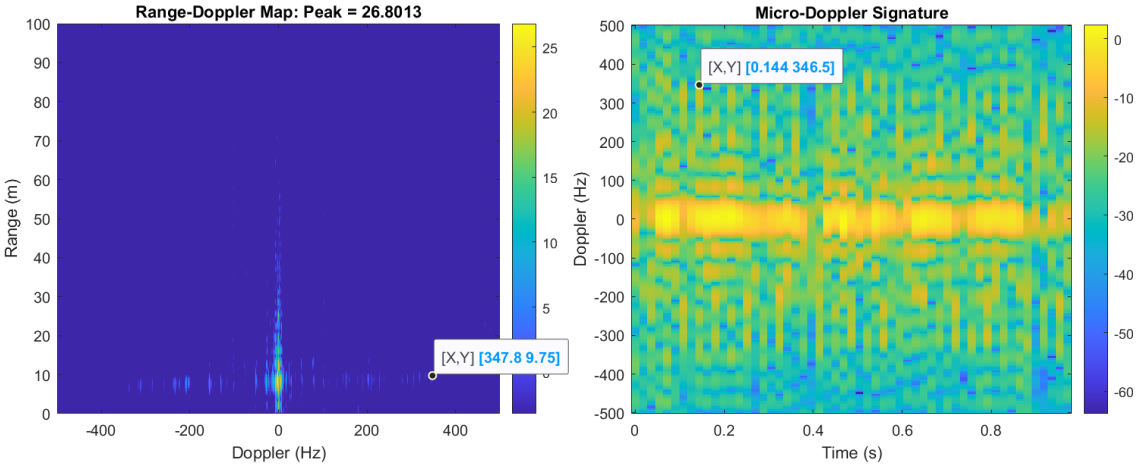

Figure 5.34: 10th Block Sequence of the Recorded Data

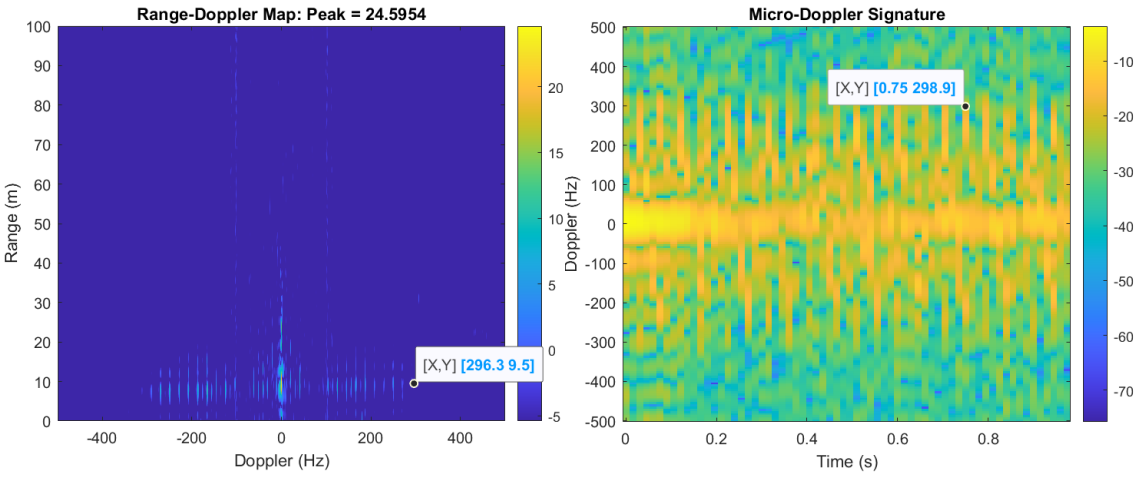

Figure 5.35: 16th Block Sequence of the Recorded Data

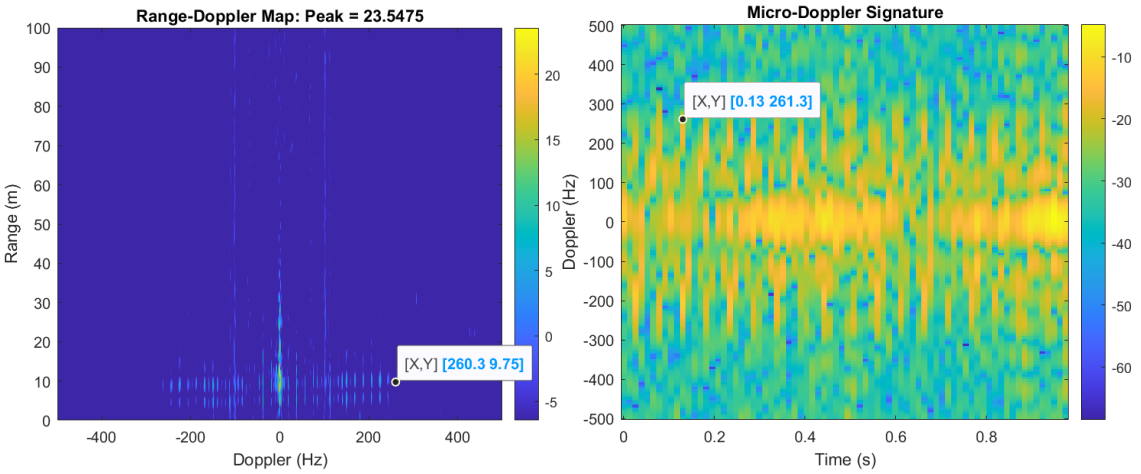

Figure 5.36: 20th Block Sequence of the Recorded Data

From the RDM, the peak of the target determines the location of the target. With that information, the range of the target is selected for micro-Doppler extraction. The tip Doppler spread in RDM presented in this case study is larger compared to the one-blade propeller which is approximately ±132 Hz, even though with a bigger blade size. This signifies that the rotational speed of the RC helicopter blade is much faster compared to the previous target.

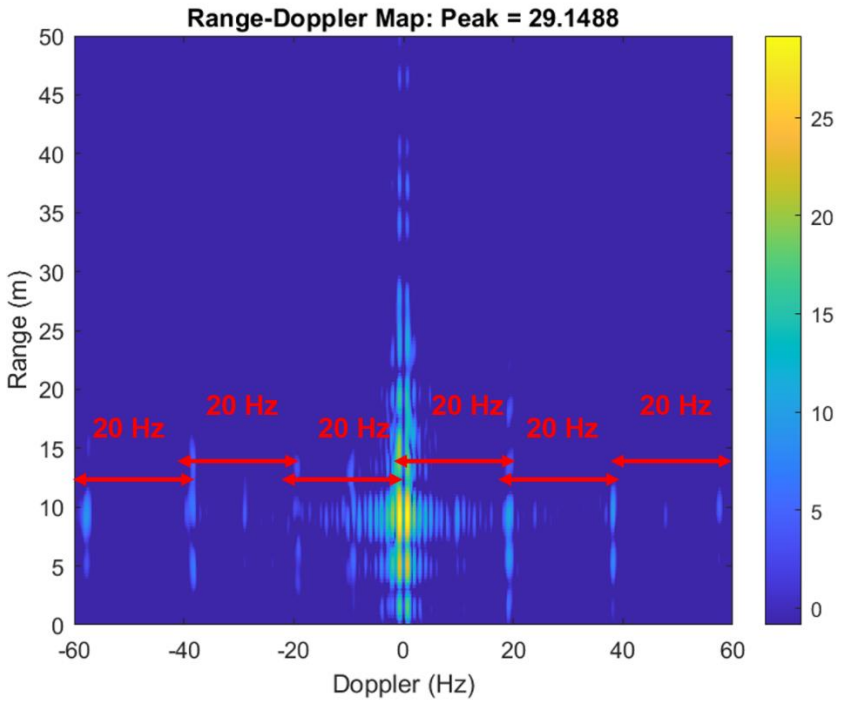

Figure 5.37: RDM Closed-Up of the Rotating Target. Integration time within 1 s.

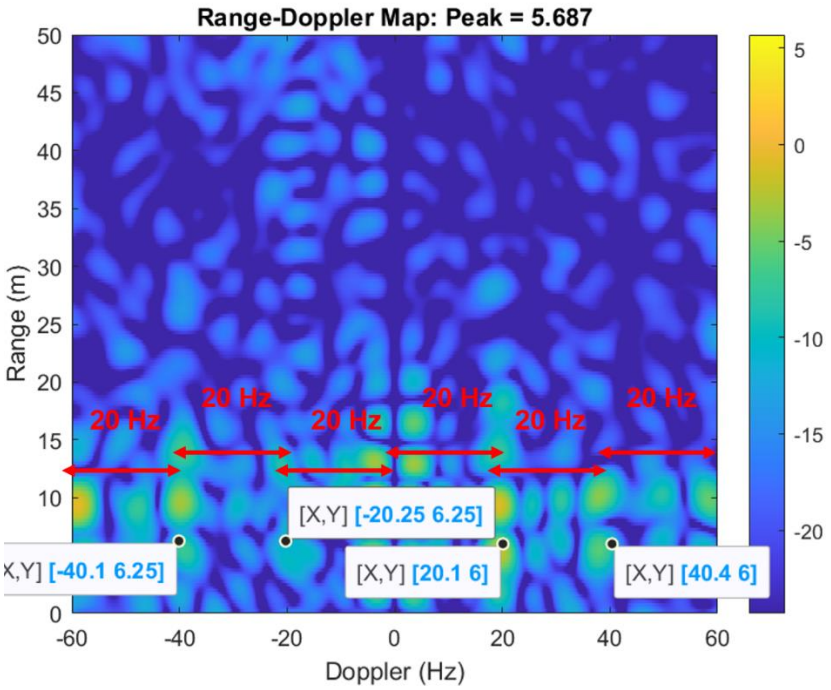

Figure 5.38: RDM Closed-Up of the Rotating Target. Integration time within 0.2 s.

Figure 5.37 is the RDM with an integration time of 1 s while Figure 5.38 with the same data but a shorter integration time of 0.2 s. The longer the integration time, the better the SNR. Both figures significantly show the rotational speed of the main blade is approximately 20Hz. The rotational rate of a blade target is defined by the frequency separation in the RDM map and divide by the number of blades in a propeller. The figure above shows the blade is approaching and receding simultaneously which indicates an even number of rotor blades. Then Figure 5.35 also illustrates roughly 20 blade flashes within 1 second which is similar to that RDM plot. The data is gathered in a duration of not more than 1 s so that the rotational speed can be determined in the micro-Doppler plot. However, if the rotational speed of the target is larger, then the blade flashes will become closer to each other and make it impossible to determine the number of blade flashes present. So, regarding this case, the integration time for the micro-Doppler analysis needs to reduce accordingly until the separation of the flashes become visible. From that, the rotational speed of the blade can be determined.

From equation (3-14), the minimum Doppler bandwidth required to avoid ambiguity is calculated as follow

$$2f_{Doppler} = \frac{8\pi L\Omega}{\lambda} = \frac{8\pi(0.18)(20/2)}{0.085} = 532.2\,Hz = 2(\pm 266.11\,Hz) \quad \textbf{(5-16)}$$

Where Ω is the rate of the rotor per blade within 1 second. Hence, related to this type of target, the required T_R to avoid ambiguity is not more than $T_{R_{min}} = \frac{1}{2f_{Doppler}} = \frac{1}{2(\pm 266.11\,Hz)} = 1.9\,ms$. Since the ramp duration chosen was 1 ms, which is smaller than 1.9 ms, the micro-Doppler signature can still be seen without ambiguity. Figure 5.33 shows that the tip Doppler (i.e. 428.4 Hz) almost reach the maximum bandwidth of the Doppler.

5.6 Case Study IV: Hexacopter

A relatively more complex target has been examined in order to observe the Doppler signature of the blade target. The drone consists of two pair blades on each of the six propellers. Each blade is 10 cm long. One of the propeller blades is wrapped with aluminium foil as in Figure 5.39, in order to get a stronger echoed signal compared to the other propeller. During the measurement, the drone was placed on the floor and allows to fly and hover in one place. Hence, the state of the drone mostly moved up and down, slightly swing left and right to stabilised it during hovering. The main body of the drone is basically vibrating and moving around.

Figure 5.39: Hexacopter Drone

The ramp duration is like the last case study which is 1 ms. The RDM of the rotating target is presented in Figure 5.40. The result shows that the interval separation between the lines is approximately 200 Hz which indicates the rotational blades of the propeller, where there is a repetition response visible in both positive and negative Doppler spectrum.

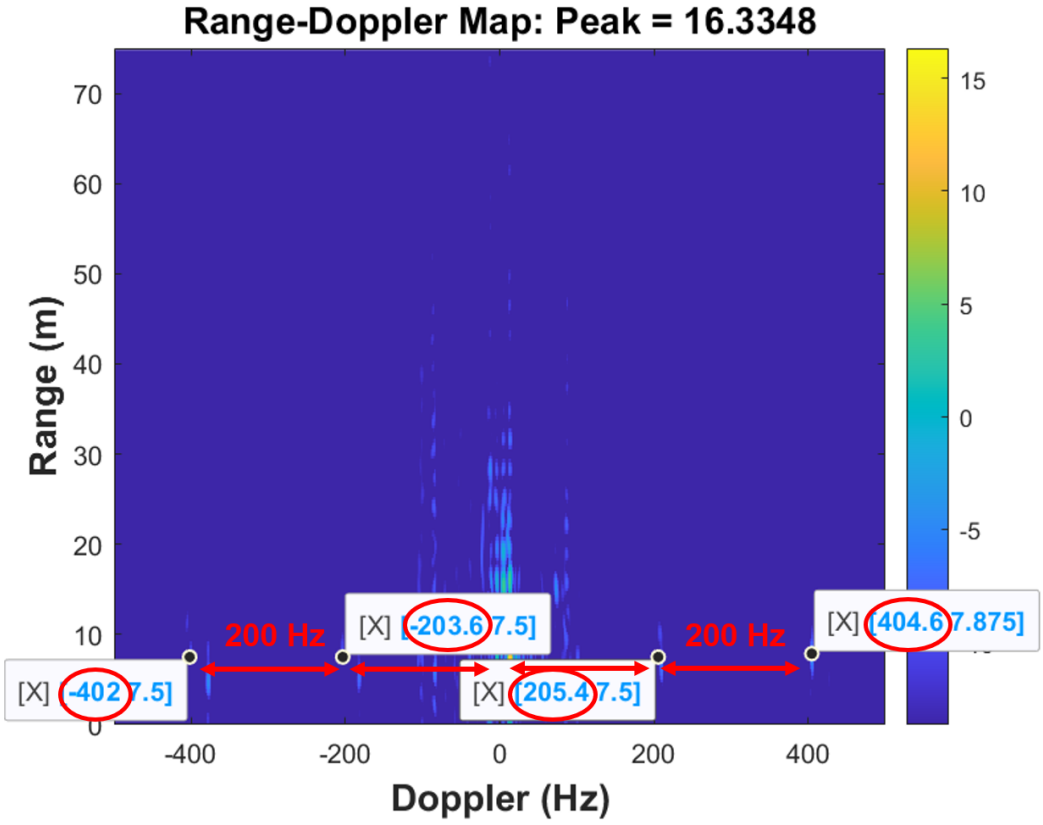

Figure 5.40: RDM of the Rotating Hexacopter

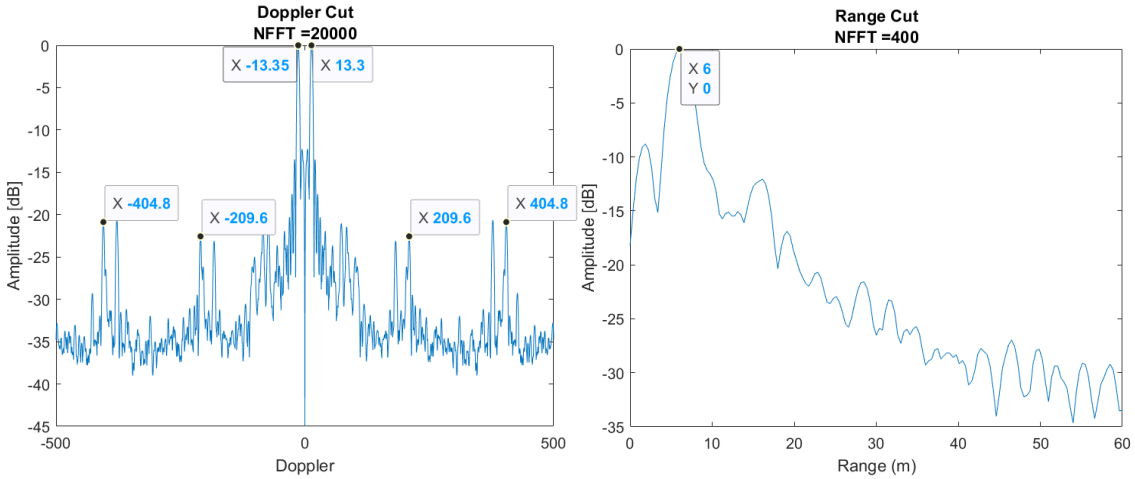

Figure 5.41: Doppler Cut (LHS) & Range Cut (RHS) of the RDM

Figure 5.41 is the Doppler cut and range cut of the RDM presented. During the data measurement, the drone is found to be 6 m away from the radar. The Doppler response at every $\pm m\Omega$ in the Doppler cut reflects the rotational rate at every $\pm m(200\ Hz)$, where m is the number of an integer. The Doppler return at $\pm 13.3\ Hz$ in the Doppler cut signifies the vibration of the main body of the drone since it is not stationary at one position. The frequency sampling was 50 kHz and 100-kilo samples, leading to a total integration time of 2 s. Figure 5.40 and Figure 5.41 shows a shorter integration time, 0.2 s. Whereas Figure 5.42 is a 1.4 s time integration at which the HERM lines are clearly visible at every $\pm m(200\ Hz)$. A few uniform line spectrums are visible centred at the frequency of the target. This corroborates the last plot which again represents the rotational blade of the propeller. The echo signal from the main body of the drone is stronger but mainly located at the zero Doppler region, while the echo signal from the blade is weaker but spread across the non-zero Doppler region.

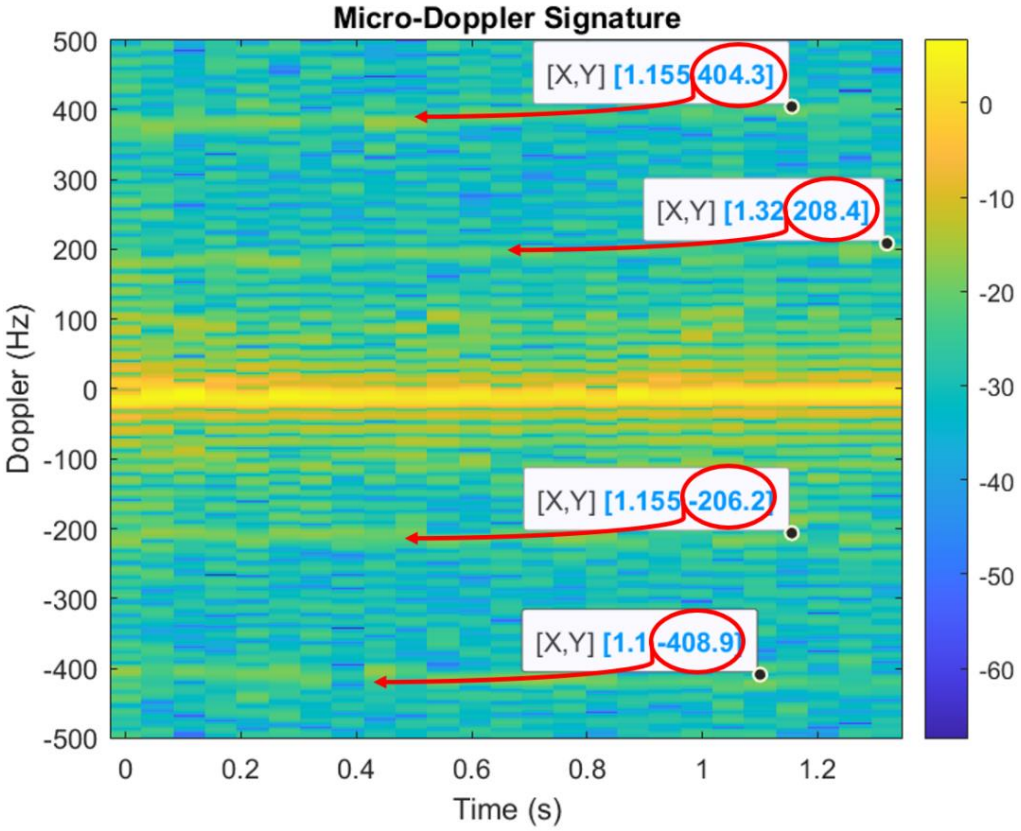

Figure 5.42: HERM lines of the Hexacopter

With the 10-cm long blade and the rotational speed of the blade is approximately 100 Hz. The v_{tip} can be calculated, $v_{tip} = 2\pi(0.1)(200/2) = 62.83\, m/s$. Hence, in order to examine the micro-Doppler signature in this case, the minimum requirement for $T_{R_{min}} = \frac{(0.085)}{4(62.83)} = 0.34\, ms$. Which in this case, because the T_R is 1 ms. So, it is insufficient to capture the blade flashes. The results summarized that the faster the rotational blade, the larger is the separation between lines in the RDM plot. The chirp duration T_r will determine the span of the Doppler axis in RDM and STFT plot (f_{span}= ±1/T_r).

All in all, the RDM helps in visualizing the state of the target's movement. It presents the connection between the distance, the radial direction of the movement with respect to the radar and the speed of the target. Throughout this research study, the transmitter and the receiver platform of the radar system are in a stationary state. So, let say if the target is in a stationary position, then the RDM will display a target response at the zero Doppler frequency bin. Meanwhile, once the target is moving relative to the radar and the radar is still in a stationary position, the RDM will display a target response at a non-zero Doppler frequency bin. The target can be detected in a varying range and varying speed. In the case of micro-motion presence, the Doppler will spread over with an interval separation between two consecutive dots which represents the rotational rate. And these dots spread over the Doppler towards the maximum Doppler which represents the velocity tip of the micro-motion. Apart from that, the RDM provides useful information in determining the position of the target by performing the peak detection in the range-Doppler profile. The detected target in a certain row is selected for STFT processing. The window duration is selected so that it is smaller than the duration of the peak-to-peak spectrum in RDM.

5.7 Summary

An S-band FMCW radar prototype has been successfully delivered. Minimum components are required using off-the-shelf components. This chapter presented that the removal of IQ demodulator from the FMCW prototype is possible and hence will reduce an additional cost to the radar. The only limitation of this is that it introduces a slight blind range which is equivalent to the range resolution of the radar. This limitation is to avoid overlapping phenomena between positive and negative spectrums. The value of this limitation, however, is manageable by selecting the bandwidth accordingly. The bigger the bandwidth, the smaller the range limitation.

A wide range of measurements with different types of targets has been demonstrated. And the results show very good consistency with the expected outcomes. The first test was on a larger target to investigate the response of the radar towards the Doppler shift. And the results corroborate with the theoretical concept presented in Chapter 3. Then, more extended experimental tests have been investigated on rotary objects to observe the prototype response towards the target. Started with the one-blade propeller, the radar can detect and determine the rotational rate, velocity tip and maximum Doppler frequency of the blade. After that, a remote-control helicopter is observed, and the properties of the blade are extracted as previous. The last observation was on a hexacopter drone. The HERM lines are visible from the micro-Doppler plot. All these evaluations suggest that the S-band prototype developed is working as expected.

6 K-BAND FMCW RADAR DESIGN

So far, we have investigated in detail the design and development of an S-band prototype. The purpose of the S-band prototype is to deliver an initial low-frequency FMCW radar demonstrator that will supply knowledge of the FMCW design steps for the next stages of research at a higher frequency. This chapter will mainly describe the design and development of a 24 GHz K-band (i.e. a wavelength of 1.25 cm) prototype. The RF components of the prototype have a large frequency bandwidth making it more flexible and versatile. The central frequency, frequency bandwidth, ramp duration and time integration can be altered and modified according to the intended performance. By increasing the operating frequency means decreasing the wavelength and narrowing target resolution. Hence, a higher frequency band provides better close-range detection for a smaller target especially in this case the target is less than 5 cm in size. A set of experimental trials were carried out in order to validate the designed and developed prototype. Then, a nano-drone have successfully detected, and the results measurement presented in this sub-section are reported in [104].

6.1 K-Band FMCW Architecture

A K-Band FMCW radar was developed at Cranfield University, Shrivenham campus using off-the-shelf connectors components. Figure 6.1 shows the block diagram of the developed prototype radar system and Table 6.1 lists the components that were used in more detail. The transmitted signal, generated with an AWG, is a built-in sawtooth standard waveform with a chosen repetition frequency, amplitude and offset as pictured in Figure 6.2. The AWG output is connected to a Voltage Control Oscillator (VCO) so that the RF output frequency varies linearly with the control voltage input (V_{Tune}). The power of the VCO output signal is also controlled with the input voltage supplied (V_{CC}). This RF signal is then split by the Power Divider (PD) into two signals, one is carried forward to the transmitting antenna and the other is used as a replica of the

transmitted signal to drive the double-balanced mixer. The block diagram of the K-band prototype is specular to the S-band prototype presented in Chapter 5. Once the signal propagates to the target and is reflected, the signal captured by the receiving antenna is first amplified with an LNA to contain the thermal noise and then multiplied with a copy of the transmitted signal. The output of the mixer is the beat signal which has been discussed in Chapter 3. This is the core output that carries all information on the target. The beat signal is first low-pass filtered (LPF) before being digitised through a TiePie oscilloscope and stored in the PC for further analysis in MATLAB.

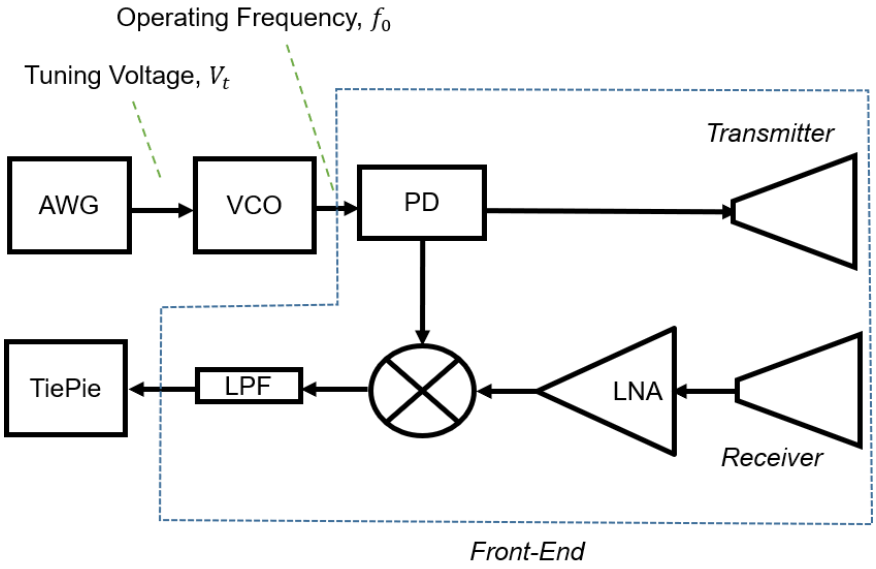

Figure 6.1: A Block Diagram of K-Band Prototype

Table 6.1: The Details of Each Radar Components

COMPONENTS	Frequency Range	MODEL NO	Company	Cost ($)
VCO (P_{Output}: +8dBm)	23.8 – 26.8 GHz	112261-HMC739LP4	Digikey	511.26
MIXER (P_{LO}: +11dBm)	8 – 32 GHz	MM1-0832HS	Marki Microwave	595.00
LOW NOISE AMP	20 – 36 GHz	HD30172	HD Communications	980.00
POWER SPLITTER	18 – 26.5GHz	ZC2PD-18263-S+	Mini-Circuits	266.95
LOW PASS FILTER	DC – 45 MHz	VLF-45+ LTCC	Mini-Circuits	26.95
K CABLES (2pcs)	DC – 40GHz	E40- KMKM+1M-	Mini-Circuits	313.44
K CONNECTORS (4pcs)	DC – 40GHz	KM-KM50+	Mini-Circuits	207.92
			TOTAL	2901.52

Because the VCO can operate over a wide frequency bandwidth, the prototype provides unique flexibility to gather measurements over user-selected carrier frequencies from 23.8 GHz until 26.5 GHz. Two identical rectangular horn antennas with an aperture of 40 x 50 mm were used on transmit and receive both with the same antenna gain of 18 dBi. However, the connectors prototype provides the user with full flexibility to change and operate different antenna sets. The radar propagation operated at a far-field radar. The radar far-field R_{ff} can be determined by

$$R_{ff} = \frac{2D^2}{\lambda} \quad \textbf{(6-1)}$$

and depends on the largest dimension of the antenna, the target size and the carrier frequency. A range R is considered in the far-field if it is larger than R_{ff} and it is considered in the near-field if R is less than R_{ff}. In this case, D^2 is 25 cm^2 and the λ is 1.25 cm (i.e., the operating frequency is 24 GHz), hence leading to a R_{ff} on transmit of 40 cm.

The following sub-sections below describe the radar system components employed in the radar prototype and the performance parameters taken individually; AWG, VCO and LNA.

6.1.1 Keysight Waveform Generator 33600A

The starting point of any radar is signal generation. An electronic device waveform generator is used to deliver the baseband signal. With a ramp waveform chosen, three parameters of the AWG input will ultimately determine the RF transmitted ramp signal. The list of the parameters are as follows;

i. The frequency of AWG will translate in the value of the ramp duration T_r by the reciprocal of the repetition frequency.

ii. The amplitude of AWG will translate in the value of the RF frequency bandwidth, the voltage peak-to-peak V_{pp}.

iii. The offset of AWG will determine the position of the RF signal spectrum in the frequency range. When a constant voltage is added to the signal, it increases the mean level and vice versa.

The amplitude and the offset do not change the shape of the waveform. But it controls the value of the waveform. Figure 6.2 illustrates the interface of the AWG with these three input parameters. A sawtooth waveform is chosen for the whole experimental work and the specific AWG parameters are listed in Table 6.2.

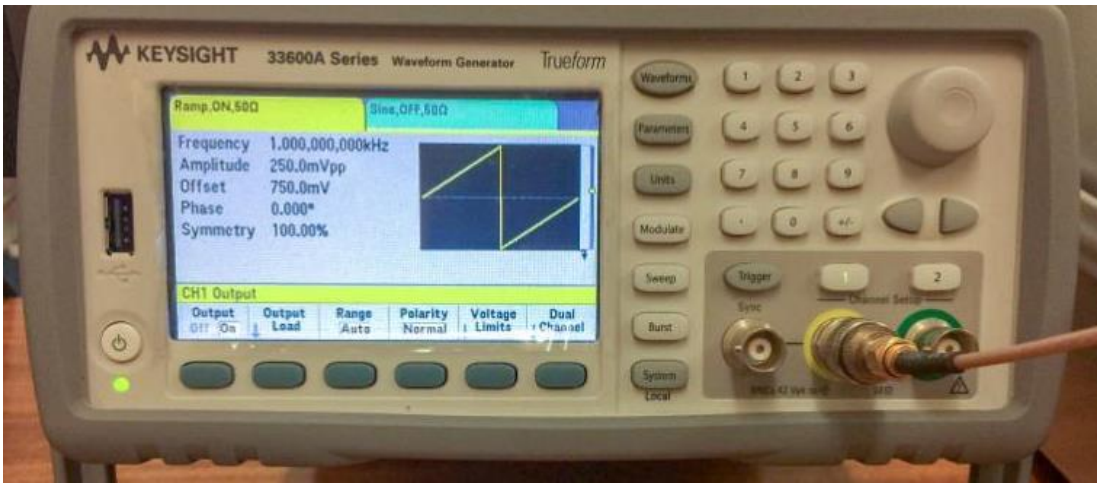

Figure 6.2: KEYSIGHT 33600A Waveform Generator

So, the carrier frequency varies according to the modulating signal. Once the signal is generated, then it is amplified and shifted to an RF signal by the VCO.

6.1.2 Voltage Controlled Oscillator, VCO

The VCO, which is coupled to the main circuit, plays a role in translating a DC signal into an RF waveform. By inputting a varying DC level, results in a change of phase, which is related to a change in frequency. The HMC739LP4, as in Figure 6.3, is a chip integrated with a varactor diode which is responsible to modulate the frequency by tuning the voltage from the function generator.

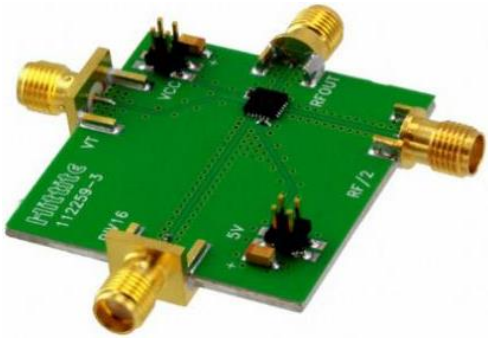

Figure 6.3: Analog Device HMC739LP4 / 739LP4E

A schematic diagram is given in Figure 6.4. It has one input for control voltage input V_{tune} and three RF outputs (i.e. main RF, half of the RF, and another pre-scaler of RF which is divided by 16). The V_{tune} range of the device is in between $0V$ to $+15V$ and was connected to the Keysight Waveform Generator as a modulation port bandwidth. Then, this VCO requires a voltage supply V_{cc} of $+5V$. The power supply is either connected to pin number 20 (in Figure 6.4) for the RF output signal or connected to pin number 4 for a pre-scaler output signal. This evaluation circuit board is manufactured by Hittite which is part of Analog Devices.

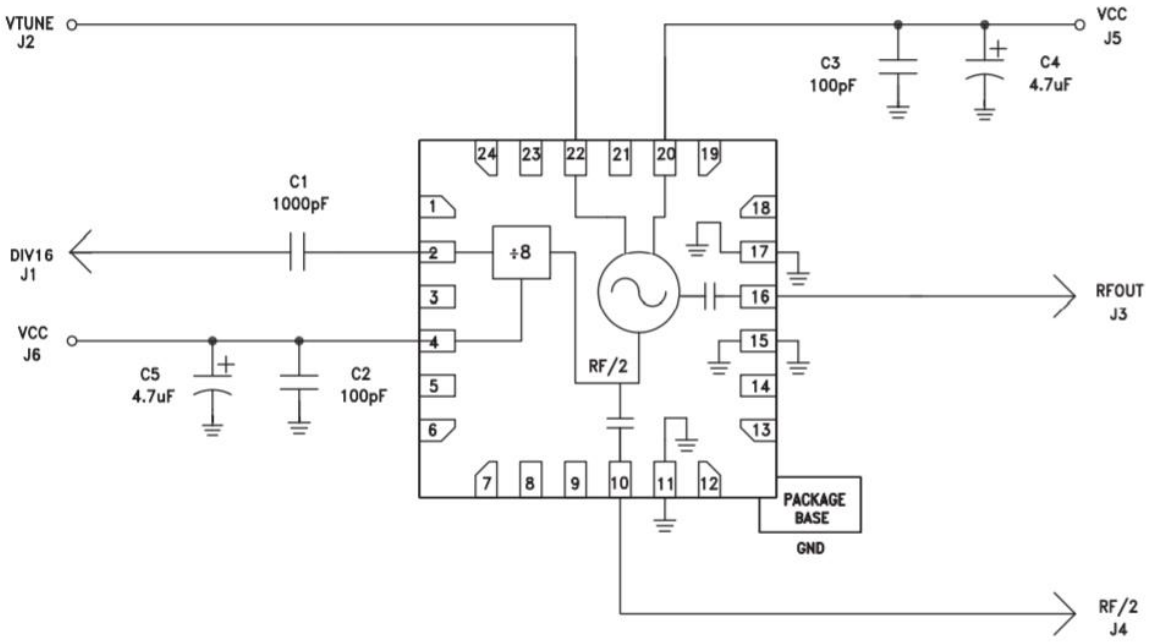

Figure 6.4: Schematic Diagram of VCO HMC739LP4 / 739LP4E [105]

The following setup in Figure 6.5 was arranged in order to verify and assess the performance of the VCO. The generated signal from the Keysight waveform generator VCO was first connected to the input of the VCO at pin number 22 (referring to Figure 6.4). At the same time, the VCO is power supplied by a GW INSTEK GPS-4303 to activate the component. The signal output of the VCO is then connected to the spectrum analyzer in order to check the sensitivity of the device, especially the RF frequency and the output power when it is tuned by the waveform generator. The phase noise stated by the supplier was -93 dBc/Hz @ 100 kHz. The lower the phase noise, the better the device performance. The output response in Figure 6.6 is then compared with the datasheet provided by the supplier and shows the agreement between the comparison.

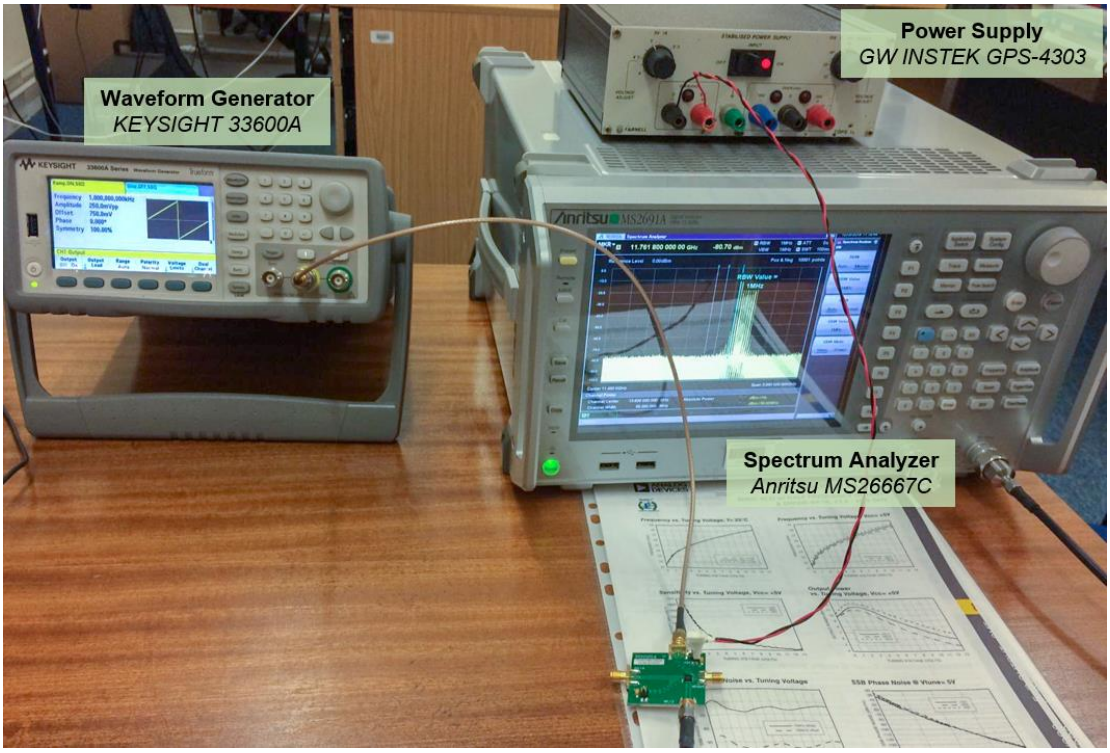

Figure 6.5: Verification of VCO Component

One of the prime limitations of this VCO is the linearity of the chirp which can be seen in Figure 6.6. This limitation is a common problem with the FMCW systems. It is shown that from 0 V to 3.5 V, the VCO response is nonlinear. This non-linearity will degrade the range resolution. To address this matter, local

points are selected locally that could deliver an almost perfectly linear chirp for the prototype. Hence, it is not ideal to optimise the bandwidth.

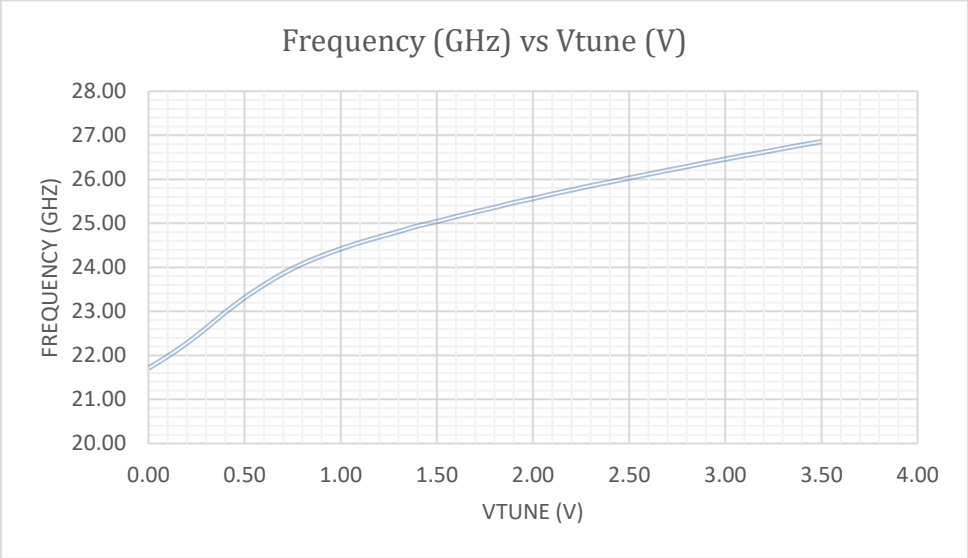

Figure 6.6: Output Response of the Signal

The centre offset is positioned at 1.3 V in Figure 6.6, and oscillate at both sides of ±200 mV from the centre. The starting point of V_{tune} at 1100 mV corresponds to the frequency 1 at 24.58 GHz. And the end point of V_{tune} at 1500 mV is corresponding to the frequency 2 at 25.06 GHz as listed in Table 6.2. The table below summarized the key parameters that are inserted in the AWG, resulting in the radar signal parameters later on.

Table 6.2: AWG Parameters for the Experimental Work of the Bearing Spheres

Arbitrary Waveform Generator	Description
Shape	Sawtooth
Frequency	2 kHz
Amplitude	400 mV
Offset	1300 mV
Radar Signal	**Description**
Ramp Duration	0.5 ms
Frequency 1	24.58 GHz
Frequency 2	25.06 GHz
Bandwidth	480 MHz

The main reasons that the frequency range was chosen are because, (i) at that bandwidth, the chirp induced is linear and (ii) the output power from VCO is sufficient to drive the double-balanced mixer, which requires a minimum of +11 dBm. At this frequency range, the VCO output power was averagely at +13 dBm. The radar bandwidth can be extended to a higher frequency range as long as it shows a linear response. And a power amplifier may be required before the LO mixer for signal amplification. However, because the prototype needs to keep to the minimum cost, so in this case, the frequency range with the highest power output from the VCO was selected.

6.1.3 Low Noise Amplifier HD30172

The LNA was procured from HD Communication Corp. The device can operate within a wide frequency bandwidth from 20 GHz until 36 GHz. Figure 6.7 illustrates the LNA with a gain of 24 dB and a noise figure of 3 dB. Even though the gain is high, one needs to be aware of output power saturation effects and adjust the absolute maximum input power accordingly. In this context, the absolute maximum rating of output power is +13 dBm and the absolute maximum rating of input power is +5 dBm. Hence, a high gain of 24 dB will be useless if the input power is already high enough (i.e., more than +5 dBm).

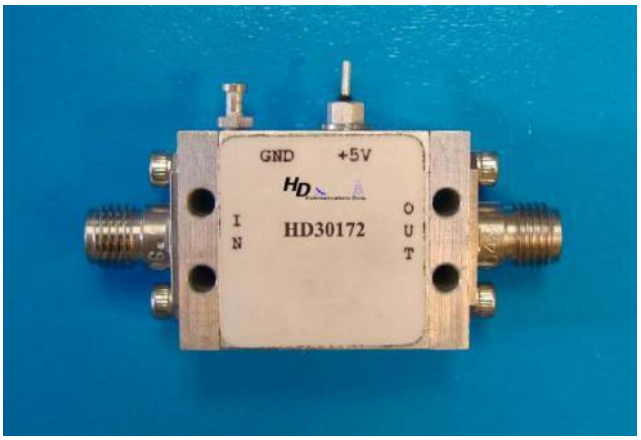

Figure 6.7: Amplifier HD30172

6.2 Prototype Evaluation

A closed-loop feedback circuit measurement is performed before the experimental measurement. The purpose of this measurement is to evaluate the reliability of the setup and verify the system accuracy altogether. This is performed by connecting the transmitter to a delay line, and the delay line is then connected to the receiver. Both transmitting and receiving antennas are excluded in this setup. Cables of different lengths were used as delay lines to measure the capability of the radar to measure the range target. The longer the delay, the higher value of beat frequency return, and the further the range of the processed signal. In this context, the distance that will be measured is half of the cable length to account for the two-way propagation through the medium. The frequency increased linearly from 24.12 GHz to 24.71 GHz within 1 ms, leading to a bandwidth of 590 MHz. Hence, the range resolution of the radar was 0.25 m and it is also considered as a blind range of the system. The radar can measure the range correctly if the range (that is, the delay lines) must be greater than the range resolution. The data was collected with a sampling rate of 1 MHz.

Figure 6.8 presents the result of the delay measurements for different cable lengths. Three 1-m long cables were used and connected to each other with MM-SMA connectors to obtain a 2 m delay and a 3 m delay. So, the longer the intended delays, the more the connectors that are being used. This could probably affect the increasing error below as the length of the connectors were not included in the calculation. The estimation of the delays is presented in Table 6.3. The error may reduce if a 2-m long cable and a 3-m long cable is used instead of several 1-m cables.

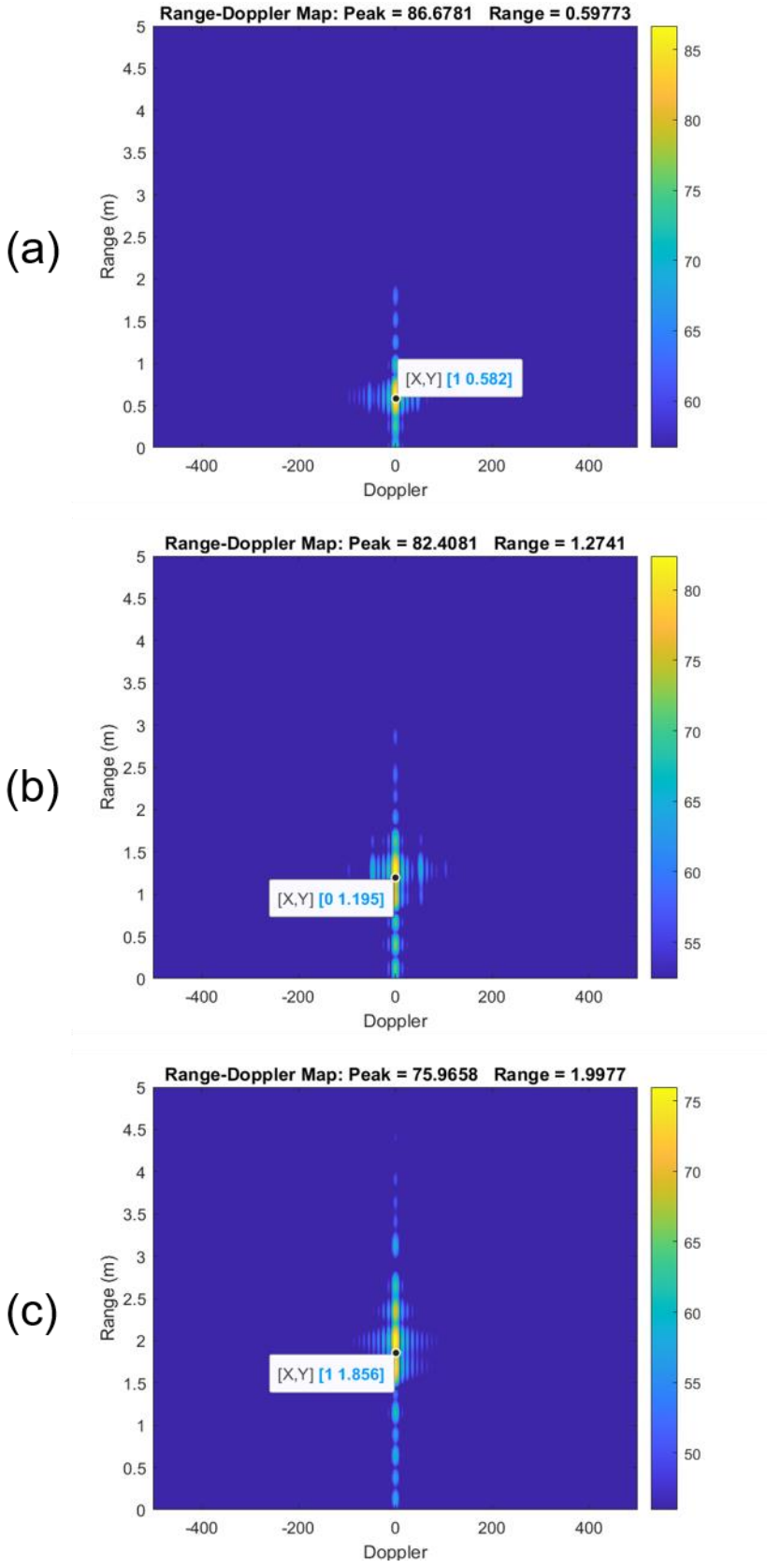

Figure 6.8: Response from Different Cable Length; (a) 1 m Long Cable, (b) 2 m Long Cable and (c) 3 m Long Cable

Table 6.3: Evaluation of the Delay Lines

DELAY CABLE	CALCULATED	MEASURED
1 m	0.500 m	0.582 m
2 m	1.000 m	1.195 m
3 m	1.500s m	1.856 m

6.3 Detection of Small Size Sphere

An experiment is carried out using a wide range of different sizes of bearing steel spheres of known RCS. Aiming at targets with a size of 5 cm and below, these spheres are being observed to assess the radar. The sphere was attached and suspended with a thin fishing line. Then, the measurements are taken for each of the spheres (1) in a stationary position, (2) oscillating from front to back and then (3) oscillating from side to side. Five different spheres are being evaluated each with a diameter of; $S_1 = 3.5\ cm$, $S_2 = 3.3\ cm$, $S_3 = 2.4\ cm$, $S_4 = 1.5\ cm$, and $S_5 = 1.0\ cm$. The measurements of each sphere are illustrated in Figure 6.9. The low power K-band FMCW system that has been developed is used in this test in order to detect and observe the Doppler response by these small targets and investigate return amplitude differences between targets of known RCS. The data were collected by TiePie and stored in the computer for further assessment. The sampling frequency used was 500 kHz and 2 s of data were recorded (1,000-kilo samples). The frequency sweep from 24.58 GHz to 25.06 GHz, leading to a range resolution of 31.25 cm.

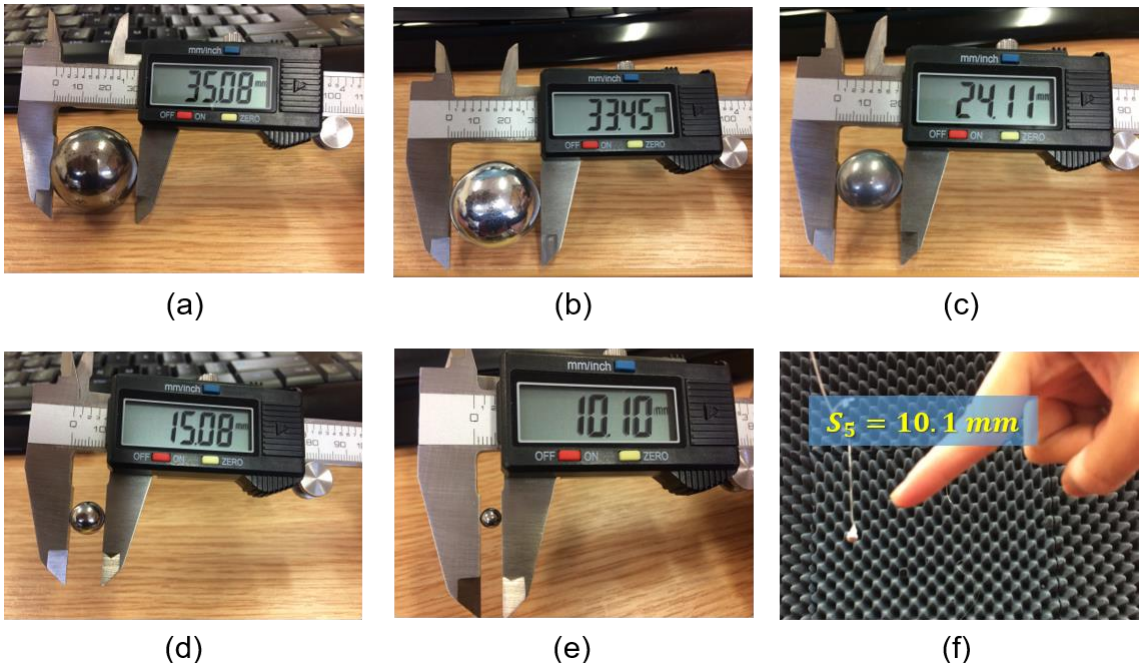

Figure 6.9: The Measurement of Different Size of Spheres; (a) S_1 (b) S_2 (c) S_3 (d) S_4 (e) S_5 (f) The Smallest Size S_5

As introduced in Chapter 2, the RCS region of a sphere RCS_{Sphere} is determined by its ratio between radius and wavelength. If the target is defined in the optical region, then the RCS_{Sphere} is estimated as follows

$$RCS_{Sphere}(m^2) = \pi r^2 \quad \textbf{(6-2)}$$

$$RCS_{Sphere}(dB) = 10 \log (\pi r^2) \quad \textbf{(6-3)}$$

where RCS_{Sphere} depends on the r radius of the sphere. A simple rule of thumb for RCS is that, in the optical at a fixed frequency, the smaller the size of the sphere, the lower is the RCS_{Sphere}. However, in this case, with the reference of operating frequency at 24.58 GHz, the ratio of the circumference of a target to the wavelength is within the Mie region as shown in Figure 6.11. The RCS_{Sphere} of all the targets are listed in Table 6.4. It is found out that these RCS_{Sphere} of bearing balls are within the range of -30 dBsm to -40 dBsm at 24.58 GHz frequency.

Table 6.4: Size and RCS of the Targets

Sphere	Size (mm)	Radius (m)	Ratio $2\pi r/\lambda$	Ratio $RCS/\pi a^2$	RCS $(m)^2$	RCS (dBsm)
S_1	35.08	0.01754	9.030	0.92	$9.665\ x\ 10^{-4}$	- 30.50
S_2	33.45	0.01673	8.610	1.04	$8.793\ x\ 10^{-4}$	- 30.40
S_3	24.11	0.01206	6.206	1.06	$4.569\ x\ 10^{-4}$	- 33.16
S_4	15.08	0.00754	3.882	1.02	$1.786\ x\ 10^{-4}$	- 37.39
S_5	10.10	0.00505	2.600	1.18	$8.012\ x\ 10^{-5}$	- 40.25

Table 6.4 shows that S_1 and S_2 almost have a similar size, however, there are large differences in weight. S_1 is far much heavier than S_2. Then, the size of S_5 sphere is much smaller than the radar wavelength λ (i.e., 1.22 cm). Figure 6.9(f) depicts that this sphere was far much smaller than a fingertip. The S_5 is almost weightless, when hanging from the string, it is almost floating and does not put any weight down towards the floor. This makes the oscillation less controllable. Figure 6.10 shows the comparison of the spheres with different sizes and different material compositions which results in different weights of the target and Figure 6.11 shows the RCS_{Sphere} distribution of the targets considered in the experiment.

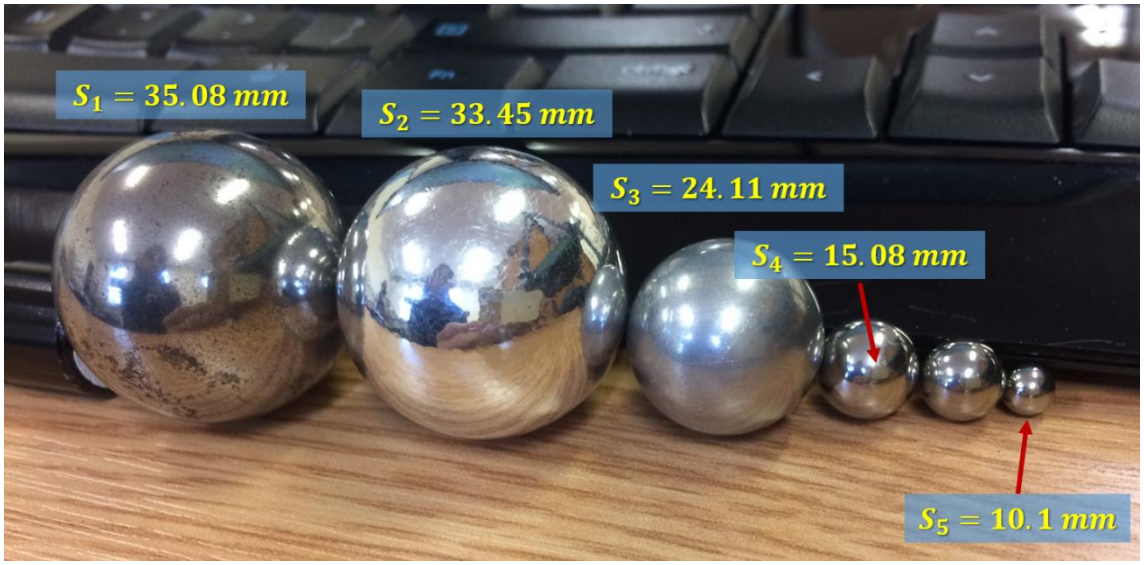

Figure 6.10: Comparison of Different Size of Spheres

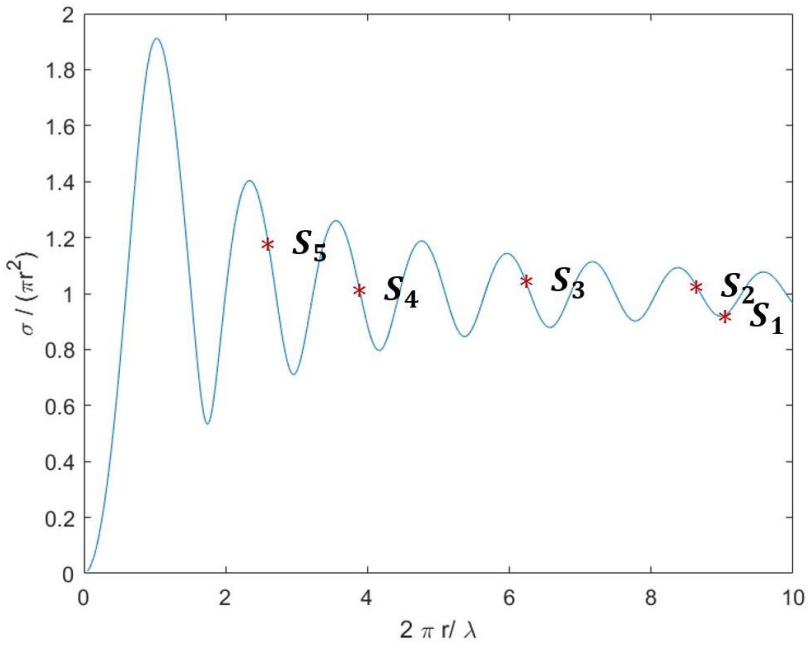

Figure 6.11: The Targets Distribution within the Mie Region

An indoor experimental setup of a K-band radar system with the spheres as a target is arranged in the lab. It is important to note that, the room is shared between two labs. During data measurement taken, the other lab was actively being used as well, so there is some possibility of unwanted longer-range reflections coming from the other side of the lab. Two different polarisations for the horn antennas were used which are HH and VV. HH is where both the transmitting and receiving antenna transmit and receive the signal in a horizontal polarization, while VV is both are vertically polarized. The co polar of HH and VV are predicted to give the same signal return from the spheres. A diagram of the radar prototype with the horn antennas is pictured in Figure 6.12. The target detection approach is based on extracting the Doppler shifts through two times FFT and STFT techniques which were described in Chapter 4. Two different scenarios of sphere ball experiments will be demonstrated in the following sub-section; one is the detection of a single moving target and another one involves multiple moving targets.

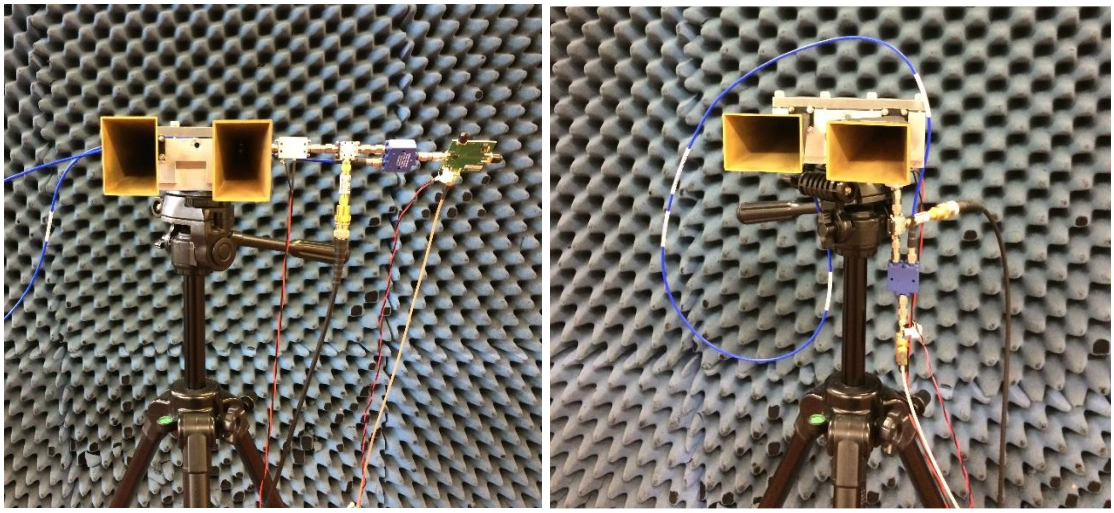

Figure 6.12: HH (Left) and VV (Right) Polarization

6.3.1 Detection of Single Target Sphere

Each sphere was suspended 1 m above the ground with the thin fisher line and it was positioned 3 m away from the radar. A Radar Absorbing Material (RAM) panel was placed 1 m away behind the sphere and another RAM panel was placed behind the radar prototype in order to reduce multipath signals in a confined space. The measurement cycles consisted of the following procedures;

(i) noise measurement was taken by disconnecting the transmit cable from the transmit horn antenna (the power supply was switched on so that the radar system is in switched on mode without signal transmitting any frequency)

(ii) a background measurement was taken with the radar completely connected, power supply and signal source were switched on with no target in the scene

(iii) one sphere ball was placed in the line of sight of the radar, the ball was in a stationary position

(iv) the sphere ball was then swung from front to back oscillation

(v) lastly the sphere ball was swung from side to side oscillation

Step (iii) to (v) was repeated with each different size of sphere balls and were recorded individually. The raw data was stored by the TiePie oscilloscope - in MAT file for further analysis.

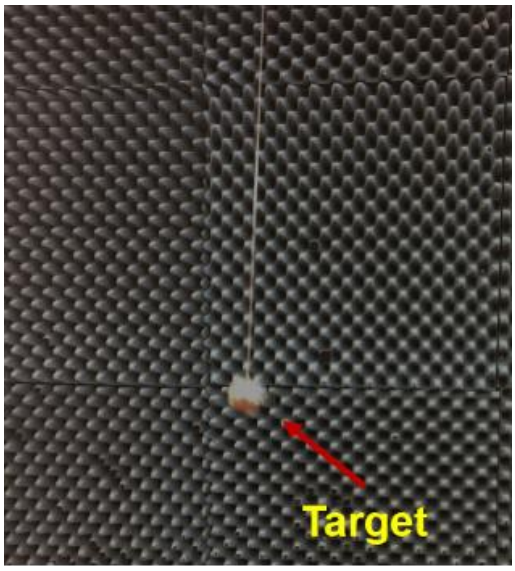

Figure 6.13: Single Target of Sphere Ball

Noise & Background Response

Every time each of the polarization of the waveform was changed, the noise and background measurement was taken. This is to ensure that at that particular time, there is no new spur noise and new interference arises. This is to make sure that each of the polarization sets of measurement is in the same conditions. The RDM was obtained by integrating 120 chirps received by the TiePie oscilloscope and zero-Doppler removal was applied. The integration time was 0.06 s leading to a theoretical Doppler resolution of 16.67 Hz. Figure 6.14 and Figure 6.15 represents the noise response of each of the polarisation. Both figures show that there are no significant noise differences and the level of the peak noise was about -21 dB to -22 dB within the integration time. From the peak noise that was identified in the RDM plot, the range bin of that particular point was selected. The normalized amplitude of the range cut also proves that the random noise is within 0 dB to -5 dB altogether and no significant noise arises than predicted.

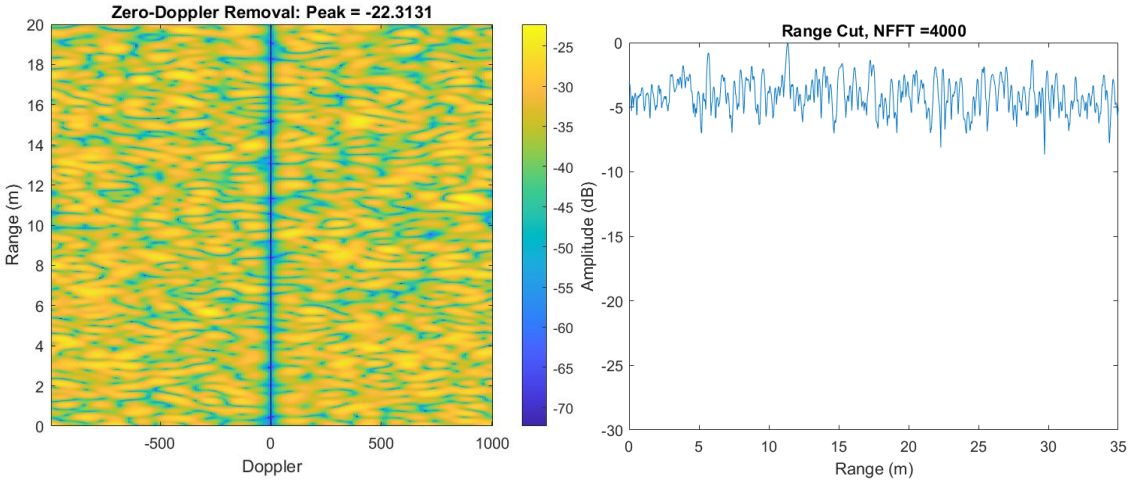

Figure 6.14: HH Polarization - Noise Response

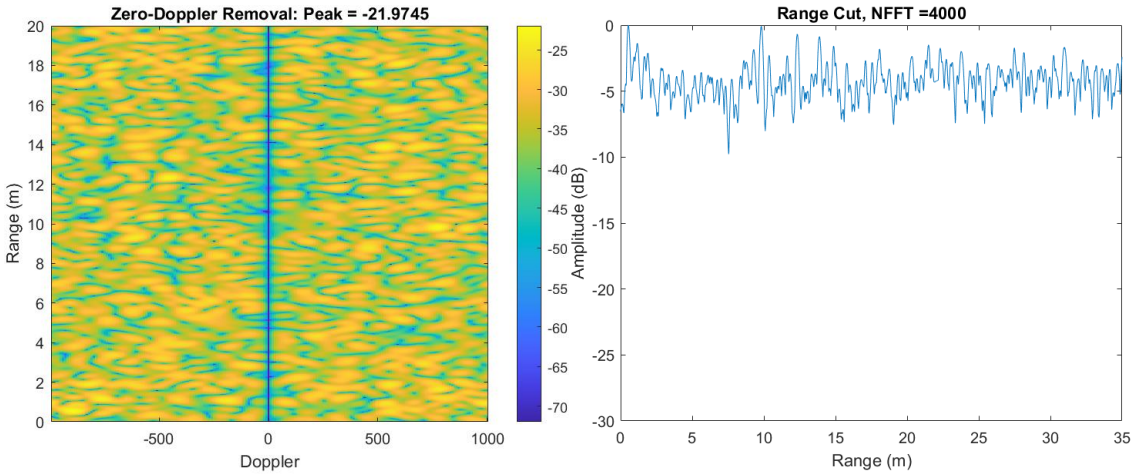

Figure 6.15: VV Polarization - Noise Response

Figure 6.16 and Figure 6.17 are the background response of the laboratory room where the measurements were actively taken. At this point, the signal was transmitted, and the purpose of this evaluation is to verify any potential of radar clutter that will disturb the echo signal of a target and cause a false alarm. The plots show that the background is very clean except for the coupling. From both observations, it is apparent that there is a peak return is at 0 Hz and 0 m which is caused by the results of miss-matched self-mixing signal, and antenna coupling. In this case, the minimum blind range is the range resolution of the prototype, i.e., 31.25 cm. The radar will then measure the correct range once it does not overlap between the left and right lobes.

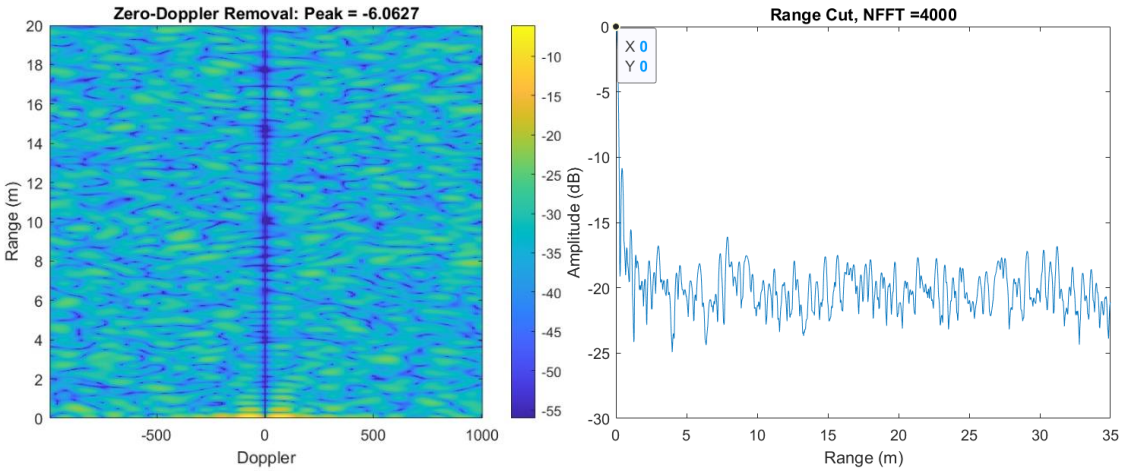

Figure 6.16: HH Polarization - Background Response

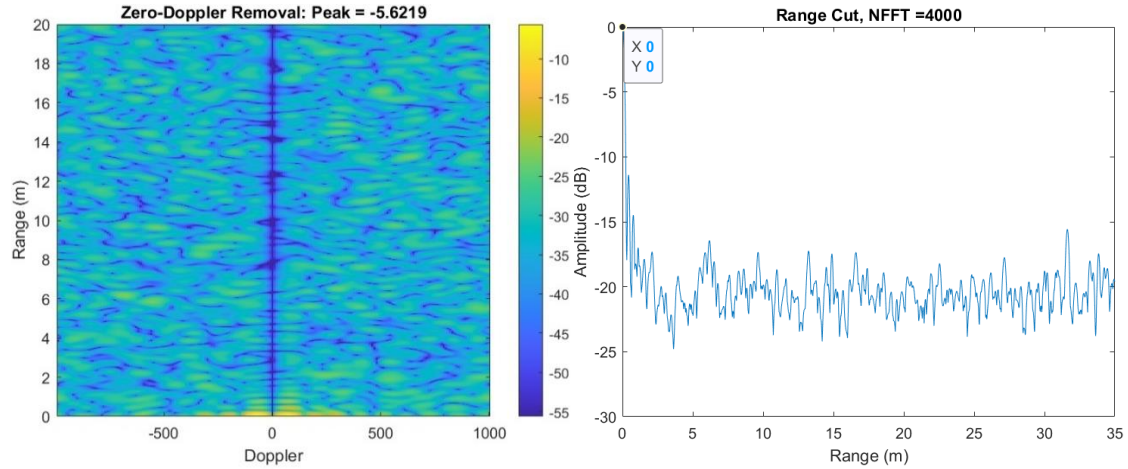

Figure 6.17: VV Polarization - Background Response

Stationary Target

Sources of interference can vary and comes from all possible directions during the measurement taking place. Accurate measurements of a fairly small size target will become tricky and challenging, as the peak spectrum of these small targets is always embedded within the noise or radar clutter. From most of the results, there is a high level of interference signal at a range less than 1m away before the zero-Doppler removal was applied. This is probably because of the reflection coming from the radar prototype itself since the radar prototype is mounted beside the horn antenna. And the metallic components from the radar

could potentially contribute to the reflection signal. After the process of the zero-Doppler removal, then there is a weak peak signal from the target. This is probably because the target is slightly moving when it is suspended to the top. Figure 6.18 is an example of the result of a bearing ball that was supposed to be in a stationary position. It can be interpreted that the ball was located at 3.2 m away from the radar. But it is -4.65 dB below the normalized amplitude. The signal response is about 10 - 12 dB above the noise level.

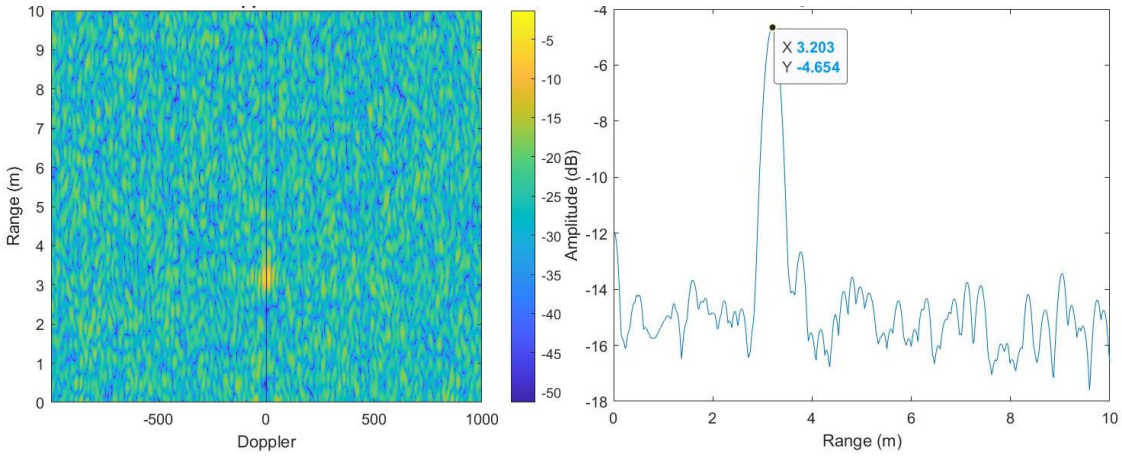

Figure 6.18: S_2 Bearing Ball in Stationary Position

Oscillating Target

At this point, the target is no longer in a stationary position. Once it is placed and suspended 3 m away from the radar, the target was swung in two different directions; (a) front to back oscillation and (b) side to side oscillation. HH and VV polarisation were compared with each of these oscillations. In all of the RDM results, the zero-Doppler component was removed from the data. Longer time duration will easily lose coherency. Hence, in order to obtain a cleaner Doppler response from a smaller target in the RDM, a shorter time integration was considered. Where in this case the time integration has taken is within 120 ramps (i.e., 0.06 s and a Doppler resolution of 16.67 Hz). But the dwell time of the micro-Doppler signature is displayed for the whole 2 seconds to see more Doppler signatures from the target. The window duration applied to obtain the micro-Doppler signatures was 40 ms and 10 ms later on.

(a) Front to Back Oscillation

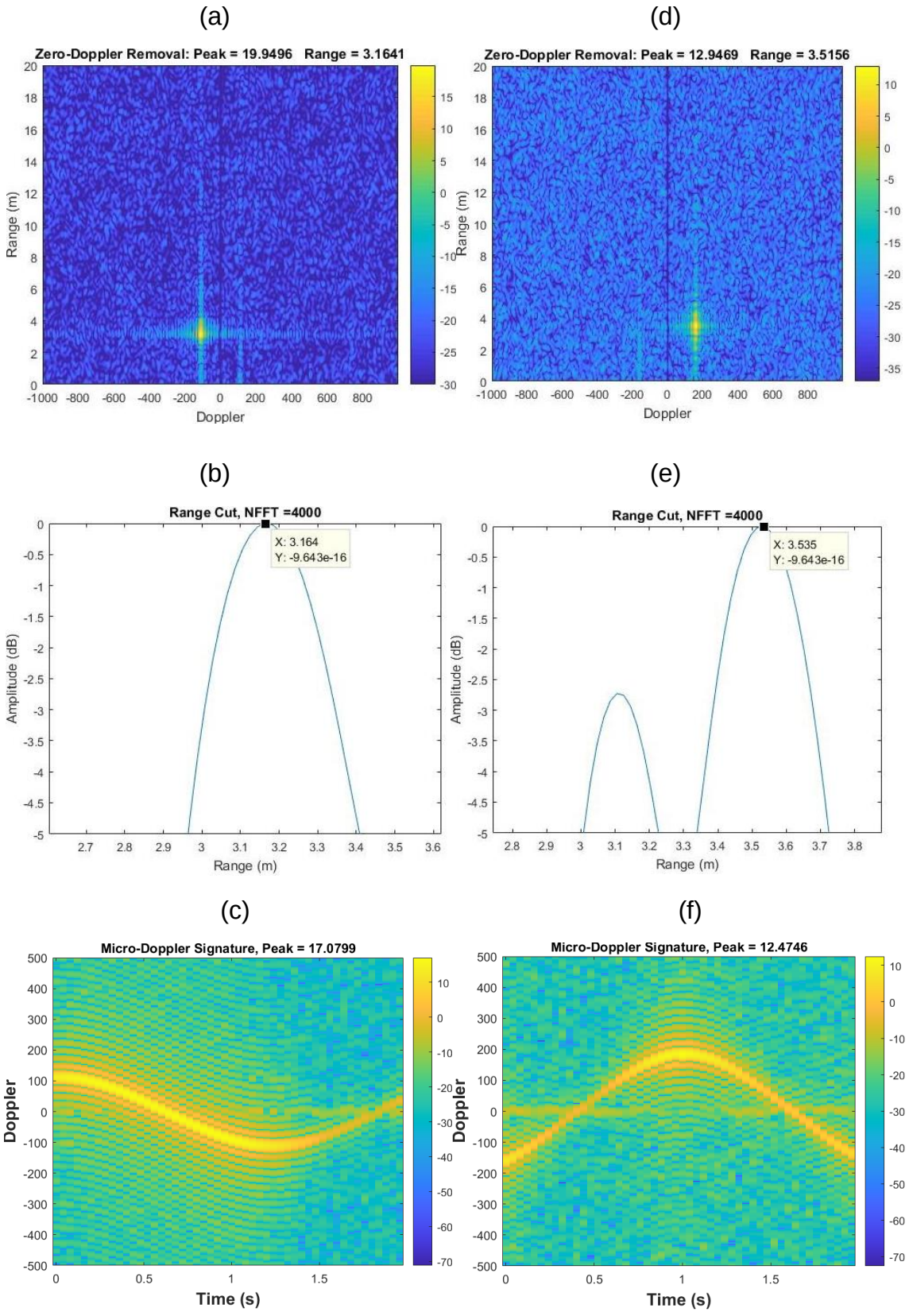

Figure 6.19: S_1 Bearing Steel Ball with Front to Back Oscillation; (a) - (c) HH Polarization, (d) - (f) VV Polarization. Window Length for STFT was 40 ms.

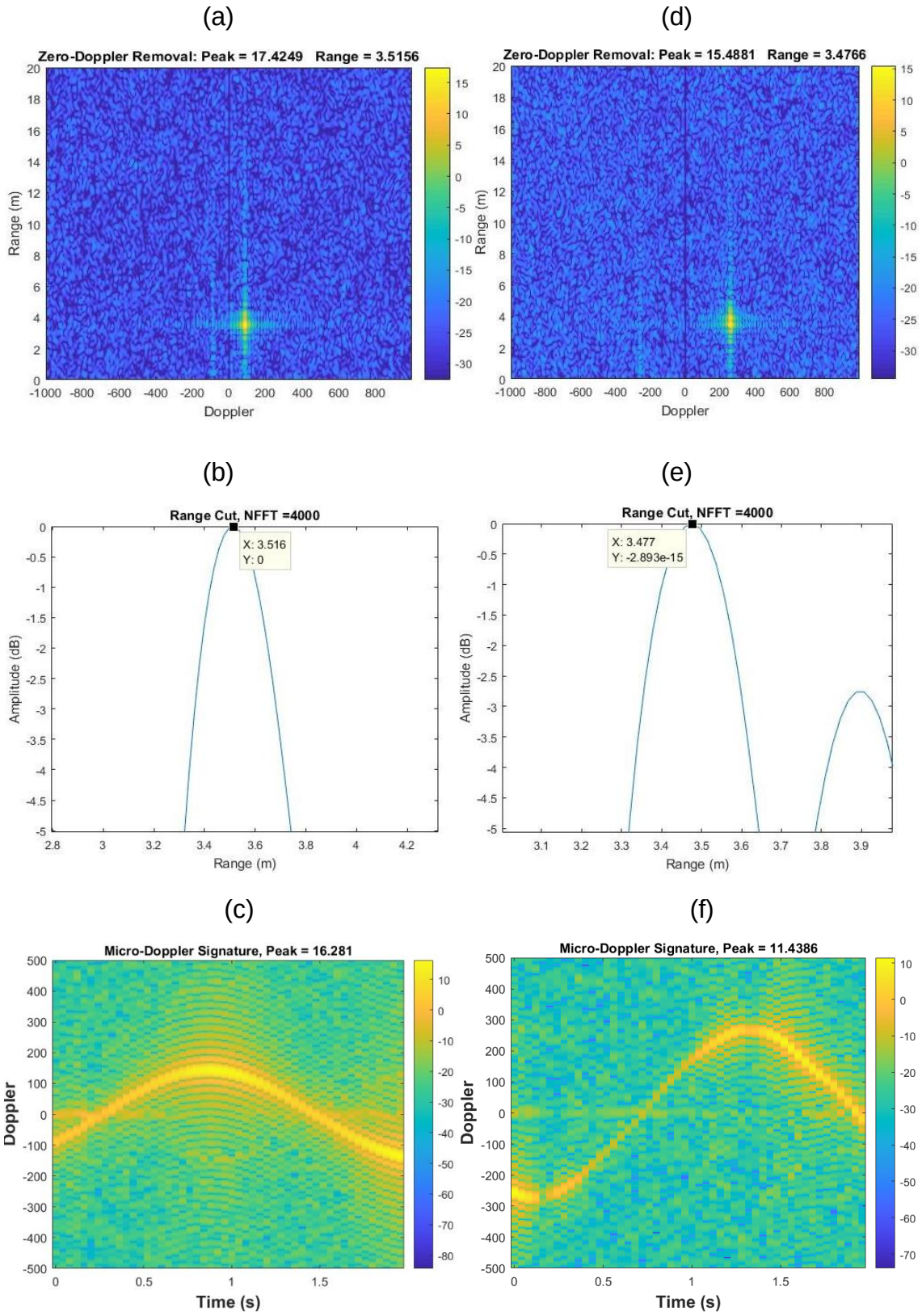

Figure 6.20: S_2 Bearing Steel Ball with Front to Back Oscillation; (a) - (c) HH Polarization, (d) - (f) VV Polarization. Window Length for STFT was 40 ms.

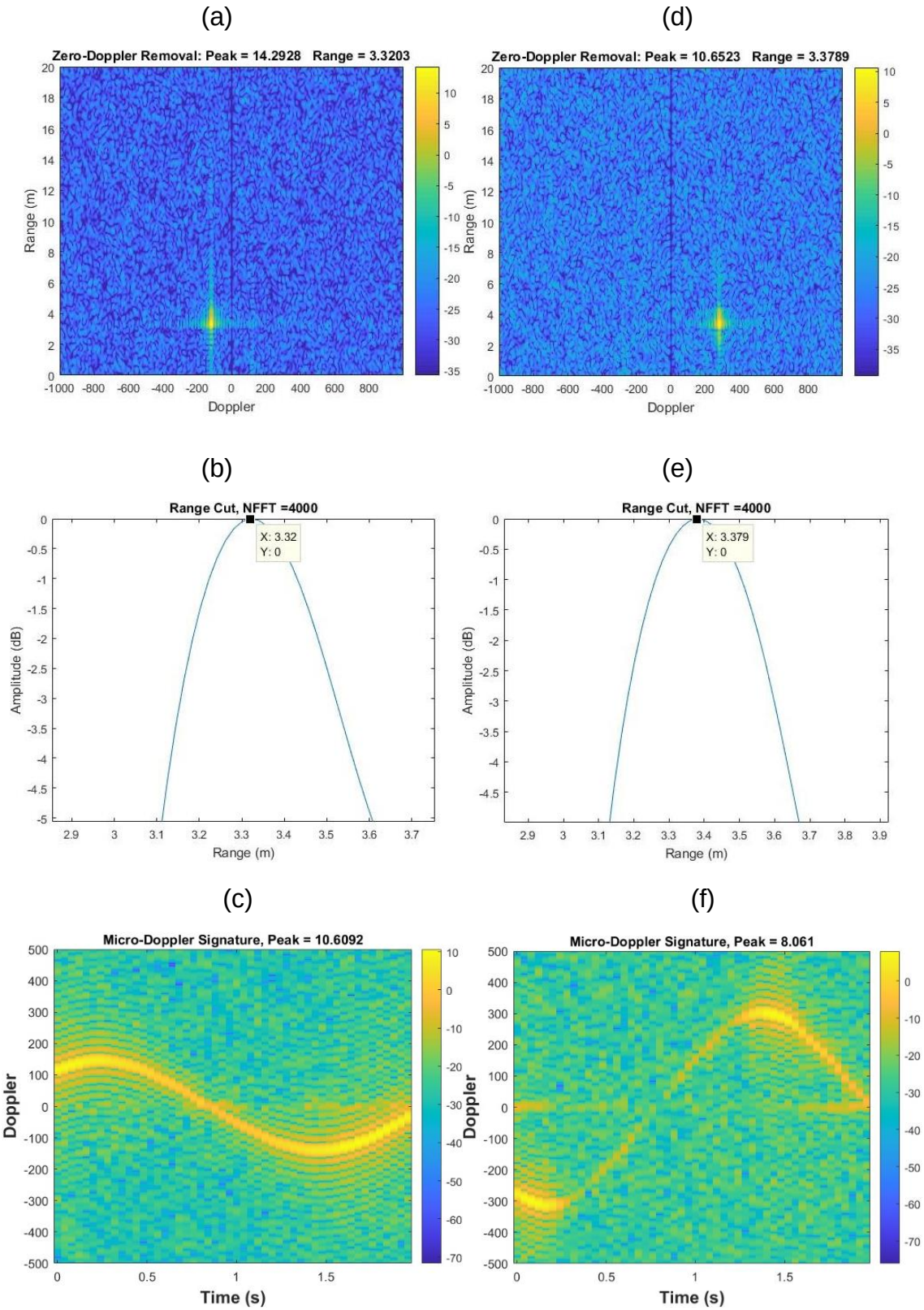

Figure 6.21: S_3 Bearing Steel Ball with Front to Back Oscillation; (a) - (c) HH Polarization, (d) - (f) VV Polarization. Window Length for STFT was 40 ms.

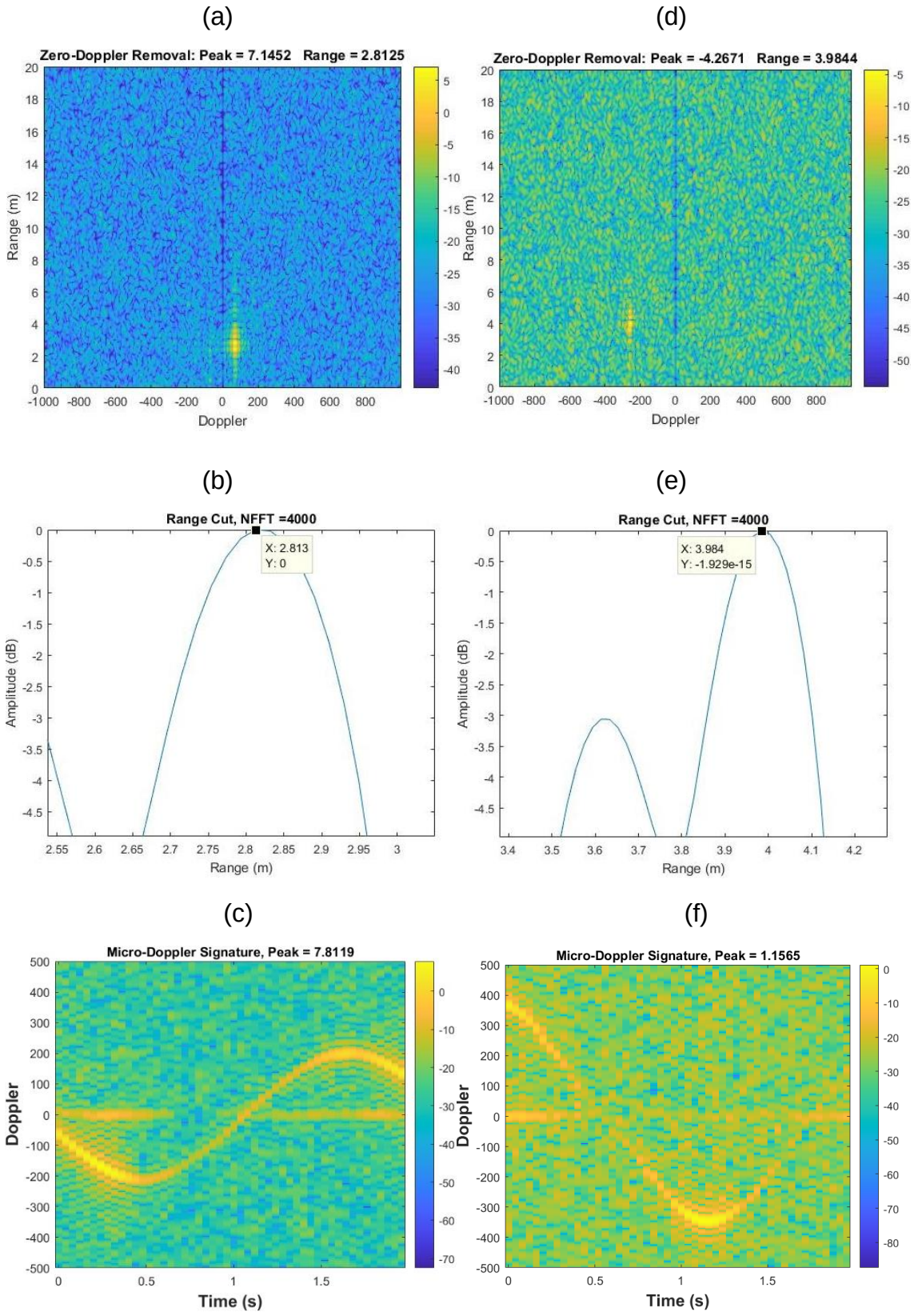

Figure 6.22: S_4 Bearing Steel Ball with Front to Back Oscillation; (a) - (c) HH Polarization, (d) - (f) VV Polarization. Window Length for STFT was 40 ms.

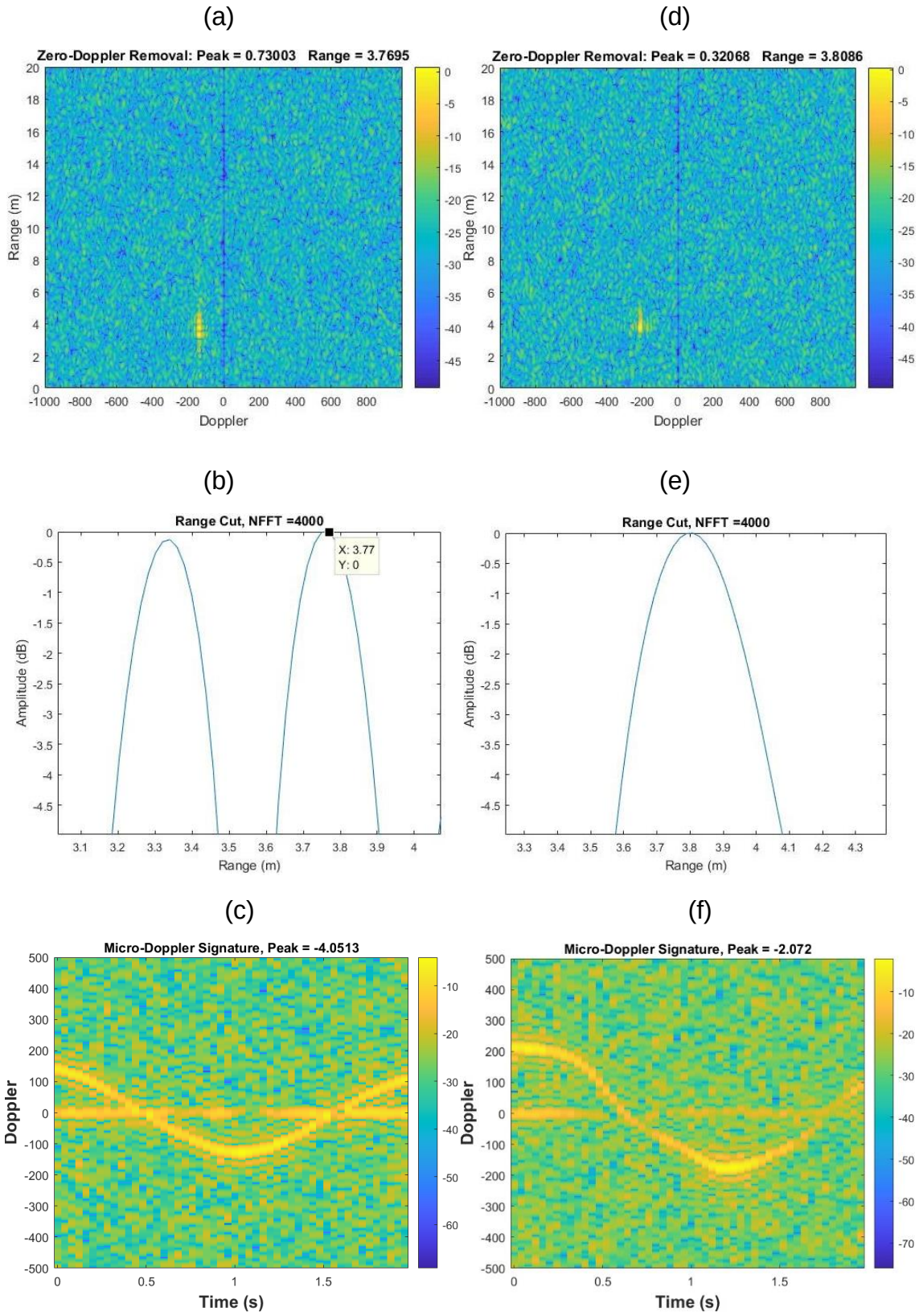

Figure 6.23: S_5 Bearing Steel Ball with Front to Back Oscillation; (a) - (c) HH Polarization, (d) - (f) VV Polarization. Window Length for STFT was 40 ms.

Figure 6.19 until Figure 6.23 demonstrated the Doppler signature of five different sizes of the bearing ball which was moved from front to back oscillation. A linear polarised (i.e., non-changing polarization) transmission was employed throughout this evaluation. Two types of co-polar were compared. Any radar engineers will attempt to maximize the intended weak signal reflected by the low RCS target for target detection. The problem with the low RCS target is that it is easily masked by the stronger response of radar clutter and make it undetectable. In order to deliver coherent integration, a shorter integration time in RDM was applied.

It is apparent from all these figures that the speed of the spheres relative to the HH polarization measurements was slightly slower and moving at a lower velocity than in VV polarization. In VV polarization, the spheres go faster, its oscillating go faster, and this clearly shows the different speeds. This is the reason why the strength of the signal response was found to be different in both co-polarizations, resulting in different returns of about 4 – 8 dB, which are concluded in Table 6.5. The spheres move differently in time. There is the presence of Doppler migration where the spheres in VV moves faster and hence integrate less within the same dwell time and window length. Or in other words, it is incoherent integration within the same integration time. From the plots in Figure 6.19 until Figure 6.22, it is obvious that the spheres were moving faster in VV. In theory, the RCS in HH-polar and VV-polar should be the same for a sphere target. This can be seen in Figure 6.23 for example, shown that the value of the peak Doppler in both polarization is nearly the same. That is about 150 Hz in HH-polar and 200 Hz in VV-polar. So, the SNR was about 1.98 dB different. The range cut in all plots was normalized and each of them illustrated the position of the sphere at a certain time integration in RDM.

From all these figures presented above, the bearing ball is found to be located within the range of 2.5 m to 3 m away from the radar and the range resolution was approximately 31 cm which agrees to the expected value. Overall, it can be

seen briefly that the S_1 shows the highest peak spectrum response compared to other spheres. This is because of the size and mass of the target that makes it easier to detect. The metallic properties might be different for the heavier sphere and it will reflect more in comparison of S_1 and S_2 that nearly have the same size but slightly different in the composition of the material. The lowest peak spectrum was found to be S_5 due to the smallest in size compared to other spheres. The spheres are different in size so as different in weight. This will affect the behaviour of the oscillation. The higher the mass, the more well-defined the oscillation trajectory of the spheres. But for a lighter mass, it will have a completely random oscillation resulting in a different local range position from other spheres. Based on the observation made, the peak signal responses are all summarized in Table 6.5 for comparison.

Table 6.5: Measured RCS Sphere of a Front to Back Oscillation

Target	T_w = 40 ms		T_w = 10 ms	
	HH	VV	HH	VV
Sphere S1	17.08	12.47	2.74	1.24
Sphere S2	16.28	11.44	1.28	0.02
Sphere S3	10.61	8.06	-0.73	-3.84
Sphere S4	7.81	1.16	-6.06	-7.46
Sphere S5	-4.05	-2.07	-10.86	-13.80

The window length for time-frequency analysis to extract the Doppler signature was 40 ms. This is to compromise between the time and frequency resolution. But it may be considered too long within that period as the target may not stay at a constant velocity vector. It does not remain constant for a very long time and this caused incoherent integration. Because of that, the window length $\boldsymbol{T_W}$ is shorten to 10 ms and the results are listed in Table 6.5. This is to make sure that a little movement of the spheres is noted and by minimizing the important information that is left behind from integration. It is apparent that once the window length of the STFT is reduced, the RCS of HH-polar and VV-polar are

nearly the same value which is consistent with the theory. It can be seen that the later results agree with the theoretical value in Table 6.4.

Referring to Table 6.5, a front to back oscillation and a window length of 10 ms for the STFT, the measured RCS difference between the two spheres are compared as follows;

(i) ($RCS_{S_1} - RCS_{S_5}$): The difference between S_1 and S_5 is 13.6 dB (HH-polar) and 15 dB (VV-polar). These results almost represent the theoretical RCS difference of the sphere S_1 and S_5 which is about 9.75 dB.

(ii) ($RCS_{S_2} - RCS_{S_5}$): The difference between S_2 and S_5 spheres is 12.14 dB and 13.82 dB. The theoretical RCS difference of the sphere S_2 and S_5 is expected to be closed as the last comparison, which is 9.85 dB.

(iii) ($RCS_{S_3} - RCS_{S_5}$): The difference between S_3 and S_5 is 10.13 dB and 9.96 dB for each polarization respectively. It is expected that theoretically, the RCS difference of the sphere S_3 and S_5 is about 7.09 dB.

(iv) ($RCS_{S_4} - RCS_{S_5}$): Lastly, the difference between S_4 and S_5 are 4.80 dB and 6.34 dB. From Table 6.4, it is projected that the RCS difference between the two spheres to be 2.86 dB.

(b) Side to Side Oscillation

Figure 6.24 until Figure 6.28 demonstrasted the Doppler signature of five different sizes of the bearing ball which move from side to side oscillation. The integration time for RDM was 0.06 s and a longer integration time for STFT was 2 s. Again, it can be seen briefly that the S_1 (as in Figure 6.24) shows the highest peak spectrum response compared to other spheres. The lowest peak spectrum was found to be S_5 (seen in Figure 6.28). It is expected that S_5 will give the lowest response of all due to its mass and size. Referring to Table 6.6, a window length of 10 ms for the STFT, the measured RCS difference between the two spheres are again compared in side to side oscillation as follows;

(i) ($RCS_{S_1} - RCS_{S_5}$): The difference between S_1 and S_5 are 14.1 dB (HH-polar) and 10.56 dB (VV-polar) for each polarization. These results almost represent the theoretical RCS difference of the sphere S_1 and S_5 which is about 9.75 dB.

(ii) ($RCS_{S_2} - RCS_{S_5}$): The difference between S_2 and S_5 spheres is 13.19 dB and 12.18 dB. The theoretical RCS difference of the sphere S_2 and S_5 is expected to be closed as the last comparison, which is 9.85 dB.

(iii) ($RCS_{S_3} - RCS_{S_5}$): The difference between S_3 and S_5 is 8.48 dB and 7.66 dB for each polarization respectively. It is expected that theoretically, the RCS difference of the sphere S_3 and S_5 is about 7.09 dB.

(iv) ($RCS_{S_4} - RCS_{S_5}$): Lastly, the difference between S_4 and S_5 are 3.07 dB and 1.41 dB. From Table 6.4, it is projected that the RCS difference between the two spheres to be 2.86 dB.

Table 6.6: Measured RCS Sphere of a Side to Side Oscillation

Target	T_w = 40 ms		T_w = 10 ms	
	HH	VV	HH	VV
Sphere S1	17.47	8.65	2.20	-3.84
Sphere S2	16.42	8.21	1.29	-2.22
Sphere S3	12.99	7.23	-3.42	-6.74
Sphere S4	8.26	3.81	-8.83	-12.99
Sphere S5	-0.66	-2.06	-11.90	-14.40

And apart from that, the signal response is affected by the viewing angle. The most reflective angles (or the greatest amplitude response) are the ones that give the maximum cross-sectional area towards the radar beam sights. Front to back oscillation results in the spheres is always at the main beam of the antenna. It will give a better antenna gain. When moving side to side, the target no longer stays within the main beam but the gain of the antenna changes with the movement. So there's modulation amplitude of the gain to the oscillation of the spheres. Because of this, the front to back will give a higher value of RCS compared to side to side oscillation. Depend on the speed and depend on the gain.

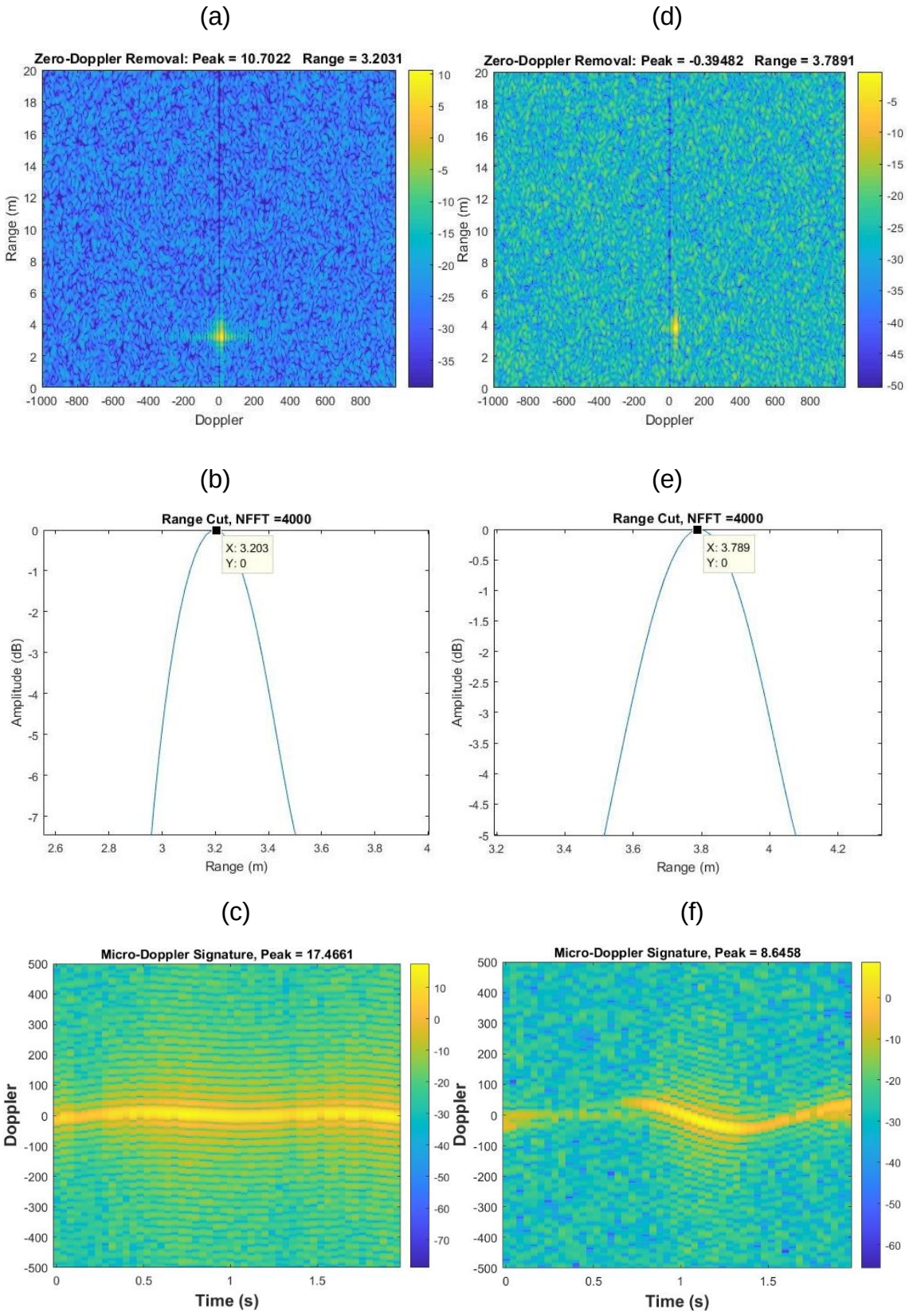

Figure 6.24: S_1 Bearing Steel Ball with Side to Side Oscillation; (a) - (c) HH Polarization, (d) - (f) VV Polarization. Window Length for STFT was 40 ms.

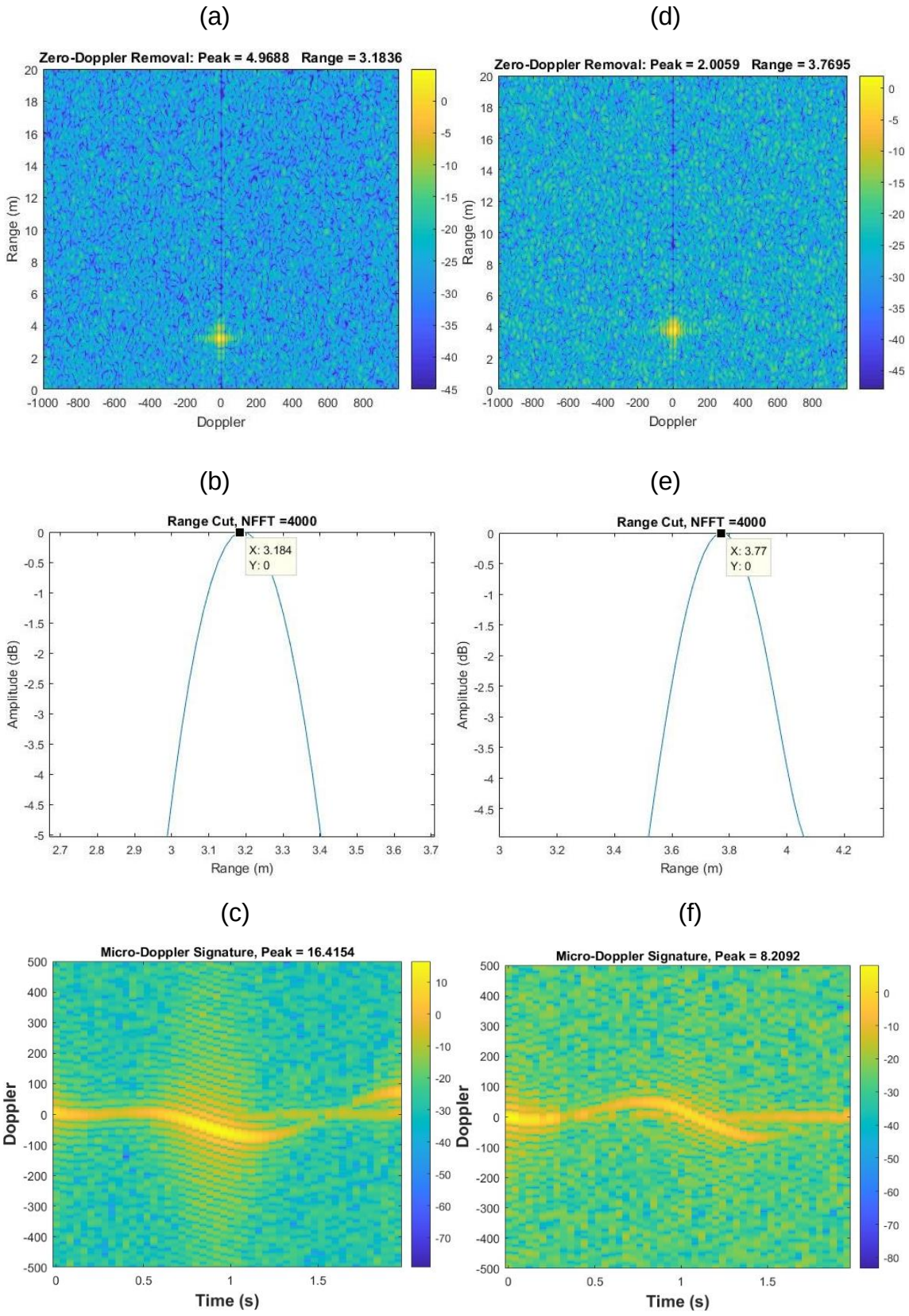

Figure 6.25: S_2 Bearing Steel Ball with Side to Side Oscillation; (a) - (c) HH Polarization, (d) - (f) VV Polarization. Window Length for STFT was 40 ms.

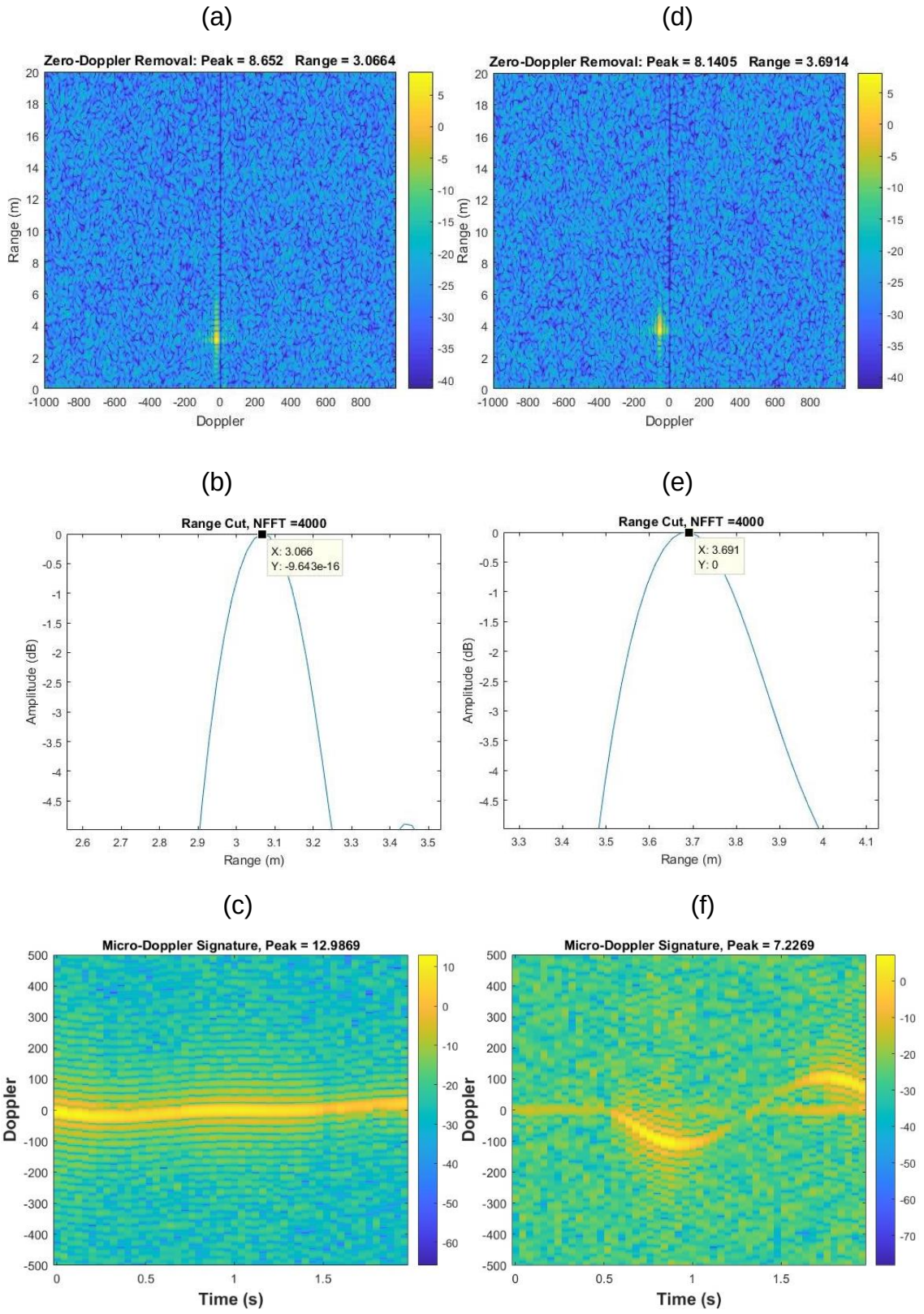

Figure 6.26: S_3 Bearing Steel Ball with Side to Side Oscillation; (a) - (c) HH Polarization, (d) - (f) VV Polarization. Window Length for STFT was 40 ms.

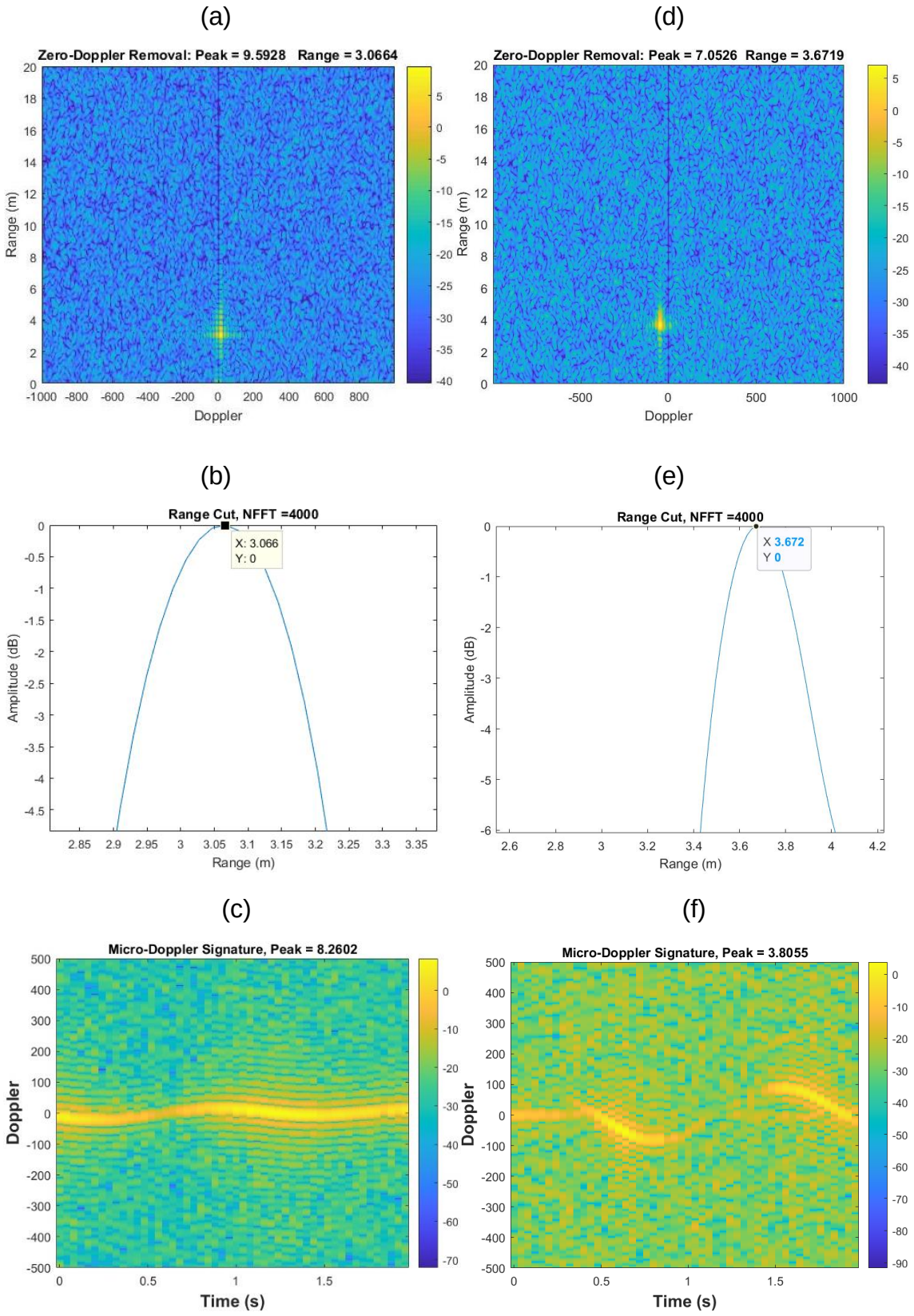

Figure 6.27: S_4 Bearing Steel Ball with Side to Side Oscillation; (a) - (c) HH Polarization, (d) - (f) VV Polarization. Window Length for STFT was 40 ms.

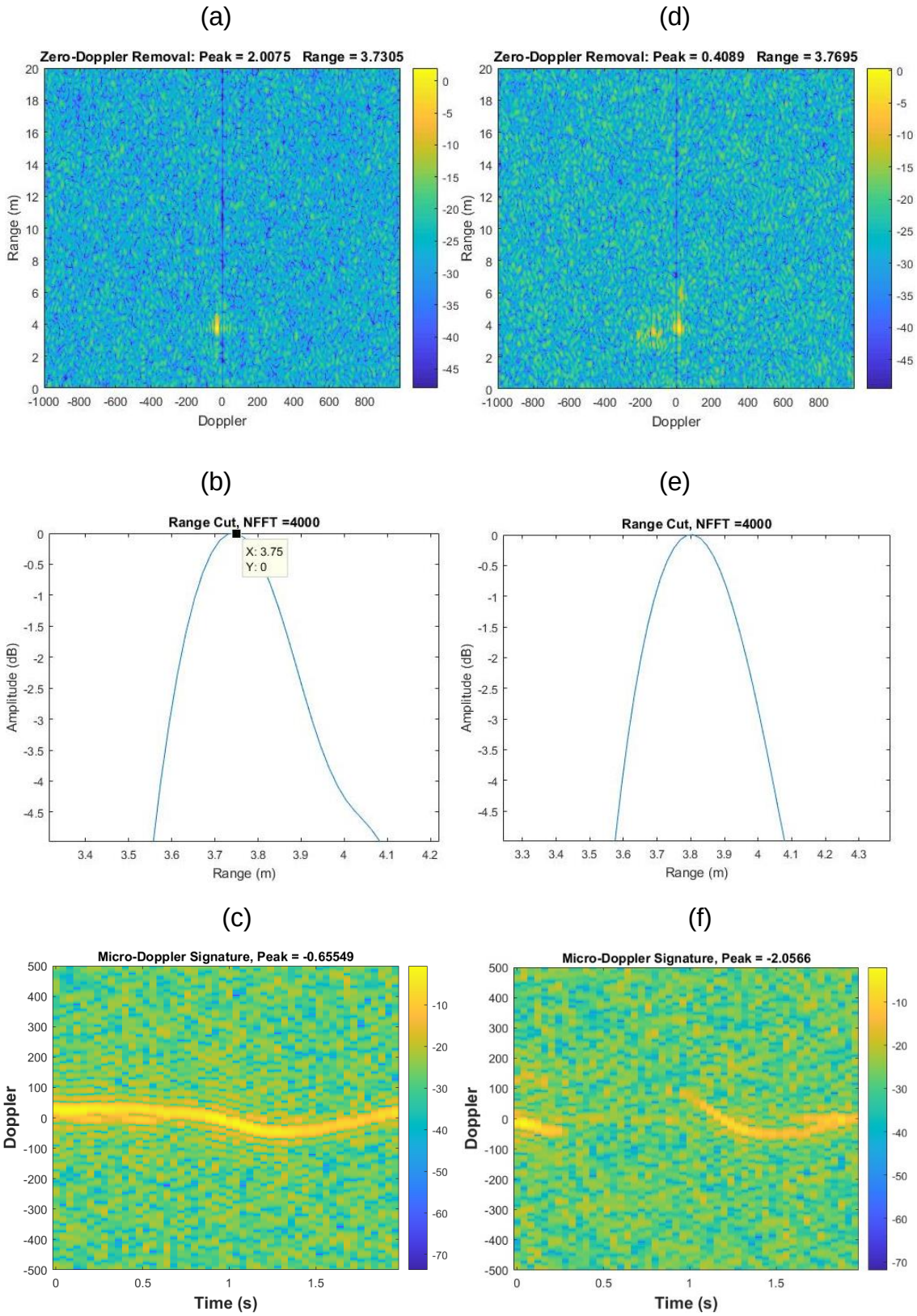

Figure 6.28: S_5 Bearing Steel Ball with Side to Side Oscillation; (a) - (c) HH Polarization, (d) - (f) VV Polarization. Window Length for STFT was 40 ms.

The purpose of studying the RCS of spheres first is that this RCS is known and can be calculated. As long as the diameter of the sphere is known. This can be used as a calibration of an experiment. Next, a nano-drone is then suspended to the ceiling at the same position as the spheres. Then the data was collected with the drone moving circularly as it is restricted to the fishing line that was attached to the ceiling. The horn antenna is in VV polarization. From Figure 6.29, the drone is found to be located at 3.7 m away from the radar, which is about where the spheres were detected previously.

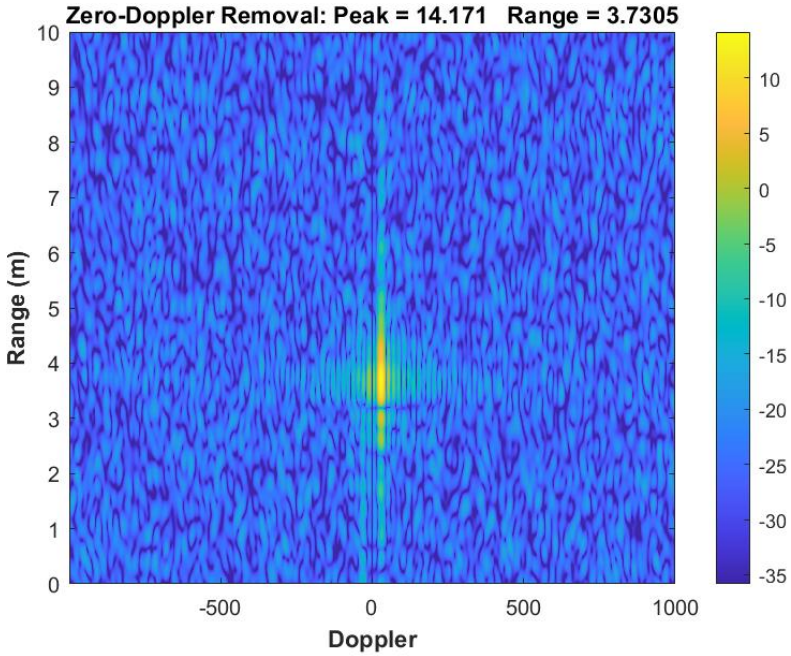

Figure 6.29: RDM of the Nano-Drone

With the same range bin selected for the spheres, the Doppler signature is extracted for comparison. The LHS of Figure 6.30 is the Doppler signature with a window length of 40 ms. The peak response shown is 9.98 dB. And the RHS of Figure 6.30 illustrated the Doppler signature with a window length of 10 ms. It is shown that the peak response was -1.72 dB. From a VV polarization in Figure 6.30, it is estimated that the RCS of the drone is higher from each of the spheres S_1, S_2, S_3, S_4 dan S_5.

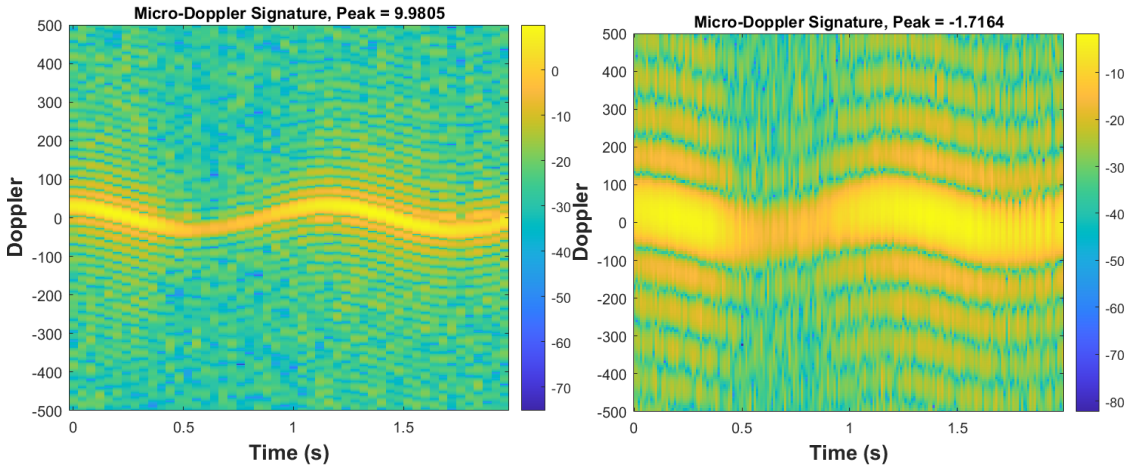

Figure 6.30: The Doppler Signature of the Drone; the Window Length for Time-Frequency Analysis was 40 ms at LHS and 10 ms at RHS

6.3.2 Detection of Multiple Spheres

The detection of a single sphere of five different sizes has been demonstrated in the last section. This section aims to detect multiple targets at one time. Two spheres were tied up, hanged and positioned 1 m apart from each other. The first target (Target 1) was the S_2 sphere. It was placed 2 m away from the radar. Then the second target (Target 2), S_3 sphere which was placed 3 m away from the radar. Both targets are positioned in the line of sight of the radar. The measurements were performed and the results are presented in the following structure: (a) with the horn antenna positioned in HH polarization, two spheres were oscillating from front to back (b) with the horn antenna positioned in VV polarization, two spheres were oscillating from front to back (c) with the horn antenna positioned in HH polarization, two spheres were oscillating from side to side and lastly (d) with the horn antenna positioned in VV polarization, two spheres were oscillating from side to side.

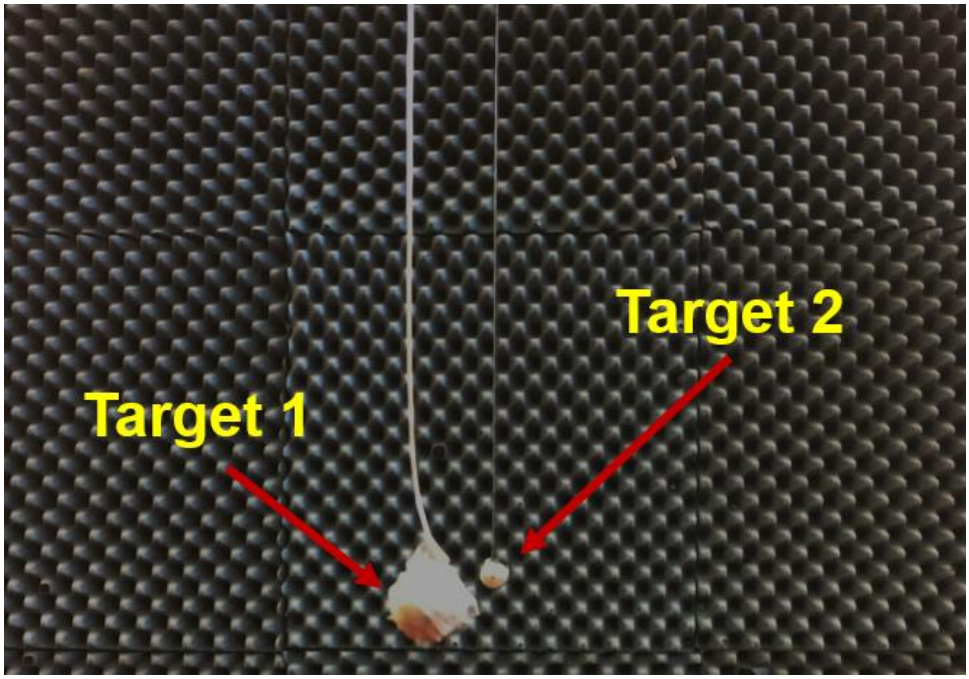

Figure 6.31: Detection of Multiple Target, with Two Sphere Balls

In order to detect a small target in the RDM with no migrations, again a shorter time integration is contemplated. In this case, the time integration taken is within 120 ramps of 0.5 ms ramp duration (i.e., 0.06 s of dwell time).

(a) HH Polarization and Front to Back Oscillation

Two spheres were pulled and released simultaneously so that both oscillated from front to back freely. The total measurement gathered was taken within 2 seconds to observe the Doppler signature.

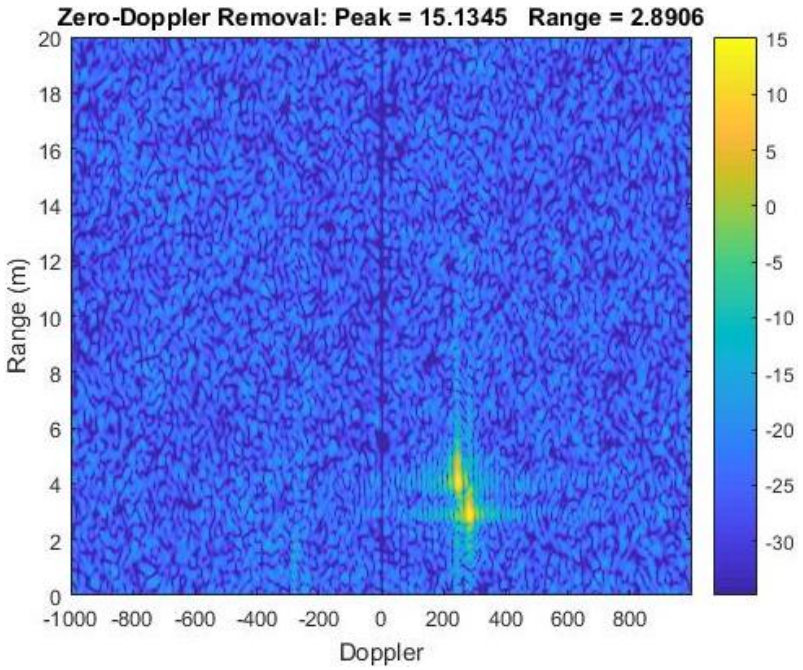

Figure 6.32: HH Polarization with Front to Back Oscillation

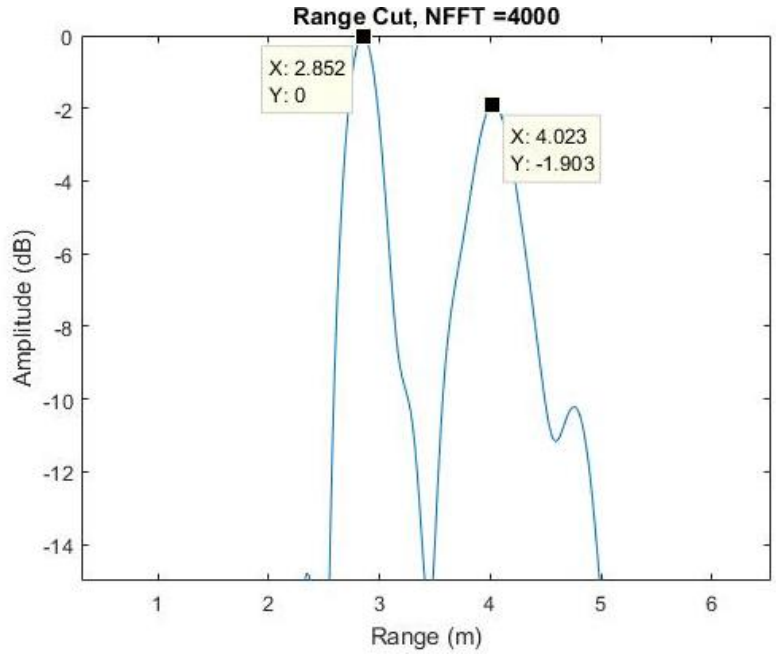

Figure 6.33: The Range Cut Representing Front to Back Oscillation

Figure 6.32 show that both targets are moving towards the radar as the positioned is further away from the original place and moving closer to the radar. Figure 6.33 presents the two peaks of different Doppler which correspond to the targets in the RDM above. Target 1 has a higher peak profile in Figure

6.33, while Target 2 was dropped by -2 dB from Target 1. This is because Target 2 is further away from the radar and the size of Target 2 is smaller than Target 1. Figure 6.32 illustrates that Target 1 has a higher Doppler shift of nearly 300 Hz and Target 2 presented a smaller Doppler shift of approximately 250 Hz. This is also proven in Figure 6.34 were taken the window duration was 50 ms. The target showed almost one complete sinusoidal within 2 seconds, indicating the rotational rate of approximately 0.5 Hz. Target 2 seems to be a little bit lagging about 0.2 – 0.3 seconds from Target 1. This is probably due to the weight of Target 1 which is slightly heavier than Target 2 and causing it to move slightly faster than the other one.

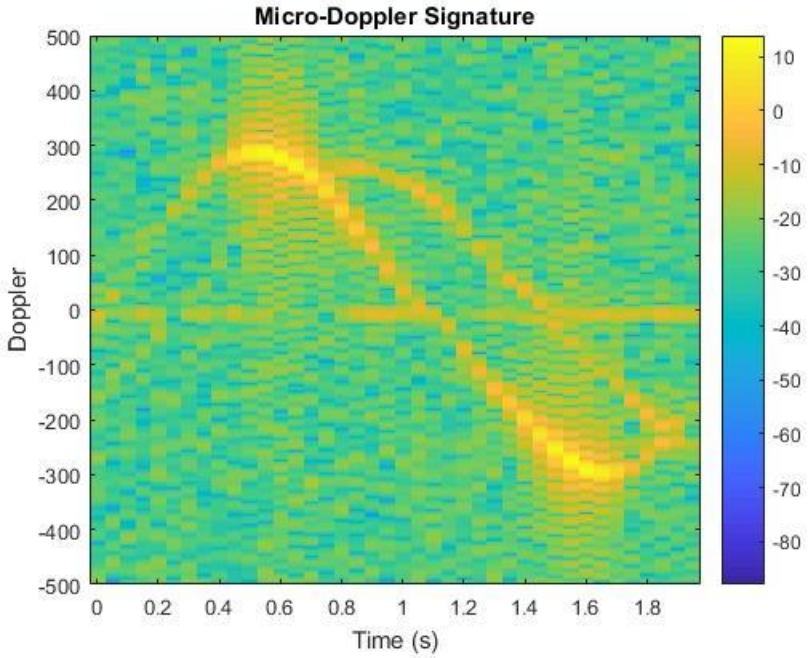

Figure 6.34: STFT of Front to Back Oscillation

(b) VV Polarization and Front to Back Oscillation

With the same position of the spheres, the polarization is then changed from HH to VV polar. Both spheres were swung from front to back and the data measurements were gathered from this evaluation.

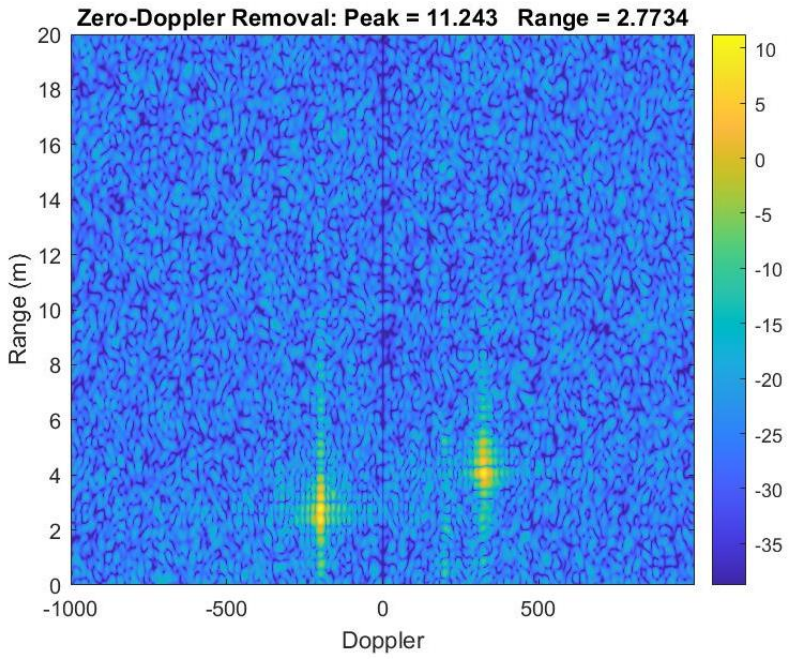

Figure 6.35: VV Polarization with Front to Back Oscillation

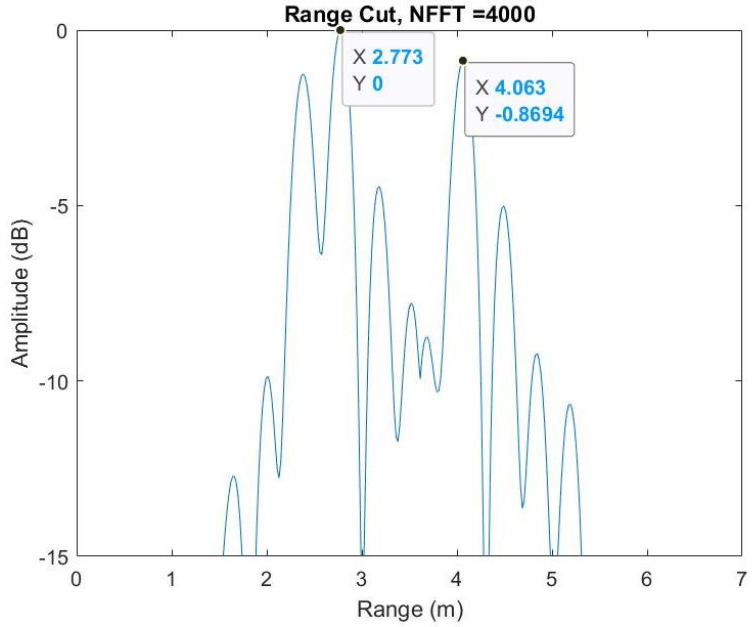

Figure 6.36: The Range Cut Representing Front to Back Oscillation

Figure 6.35 and Figure 6.36 is the time integration for 0.06 seconds. At this point, the spheres were moving in the opposite direction, as one was moving away from the radar and another one was moving towards the radar. One target with a Doppler shift of 400 Hz was located at 4 cm and another one with a Doppler shift of -200 Hz at point 2.7 cm from the radar at that time integration. Figure 6.37 proves that the spheres were oscillating in the opposite direction, where one was moving away, and another one was moving towards the radar. One target has reached the maximum Doppler tip of about 400 Hz and another one with a Doppler tip of 200 Hz. Again, both were representing a one cycle sinusoidal oscillation within 2 seconds period indicating a rotational rate of about 0.5 Hz.

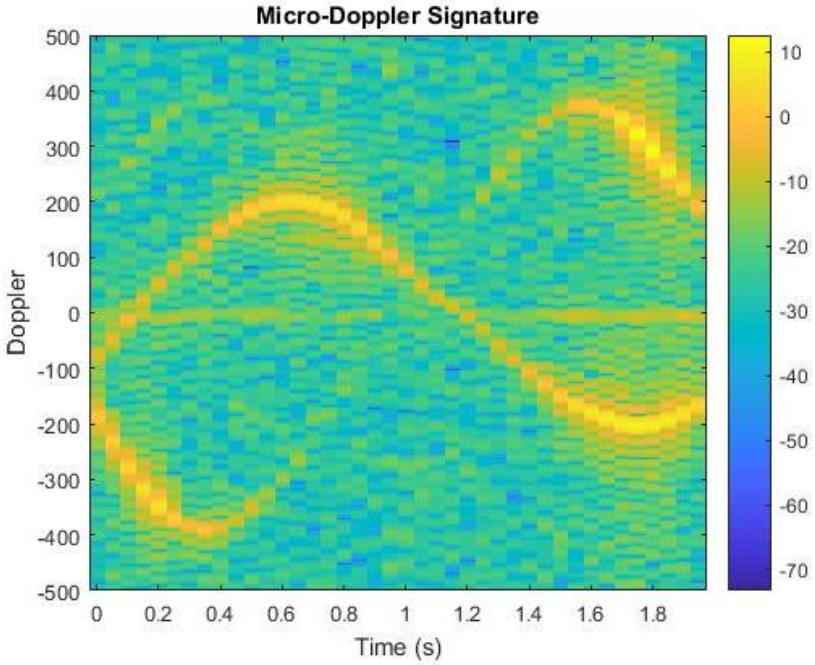

Figure 6.37: STFT of Front to Back Oscillation

(c) HH Polarization and Side to Side Oscillation

In the previous evaluation, the ball sphere has oscillated perpendicular to the plane of the horn antenna. But this time the oscillation of the ball sphere was oscillating in the parallel direction to the plane aperture of the antenna. A much lower Doppler shift is expected for this test measurement as it is moving sideways.

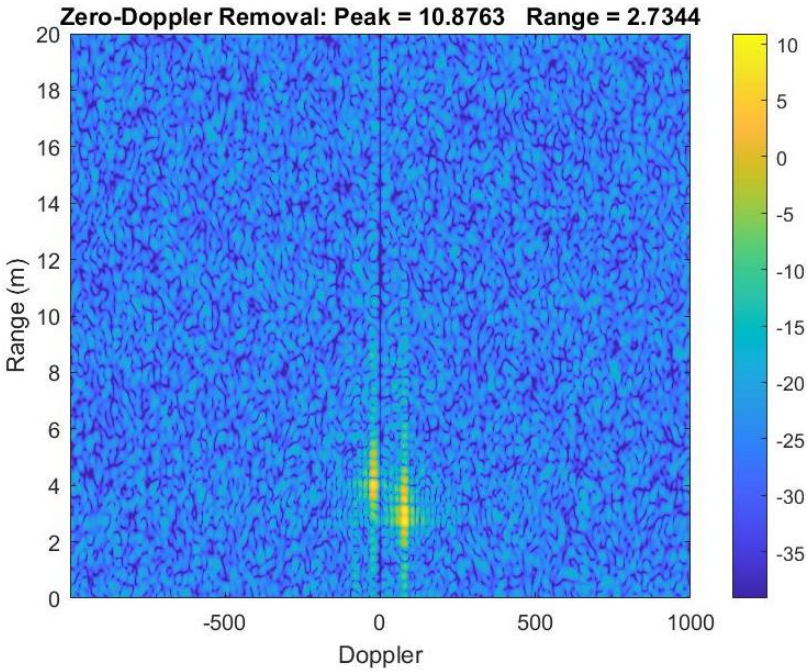

Figure 6.38: HH Polarization with Side to Side Oscillation

Figure 6.38 and Figure 6.39 is the integration time at point 0.30 s until 0.36 s. Target 1 has a higher peak profile than Target 2. The RDM shows that one target is moving at a Doppler shift of 90 Hz and another target moving at the opposite direction with a Doppler shift of -15 Hz. Strong evidence of both Doppler signatures was found in Figure 6.40. The LHS of the figure represents the Doppler signature of Target 1. From the RDM, the micro-Doppler signature was extracted by taking an FFT of the range bin the Target 1 is in. A similar process was applied for Target 2, where the location of the target is identified and chosen for STFT analysis. The Doppler signature of Target 2 is represented on the RHS of the figure below. Those figures conclude that both targets were oscillating in the opposite direction to each other. For Target 1, one and a half sinusoidal cycle was found within 2 seconds integration time while for Target 2, approximately one and a quarter cycles were found within 2 seconds.

Within that period of time, the maximum Doppler tip for Target 1 was nearly 100 Hz and for Target 2 was roughly 50 Hz.

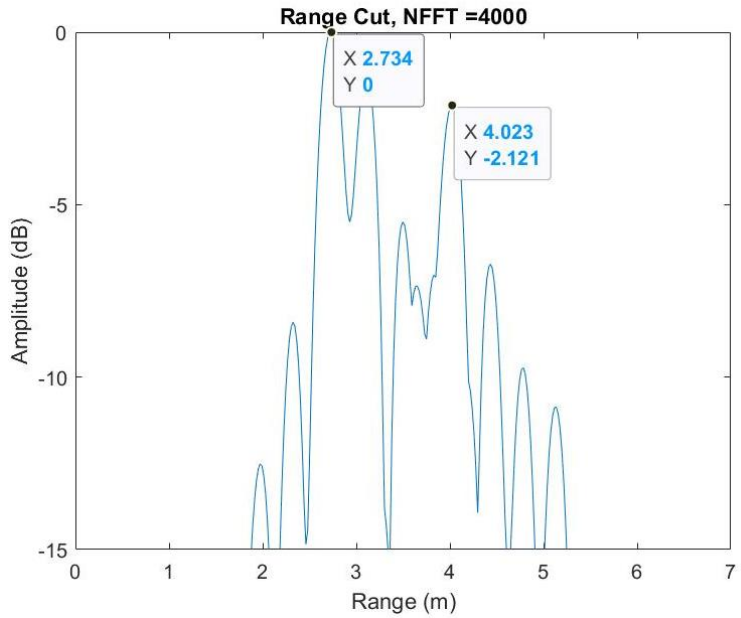

Figure 6.39: The Range Cut Representing Side to Side Oscillation

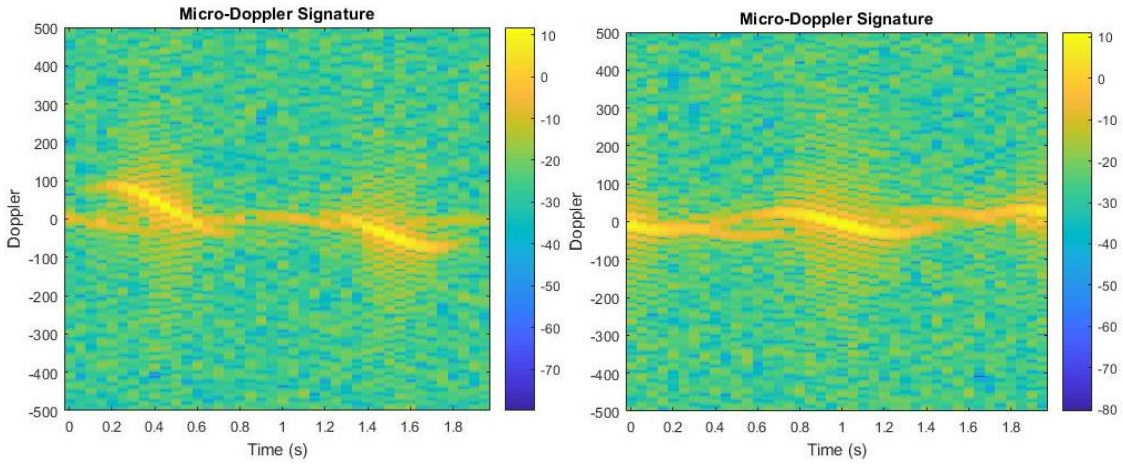

Figure 6.40: STFT of Side to Side Oscillation. LHS: Doppler Signature of Target 1. RHS: Doppler Signature of Target 2.

(d) VV Polarization and Side to Side Oscillation

The polarization of the antenna was changed to VV polar and the two spheres again were pulled and released simultaneously so that both oscillate sideways.

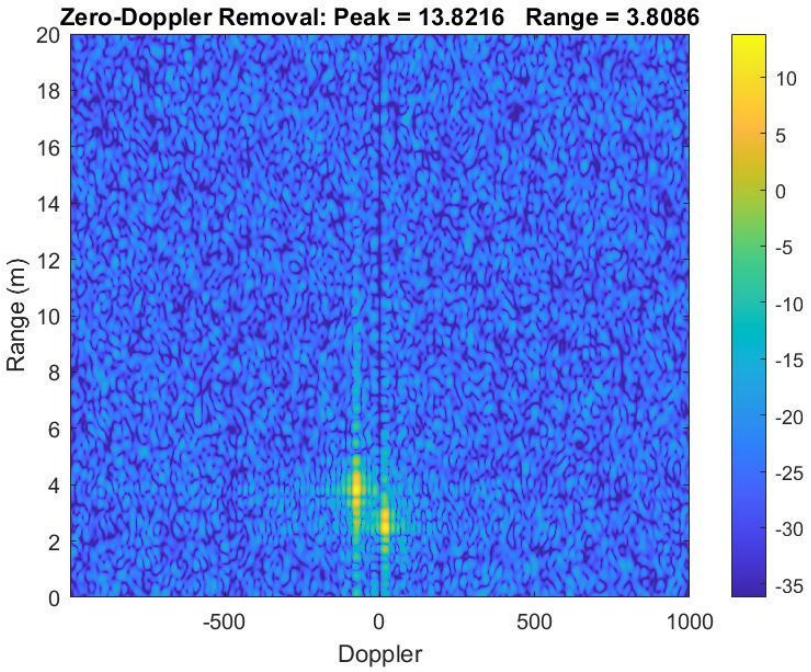

Figure 6.41: VV Polarization with Side to Side Oscillation

It is apparent from Figure 6.41 and Figure 6.42 that two targets were detected, both are located at 2.48 m and 3.81 m respectively. At this integration time, from 0.78 s to 0.84 s, it is found that Target 1 is oscillating with a Doppler shift of 20 Hz and Target 2 with a Doppler of -70 Hz. This is proven in Figure 6.43 below. Two targets were found to be oscillating about at zero-Doppler. The time integration of the STFT analysis was 2 seconds, and within that time one target reached the maximum Doppler tip of 120 Hz and another one is 25 Hz.

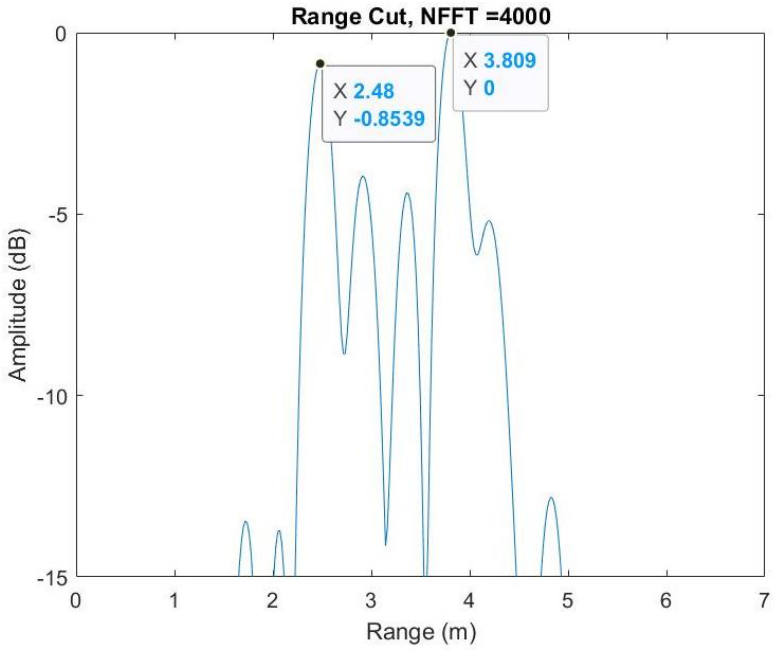

Figure 6.42: The Range Cut Representing Side to Side Oscillation

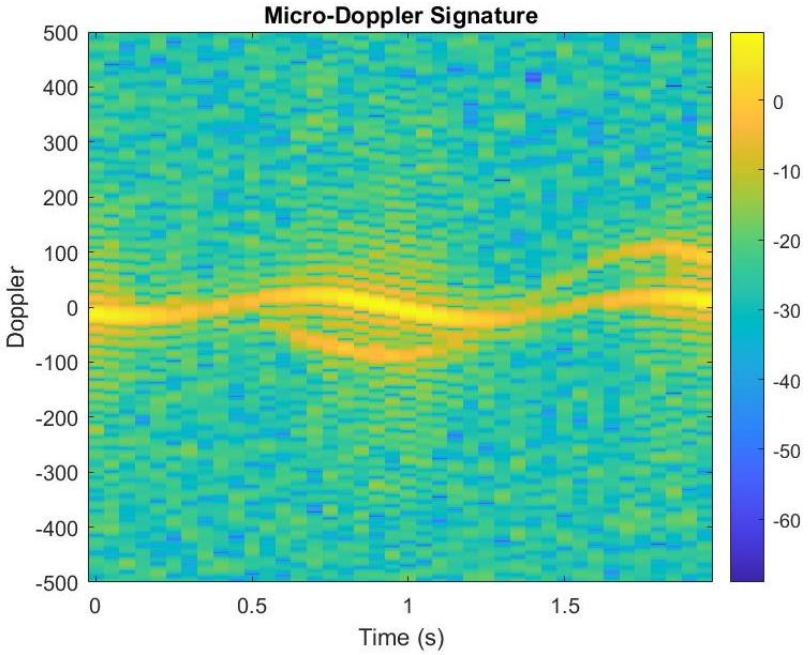

Figure 6.43: STFT of Side to Side Oscillation

This finding suggests that, as long as the separation of the two targets is bigger than the range resolution, then the two targets can be resolved, and the Doppler

signature is significantly visible. In this context, the range resolution was 31.25 cm. So, the separation between those two targets needs to be larger than 31.25 cm. Otherwise, it is detected as only one target.

6.4 Detection of Nano-Drone

In an attempt to meet the main objective of the research study as outlined in Chapter 1, the detection of nano-drone is evaluated and presented. The data measurement was carried out in the same place as explained in the previous section, in the Radar Laboratory of Cranfield University, Shrivenham campus. In this scenario, apart from detecting the bulk motion of the target, the micro-motion of the propeller is being observed and studied. The target chosen was an ARCADE Nano Quadcopter. This drone consists of four sets of two-propeller blades with a length L of 1.2 cm long on each side. And the body size of the drone was about 3 cm in size. The drone was first attached with a string of fisher line and tied upwards to the ceiling. Then, the second string of fisher line was tied towards the bottom to the floor. The state of the drone is illustrated in Figure 6.44. This is in order to avoid unintended flight trajectories and for the easiness to control the drone. The smaller the drone, the trickier and challenging the drone to keep it balance as they are lightweight objects.

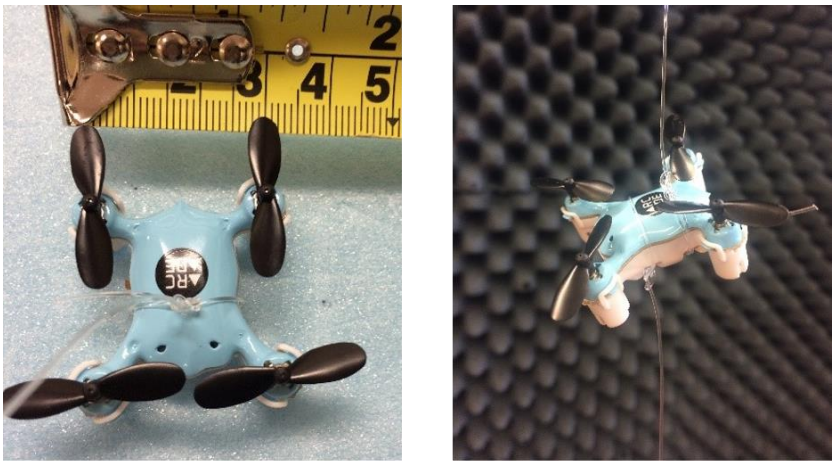

(a) (b)

Figure 6.44: (a) Close-Up Photo of Arcade Nano-Drone, (b) The Hanging of Nano-Drone for Target Detection

The radar prototypes in Figure 6.45 was mounted on a tripod with the help of a bracket to firmly hold the horn antenna and was adjusted so that the height is about 1.5 m above the ground. Then, the drone was positioned exactly at the antenna boresight and the same level as the antennas in order to retrieve the optimum signal return. A panel of RAM was placed behind the radar prototype and another RAM panel was placed behind the nano-drone. This is to reduce the multipath effects. The drone was placed at 3 m away from the radar. The drone is then switched on and ready for data collection.

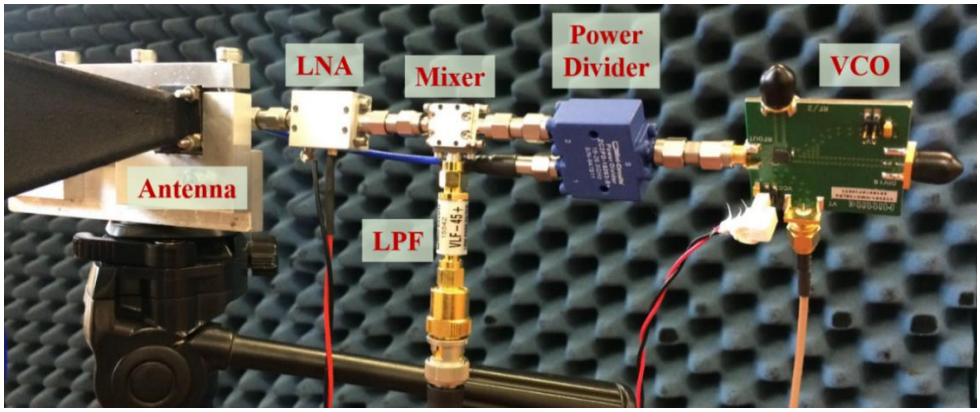

Figure 6.45: K-Band FMCW Radar Prototype

Different to the last measurement taken for the spheres, the parameters of the radar prototype is summarized in Table 6.7. The nano-drone results presented here can not be compared with the RCS spheres in the last section as the radar settings were different. The data were sampled at a sampling frequency of 500 kHz and 1 M number of samples leading to a 2 seconds integration time. Two different ramp durations were used in this evaluation. The first case was 1 ms and the second one was reduced to 0.5 ms. Theoretically, there will be not much difference in the radar performance except that the unambiguous Doppler will be increased as the ramp duration is shortened. The frequency sweeps linearly from 24.764 GHz to 24.884 GHz leading to a frequency bandwidth of 120 MHz.

Table 6.7: The Parameters and Performance of the Prototype

CASE	1	2
AWG Parameters		
Frequency (kHz)	1	2
Amplitude (mV)	100	100
Offset (mV)	1300	1300
TiePie Parameters		
Sampling Frequency (kHz)	500	500
Number of Samples (kS)	1000	1000
Radar Signal		
Ramp Duration (ms)	1	0.5
Frequency 1 (GHz)	24.764	24.764
Frequency 2 (GHz)	24.884	24.884
Bandwidth (GHz)	0.12	0.12
Radar Performances		
Range Resolution (cm)	125.000	125.000
Maximum Range (m)	312.500	156.250

The result in Figure 6.46(a) indicates that the target is detected to be 2.42 m away from the radar. The peak of 36 dB energy indicates the main body of the target, which is slightly moving about at the zero-Doppler. Figure 6.46(b) clearly shows that the HERM lines induced by the blade propeller are visible at approximately 300 Hz to 400 Hz (i.e., 18,000 RPM to 24,000 RPM). The rotational rate of the blade could not be traced from these two figures in Figure 6.46, however, it is suggested that the periodicities of the Doppler return are about 25,000 RPM [106] [107]. The estimation of the minimum Doppler bandwidth required is almost similar to equation (5-16). Since each of the propellers has two blades, the approximation is as follows

$$2f_{Doppler} = \frac{8\pi L\Omega}{\lambda} = \frac{8\pi(0.012)(400/2)}{0.0125} = 4825.5\ Hz = 2(\pm 2412.75\ Hz)$$

From this estimation, it is believed that the ramp duration needed is roughly about $T_{R_{min}} = \frac{1}{2f_{Doppler}} = \frac{1}{2(\pm 2412.75\ Hz)} = 0.2\ ms$.

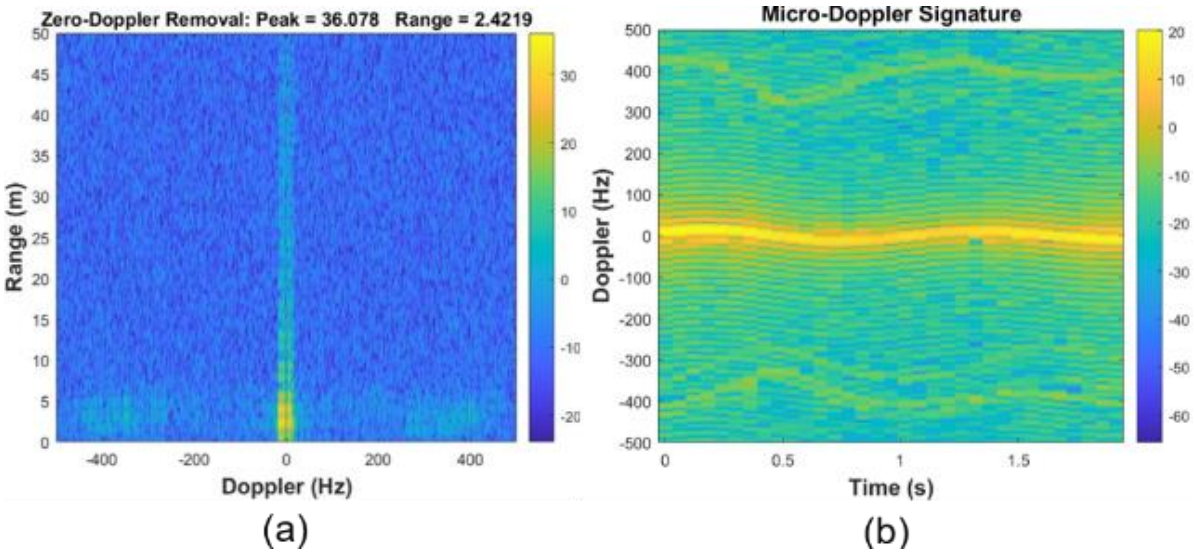

Figure 6.46: Ramp Duration of 1 ms; (a) RDM (b) Micro-Doppler

Then, a second case is observed with a shorter ramp duration. It is noticed that both figures in Figure 6.47 have expanded their Doppler bandwidth. As a result, the blade behaviour is much more obvious and visible. Figure 6.47(a) indicates that the maximum Doppler frequency returns are approximately between 500 Hz. And the HERM lines induced by the blade propeller again is found to be about 500 Hz to 600 Hz (i.e., 30,000 RPM to 36,000 RPM) as in Figure 6.47(b). The comparison of the two cases reveals that for a high rotational rate of the target, a shorter ramp duration may become the best option as it requires a larger Doppler bandwidth. In this case, the estimation is as follows

$$2f_{Doppler} = \frac{8\pi L\Omega}{\lambda} = \frac{8\pi(0.012)(600/2)}{0.0125} = 7238.2\ Hz = 2(\pm 3619.1\ Hz)$$

From this estimation, it is believed that the ramp duration needed is roughly about $T_{R_{min}} = \frac{1}{2f_{Doppler}} = \frac{1}{2(\pm 3619.1\ Hz)} = 0.14\ ms$.

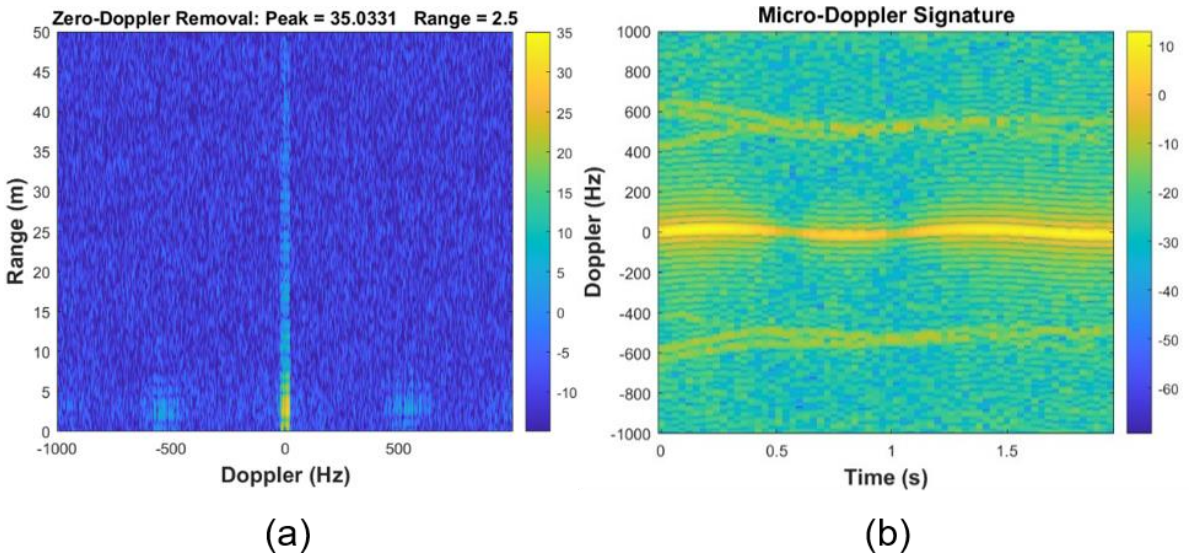

Figure 6.47: Ramp Duration of 0.5 ms; (a) RDM (b) Micro-Doppler

After considering both cases, the approximation $T_{R_{min}}$ may be required about 0.1 ms to capture the signature without ambiguity. The micro-Doppler signature observed depends on the aspect angle of the drone captured by the radar. Since the drone move in a circular motion about the fisher line, hence, the micro-Doppler signature from the body of the drone looks similar to the sphere oscillation where it goes forward and backwards from the radar.

6.5 Summary

An affordable high-frequency flexibility K-band FMCW radar prototype has been successfully delivered. The prototype offers a wide range of flexibility that the user can select including the carrier frequency, ramp duration, bandwidth and time integration. Off-the-shelf components have been used in this research and demonstrated positive and promising results that could potentially improve later on. The procured components were initially verified its functionality and found out that all components are in agreement with the datasheet provided by the supplier except for the VCO which slightly differs. Then, the components are assembled and the radar prototype was first tested within the closed-loop circuit to observe the capability of the range measurement using the delay lines.

Next, five different ball spheres were evaluated. With the reference to the carrier frequency, these five balls are in the Mie region which has the RCS value in between a small size bird to a large size insect. All of the sphere balls can be detected, and the multiple target spheres can be resolved. Lastly, an ARCADE Nano Quadcopter which is widely available in the market was tested for the next experimental work. The results found out that the drone which is less than 5 cm in size could be detected by the radar developed in an indoor environment. The drone which was suspended 3 m away from the radar shows the visibility of the HERMS line induced from the 1.2-cm long rotor blade.

All these experiments demonstrated that a K-band FMCW radar is sufficient to detect the nano-targets with a low RCS value without using the millimetre wave radar. Using a K-band radar instead will apparently save the cost and retain a larger radial detection by the power of fourth. Because these experiments were carried out indoor, some of the results suffer from multipath and background reflections. An outdoor scenario will keep the background noises to a minimum especially the reflections due to the wall and ceiling buildings. However, it may introduce other problems like radar clutter, unwanted echoes from a certain object movement.

7 CONCLUSION & FUTURE WORK

7.1 General Conclusion

Therefore, in general, it can be concluded that all the objectives of the research which has been outlined in Chapter 1 were successfully achieved. A nano-size target that is less than 5 cm in size can be detected with the designed and developed prototype. This research is interested in a single target detection within an enclosed building. The detection and classification of this nano-size target can be facilitated with the help of a micro-Doppler signature. The micro-motion of the target induces a high frequency of micro-Doppler which enables and assists the radar to detect and classify.

FMCW radar has opted in this research study over other available sensors as it is robust even to the harsh weather condition and able to extract information of the target like angle, velocity and range. A diverse approach has been employed in drone detection with FMCW radar where a comprehensive review has been presented in Chapter 2. And the advantage of using FMCW instead of pulsed radar is that it could eliminate the blind range. On top of that, it is abundantly useful for nano-drone detection in an enclosed building where a high transmit power is not required and hence could reduce the cost of the prototype.

Special attention to the theoretical background of the prototype is described in Chapter 3. Detail attention to the basic parameters and performance of FMCW radar is discussed specifically. This chapter also presents the principle of FMCW radar without the presence of the IQ demodulator. The process of micro-Doppler extraction is also deliberately explained. Then, numerical simulations of several different cases are compared in Chapter 4. The size of the target

simulated was less than 5 cm. The extraction of the micro-Doppler signature has been studied with CW and FMCW radar.

Moving to the next chapter, which focuses on the design and development of an S-band and K-band FMCW radar prototype. The experimental results of the analysis are in line with the predicted outcomes. The S-Band FMCW radar prototype is tested and validated against a bigger target in Chapter 5 while the K-Band FMCW radar prototype is tested against a smaller target that is less than 5 cm in size. The results were demonstrated in Chapter 6. Both chapters showed that the micro-Doppler signature is visible in the return signal and useful for target classification. Although the K-band prototype has not been tested outside the building due to unavoidable circumstances, it is already proven positive in nano-target detection for a short-range radar prototype in an enclosed building. The results are in good agreement, justifying the working principle of the radar system built.

Every design and development involve a trade-off within the high-quality performance. There is no ideal prototype. A high-end radar may have the best performance, but it comes with the cost that is being invested. Nevertheless, if the main objectives of the research are achievable with a low-end radar, then that is a major success, and everyone can enjoy it.

7.2 Main Contributions

The research is significant in three respects:

(i) The successful delivery of the S-band FMCW radar prototype. The prototype proves that despite the IQ demodulator exclusion, the radar does still work but with a slight range limitation which is equivalent to the range resolution of the radar.

(ii) The successful delivery of the K-band FMCW radar prototype with friendly user selectivity. It offers flexible parameters of ramp duration, operating frequency, bandwidth, and time integration.

(iii) Successful delivery in nano-drone detection using the developed prototype. This concludes that an individual insect-size target can potentially be detected.

7.3 Future Work

The detection of drone has become an active and popular study among researchers as the fast-growing of drones have become a critical issue. Much work remains to be done. Several works can be implemented in the future for a significant improvement to the designed and developed radar which will offer a more sensitive and robust prototype.

1. Practical radar shares practical limitations and challenges as well. Within the limited time and limited budget, that is the best resource to procure the off-the-shelf components. However, there are other wide ranges of choices that offer better and more enhanced performance. For example, the power amplifier can be placed at the transmitter so that the power propagated to the target is higher and this will enhance the SNR signal resulting in better detection.
2. The results are promising and should be validated by a larger sample size. This research study only managed to present one type of nano-drone. There is a plan to compare the micro-Doppler signature with the other types of drones which are Nano-Falcon and Pico-Falcon. Instead of the nano-quadcopter that was demonstrated in Chapter 6, these both are nano mini size helicopters. They are about the same size as this nano-drone. However, due to the Covid-19 outbreak, the work must be delayed and stopped. Further data collection is recommended to analyse the complexity of the signature induced by another different target.

3. There is a great opportunity to employ this FMCW radar prototype for the detection of pest insects. As the insects and nano-drones almost share the same RCS's. A short-range radar would be useful in this application especially in order to curb the devastating infestation. Micro-Doppler techniques can help in the detection and classification of these types of insects.
4. Future work should also concentrate on classification aspects. The characteristic signature of each feature target will show the group belonging. Future studies could examine and classify the diverse model of nano-drones and various types of insects. A comparison study between the man-made target (i.e., nano-drones) and biological target (i.e., insects) could also be carried out. The comparison will be more challenging if it involves a biologically inspired nano-drone like a cyborg dragonfly and a Metafly bionic bird that has a flapping wing feature. It is assumed that bioinspired drones may have a strong signal return due to their material which is made of metal. Another possibility of comparison is between a real insect with no payload and an insect that is strapped with a small camera for surveillance purposes, for example, is another work to venture.
5. Apart from that, to have a target of less than 5 cm in size, it is also possible to do a DIY motor blade where the number of blades that will be observed can be switched accordingly, either from one to four propeller blades. This offers an advantage as well in terms of the body of the target is placed at one position without any unintended bulk movement. There may be a slight vibration that comes from the electric motor, but the micro-Doppler from the blade is assumed to be higher. And for the easiness of calculation, a two-bladed single propeller can be considered first before adding more propellers. However, extra safety and precautions need to be aware once the motor is switched on.
6. This research used STFT techniques to extract the micro-Doppler components from the target. The weakness of this method is that the frequency resolution is constant. One of the ways to trade in the time-

frequency resolution is by using wavelet transform where it is known as multi-resolution representation.

7. Measurement of RCS nano-drone is also a big potential to explore. There is a lot of literature that presented micro-drone RCS measurement. But there is nothing yet literature discovered for this small size nano-target apart from the insects' prospect.
8. A 30 cm range resolution is still quite big for a 5 cm target. To have a better radar performance, the bandwidth of radar can be increased. The bandwidth of the prototype can be extended up to 3 GHz with a range resolution of 5 cm. But need to be aware of the linearity of the signal to avoid the mismatch. And this will be one of the boundaries in radar design.

REFERENCES

1. B. P. Tice, "Unmanned Aerial Vehicles – The force multiplier of the 1990s," *Airpower Journal,* 1991. (Accessed 23 October 2020).
2. M. Hassanalian and A. Abdelkefi, “Classifications, applications, and design challenges of drones: A review,” *Progress in Aerospace Sciences, 2017*. doi:10.1016/j.paerosci.2017.04.003
3. V. John, “The drone threat to national security,” available at: https://www.scientificamerican.com/article/the-drone-threat-to-national-security/. (Accessed 30 October 2020).
4. V. John, “The drone threat to privacy,” available at: https://www.scientificamerican.com/article/the-drone-threat-to-privacy//. (Accessed 30 October 2020).
5. A. Foster, “The pocket-sized drone changing the way the military operates,” available at: https://www.cnet.com/news/heres-the-tiny-drone-the-us-army-just-purchased-for-soldiers/. (Accessed 24 October 2020).
6. T. Knowles, “Tiny Black Hornet drone gives combat soldiers an eye in the sky”, *The Times*, 2019, available at: https://www.thetimes.co.uk/article/tiny-black-hornet-drone-gives-combat-soldiers-an-eye-in-the-sky-3vnwwldmn. (Accessed 25 October 2020).
7. G. Roberts, “Palm-size Australian army Black Hornet nano helicopters to save lives on battlefield,” *The Courier Mail*, 2018, available at: https://www.couriermail.com.au/questnews/north/palmsize-australian-army-black-hornet-nano-helicopters-to-save-lives-on-battlefield/news-story/93dd35ba0eaf10351ed022a930551de2. (Accessed 25 October 2020).
8. G. L. Barrows, "Future visual microsensors for mini/micro-UAV applications," *Proceedings of the 2002 7th IEEE International Workshop on Cellular Neural Networks and Their Applications, Frankfurt, Germany*, 2002, pp. 498-506, DOI: 10.1109/CNNA.2002.1035087.
9. V. C. Chen, D. Tahmoush, and W. J. Miceli, *Radar Micro-Doppler Signatures: Processing and Applications.* Stevenage: The Institution of Engineering and Technology, 2014, Ebook Library, Web, 04 January 2017.

10. V. C. Chen, *The Micro-Doppler Effect in Radar*. Second Edition. Norwood, MA: Artech House, 2019.
11. A. G. Stove, A. L. Hume, P. R. Williams, and C. J. Baker, "Monostatic LPI radar architectures," *Proc. NATO RTO Meeting on Passive and LPI (Low Probability of Intercept) Radio Frequency Sensors' Warsaw,* 2001.
12. M. Jankiraman, *FMCW Radar Design*. Norwood, MA: Artech House, 2018.
13. M. Vidmar, “Design improves 4.3GHz radio altimeter accuracy. USA: Microwaves & RF,” 2005, available at: https://www.mwrf.com/systems/design-improves-43-ghz-radio-altimeter-accuracy#close-olyticsmodal. (Accessed 14th October 2019).
14. M. Salhi, M. Sliti and N. Boudriga, "An Array-based Laser Radar for UAV detection," *2019 26th IEEE International Conference on Electronics, Circuits and Systems (ICECS)*, 2019, pp. 662-665, doi: 10.1109/ICECS46596.2019.8964828
15. A. Rozantsev, S. N. Sinha, D. Dey, and P. Fua: Flight dynamics-based recovery of a UAV trajectory using ground cameras, in Proc. IEEE Conference on Computer Vision and Pattern Recognition (CVPR), 2017
16. Gonzalo R Rodriguez-Canosa Stephen Thomas Jaime Del Cerro Antonio Barrientos and Bruce MacDonald "A real-time method to detect and track moving objects (datmo) from unmanned aerial vehicles (UAVs) using a single camera" Remote Sensing vol. 4 no. 4 pp. 1090-1111 2012
17. Jian Chen and Darren M Dawson "UAV tracking with a monocular camera" Proceedings of the 45th IEEE Conference on Decision and Control pp. 3873-3878 2006
18. S. Jeon, J. Shin, Y. Lee, W. Kim, Y. Kwon and H. Yang, “Empirical study of drone sound detection in real-life environment with deep neural networks“, 2017 25th European Signal Processing Conference (EUSIPCO), Kos, 2017, pp. 1858-1862
19. J. Kim, C. Park, J. Ahn, Y. Ko, J. Park, and J. C. Gallagher: Real-time UAV sound detection and analysis system, in Proc. IEEE Sensors Applications Symposium (SAS), Glassboro, NJ, USA, 2017

20. Ellen E Case Anne M Zelnio and Brian D. Rigling "Low-cost acoustic array for small uav detection and tracking" Aerospace and Electronics Conference 2008. NAECON 2008. IEEE National pp. 110-113 2008
21. C. Aker and S. Kalkan, “Using deep networks for drone detection“, 2017 14th IEEE International Conference on Advanced Video and Signal Based Surveillance (AVSS), Lecce, 2017, pp. 1-6.
22. P. M. Miller and M. K. Goodrich, “Mini, Micro and Swarming Unmanned Aerial Vehicles: A baseline study,” *Library of Congress*, Nov 2006, https://apps.dtic.mil/dtic/tr/fulltext/u2/a521374.pdf.
23. M. Caris, W. Johannes, S. Stanko, and N. Pohl, "Millimeter wave radar for perimeter surveillance and detection of MAVs (Micro Aerial Vehicles)," *2015 16th International Radar Symposium (IRS), Dresden*, pp. 284-287, 2015.
24. M. Caris, S. Stanko, W. Johannes, S. Sieger, and N. Pohl, "Detection and tracking of Micro Aerial Vehicles with millimeter wave radar," *2016 European Radar Conference (EuRAD), London*, pp. 406-408, 2016.
25. M. Caris, W. Johannes, S. Sieger, V. Port, and S. Stanko, "Detection of small UAS with W-band radar," *2017 18th International Radar Symposium (IRS), Prague,* pp. 1-6, 2017.
26. J. Drozdowicz et al., "35 GHz FMCW drone detection system," *2016 17th International Radar Symposium (IRS), Krakow,* 2016*,* pp. 1-4.
27. D. Shin, D. Jung, D. Kim, J. Ham, and S. Park, "A distributed FMCW radar system based on fiber-optic links for small drone detection," *IEEE Transactions on Instrumentation and Measurement*, vol. 66, no. 2, pp. 340-347, February 2017.
28. J. Lee, M. Park, I. Eo and B. Koo, "An X-Band FMCW Radar for Detection and Tracking of Miniaturized UAVs," 2017 International Conference on Computational Science and Computational Intelligence (CSCI), Las Vegas, NV, 2017, pp. 1844-1845, doi: 10.1109/CSCI.2017.342
29. K. Stasiak, M. Ciesielski, A. Kurowska and W. Przybysz, "A study on using different kinds of continuous-wave radars operating in C-band for drone detection," 2018 22nd International Microwave and Radar Conference (MIKON), Poznan, 2018, pp. 521-526, doi: 10.23919/MIKON.2018.8405275

30. K. Stasiak, M. Ciesielski, P. Samczyński, D. Gromek and K. Kulpa, "Preliminary Results of Drone's Propellers Detection Using K-band and mm-Wave FMCW Radar," 2019 20th International Radar Symposium (IRS), Ulm, Germany, 2019, pp. 1-7, doi: 10.23919/IRS.2019.8768145.
31. K. Stasiak and P. Samczynski, "FMCW radar implemented in SDR architecture using a USRP device," 2017 Signal Processing Symposium (SPSympo), Jachranka, 2017, pp. 1-5, doi: 10.1109/SPS.2017.8053654
32. D. Gromek, M. Urbański, P. Krysik, P. Samczynski, A. Abramowicz and K. Kulpa, "Two channel balanced RF FMCW FrontEnd for radar applications," 2016 17th International Radar Symposium (IRS), Krakow, 2016, pp. 1-5, doi: 10.1109/IRS.2016.7497265
33. I. Hinostroza, T. Letertre and V. Mazières, "UAV detection with K band embedded FMCW radar," 2017 Mediterranean Microwave Symposium (MMS), Marseille, 2017, pp. 1-4, doi: 10.1109/MMS.2017.8497143
34. Y. Kwag, I. Woo, H. Kwak and Y. Jung, "Multi-mode SDR radar platform for small air-vehicle Drone detection," 2016 CIE International Conference on Radar (RADAR), Guangzhou, 2016, pp. 1-4, doi: 10.1109/RADAR.2016.8059254
35. Y. Wang, T. Phelps, K. Kibaroglu, M. Sayginer, Q. Ma and G. M. Rebeiz, "28 GHz 5G-Based Phased-Arrays for UAV Detection and Automotive Traffic-Monitoring Radars," 2018 IEEE/MTT-S International Microwave Symposium - IMS, Philadelphia, PA, 2018, pp. 895-898, doi: 10.1109/MWSYM.2018.8439272
36. Á. D. de Quevedo, F. I. Urzaiz, J. G. Menoyo and A. A. López, "Remotely Piloted Aircraft Detection with Persistent Radar," 2018 15th European Radar Conference (EuRAD), Madrid, 2018, pp. 317-320, doi: 10.23919/EuRAD.2018.8546546
37. Á. D. De Quevedo, F. I. Urzaiz, J. G. Menoyo and A. A. López, "Drone Detection and RCS Measurements with Ubiquitous Radar," 2018 International Conference on Radar (RADAR), Brisbane, QLD, 2018, pp. 1-6, doi: 10.1109/RADAR.2018.8557320

38. F. I. Urzaiz, Á. D. de Quevedo, A. M. Ayuso, Á. G. Machado, J. G. Menoyo and A. A. López, "Design, implementation and first experimental results of an X-band ubiquitous radar system," 2018 IEEE Radar Conference (RadarConf18), Oklahoma City, OK, 2018, pp. 1150-1155, doi: 10.1109/RADAR.2018.8378724
39. F. Ibañez Urzaiz, Á. Duque de Quevedo, J. Gismero Menoyo, and A. Asensio Lopez, “Design of radio frequency subsystems of a ubiquitous radar in X band,” in 2017 International Carnahan Conference on Security Technology (ICCST), 2017, pp. 1–5
40. A. Duque de Quevedo, F. Ibañez Urzaiz, J. Gismero Menoyo, and A. Asensio Lopez, “X-band ubiquitous radar system: First experimental results,” in 2017 International Carnahan Conference on Security Technology (ICCST), 2017, pp. 1–6
41. V. C. Chen, F. Li, S. S. Ho, and H. Wechsler, “Micro-Doppler effect in radar: Phenomenon, model, and simulation study,” *IEEE Trans. Aerosp. Electron. Syst.*, vol. 42, no. 1, pp. 2–21, January 2006.
42. D. Tahmoush, "Review of micro-Doppler signatures," *IET Radar, Sonar & Navigation*, vol. 9, no. 9, pp. 1140-1146, 2015, doi: 10.1049/iet-rsn.2015.0118.
43. C. Clemente, A. Balleri, K. Woodbridge et al., “Developments in target Micro-Doppler signature analysis: Radar imaging, ultrasound and through-the-wall radar,” *EURASIP J. Adv. Signal Process*, 2013, doi:10.1186/1687-6180-2013-47.
44. V. C. Chen, F. Li, S. S. Ho, and H. Wechsler, "Analysis of micro-Doppler signatures," *IEE Proceedings - Radar, Sonar and Navigation*, vol. 150, no. 4, pp. 271-6, 1 August 2003, doi: 10.1049/ip-rsn:20030743.
45. M. O. Padar, A. E. Ertan, and Ç. ĝ. Candan, "Classification of human motion using radar micro-Doppler signatures with hidden Markov models," *2016 IEEE Radar Conference (RadarConf)*, Philadelphia, PA, pp. 1-6, 2016, doi: 10.1109/RADAR.2016.7485201.

46. R. Ricci and A. Balleri, "Recognition of humans based on radar micro-Doppler shape spectrum features," *IET Radar, Sonar & Navigation*, vol. 9, no. 9, pp. 1216-1223, 12 2015, doi: 10.1049/iet-rsn.2014.0551.
47. M. Perassoli, A. Balleri, and K. Woodbridge, "Measurements and analysis of multistatic and multimodal micro-Doppler signatures for automatic target classification," *2014 IEEE Radar Conference*, Cincinnati, OH, pp. 0324-0328, 2014, doi: 10.1109/RADAR.2014.6875608.
48. J. Martin and B. Mulgrew, "Analysis of the theoretical radar return signal form aircraft propeller blades," *IEEE International Conference on Radar*, Arlington, VA, USA, pp. 569-572, 1990, doi: 10.1109/RADAR.1990.201091.
49. C. E. Rotander and H. Von Sydow, "Classification of helicopters by the L/N-quotient," *Radar 97* (Conf. Publ. No. 449), Edinburgh, UK, pp. 629-633, 1997, doi: 10.1049/cp:19971751.
50. S. H. Yoon, B. Kim, and Y. S. Kim, "Helicopter classification using time-frequency analysis," *Electronics Letters*, vol. 36, no. 22, pp. 1871-1872, 26 October 2000, doi: 10.1049/el:20001306.
51. L. Zuo, M. Li and X. Zhang, "Helicopter classification with a high PRF radar," *2012 International Conference on Systems and Informatics (ICSAI2012)*, Yantai, pp. 1682-1686, 2012, doi: 10.1109/ICSAI.2012.6223365.
52. V. Agnihotri, M. Sabharwal, and V. Goyal, "The extraction of key distinct features for identification and classification of helicopters using Micro-Doppler signatures," *2019 IEEE Intl Conf on Dependable, Autonomic and Secure Computing, Intl Conf on Pervasive Intelligence and Computing, Intl Conf on Cloud and Big Data Computing, Intl Conf on Cyber Science and Technology Congress* (DASC/PiCom/CBDCom/CyberSciTech), Fukuoka, Japan, pp. 893-896, 2019, doi: 10.1109/DASC/PiCom/CBDCom/CyberSciTech.2019.00164.
53. M. A. Govoni, “Micro-Doppler signal decomposition of small commercial drones,” *2017 IEEE Radar Conference,* pp. 042, May 2017.
54. X. Pan et al., "Extraction of Micro-Doppler Frequency from HRRPs of Rotating Targets," *IEEE Access*, vol. 5, pp. 26162-26174, 2017.

55. J. Ren and X. Jiang “Regularized 2-D complex-log spectral analysis and subspace reliability analysis of micro-Doppler signature for UAV detection,” *Pattern Recognition 69*, pp. 225–237, September 2017.
56. B. Wang, W. Li, L. Du, and H. Shi, "Modelling of micro-Doppler signatures from rotor blades," *IET International Radar Conference 2015*, Hangzhou, pp. 1-7, 2015, doi: 10.1049/cp.2015.1133.
57. C. Yong-bin, L. Shao-dong, and Y. Jun, "Research on micro-motion modulation characteristics of multi-rotor aircraft's rotors," *2016 CIE International Conference on Radar (RADAR)*, Guangzhou, pp. 1-4, 2016, doi: 10.1109/RADAR.2016.8059201.
58. P. Molchanov, A. Totsky, J. Astola, K. Egiazarian, S. Leshchenko, and M. Rosa-Zurera, "Aerial target classification by micro-Doppler signatures and bicoherence-based features," *2012 9th European Radar Conference*, Amsterdam, pp. 214-217, 2012.
59. C. Clemente and J. J. Soraghan, "Passive bistatic radar for helicopters classification: A feasibility study," *2012 IEEE Radar Conference*, Atlanta, GA, pp. 0946-0949, 2012, doi: 10.1109/RADAR.2012.6212273.
60. C. Clemente and J. J. Soraghan, "Application of the singular spectrum analysis for extraction of micro-doppler signature of helicopters," *IET International Conference on Radar Systems (Radar 2012)*, Glasgow, UK, pp. 1-5, 2012, doi: 10.1049/cp.2012.1662.
61. C. Clemente and J. J. Soraghan, "GNSS-based passive bistatic radar for micro-doppler analysis of helicopter rotor blades," *IEEE Transactions on Aerospace and Electronic Systems*, vol. 50, no. 1, pp. 491-500, January 2014, doi: 10.1109/TAES.2013.120018.
62. R. Zhang, G. Li, C. Clemente, and J. J. Soraghan, "Multi-aspect micro-Doppler signatures for attitude-independent L/N quotient estimation and its application to helicopter classification," *IET Radar, Sonar & Navigation,* vol. 11, no. 4, pp. 701-708, 2017, doi: 10.1049/iet-rsn.2016.0271.
63. D. Gaglione, C. Clemente, F. Coutts, Gang Li, and J. J. Soraghan, "Model-based sparse recovery method for automatic classification of helicopters,"

2015 IEEE Radar Conference (RadarCon), Arlington, VA, pp. 1161-1165, 2015, doi: 10.1109/RADAR.2015.7131169.

64. D. Gaglione, "Student research highlights: MACHe — Model-based algorithm for classification of helicopters," *IEEE Aerospace and Electronic Systems Magazine*, vol. 31, no. 8, pp. 38-40, August 2016, doi: 10.1109/MAES.2016.150246.
65. J. J. M. de Wit, R. I. A. Harmanny, and G. Prémel-Cabic, "Micro-Doppler analysis of small UAVs," *2012 9th European Radar Conference*, Amsterdam, pp. 210-213, 2012.
66. P. Molchanov, K. Egiazarian, J. Astola, R. I. A. Harmanny, and J. J. M. de Wit, "Classification of small UAVs and birds by micro-Doppler signatures," *2013 European Radar Conference*, Nuremberg, pp. 172-175, 2013.
67. R. I. A. Harmanny, J. J. M. de Wit, and G. P. Cabic, "Radar micro-Doppler feature extraction using the spectrogram and the cepstrogram," *2014 11th European Radar Conference*, Rome, pp. 165-168, 2014.
68. J. J. M. de Wit, R. I. A. Harmanny, and P. Molchanov, "Radar micro-Doppler feature extraction using the Singular Value Decomposition," *2014 International Radar Conference,* Lille, pp. 1-6, 2014.
69. D. Tahmoush, “Detection of small UAV helicopters using micro-Doppler,” *Proc. SPIE 9077 Radar Sensor Technology XVIII*, Baltimore, USA, May 2014.
70. A. Brewster and A. Balleri, "Extraction and analysis of micro-Doppler signatures by the Empirical Mode Decomposition," *2015 IEEE Radar Conference (RadarCon)*, Arlington, VA, pp. 0947-0951, 2015, doi: 10.1109/RADAR.2015.7131131.
71. F. Fioranelli, M. Ritchie, H. Griffiths, and H. Borrion, "Classification of loaded/unloaded micro-drones using multistatic radar," *Electronics Letters*, vol. 51, no. 22, pp. 1813-1815, 2015.
72. F. Hoffmann, M. Ritchie, F. Fioranelli, A. Charlish, and H. Griffiths, "Micro-Doppler based detection and tracking of UAVs with multistatic radar," *2016 IEEE Radar Conference (RadarConf)*, Philadelphia, PA, pp. 1-6, 2016.

73. M. Ritchie, F. Fioranelli, H. Griffiths, and B. Torvik, "Monostatic and bistatic radar measurements of birds and micro-drone," 2016 IEEE Radar Conference (RadarConf), Philadelphia, PA, pp. 1-5, 2016.
74. M. Ritchie, F. Fioranelli, H. Borrion, and H. Griffiths, "Multistatic micro-Doppler radar feature extraction for classification of unloaded/loaded micro-drones," *IET Radar, Sonar & Navigation*, vol. 11, no. 1, pp. 116-124, 2017.
75. L. Fuhrmann, O. Biallawons, J. Klare, R. Panhuber, R. Klenke, and J. Ender, "Micro-Doppler analysis and classification of UAVs at Ka band," *2017 18th International Radar Symposium (IRS)*, Prague, pp. 1-9, 2017.
76. S. Björklund, "Target detection and classification of small drones by boosting on radar Micro-Doppler," *2018 15th European Radar Conference (EuRAD)*, Madrid, pp. 182-185, 2018.
77. B. S. Oh, X. Guo, F. Wan, K. A. Toh, and Z. Lin, “Micro-Doppler Mini-UAV classification using empirical-mode decomposition features,” *IEEE Geoscience and Remote Sensing,* Letters 15.2., pp. 227–231, February 2018.
78. S. Rahman & D. A. Robertson, “Millimeter-wave micro-Doppler measurements of small UAVs,” *Proc. SPIE 10188, Radar Sensor Technology XXI*, Anaheim, CA, USA, vol. 10188, p. 101880T, 2017.
79. S. Rahman and D. Robertson, "Time-frequency analysis of Millimeter-wave radar Micro-Doppler data from small UAVs," *2017 Sensor Signal Processing for Defence Conference (SSPD)*, London, pp. 1-5, 2017.
80. S. Rahman & D. A. Robertson, “Coherent 24 GHz FMCW radar system for micro-Doppler studies,” *Radar Sensor Technology XXII* (eds Ranney, K. I. & Doerry, A.) 10633, 17 (SPIE, 2018), 2018.
81. S. Rahman, D. A. Robertson, “Radar micro-Doppler signatures of drones and birds at K-band and W-band,” *Sci Rep 8*, 17396, 2018.
82. A. Aldowesh, T. Alnuaim, and A. Alzogaiby, "Slow-Moving Micro-UAV detection with a small-scale Digital Array Radar," *2019 IEEE Radar Conference (RadarConf)*, Boston, MA, USA, pp. 1-5, 2019.
83. A. Aldowesh, T. BinKhamis, T. Alnuaim, and A. Alzogaiby, "Low power digital array radar for drone detection and Micro-Doppler classification,"

2019 Signal Processing Symposium (SPSympo), Krakow, Poland, pp. 203-206, 2019.

84. S. A. Musa, R. A. Raja Syamsul Azmir, A. Sali, A. Ismail, and N. E. Abd Rashid, "Micro-Doppler signature for drone detection using FSR: a theoretical and experimental validation," The Journal of Engineering, vol. 2019, no. 21, pp. 7918-7923, 11, 2019, doi: 10.1049/joe.2019.0795.
85. M. Ezuma, O. Ozdemir, C. K. Anjinappa, W. A. Gulzar, and I. Guvenc, "Micro-UAV detection with a low-grazing angle millimeter wave radar," *2019 IEEE Radio and Wireless Symposium (RWS)*, Orlando, FL, USA, pp. 1-4, 2019, doi: 10.1109/RWS.2019.8714203.
86. A. Huang, P. Sévigny, B. Balaji, and S. Rajan, "Fundamental Frequency Estimation of HERM Lines of Drones," *2020 IEEE International Radar Conference (RADAR),* Washington, DC, USA, pp. 1013-1018, 2020, doi: 10.1109/RADAR42522.2020.9114676.
87. Zaugg S, Saporta G, van Loon E, Schmaljohann H, and Liechti F, “Automatic identification of bird targets with radar via patterns produced by wing flapping,” *J R Soc Interface*.; 5(26): 1041-1053, 2018 doi:10.1098/rsif.2007.1349.
88. Q. Zhang, Y. Zeng, Y. He, and Y. Luo, "Avian detection and identification with high-resolution radar," *2008 IEEE Radar Conference,* Rome, pp. 1-6, 2018, doi: 10.1109/RADAR.2008.4721116.
89. C. M. Alabaster and E. J. Hughes, "Is it a bird or is it a plane?," *Proc. IEEE 6th International Conference on Waveform Diversity & Design*, Lihue, HI, 22nd – 27th January 2012.
90. B. Torvik, K. E. Olsen, and H. Griffiths, "K-band radar signature analysis of a flying mallard duck," *2013 14th International Radar Symposium (IRS)*, Dresden, pp. 584-591, 2013.
91. B. Torvik, K. E. Olsen, and H. D. Griffiths, "X-band measurements of radar signatures of large sea birds," *2014 International Radar Conference*, Lille, pp. 1-6, 2014, doi: 10.1109/RADAR.2014.7060266.

92. Rosa, L. et al. “Classification success of six machine learning algorithms in radar ornithology,” *International Journal of Avian Science.* Ibis, 158, pp: 28-42, 2016.
93. M. I. Skolnik, *Radar Handbook*, Third Edition, Mc Graw Hill, New York, NY, USA, 2008.
94. O’Donnell, R. M, Radar Systems Engineering. Lecture 7 – Part 1. Radar Cross Section. IEEE New Hampshire Section, IEEE AES Society. Available at: Radar 2009 a 7 radar cross section 1 (slideshare.net) (Accessed 25 October 2020)
95. https://www.globalsecurity.org/military/world/stealth-aircraft-rcs.htm
96. L. E. Frenzel Jr., *Principles of Electronic Communication Systems*, Fourth Edition, Mc Graw Hill Education, New York, 2016.
97. S. Haykin and M. Moher, *Communication Systems*. Fifth Edition, John Wiley & Sons, 2010.
98. R. Fischman, “The phase vocoder: theory and practice,” *Journal of Organised Sound*. Vol 2, pp: 127 – 145, 1997 Doi: 10.1017/S1355771897009060.
99. G. W. Stimson, *Introduction to Airborne Radar*; Second Edition, SCITECH Publishing Inc, New Jersey, 1983.
100. J. Heath, “Nyquist rate basics and sufficient sampling for ADCs,” available at: https://www.analogictips.com/adcs-sufficient-sampling-nyquists-rate/. (Accessed 14th October 2020).
101. D. N. Byrne, S. L. Buchmann, and H. G. Spangler, “Relationship between wing loading, wingbeat frequency and body mass in Homopterous insects,” *Journal of Experimental Biology,* 135: 9-23, 1988.
102. “FCC online table of frequency allocations,” *Federal Communications Commission Office of Engineering and Technology Policy and Rules Division*, Revised 7 May 2019, Page 41, available at: https://transition.fcc.gov/oet/spectrum/table/fcctable.pdf. (Accessed 6 May 2019).

103. S. Zulkifli and A. Balleri, “FMCW radar prototype development for detection and classification of nano-targets,” *2020 IEEE International Radar Conference*, Washington DC, US, April 2020.
104. S. Zulkifli and A. Balleri, “Design and development of K-Band FMCW radar for nano-drone detection,” *2020 IEEE Radar Conference*, Florence, Italy, September 2020.
105. https://www.analog.com/media/en/technical-documentation/data-sheets/hmc739.pdf. (Accessed by 24th October 2019).
106. QAV250 DIY Quadcopter Multirotor Kit & Emax MT1806 Brushless Motor & Simonk 12A ESC & CC3D & 5030 Carbon Fiber Props|12a esc|simonk 12a escemax mt1806 - AliExpress (Accessed by 20th June 2021)
107. REES52 3.7V Mini Drone DC Motor 25000 RPM -Pack of 4 pcs 55 m Propeller (Multucolour): Amazon.in: Industrial & Scientific (Accessed by 20th June 2021)